DLR-IB-FA-BS-2019-151

Development and characterization of elastic hinges for large-area, ultra-light, deployable space structures

Masterarbeit

Daniel Robert Müller

Deutsches Zentrum
für Luft- und Raumfahrt

MH-FA-56-FB03_v1.3

Institut für Faserverbundleichtbau und Adaptronik

DLR-IB-FA-BS-2019-151

Development and characterization of elastic hinges for large-area, ultra-light, deployable space structures

Zugänglichkeit:

Stufe 2 DLR intern zugänglich: analog „allgemein zugänglich“, allerdings ist dieser in ELIB nur für intern zugänglich abzulegen.

Braunschweig, *August, 2019*

Der Bericht umfasst: 150 Seiten

Abteilungsleiter: Prof. Dr.-Ing. Christian Hühne

Autoren: Daniel Robert Müller

Autor 2 / Betreuer:
Dipl.-Ing. Martin Eckhard Zander

DLR Deutsches Zentrum für Luft- und Raumfahrt

MH-FA-56-FB03_v1.3

Eidgenössische Technische Hochschule Zürich
Swiss Federal Institute of Technology Zurich

Laboratory of
Composite Materials
and Adaptive Structures

Deutsches Zentrum
für Luft- und Raumfahrt
German Aerospace Center

Master Thesis No. 19-055

Development and characterization of elastic hinges for large-area, ultra-light, deployable space structures

Daniel R. Müller

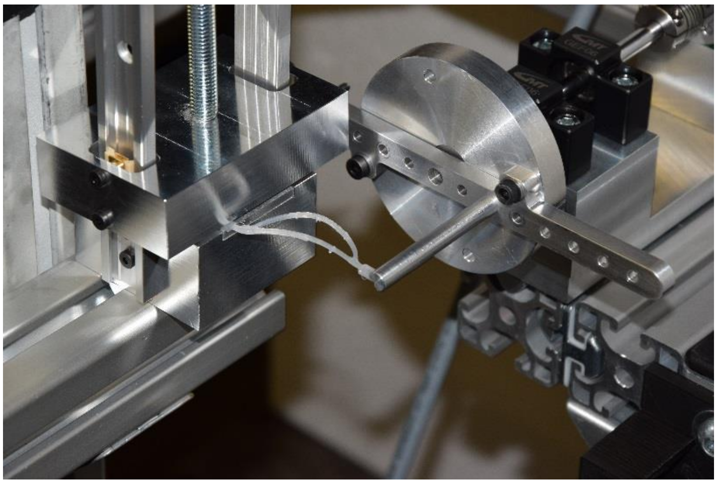

Advisor DLR: Martin E. Zander
Deutsches Zentrum für Luft- und Raumfahrt (DLR)
Institut für Faserverbundleichtbau und Adaptronik

Advisor ETH Zürich: Michael Kölbl
Laboratory of Composite Materials and Adaptive Structures (CMAS)

IDMF – Laboratory of Composite Materials and Adaptive Structures
Prof. Dr. Paolo Ermanni
ETH Zürich

16.06.2019

ETH Zürich
IDMF - Laboratory of Composite Materials and Adaptive Structures
LEE O 203
Leonhardstrasse 21
8092 Zürich

Telefon: +41 (0)44 633 63 02

www.structures.ethz.ch

Abstract

Even though they are mostly out of sight, it is hard to imagine modern life without any satellites providing us with GPS signals, radio communication or data for weather forecasts. For economic reasons, these space structures need to be lightweight and packaged to a small volume. Hence, large areas need to be folded and packed during launch. Different approaches are studied within the *Joint Deployable Space Structures* project between the *German Aerospace Center* (DLR) and the *National Aeronautics and Space Administration* (NASA). A sub-project focuses on membranes for small satellites, where solar sails, photovoltaic arrays, sunshields or drag sails are interesting applications. This thesis is placed within this sub-project and focuses on the deployment method and stiffening structure of such a membrane. Inspired by foldable insect wings, different geometries of elastic hinges are developed, parametrized and their parameters are optimized. Their performance is evaluated by a finite element (FE) model. The elastic hinges are produced by a 3D printer using the fused deposition modeling (FDM) principle. An appropriate test rig has been developed and calibrated with sample material specimens. It is independent of other commercial test rigs and only needs a data acquisition system, power supply and a *LabVIEW* capable computer. Designing the test rig has been challenged by the small reaction torques of the specimens, which showed the need for a very precise torque sensor and a good bearing of the moving parts in the test. The test station is able to measure the reaction torque of specimens during the folding as well as the deployment phase. Various different geometries and model sizes can be tested with this new test rig.

The designed test shows repeatable results and the experimental data of the tests have been collated with the FE simulations. The FE model has been adapted to the test results of the so-called *Torsion Hinge* design in order to provide correct values for further geometries. Tests on the insect wing inspired *Z-shape*, *oval-shape straight*, *tilted* and *spring* designs showed a good match with the adapted FE model.

Another big challenge was the optimization part. The calculation of an optimal solution of a parametrized model uses a lot of time and the model needs to be stable for very different parameter combinations. In addition, it has been shown that the optimization of the parametrized models is highly dependent on the parameter boundaries. Unfortunately, not all models could be optimized as far as intended. Nevertheless, good solutions have been found for all models, which could be tested. It could be shown that the four bio-inspired hinges do not differ very largely regarding their reaction torque to weight ratio. Still, the *oval-shape spring* and *tilted* models show a slightly better performance. Therefore, the *oval-shape tilted* model might be a good choice for in-plane folding as its rods are shifted, leading to a more compact folding. In addition, the spring model could be used at the connection to the satellite structure where the hinge would be outside of the fold line, leading to a compact stowage. An exemplary design of such a complete structure is shown, whereas the hinges are connected to each other with rods, which are extensions of the hinges' rods. The complete stiffening structure composed of hinges and rods shall be printed directly onto the membrane. If these rods are bonded to the membrane, they might also work as rip-stoppers to confine possible rips in the membrane due to hits of space debris or other particles in space.

Zusammenfassung

Obwohl meistens unbeachtet, ist es schwer sich ein Leben ohne Satelliten vorzustellen, die uns mit GPS-Signalen, Telekommunikation oder Daten für Wettervorhersagen versorgen. Aus wirtschaftlichen Gründen müssen diese Weltraumstrukturen leicht und möglichst klein sein. Deshalb müssen grossflächige Strukturen während des Starts gefaltet und verstaut werden. Das *Deutsche Zentrum für Luft- und Raumfahrt* (DLR) und die *National Aeronautics and Space Administration* (NASA) untersuchen verschiedene Methoden dazu im gemeinsamen Projekt *Joint Deployable Space Structures*. Ein Unterprojekt setzt den Fokus auf Membranen für kleine Satelliten. Interessante Anwendungen dabei sind Sonnensegel, Photovoltaikelemente, Sonnenschutzschirme oder Bremssegel. Die vorliegende Arbeit ist in diesem Unterprojekt untergebracht und fokussiert sich auf die Entfaltungsmethoden und Versteifungsstrukturen solcher Membranen. Inspiriert durch faltbare Insektenflügel werden verschiedene Geometrien für elastische Gelenke entwickelt, parametrisiert und die Parameter optimiert. Die Leistungsfähigkeit wird mittels eines Modells der finiten Elemente (FE) evaluiert. Die elastischen Gelenke werden mit einem 3D Drucker im Fertigungsverfahren der Schmelzschichtung (engl. Fused Deposition Modeling, FDM) hergestellt. Es wurde ein entsprechender Teststand entwickelt und mit Materialprobenmustern kalibriert. Der Teststand ist unabhängig von kommerziellen Testanlagen und benötigt einzig ein Datenerfassungssystem, Stromzufuhr und einen *LabVIEW*-fähigen Rechner. Eine grosse Herausforderung bei der Entwicklung des Teststandes war das kleine Reaktionsmoment der Prüfkörper, was einen sehr präzisen Drehmomentsensor und eine gute Lagerung der sich drehenden Teile benötigte. Der Teststand kann das Reaktionsmoment der Prüfkörper während der Phasen der Faltung und der Entfaltung aufzeichnen. Zahlreiche verschiedene Geometrien und Modellgrössen können mit diesem Teststand getestet werden.

Der entwickelte Teststand zeigt wiederholbare Resultate und die Experimente wurden mit den FE-Simulationen abgeglichen. Das FE-Modell wurde an die Testresultate der sogenannten Torsionsgelenke (engl. torsion hinge) angepasst um korrekte Werte für weitere Geometrien zu liefern. Tests mit den durch Insektenflügel inspirierten Designs *Z-Form* (engl. Z-shape)*, Oval-Form gerade* (engl. Oval-shape straight)*, schräg* (engl. Oval-shape tilted) und *Feder* (engl. Oval-shape spring) zeigen gute Übereinstimmungen mit dem angepassten FE-Modell.

Eine weitere grosse Herausforderung war der Teil der Optimierung. Die Berechnung der optimalen Lösung eines parametrisierten Modells benötigt viel Zeit und das Modell muss für sehr unterschiedliche Parameterkombinationen stabil bleiben. Dazu konnte gezeigt werden, dass die Optimierung der parametrisierten Modelle sehr von den Randbedingungen abhängig ist. Allerdings konnten nicht alle Modelle so weit optimiert werden wie zuerst gedacht. Trotzdem wurden für alle Modelle gute Resultate erzielt. Es konnte gezeigt werden, dass sich die vier durch die Natur inspirierten Gelenke in Bezug auf ihr Reaktionsmoment-zu-Gewicht-Verhältnis nicht allzu gross unterscheiden. Dennoch schnitten die Modelle *Oval-Form Feder* und *Oval-Form schräg* leicht besser ab. Deshalb wäre das Modell *Oval-Form schräg* eine gute Wahl für das Falten in der Ebene, da seine Stäbe verschoben sind, was zu einer kompakteren Faltung führt. Dazu könnte das Modell *Oval-Form Feder* an der Verbindung zur Satellitenstruktur benutzt werden wo das Gelenk aussen an der Faltlinie zu einer kompakten Verstauung führen würde. Ein Beispieldesign einer solchen kompletten Struktur wird am Ende dieser Arbeit gezeigt, wobei die Gelenke durch Stäbe, welche Verlängerungen der Gelenkstäbe sind, miteinander verbunden werden. Die Gesamte Stützstruktur aus Gelenken und Stäben soll direkt auf die Membran gedruckt werden können. Dabei könnten durch einen Einschlag durch Weltraumschrott oder andere Gegenstände hervorgerufene Risse in der Membran eingeschlossen und daran gehindert werden sich auszubreiten.

Acknowledgments

The present work has been performed at the *German Aerospace Center* (DLR) in Braunschweig, Germany. It would not have been possible without the help and support of many people.

I would like to thank Prof. Dr. Paolo Ermanni of the Laboratory of Composite Materials and Adaptive Structures (CMAS) at ETH Zurich for letting me conduct this thesis work at *DLR* in Germany and for supervising this work on behalf of ETH Zurich. A big thank you goes to my advisor in Zurich, Michael Kölbl, for building the bridges between Zurich and Braunschweig.

Special thanks go to my supervisor at *DLR*, Martin Zander, who supported me whenever needed and always had a good input when I had any questions or doubts. I would also like to thank the entire team of the *Institute of Composite Structures and Adaptive Systems* (FA) of *DLR* and the *Institute of Adaptronics and Function Integration* (IAF) of the technical university of Braunschweig for being such great colleagues.

Finally, I must express my very profound gratitude to my parents and to my brother for providing me with unfailing support and continuous encouragement throughout my years of study and through the process of researching and writing this thesis. This accomplishment would not have been possible without them. Thank you.

Deutsches Zentrum
für Luft- und Raumfahrt e.V.
in der Helmholtz-Gemeinschaft

Aufgabenstellung zur Masterarbeit

von
Herrn Daniel Robert Müller
Matr.-Nr.: 13-811-039

Thema:

Entwicklung und Charakterisierung von elastischen Gelenken für großflächige, ultra-leichte, entfaltbare Raumfahrtstrukturen

Einführung

Im Rahmen eines Kooperationsprojektes zwischen DLR und NASA werden aktuell verschiedene entfaltbare Struktursysteme für zukünftige Weltraumanwendungen entwickelt. Denkbare Anwendungen sind dabei Solar Shades (zum Abschatten von Instrumenten), Bremssegel zur Reduzierung von Weltraumschrott sowie Sonnensegel (treibstoffloser Antrieb durch Sonnenlicht). Hierzu werden grundlegend neue falt- und entfaltbare bionische, flächig verteilte Strukturen, ähnlich denen von Insektenflügeln und Blättern, entwickelt und untersucht.

Mögliche Aufgabenstellung

Innerhalb einer Masterarbeit soll ein grundlegend bestehendes FE-Modell zu elastischen Gelenk-Elementen, einer flächig verteilter Struktur, erweitert und mit praktischen Versuchen abgeglichen werden, um die mechanischen Eigenschaften zu charakterisieren. Dazu soll ein geeigneter Versuchsaufbau konstruiert und umgesetzt, sowie damit Versuche durchgeführt werden. Des Weiteren ist es notwendig die Konstruktion des Gelenk-Elements zu variieren und den Anforderungen entsprechend zu optimieren. Auf konzeptioneller Ebene sollen die erzeugten Ergebnisse anschließend in den Entwurf eines Gesamtstrukturmodells überführt werden.

Arbeitsschritte

Im Einzelnen gliedert sich die Aufgabe in folgende wesentliche Teilbereiche:

Einführende Recherche zu:

- Entfaltbaren flächigen Raumfahrtstrukturen
- Bisherigen Untersuchungen zu verteilten Strukturen
- Faltungs-/Entfaltungsmechanismen in der Bionik

Simulationen:

- Analyse und Simulation von Gelenk-Elementen der flächig verteilten, entfaltbaren Raumfahrtstruktur mittels FE (Erweiterung eines vorhandenen Modells)
- Optimierung der Gelenk-Elemente

Konstruktion:

- Definition von Anforderungen und Randbedingungen an einen Teststand für entwickelte Gelenk-Elemente
- Bewerten gefundener Konzepte bzw. Teilkonzepte
- Konstruktion und Aufbau eines Gelenk-Teststandes

Versuche:

- Teststandvalidierung mit Prüfkörpern
- Prototypen-/Probenbau mit ALM-Verfahren (Additive Layer Manufacturing)
- Durchführung von mechanischen Versuchen zur Charakterisierung von entwickelten Gelenk-Elementen

Auswertungen/Analyse:

- Auswertung der Messergebnisse und Dokumentation
- Validierung des FE-Modells mittels erzeugten Versuchsergebnissen
- Entwurf zur Konstruktion und Implementierung von Strukturelementen in das Gesamtstruktursystem

Dokumentation der Ergebnisse in einem Bericht, mündliche Präsentation der Ergebnisse

Zusätzliche Bemerkungen zu organisatorischen Punkten

Die Masterarbeit wird am Deutschen Zentrum für Luft- und Raumfahrt e.V. (DLR), Institut für Faserverbundleichtbau und Adaptronik, in der Abteilung Funktionsintegration, in Braunschweig, seitens des DLR von Herrn Dipl.-Ing. Martin E. Zander betreut.

Für Planung, Berechnung, Programmierung und Dokumentation können Labore, Werkzeuge, Einrichtungen, Programme und Rechenanlagen des DLR benutzt werden. Die Unterstützung durch das Institut für Faserverbundleichtbau und Adaptronik umfasst die Beratung sowie Hilfe bei der Einarbeitung in die Theorie und Praxis. Die Ergebnisse sind entsprechend dem Fortschritt der Arbeit, mindestens einmal wöchentlich mit dem Betreuer abzusprechen.

Dipl.-Ing. Martin E. Zander
(Betreuer DLR)

ETH
Eidgenössische Technische Hochschule Zürich
Swiss Federal Institute of Technology Zurich

Eigenständigkeitserklärung

Die unterzeichnete Eigenständigkeitserklärung ist Bestandteil jeder während des Studiums verfassten Semester-, Bachelor- und Master-Arbeit oder anderen Abschlussarbeit (auch der jeweils elektronischen Version).

Die Dozentinnen und Dozenten können auch für andere bei ihnen verfasste schriftliche Arbeiten eine Eigenständigkeitserklärung verlangen.

Ich bestätige, die vorliegende Arbeit selbständig und in eigenen Worten verfasst zu haben. Davon ausgenommen sind sprachliche und inhaltliche Korrekturvorschläge durch die Betreuer und Betreuerinnen der Arbeit.

Titel der Arbeit (in Druckschrift):

Development and characterization of elastic hinges for large-area, ultra-light, deployable space structures

Verfasst von (in Druckschrift):
Bei Gruppenarbeiten sind die Namen aller Verfasserinnen und Verfasser erforderlich.

Name(n):	**Vorname(n):**
Müller	Daniel Robert

Ich bestätige mit meiner Unterschrift:
- Ich habe keine im Merkblatt „Zitier-Knigge“ beschriebene Form des Plagiats begangen.
- Ich habe alle Methoden, Daten und Arbeitsabläufe wahrheitsgetreu dokumentiert.
- Ich habe keine Daten manipuliert.
- Ich habe alle Personen erwähnt, welche die Arbeit wesentlich unterstützt haben.

Ich nehme zur Kenntnis, dass die Arbeit mit elektronischen Hilfsmitteln auf Plagiate überprüft werden kann.

Ort, Datum	**Unterschrift(en)**

Bei Gruppenarbeiten sind die Namen aller Verfasserinnen und Verfasser erforderlich. Durch die Unterschriften bürgen sie gemeinsam für den gesamten Inhalt dieser schriftlichen Arbeit.

Contents

Abstract i

Zusammenfassung.....iii

Acknowledgments v

Task Assignement.....vii

Declaration of Originality ix

Contents xi

List of Figures.....xiii

List of Tables.....xx

Abbreviation.....xxi

List of Symbols.....xxii

1 Introduction.....1

  1.1 DLR-NASA joint project.....2

  1.2 Aim of Thesis & Approach 2

2 State of the art 5

  2.1 Deployable Satellite Structures 5

    2.1.1 Solar Arrays.....5

    2.1.2 Solar Sail 6

    2.1.3 Drag Sail.....7

    2.1.4 Solar Shades 7

  2.2 Folding & deployment techniques of lightweight structures.....8

    2.2.1 Folding techniques of technical areas 8

    2.2.2 Deployment techniques of technical elements.....9

    2.2.3 Folding and unfolding of insect wings 11

    2.2.4 Rip-Stop 19

    2.2.5 Synthesis of folding & deployment techniques..... 19

    2.2.6 Elastic Hinges..... 19

  2.3 Existing Test Mechanisms 23

3 Finite Element Simulation & Optimization..... 29

  3.1 Model generation & mesh convergence study 29

  3.2 Simulations of torsion hinges 33

  3.3 Optimization of elastic hinge design 36

    3.3.1 Topology optimization..... 37

    3.3.2 Parameter study & sensitivity analysis..... 41

3.3.3 Optimization of parametrized hinges 48
3.3.4 Optimization results 52
4 Design and evaluation of a new test stand 61
4.1 Concept determination 61
4.1.1 Partial Solutions 61
4.1.2 Morphological Box 66
4.1.3 Combination of Concepts 67
4.1.4 Evaluation 69
4.2 Test stand design 74
4.3 Test stand software 78
5 Experiments and Mechanical Characterization 79
5.1 Preliminary Testing 79
5.1.1 Results from preliminary tests 80
5.1.2 Conclusions from preliminary tests 84
5.2 Mechanical testing 85
5.2.1 Test procedure 85
5.2.2 Specimen Design & Manufacturing 85
5.2.3 Calibration & preparations 88
5.3 Results of torsion hinges 97
5.4 Results of optimized hinge models 103
5.5 Results of hinge models directly printed on a foil 106
5.5.1 Some thoughts on the long-time behavior of polymer hinges 109
6 Comparison and analysis 111
6.1 Torsion Hinge Models 111
6.2 Optimized Models 114
7 Implementation of hinges into foldable membrane structure 115
8 Conclusion and Outlook 119
8.1 Conclusions 119
8.2 Future work 120
9 Bibliography 121
A. Appendix 127
A.1. Mesh convergence study 127
A.2. Parameter study oval-shape tilted & oval-shape spring models 129
A.3. Von Mises stress of optimized models 133
A.4. Block diagrams of test stand software 134

List of Figures

Fig. 2-1: Folded solar arrays of the ISS [9] 5

Fig. 2-2: Hubble Space Telescope with deployable solar array [10] 5

Fig. 2-3: Deployment Sequence of the MegaFlex solar array [13] 6

Fig. 2-4: Artists illustration of NASA´s NanoSail-D [16] 6

Fig. 2-5: Boom during deployment [8] 6

Fig. 2-6: Different views of artist’s illustration of the JWST [18] 7

Fig. 2-7: Miura-Ori folding process [22] 8

Fig. 2-8: Wrapping around a hub folding pattern [22] 8

Fig. 2-9: Packaging concept consisting of two steps: 1. Z-folding with slipping folds, 2. Symmetric wrapping [24] 9

Fig. 2-10: Slipping folds with hinged connection (left) and ligament fold (right) [25] 9

Fig. 2-11: Packaging concept according to Arya et al. [23] 9

Fig. 2-12: Demonstration of packaging concept using a 1m x 1m, 50 µm-thick Mylar membrane. Packaged, the cylinder has a diameter of 51mm and is 40mm high [23] 9

Fig. 2-13: Different typical boom cross-sections: (A) Single open-section. (B) Closed omega-section. (C) Biconvex section. (D) Trac boom (two c-shapes bonded together) [27] 10

Fig. 2-14: Opposite sense bending of tape spring [28] 10

Fig. 2-15: Side view of partially coiled tape spring [29] 10

Fig. 2-16: The CoilABLE boom by ATK [30] 10

Fig. 2-17: Earwig unfolding its wings. (A) Both wings are folded and the cerci begin the process of deploying the right wing. (B) The right wing is completely unfolded while the left wing is still in the phase of deployment. [37] 11

Fig. 2-18: Circumferential crossing vein exhibiting a reduced degree of sclerotization (red arrow) [35] 11

Fig. 2-19: Wing of a Coleoptera beetle species (Chelorrhina polyphemus). Solid lines indicate mountain folds and dashed lines indicate valley folds [39] 12

Fig. 2-20: Wing joint and folding pattern of a beetle Monochamus sartor F. (adapted from [39]) 13

Fig. 2-21: Wing joint and folding pattern from a beetle Prionus coriarius (L.) (adapted from [39]) 13

Fig. 2-22: Diagram of wing folding pattern in the wasp-beetle Clytus [40] 13

Fig. 2-23: Annulate cross-vein in a drone fly (Eristalis tenax) (A) and a desert locust (S. gregaria) (B). Scale bars: 0.5 mm. [41] 13

Fig. 2-24: The basic mechanisms of a four-crease knot [36] 14

Fig. 2-25: Exemplary angular movement of the line *OD* from Fig. 2-24 in a bistable system (i.e. type 1 mechanism). The angles only add up to 300°. The forbidden range is shaded gray. [36] 14

Fig. 2-26: Schematic cross section of the abdomen of a beetle. A completely folded wing does not occupy the whole space available (A), whereas a slightly unfolded wing does (B). [36] 15

Fig. 2-27: Schematic of unfolded left hind wing of Forficula auricularia (common earwig) in dorsal view [36] 16

Fig. 2-28: Exemplary structure to show the function of the Zwischenfeld (Zw). In model (A) it is difficult to snap from one stable position to the other. In (B), with the cutout representing the Zwischenfeld, this can be done much easier. [36] 17

Fig. 2-29: Schematics of the force relations in an unfolded (A) and partly folded (B) wing section. The radial (R) and intercalary (I) veins point in opposite directions. (C) Hypothetical case of broadened areas pointing in the same direction. [36] 17

Fig. 2-30: Bistable gripper in open, first stable state (A) and closed, second stable state (B) [21] 18

Fig. 2-31: 4D-printed artificial earwigs hindwing unfolded (A) and folded (B) [21] 18

Fig. 2-32: Bending Radii Difference Designs [6] 21

Fig. 2-33: Torsional Hinge Designs [6] 21

Fig. 2-34: Multiple Material Designs [6] 21

Fig. 2-35: Parameters and boundary conditions of the torsion hinge model [6] 22

Fig. 2-36: CAD model of a 2TR-Hinge [6] 22

Fig. 2-37: Schematics of initial and final position of rods and connecting hinge during folding 23

Fig. 2-38: Schematics of flexure tests [49] 23

Fig. 2-39: More developed flexure tests for large deformations [50] 24

Fig. 2-40: Test set-up for biaxial bending of CFRP specimen: (A) Initial Stage. (B) Spring rule added to attach specimen. (C) Readily installed test. [52] 25

Fig. 2-41: Progressive schematic views of the LD-FPB during a test [53] 25

Fig. 2-42: CBT fixture with a thin specimen clamped during bending test [50] 25

Fig. 2-43: Idealization of the CBT showing all test parameters involved [50] 25

Fig. 2-44: Free body diagram of CBT system [50] 26

Fig. 2-45: Worst case gravity-induced sagging on CBT fixture [50] 26

Fig. 2-46: CWB CBT fixture at different stages of rotation during a test. Initial (A), Intermediate (B) & Final stage (C). [50] 26

Fig. 2-47: Buckling with both ends pinned, Euler buckling case 2 [54] 27

Fig. 2-48: Test stand to investigate the relocation of the axis of rotation by bending flexure hinges. (A) Test stand. (B) Load introduction. (C) Deflected specimen. [55] 27

Fig. 2-49: Schematic mechanisms of fatigue test stand [56] 28

Fig. 2-50: Built fatigue test stand with possibility to test 6 specimens at a time (Adapted from [56] 28

Fig. 2-51: Fixed position bending test system with hinge in tension (A) and free hinge (B) [57] 28

Fig. 3-1: Flowchart of FE modeling approach 29

Fig. 3-2: Boundary conditions for torsion hinge model (the same boundary conditions have been applied to all models) 30

Fig. 3-3: Contact pair definition for torsion hinges 30

Fig. 3-4: Comparison of maximum total displacement for model with fillets and without fillets 32

Fig. 3-5: Comparison of reaction force for models with fillets and without fillets 32

Fig. 3-6: Normalized results for model without fillets 32

Fig. 3-7: Displacements of TH-19-5-30-2-2 during simulation 34

Fig. 3-8: Von Mises stress of TH-19-5-30-2-2 during simulation 34

Fig. 3-9: Reaction forces of TH-19-5-30-2-2 during simulation 34

Fig. 3-10: Topology optimization of a beam under axial pressure 38

Fig. 3-11: Initial model for topology optimization 40

Fig. 3-12: Result for a mass restriction of 20% of the initial mass 40

Fig. 3-13: Initial model with central hole for topology optimization 40

Fig. 3-14: Result with initial hole for a mass restriction of 8% of the initial mass 40

Fig. 3-15: Overview of parametrized hinges: *Z-shape*, *oval-shape straight*, *tilted* & *spring* (from left to right) 41

Fig. 3-16: Parametrization of *Z-shape* hinge 41

Fig. 3-17: Workflow of Python script for parameter studies 42

Fig. 3-18: Pareto diagram for standardized effects with regard to maximum von Mises equivalent stress for *Z-shape* hinge 43

Fig. 3-19: Pareto diagram for standardized effects with regard to reaction force at displaced nodes for *Z-shape* hinge 43

Fig. 3-20: Parametrization of *oval-shape straight* hinge 44

Fig. 3-21: Pareto diagram for standardized effects with regard to maximum von Mises equivalent stress for *oval-shape straight* hinge 44

Fig. 3-22: Pareto diagram for standardized effects with regard to reaction force at displaced nodes for *oval-shape straight* hinge 45

Fig. 3-23: Interaction plot for adjusted means with regard to maximum von Mises equivalent stress for *oval-shape straight* hinge 45

Fig. 3-24: Interaction plot for adjusted means with regard to reaction force at displaced nodes for *oval-shape straight* hinge 46

Fig. 3-25: Parametrization of *oval-shape tilted* hinge 46

Fig. 3-26: Parametrization of *oval-shape spring* hinge 47

Fig. 3-27: Flow chart of optimization process 49

Fig. 3-28: Stress and reaction force for each iteration of the thick *Z-shape* model optimization run 1, starting point I 55

Fig. 3-29: Stress and reaction force for each iteration of the thin *Z-shape* model optimization run I 56

Fig. 3-30: Stress and reaction force for each iteration for the *oval-shape straight* model optimization run I 57

Fig. 4-1: Point Load Beam Bending 61

Fig. 4-2: Distributed Load Beam Bending 61

Fig. 4-3: Central Beam Torsion 62

Fig. 4-4: Oblique Bending 62

Fig. 4-5: Three-Point Bending 62

Fig. 4-6: Four-Point Bending 62
Fig. 4-7: Beam Bending from 2 Sides 62
Fig. 4-8: Offset Buckling 62
Fig. 4-9: Example of force sensitive resistor [66] 63
Fig. 4-10: Example of a torque sensor [67] 63
Fig. 4-11: Example of a strain gauge [68] 63
Fig. 4-12: Schematics of triangulation method (Adapted from [69]) 65
Fig. 4-13: Schematics of light travel time method (Adapted from [69]) 65
Fig. 4-14: Morphological box of partial solutions for test stand. Picture source Section 4.1.1 and [70–79] Found partial solutions marked with orange (section 4.1.3.1) & blue (section 4.1.3.2) arrows 66
Fig. 4-15: Schematics of motor-driven bending 67
Fig. 4-16: Schematics of motor-driven pulling 68
Fig. 4-17: Evaluation Matrix for Test Design 70
Fig. 4-18: Simplified idea of motor-driven bending test device 74
Fig. 4-19: Complete assembly of developed test stand 74
Fig. 4-20: Rotating part of test stand 75
Fig. 4-21: Rotating part of test stand, side-view 75
Fig. 4-22: Section through torque sensor [81] 76
Fig. 4-23: Clamping part of test stand 76
Fig. 4-24: Fixed specimen 76
Fig. 4-25: Alignment of specimen onto alignment block 77
Fig. 4-26: Fixing the upper fixture block with a fixation to change specimen 77
Fig. 4-27: Clamped and aligned specimen, initial set-up 77
Fig. 4-28:Position switch (blue) for initial adjustment of horizontal position of rotating arm (green)...... 77
Fig. 4-29: Front panel of test stand program 78
Fig. 5-1: Specimen design with geometry naming 80
Fig. 5-2: Test stand during testing 80
Fig. 5-3: 3D-Model of used test stand for preliminary tests 80
Fig. 5-4: Maximum force reached during bending up to ≈ 55° for all specimen types (torsion hinges black, round hinges blue) 81
Fig. 5-5: Influence of width parameter W on maximum force during bending up to ≈ 55° for comparable specimen types 81
Fig. 5-6: Exemplary force diagram for specimen type TH-20-4-48-1-1.5 with individual specimen reaction force and averaged force for bending during Test 1 81
Fig. 5-7: Initial state and end of ≈ 55° bending during Test 1 81
Fig. 5-8: Increase of maximum force when bending angle is increased for chosen specimens 82

Fig. 5-9: Exemplary force diagram for specimen type TH-19-5-33-2-2 with individual specimen reaction force and averaged force for release during Test 3 82

Fig. 5-10: Ratio of reaction force between full bending and 55° bending for every specimen (torsion hinges black, round hinges blue) 82

Fig. 5-11: Maximum opening force during release of fully folded specimens for all specimen types (torsion hinges black, round hinges blue) 83

Fig. 5-12: Influence of width parameter W (value red shaded in specimen name [mm]) during release of fully folded specimens for comparable specimen types 83

Fig. 5-13: Maximum reaction torque during release of fully folded specimens for all specimen types (torsion hinges black, round hinges blue) 83

Fig. 5-14: Test procedure 85

Fig. 5-15: Printing specimens with the assembly design, adding connecting cylinders to increase flatness of specimens 87

Fig. 5-16: Overview of all specimen models (only one torsion hinge model is shown for simplicity): torsion hinge (A), Z-shape thin (B), oval-shape spring (C), straight thin (D), tilted (E), tilted on foil (F), straight thick (G) & Z-shape thick (H) 87

Fig. 5-17: Printing defects for the *Z-shape* model 87

Fig. 5-18: “Zero torque” measured during sensor calibration 89

Fig. 5-19: Torque measured during sensor calibration for calibration weights of 500 g, 200 g, 100 g & 50 g 89

Fig. 5-20: Torque measured during sensor calibration for calibration weights of 20 g, 10 g & 5 g 89

Fig. 5-21: Angles measured during sensor calibration 90

Fig. 5-22: Sample material specimen 91

Fig. 5-23: Schematics of the beam bending situation 93

Fig. 5-24: Free body diagram of the beam 93

Fig. 5-25: Boundary conditions of FE model 93

Fig. 5-26: Normalized results of mesh convergence study 94

Fig. 5-27: Comparison of maximum stress in x-direction and bending torque 94

Fig. 5-28: Results for S_x with the finest mesh used in the mesh convergence study 94

Fig. 5-29: Enlargement of results for S_x from Fig. 5-28 94

Fig. 5-30: Results for S_x with the converged mesh size of 1 mm 95

Fig. 5-31: Enlargement of results for S_x from Fig. 5-30 95

Fig. 5-32: Sample material specimen installed in test stand 95

Fig. 5-33: Experimental results for bending torque of sample material specimens with theoretical level lines 96

Fig. 5-34: Overview of all torsion hinge models: TH-19-5-30-2-2 Assembly Print (A), TH-19-5-30-2-2 Individual Print (B), TH-28-6-30-2-1.5 (C), TH-28-4-30-1-1.5, trod = 1.5 mm (D), TH-28-4-30-1-1.5, trod = 2 mm (E) 97

Fig. 5-35: Overview of complete test stand during testing 97

Fig. 5-36: Geometry and naming parameters for torsion hinge models. Nomenclature: TH-L1-L2-W-T-H 97

Fig. 5-37: Experimental results for bending torque of TH-19-5-30-2-2 (Assembly Print Configuration) (Experiment 1) 99

Fig. 5-38: Experimental results for bending torque of TH-19-5-30-2-2 (Assembly Print Configuration) (Experiment 2) 99

Fig. 5-39: Visco-elastic deformation of specimen 99

Fig. 5-40: No deformation observable after leaving the specimen for 2 minutes 99

Fig. 5-41: Experimental results for bending torque of TH-19-5-30-2-2 (Individual Print Configuration) (Experiment 1) 100

Fig. 5-42: Experimental results for bending torque of TH-19-5-30-2-2 (Individual Print Configuration) (Experiment 2) 100

Fig. 5-43: Experimental results for bending torque of TH-28-6-2-1.5 (Experiment 1) 101

Fig. 5-44: Thick *Z-shape* specimen in test stand with adapted fixation (green parts) 103

Fig. 5-45: Thin *Z-shape* specimen during testing 103

Fig. 5-46: Thick *oval-shape straight* specimen during test 104

Fig. 5-47: Thin *oval-shape straight* specimen during test with adapted punch rod fixation (black) 104

Fig. 5-48: Experimental results for thin o*val-shape straight* specimen 104

Fig. 5-49: *Oval-shape tilted* specimen in test stand prepared to start bending 105

Fig. 5-50: *Oval-shape spring* specimen during test (side view) 105

Fig. 5-51: Out-of-plane displacement reducing reaction torque in bending plane (top view) 105

Fig. 5-52: Peel off during bending with foil inside 107

Fig. 5-53: Permanent deformation of *oval-shape tilted* model printed onto foil after being folded in test stand 107

Fig. 5-54: Testing of the model *oval-shape tilted* solely (A) and printed on a foil (B); one image every ten seconds during folding 108

Fig. 6-1: Von Mises stress for TH-28-6-30-2-1.5 with Young's modulus from datasheet 112

Fig. 6-2: Von Mises stress for TH-28-6-30-2-1.5 with adapted Young's modulus 112

Fig. 6-3: Comparison of Torque during folding for TH-28-4-30-1-1.5 (t_{rod} = 2.0 mm) 113

Fig. 6-4: Comparison of Torque during folding for TH-19-5-30-2-2 (Assembly Print) 113

Fig. 7-1: Wing design 1 (A) with schematic description of folding procedure (B – D) 115

Fig. 7-2: Wing design 2 (A) with schematic description of folding procedure (B –D) 116

Fig. 7-3: *Oval-shape spring* hinges at connection to the satellite 117

Fig. 7-4: Design study of CubeSat with deployable wings (right wing: Design 1; left wing: Design 2) . 117

Fig. A-1: Von Mises Stress for TH-19-5-30-2-2, mesh size: 0.25 127

Fig. A-2: Close-up of von Mises Stress for TH-19-5-30-2-2, mesh size: 0.25 127

Fig. A-3: Close-up of von Mises Stress for TH-19-5-30-2-2, mesh size: 0.25, maximum stress to plot: 80 MPa 127

Fig. A-4: Von Mises Stress for TH-19-5-30-2-2, global mesh size: 0.3, fillets: 0.1 128

Fig. A-5: Close-up of von Mises Stress for TH-19-5-30-2-2, , global mesh size: 0.3, fillets: 0.1 128

Fig. A-6: Close-up of von Mises Stress for TH-19-5-30-2-2, , global mesh size: 0.3, fillets: 0.1, maximum stress to plot: 100 MPa 128

Fig. A-7: Pareto Diagram for standardized effects with regard to maximum von Mises equivalent stress for *oval-shape tilted* hinge 129

Fig. A-8: Pareto Diagram for standardized effects with regard to reaction force at displaced nodes for *oval-shape tilted* hinge 129

Fig. A-9: Interaction plot for adjusted means with regard to maximum von Mises equivalent stress for *oval-shape tilted* hinge 130

Fig. A-10: Interaction plot for adjusted means with regard to reaction force at displaced nodes for *oval-shape tilted* hinge 130

Fig. A-11: Pareto Diagram for standardized effects with regard to maximum von Mises equivalent stress for *oval-shape spring* hinge 131

Fig. A-12: Pareto Diagram for standardized effects with regard to reaction force at displaced nodes for *oval-shape spring* hinge 131

Fig. A-13: Interaction plot for adjusted means with regard to maximum von Mises equivalent stress for *oval-shape spring* hinge 132

Fig. A-14: Interaction plot for adjusted means with regard to reaction force at displaced nodes for *oval-shape spring* hinge 132

Fig. A-15: Von Mises stress for best solution of thick model *Z-shape* folded to 110° 133

Fig. A-16: Von Mises stress for best solution of thin model *Z-shape* folded to 125° 133

Fig. A-17: Von Mises stress for best solution of thick model *oval-shape straight* folded to 110° 133

Fig. A-18: Von Mises stress for best solution of thin model *oval-shape straight* folded to 125° 133

Fig. A-19: Von Mises stress for best solution of model *oval-shape tilted* folded to 150° 133

Fig. A-20: Von Mises stress for best solution of model *oval-shape spring* folded to 150° 133

Fig. A-21: Block diagram of motion control subprogram 134

Fig. A-22: Block diagram of data collection subprogram 135

Fig. A-23: Block diagram of switch control 135

List of Tables

Tab. 3-1: Material properties of Nylon [58] used in FE model 30
Tab. 3-2: Results for FE simulations of all torsion hinge models 35
Tab. 3-3: Reaction torque to weight ratio for all torsion hinge models 35
Tab. 3-4: Overview of elastic hinges for wing folding in insect wings (picture source section 2.2.3) 36
Tab. 3-5: Setup for topology optimization 39
Tab. 3-6: Definition of optimization variables and best solution values for all models 53
Tab. 3-7: Results for best solutions for all optimized models 54
Tab. 3-8: Summary of optimization results 59
Tab. 4-1: Chosen partial solutions for motor-driven bending 67
Tab. 4-2: Chosen partial solutions for motor-driven pulling 68
Tab. 4-3: Evaluation criteria and weighting factors 69
Tab. 4-4: Resulting weighted values and ranking of each test method 72
Tab. 5-1: Desired and actual values for thickness for all torsion hinge design specimens 86
Tab. 5-2: Desired and actual values for inaccurate dimensions for optimized hinge designs 87
Tab. 5-3: Relative Errors of nominal and measured torque 89
Tab. 5-4: Material properties and dimensions of reference specimens 91
Tab. 5-5: Comparison of results for sample specimens 96
Tab. 5-6: Experimental results of torsion hinge models 102
Tab. 5-7: Experimental results of all optimized models 103
Tab. 5-8: Material properties of Makrofol® DE 1-4 000000 [93] 106
Tab. 5-9: Experimental results of optimized model: Tilted printed on foil 107
Tab. 5-10: Results for FE simulations (150° bending) of optimized model: Tilted printed on foil 107
Tab. 6-1: Test & FE results of the reaction torque for all tested torsion hinge models 112
Tab. 6-2: Maximum von Mises stress for all tested torsion hinge models with adapted stiffness 112
Tab. 6-3: Test & FE results of the reaction torque for all tested optimized models 114

Abbreviation

ABS	Acrylonitrile Butadiene Styrene
APDL	ANSYS Parametric Design Language
ASTM	American Society for Testing and Materials
CAD	Computer Aided Design
CBT	Column Bending Test
CLF	Concave Longitudinal Fold
cv	Concave
CWB CBT	Counter-Weight Balanced CBT
cx	Convex
DAQ	Data Acquisition System
DLR	Deutsches Zentrum für Luft- und Raumfahrt (German Aerospace Center)
EAP	Electroactive Polymers
FE / FEA	Finite Element (Analysis)
FDM	Fused Deposition Modeling
FMG	Flügelmittelgelenk (Wing Central Joint)
IKAROS	Interplanetary Kite-craft Accelerated by Radiation of the Sun
ISS	International Space Center
JAXA	Japan Aerospace Exploration Agency
JWST	James Webb Space Telescope
LD-FPB	Large Deformation Four-Point Bending
LEO	Lower Earth Orbit
LET-Joint	Lamina Emergent Torsional Joint
NASA	National Aeronautics and Space Administration
PA	Polyamide (Nylon)
PLA	Polylactic Acid
SMA	Shape Memory Alloys
SOW	Sagging under its own weight
TRL	Technology Readiness Level

List of Symbols

α	Angle of displacement per increment / Bending angle
β	Prescribed angle of final displacement
E	Young's modulus
F_{react}	Total reaction force
F_x	Reaction force in x-direction
F_y	Reaction force in y-direction
F_z	Reaction force in z-direction
g	Inequality constraint
I	Moment of inetria
L	Length
M	Torque
m	Mass
n	Increment number
ν	Poisson's ratio
N	Number of increments
P	Point load / force
p	Distributed force
$R_{p,0.2}$	Maximum yield stress
ρ	Specific material density
σ	Von Mises stress
U_x	Displacement in x-direction
U_y	Displacement in y-direction
U_z	Displacement in z-direction
V	Volume
w	Beam deflection

1 Introduction

Today, space is a widely used environment not only for space exploration itself as is done for example with the Hubble space telescope, but also for daily use. Imagine no satellites providing earth with information about the earth's atmosphere for meteorological weather predictions. In addition, today's communication or positioning systems are relying on satellite communication. However, catapulting a satellite into space is very expensive. To lift a payload of one kilogram to the lower earth orbit (LEO) where for example the International Space Station ISS is located, costs about 8900 USD with an Ariane 5 ECA and between 9500 to 13400 USD with an Atlas V. Even with a Falcon 9 from SpaceX reusing some parts of the spacecraft, it costs about 2150 USD per kilogram payload to lift it into LEO. [1]

To lower the price of launching but also decreasing the fuel consumption during the spacecraft's service life, the aim is to design lighter structures for every part of a spacecraft. Some structures like solar arrays or antennas cannot be reduced in their dimensions due to their purpose. To optimize their functions their areas need to be as large as possible which is contradictory to the mass saving goals explained before. Therefore, the stabilizing structures need to be as lightweight as possible. Thus, membrane dominated structures have been found being lightweight and package efficiently for launch. [2]

However, these packaged structures need to be deployed in space to achieve their desired geometry and be able to perform their tasks according to their requirements. Such structures include solar arrays, large antennas, solar sails, sunshields and other large structures that are used to collect, reflect or transmit any kind of radiation. Especially for small satellites which are used more and more today due to their lower payload, these structures need to be packed during lift-off and then deployed when the satellite has reached its orbit.

Today, deployment is commonly done by external power like electrical motors or inflation. These mechanisms are only used during deployment and add unnecessary and unwanted weight to the spacecraft. Therefore, a goal of current research is to generate and conserve the deployment forces on earth by the use of elastic deformation of a structure. [3] The stored intrinsic elastic energy in a folded structure would then be released in orbit to deploy the structure.

What is also important to consider for large area structures is that in the range of satellite orbits there are many micrometeoroids and especially lots of orbital debris. Collisions between such debris and the satellite structure can cause damage to the membrane and therefore the structure need to be able to withstand such impacts. This means that tears or rips need to be stopped by the structure itself by use of rip-stops. [3] Again, to reduce the overall structure's weight, the rip-stop mechanism should be included in the membrane reinforcing structure, which is responsible for the elastic deployment.

Concluding those aspects, one can summarize that the large membrane structures need to be developed such that they can be packed efficiently, deploy under stored elastic energy and have an inherent rip-stop mechanism in order to be cost-effective and durable.

1.1 DLR-NASA joint project

The decreasing size of satellites also leads to adapting its subsystems. To increase the performance of small satellites, new methods for packaging and deployment of large structures need to be developed. Nowadays, boom concepts are used for deployment, which are designed for large satellites with large equipment. Downscaling these boom designs for small satellites leads to manufacturing issues due to restricted packing capacity. To outrun this problem, boom and array deployment concepts for small satellites, such as solar sails, solar shields or drag sails shall be developed in a DLR-NASA joint project started in 2016. The project is especially focusing on booms with a reliable deployment in the range of 5 to 20 meters length which can be stowed in small satellites as for example a 3U CubeSat[1]. [5]

The goal of the project is to advance at least one boom concept to a technology readiness level (TRL) of six and to overcome the lack of predictable, testable and reliable technology for small satellite deployable booms. [5]

1.2 Aim of Thesis & Approach

This thesis is placed within a sub-project of the above-described collaborative project. The goal is to develop a small membrane structure suitable for CubeSat applications. Possible applications for those structures are drag sails, solar sails or solar shields. However, the final application of the membrane is not yet specified and will depend on the results of this project. The new deployment method should overcome the downscaling problem of the boom structures. Those new foldable and deployable structures follow the ideas of nature whereby tree leafs and insect wings are an inspiration to bionic and planar distributed structures.

The main objectives of this sub-project are [6]:

- Developing a stiffening structure for a membrane. This structure needs to be lightweight and integrated into or distributed onto the membrane such that the membrane can be packed and stowed inside a CubeSat.
- Developing a lightweight and low-volume deployment method and examining the potential of self-deployment through stored intrinsic energy.

Previous works have shown that elastic hinges seem to be a promising solution for future deployable satellite structures. In his master's thesis at DLR, Jannic Völker proposed different elastic hinge configurations and made qualitative tests [6]. He found a so-called *Torsion Hinge* configuration, which can be folded and then reopens itself after being released from folding. His results will be further investigated in the present thesis. To do so, the torsion hinge will be the basis for improving an existing finite element (FE) model from Jannic Völker. In addition, a test stand will be designed to validate the FE simulation results.

Hence, the aim of the present thesis is to design a test stand applicable to test the force and torque reaction of the elastic hinges together with their respective angle change during their folding and deployment. The resulting information should then be integrated into the existing FE model to improve its predictions. Then, the FE model should be adapted to different elastic hinge configurations in order to find the best hinge configuration regarding opening angle and reaction forces and torques. The chosen hinges should then constitute the basis for an initial rod and hinge placement on a planar field in order to build a demonstrator for the new elastic-hinge-based deployment technique studied in the present work. The obtained information in this thesis should present a basis for a deployment demonstrator, which should be tested in a parabolic flight campaign by DLR and NASA in 2020.

---

[1] A CubeSat is a standardized small satellite with dimensions of 10 x 10 x 10 cm and a maximum weight of 1.33 kg (3 lbs) per unit (1U). [4] Therefore, a 3U CubeSat can weigh up to 4 kg and has dimensions of 30 x 10 x 10 cm.

The main goal of this thesis is to extend and adapt an existing finite element model for the folding and deployment of elastic hinges. The model should be collated with experimental data to characterize the mechanical properties of different elastic hinge configurations or shapes. To do so, an appropriate test stand should be developed and constructed. The boundary conditions and load introduction of the test and the FE model should be consistent. Therefore, the FE simulations can be verified.

The major tasks can be subdivided into the following:

1. Carry out a literature research on deployable space structures and bionic structures and their mechanisms, as well as bending test methods.
2. Develop a test stand for a realistic bending test, based on the literature research about testing methods.
3. Extend and adapt an existing FE model of elastic hinges according to the developed test stand.
4. Print prototypes of the elastic hinges with 3D printers.
5. Perform tests with the prototypes on the test stand and collate the results with the FE model.
6. Make suggestions on how to implement the elastic hinges as structural elements into the overall structure.

2 State of the art

This thesis is confronted with several different backgrounds and with a wide range of subjects. To account for that, a systematic literature research has been conducted. The state of the art of deployable satellite structures is examined first, followed by the development of different approaches to folding and deployment techniques as well as different testing techniques.

2.1 Deployable Satellite Structures

2.1.1 Solar Arrays

Compared to the service life of a satellite, the sun is an unlimited energy provider. Therefore, every space structure that needs more energy than can be supplied by an inherent battery is equipped with solar arrays. Those arrays are most often bigger than the space structure itself, which means that the arrays need to be deployed in orbit. To be able to do this, the solar arrays need to be flexible and to save payload cost, they also need to be lightweight. Therefore, important characteristics for solar panels in space applications are the power-to-mass ratio (W/kg) and its volume during launch (W/m^3 folded). Different thin film solar cells have been developed. An example is the process of printing solar cells onto a substrate which is foldable, developed at the Massachusetts Institute of Technology (MIT) [7].

An example for using such a deployable solar array is the International Space Station (ISS). Its solar cells on a thin flexible body have been folded in a zigzag-shape and where then pulled apart by a truss when having reached the orbit. The reinforcement of the solar cells has been done by hinge bands, which are located between the solar cells (white parts in Fig. 2-1). The ISS solar arrays can also be retracted and restowed. [8]

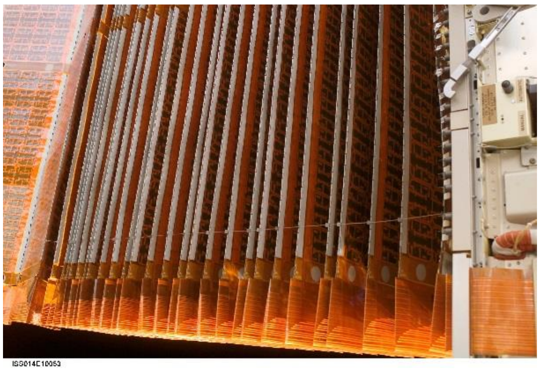

Fig. 2-1: Folded solar arrays of the ISS [9]

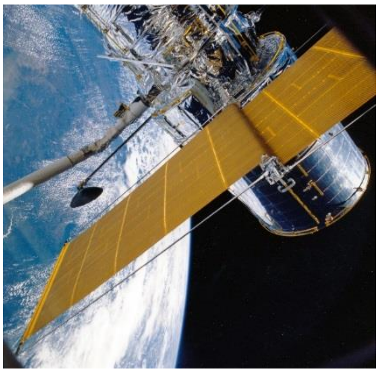

Fig. 2-2: Hubble Space Telescope with deployable solar array [10]

Another example for this type of system is the Hubble space telescope, which also uses this kind of tensioned blanket solar array for the initial arrays (See Fig. 2-2). The difference is that for the Hubble telescope the blanket was unrolled from a cylinder, pulled by two booms. However, vibrational disturbances have been observed soon after deployment, which could not be controlled to all extent. Therefore, mechanically and thermally redesigned solar arrays have been installed during the first service mission. [11]

This problem is typical for thin structures and membranes possessing low natural frequencies and low damping rate. In addition, by pointing one side of the membrane to the sun, the large thermal loads increase the possibility of disturbances.

An alternative folding and deployment technique has been developed by the company Orbital ATK for the solar arrays UltraFlex and MegaFlex. The flexible solar arrays are folded like an accordion and look like a closed-circle handheld fan in the deployed state as can be seen in Fig. 2-3. The MegaFlex has been developed for NASA´s Solar Electric Propulsion systems and is an evolution of the UltraFlex aboard the recent mission to Mars called "InSight". [12]

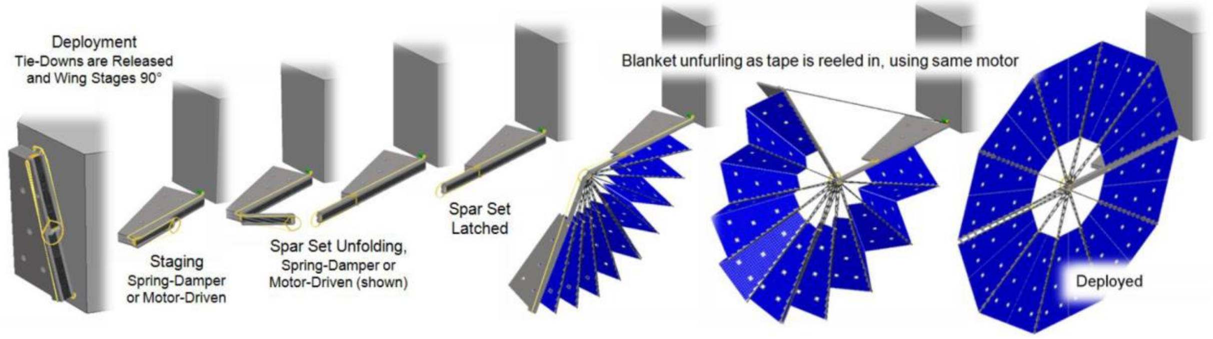
Deployment
Tie-Downs are Released
and Wing Stages 90°
Staging
Spring-Damper
or Motor-Driven
Spar Set Unfolding,
Spring-Damper or
Motor-Driven (shown)
Spar Set
Latched
Blanket unfurling as tape is reeled in, using same motor
Deployed

Fig. 2-3: Deployment Sequence of the MegaFlex solar array [13]

2.1.2 Solar Sail

In order to increase possible future mission duration and distance, solar sails could be an elegant form of propulsion. Unlike state-of-the-art propellants, solar sails do not need reaction mass but gain momentum from impacting photons, the packages of which the sunlight is composed. The idea is the same as for sailing boats with the only difference that the impinging wind is replaced by the impacting photons, called radiation pressure. As the photons are vanishingly small the solar sail must have a large surface to intercept a large number of photons and has to be extremely lightweight such that the acceleration due to the photon impact can get as high as possible. Then, the propulsion system is only limited by the service life of the sail membrane in space. [14]

An exemplary mission using a solar sail was the "Interplanetary Kite-craft Accelerated by Radiation of the Sun" (IKAROS) mission which was launched in 2010 by the Japan Aerospace Exploration Agency (JAXA) onto a Venus transfer orbit and was only accelerated through radiation pressure. In addition, JAXA also used the deployed solar sail as a base for thin-film solar cells killing two birds with one stone. [15]

A typical configuration for solar sails consists of four booms deploying from the spacecraft in an X-configuration leading to a rectangular deployed sail as can be seen in Fig. 2-4.

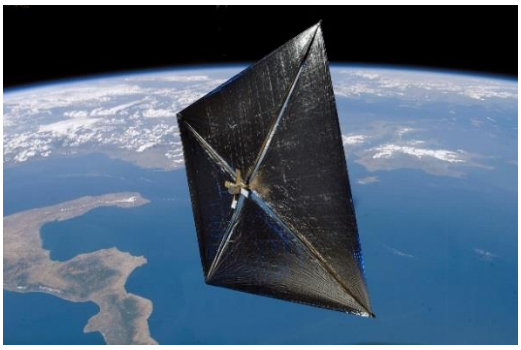

Fig. 2-4: Artists illustration of NASA´s NanoSail-D [16]

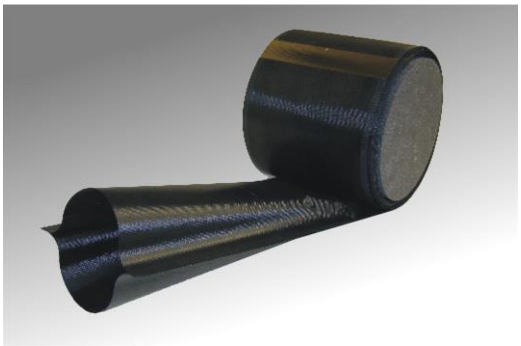

Fig. 2-5: Boom during deployment [8]

The deploying booms usually have a “double-omega” cross-section when deployed. Stowed, they are flat and rolled until they are unrolled by an external trigger (i.e. motor) changing their cross-section back to the “double-omega” as can be seen in Fig. 2-5. Together with or shortly after the booms, the membranes connected to the tip of the booms are pulled out of the spacecraft.

2.1.3 Drag Sail

To decrease the amount of orbital space debris in Earth’s orbit, a satellite orbiting the earth should be deorbited after its service life. To do so, one could deploy a drag sail to enlarge the spacecraft’s area, increasing the aerodynamic drag. As a satellite mission can take up to 10 to 15 years, these drag sails need to be stowed for a long time. Hence, finding appropriate materials and mechanisms still working after such a long stowing time is a big challenge.

Apart from the different usage and deployment time during its life cycle, drag sails have a similar architecture as solar sails, differing only in the membrane properties and stability requirements. [6]

2.1.4 Solar Shades

Solar shades, also called sunshields or thermal shields, are used to block radiation coming from the sun or warm heat emitting spacecraft subsystems. One example to mention is the thermal protection of sensitive optical instruments such as infrared telescopes. The solar shades not only prevent the telescope from disturbing sunlight but also act as barriers blocking radiant transfer of heat to the instrument. An example for such an application is the James Webb Space Telescope (JWST) (See Fig. 2-6). This telescope is a large infrared space telescope, which means that the installed instruments work primarily in the infrared range of the electromagnetic spectrum. The goal of the JWST is to peer back over 13.5 billion years and see the first stars and galaxies of the early universe. Additionally, the atmosphere of extrasolar planets should be observed. [17]

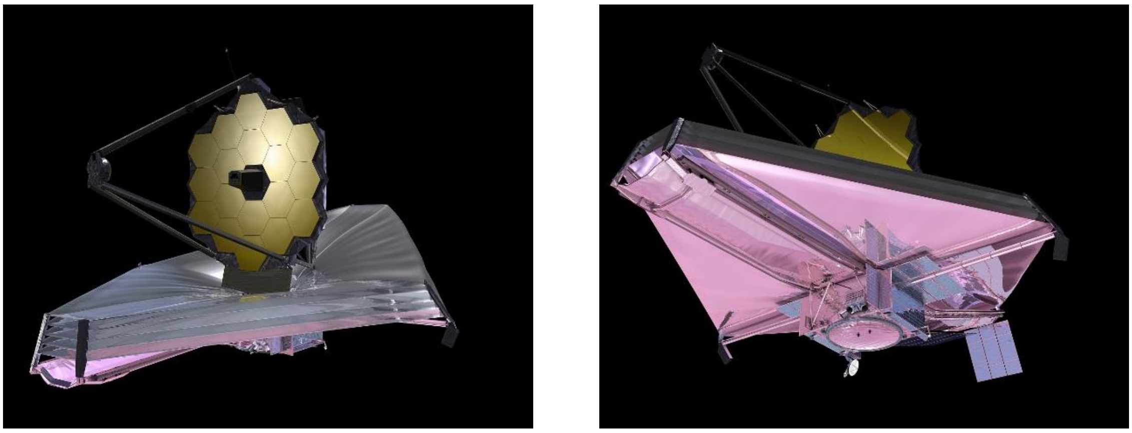
(A) Cold, space-facing top (B) Warm, sun-facing bottom

Fig. 2-6: Different views of artist’s illustration of the JWST [18]

The JWST had several difficulties during its development and therefore had numerous delays and cost overruns. Just recently, the launch needed to be delayed again due to rips in the sunshield [19]. A new launch date is set for March 2021. [20]

2.2 Folding & deployment techniques of lightweight structures

As already seen in the previous chapter, several folding and deployment techniques have been used for space structures. This chapter gives an overview of possible folding and deployment techniques and designs including bioinspired techniques.

2.2.1 Folding techniques of technical areas

There are several methods to get a repeatable folding scheme but, in the end, it depends on the deployment method, the available stowing volume and how the structure will be folded. Simple folding techniques as the “Z-Folding” for the ISS solar arrays (Fig. 2-1) or the “Fan-folding” (Fig. 2-3) have already been used on space missions. A more complicated folding process is the Miura-Ori folding, a further stage of the well-known Origami. The difference from normal folding is that the angle between the folding lines is not 90°. This leads to the advantage that a movement in one direction directly leads to the same movement in the other direction. A general folding process is shown in Fig. 2-7. A major drawback of Origami structures is that they only have one degree of freedom, not associated with a stiffness during folding and unfolding. Therefore, the mechanisms are purely kinematic and cannot have load-bearing functions. [21]

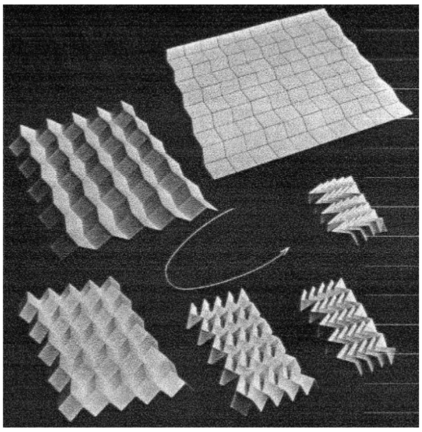

Fig. 2-7: Miura-Ori folding process [22]

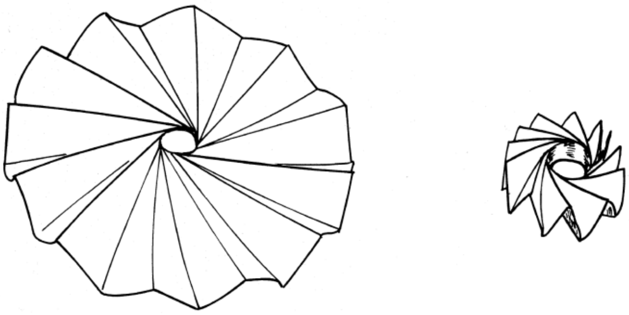

Fig. 2-8: Wrapping around a hub folding pattern [22]

Another membrane folding technique used for OrigamiSat-1 is the wrapping around a hub method as shown in Fig. 2-8. This technique has further been improved by Arya et al. [23]. To avoid local buckles and wrinkling leading to deformation, they introduced a wrapping method with slipping folds, which allow for both rotation and translation along the axis of the fold as can be seen in Fig. 2-9. By using this technique, one can fold and wrap membranes very tightly while still accommodating the thickness of each strip. What is important is that the connections between the sheets, where the folds take place are stiff enough (Fig. 2-10). The developed packaging concept is based on the slipping folds connecting the strips to each other. The fold pattern has equally spaced squares, alternating between mountain and valley folds. This produces a star-like shape and has four arms as shown in Fig. 2-11 (c). By wrapping those arms around a cylinder, one gets a very tense packed cylindrical form. [23]

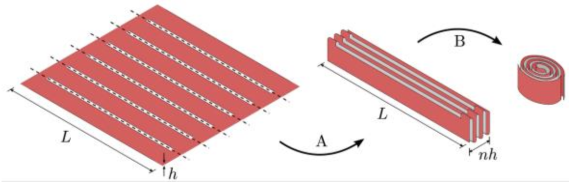

Fig. 2-9: Packaging concept consisting of two steps: 1. Z-folding with slipping folds, 2. Symmetric wrapping [24]

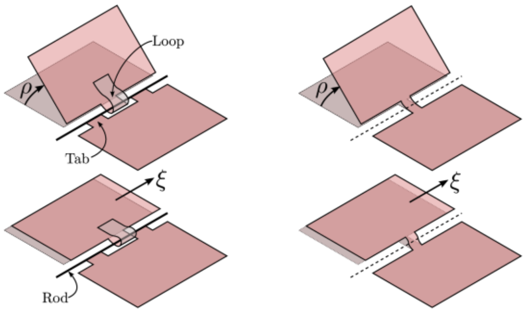

Fig. 2-10: Slipping folds with hinged connection (left) and ligament fold (right) [25]

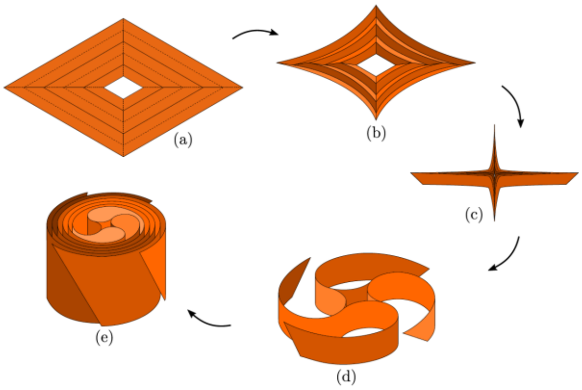

Fig. 2-11: Packaging concept according to Arya et al. [23]

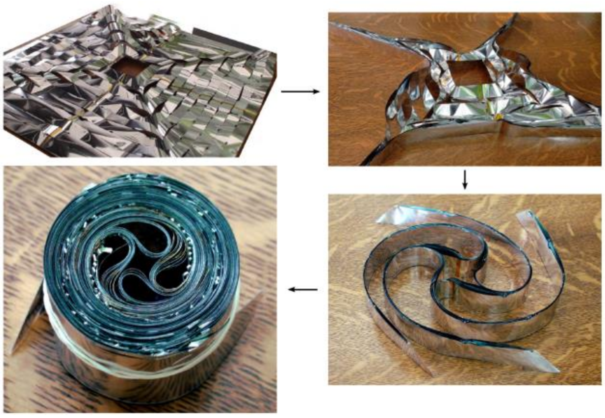

Fig. 2-12: Demonstration of packaging concept using a 1m x 1m, 50 µm-thick Mylar membrane. Packaged, the cylinder has a diameter of 51mm and is 40mm high [23]

2.2.2 Deployment techniques of technical elements

A simple method to deploy a structure is the use of a motor. However, this adds unnecessary mass and volume. One can also inflate the packed structure by using an inflation gas, as done by NASA´s ECHO balloon satellites deploying a 0.67 meter diameter packed container to a 30 meter diameter balloon. [26]

Using centrifugal forces for an even deployment around a rotatable axis has been used for the already mentioned IKAROS Mission to deploy its solar sail. A drawback of this technique is that fuel is needed to initialize the spin and that a rotating spacecraft might lead to disadvantages. [15]

Another possibility are deployable booms. As described in section 2.1.2, the boom is pressed flat and rolled around a cylinder. When the boom is deployed, it unrolls from the cylinder and changes its cross-section to form a rigid boom. The cross-section does not necessarily need to be the “double-omega” but can also have different cross-sections as shown in Fig. 2-13. Simplifying or downscaling the boom design, the boom can be reduced to only one arc instead of the two opposing arcs in the boom (Fig. 2-15). This design is called “Tape Spring” and can be used as a tape spring hinge as can be seen in Fig. 2-14.

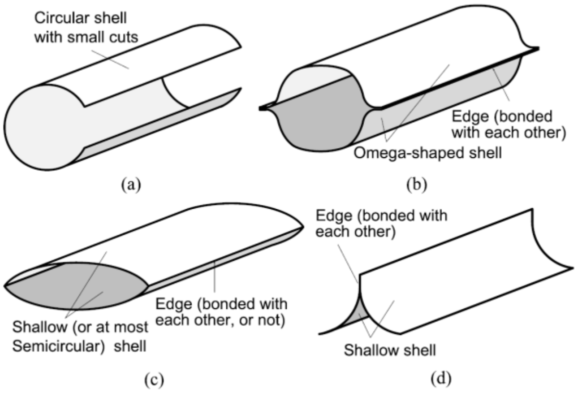

Fig. 2-13: Different typical boom cross-sections: (A) Single open-section. (B) Closed omega-section. (C) Biconvex section. (D) Trac boom (two c-shapes bonded together) [27]

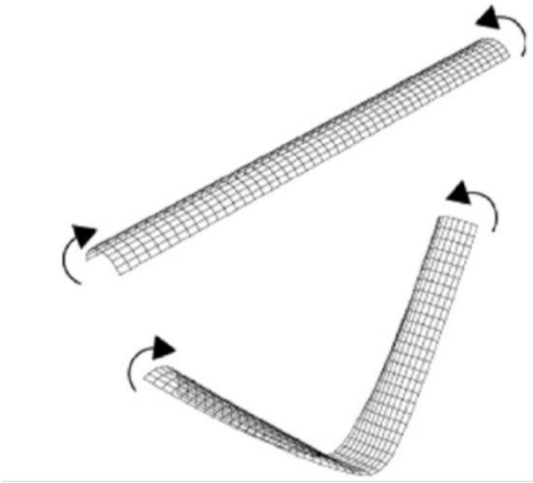

Fig. 2-14: Opposite sense bending of tape spring [28]

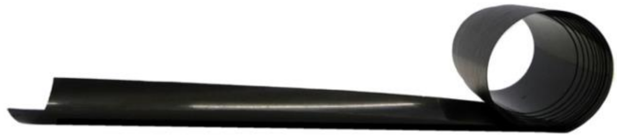

Fig. 2-15: Side view of partially coiled tape spring [29]

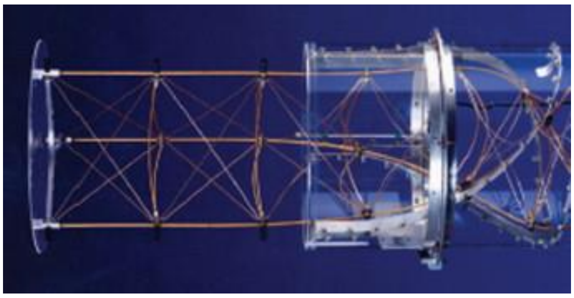

Fig. 2-16: The CoilABLE boom by ATK [30]

Truss booms are much stiffer and provide a higher strength than tubular booms. They have proven their reliability and efficiency for many space missions in the last years (see Fig. 2-16). The idea is that continuous carbon fiber longerons can be elastically coiled into a box for stowage. During deployment, the coiled longerons will either be uncoiled by a motor at the bottom of the box or the stowed package will rotate itself for deployment. A major drawback is that they require a box for packaging which normally exceeds the allowable volume on a small satellite and therefore will not be studied further in this thesis.

Very recent studies also showed progress on the investigation of shape memory alloys (SMA) and electroactive polymers (EAP). An SMA can be deformed and stays in that new form until it is heated and then returns to its initial shape. There are one-way SMAs keeping their original shape independent of the following temperatures as opposed to two-way SMAs, which can change their shape again by cooling back. [31] Hill et al. [32] studied a thin film of Nickel Titanium (NiTi) added to membranes as a deployment method.

Compared to SMA’s changing shape due to a temperature change, EAP change their shape in response to electrical stimulation and are therefore also called artificial muscles. However, the technology has not been developed enough such that it could be incorporated into a space application without a substantial increase in development resources. [33]

The deployment technique, which will be studied further in this thesis, is using a structure under tension, working like a spring. Mini rods with elastic hinges distributed over a membrane, which are tensioned while being folded, are an example for such a structure.

2.2.3 Folding and unfolding of insect wings

An inspiring example of a self-deploying or self-folding structure is coming from nature. Some insect groups as beetles or earwigs are able to fold and deploy their hindwings with a large unfold-to-fold ratio. The reason why many insects fold their wings is straightforward. If the wings of soil and ground living insects would always be deployed, they would quickly be damaged by water, dirt and other external factors. To protect the fragile wings, they are stowed under leathery or firm forewings, also called tegmina or elytra, respectively. Still, it is important for many insects to have relatively large wings to be able to disperse and find new habitats. To do so, the wings of those insects are usually longer than their abdomen and the forewings, which means that they have to be folded and stowed under the forewings. To maintain the insect's maneuverability, the stiff forewings need to be smaller than the total abdomen, which requires the wings' folding pattern to be even better. The solutions to maintain both of these conflicting requirements, the protection and the maneuverability, brought up some complex folding techniques in insects. A very impressive example is the earwig (Dermaptera) as its package ratio is reported to be in the order of 1:10 [34] up to 1:18 [35] compared to the deployed wing. [36]

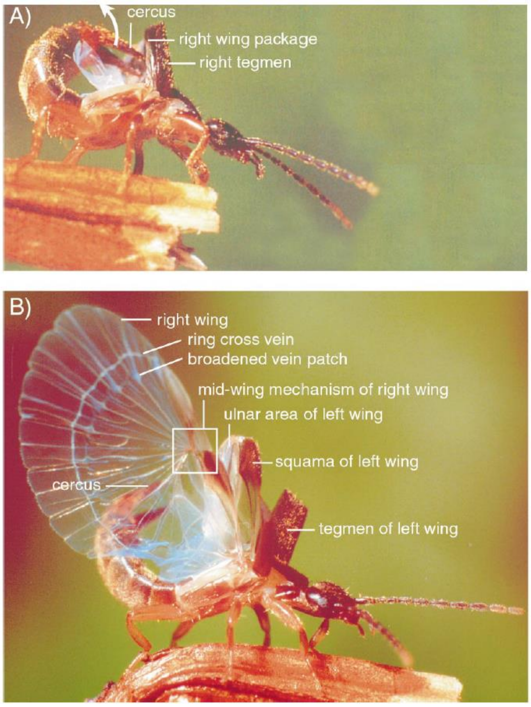

Fig. 2-17: Earwig unfolding its wings. (A) Both wings are folded and the cerci begin the process of deploying the right wing. (B) The right wing is completely unfolded while the left wing is still in the phase of deployment. [37]

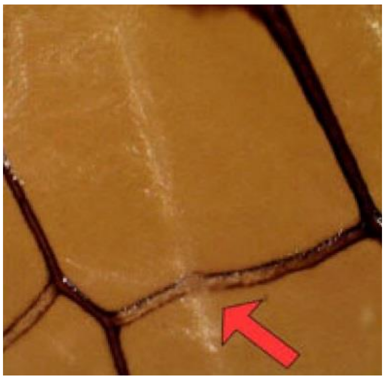

Fig. 2-18: Circumferential crossing vein exhibiting a reduced degree of sclerotization (red arrow) [35]

Fig. 2-17 shows an earwig unfolding its right wing. The folding scheme is so complicated that it needs more than a single muscle to unfold the wing (see Fig. 2-27 for the folding scheme). It has been shown that elasticity in the wing's veins is used to perform this cyclic activity [34]. Haas et al. [37] describe that the folding is achieved by intrinsic elastic forces. Resilin, a rubberlike protein has been found as being the major aspect for folding and preventing material fatigue during the multiple folding and unfolding cycles. It is assumed that the wing folding is driven by elastic recoil of the anisotropically distributed resilin on either the lower or upper sides of broadened vein patches in the intercalary and radiating veins [38]. Opposing bending directions are also due to a different placement of a layer of resilin. It has been suggested that the wing hinge ligaments can take up compressive as well as tensile forces and contribute to the kinetic energy storage at the maximum wing deflection and the wing acceleration during the downstroke by elastic recoil [38]. In addition, resilin also stores the energy to keep the mid-wing mechanism in the locked position during flight. The mid-wing mechanism is bistable and is used to lock the wing in its unfolded state. [37]

Fig. 2-18 shows that along the folding line, the circumferential crossing vein exhibits a reduced degree of sclerotization (hardening). Therefore, the folding can be done without plastic deformation of the wing [35]. Even more interesting is the shape of the broadened vein patches in the intercalary and radiating veins (see Fig. 2-27). The base structure has a round or oval shape and the vein patches exhibit a large variability of the placement of leading and trailing veins. In some patches, the leading and trailing veins are on one line and parallel to each other, while in other patches the two veins are strongly shifted and tilted up to about 40°. The shifting and tilting also induces that the vein patches are not circular anymore but tilted as well. This might lead to a better stress distribution along the fold line, as the vein patches might not only be bent but are able to move out of plane and rotate.

Other beetle species (Coleoptera) have been investigated in Geisler et al [39]. It could be shown that most fold lines of the various beetle species belonging to the order of Coleoptera try to avoid folding the veins. The fold lines are therefore mostly along the veins, only folding the wing membrane (Fig. 2-19). However, to be able to fold the wing parallel to the insect's body a fold line passing through the veins is needed as it is achieved without fatigue damage in earwigs with the broadened vein patches. The Coleoptera have developed a somewhat different structure. Some of the veins are reduced in cross section as for the circumferential crossing veins in earwigs, however, not a clear design structure can be observed. There are veins that are L-shaped, some are more Z-shaped and some are more bulky and broadened at the fold line resulting in a kidney-shape (Fig. 2-20 & Fig. 2-21).

The Z-shaped hinge has also been observed in the wasp-beetle Clytus [40], where the wing rotates around the so-called costal hinge (Fig. 2-22). This rotation is mechanically preferred over pure bending as the stresses are distributed over the whole length of the middle part of the Z while in pure bending the stresses are only distributed through the small cross-section.

A very different approach has been found in drone flies and desert locusts, where the veins exhibit an annular shape, which decreases the vein cross-section in between two adjacent annuli. This makes the veins more flexible and reduces the bending strain and therefore also the bending stress. Vacuum cleaner hoses are daily-use example for this design approach. [41]

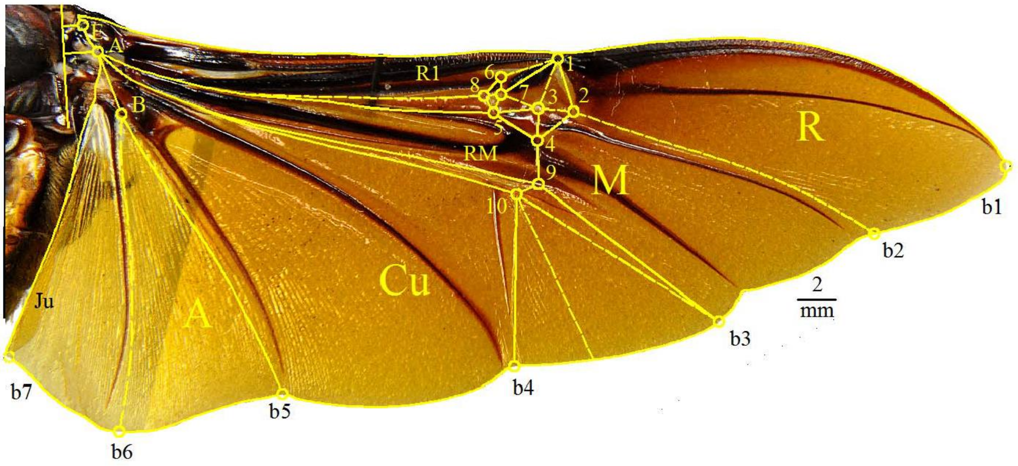

Fig. 2-19: Wing of a Coleoptera beetle species (Chelorrhina polyphemus). Solid lines indicate mountain folds and dashed lines indicate valley folds [39]

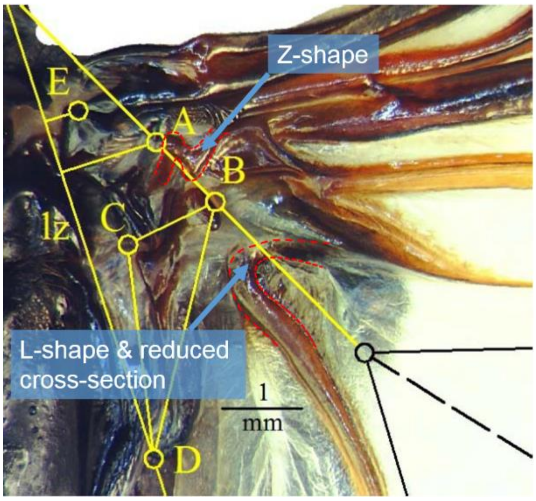
Z-shape
E
A
B
lz
C
L-shape & reduced cross-section
1 mm
D

Fig. 2-20: Wing joint and folding pattern of a beetle Monochamus sartor F. (adapted from [39])

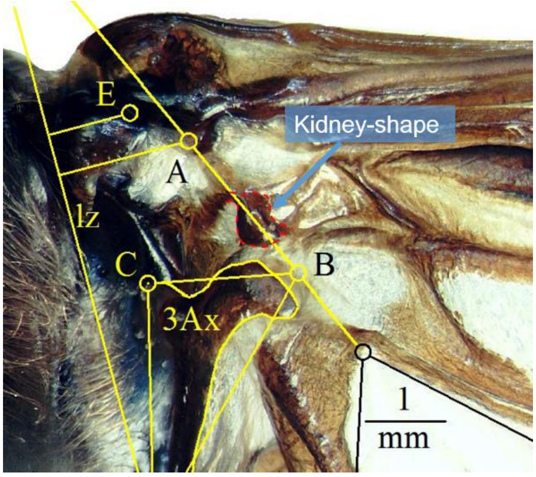
E
A
Kidney-shape
lz
C
B
3Ax
1 mm

Fig. 2-21: Wing joint and folding pattern from a beetle Prionus coriarius (L.) (adapted from [39])

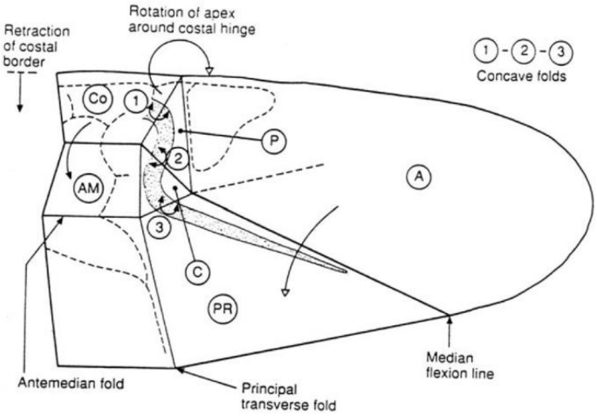
Retraction of costal border
Rotation of apex around costal hinge
①-②-③ Concave folds
Co
1
P
2
AM
A
3
C
PR
Antemedian fold
Principal transverse fold
Median flexion line

Fig. 2-22: Diagram of wing folding pattern in the wasp-beetle Clytus [40]

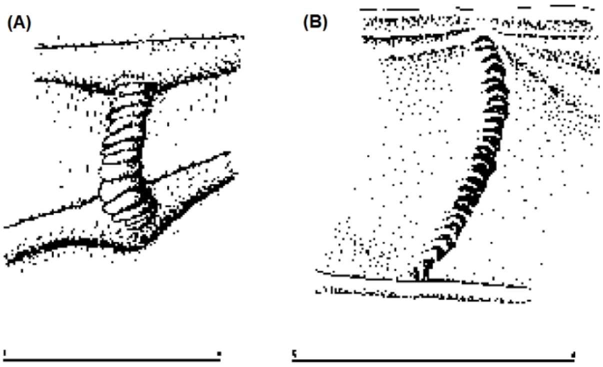

Fig. 2-23: Annulate cross-vein in a drone fly (Eristalis tenax) (A) and a desert locust (S. gregaria) (B). Scale bars: 0.5 mm. [41]

Haas [36] treated the folding mechanisms of the earwigs and developed a mathematical description for them. He distinguishes between creases, which are single folding lines, and folds, which are used for the whole wings. A fold of a wing means a crease, which runs across the whole wing. Therefore, a fold normally consists of several mechanisms with multiple creases. There exist two kinds of creases. A valley crease, also called concave and depicted as "-" in figures, and a mountain crease, called convex and depicted as "+" in figures. A mechanism consists of a knot where the creases intersect. Haas studied knots with four creases. For a mechanism to be foldable, it cannot have any combination of convex and concave creases. Haas states, that "the absolute value of the difference between the number of convex and concave folds must equal 2": [36]

$$|n_{convex} - n_{concave}| = 2 \tag{2.1}$$

His basic model is depicted in Fig. 2-24 where the four possible configurations and their individual creases are shown. The mechanisms are named "+-type" if there are three convex creases around the knot and "-type" in case there are three concave creases. It is clear that every mechanism will have a different movement.

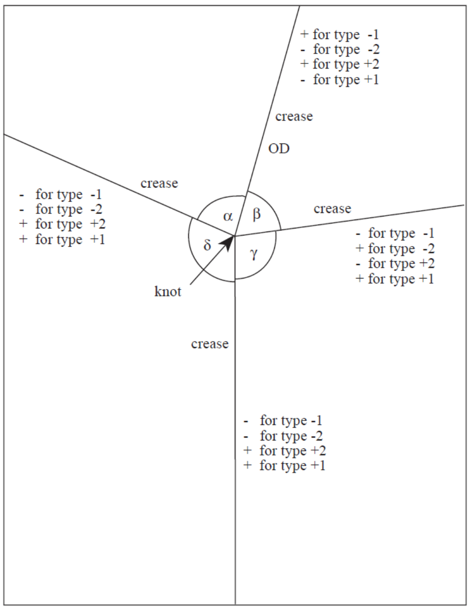

Fig. 2-24: The basic mechanisms of a four-crease knot [36]

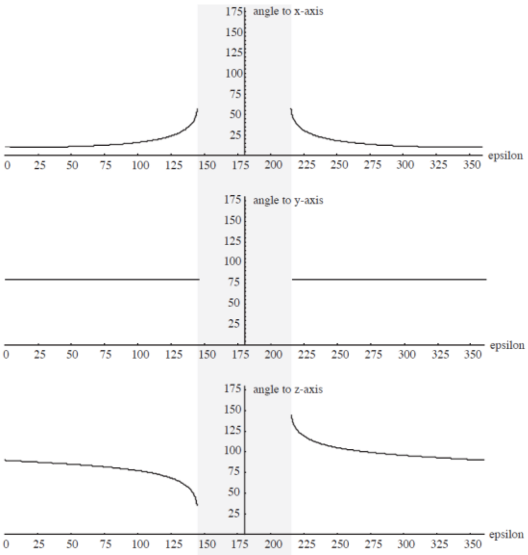

Fig. 2-25: Exemplary angular movement of the line *OD* from Fig. 2-24 in a bistable system (i.e. type 1 mechanism). The angles only add up to 300°. The forbidden range is shaded gray. [36]

Haas then calculated the angular movement of the crease "*OD*" from Fig. 2-24 for all mechanisms and increased the complexity of the problem by adding more knots to a mechanism. There are two rules pointed out. First, for a mechanism to be able to fold completely (all four panels lie in a parallel plane) the angles of non-adjacent sectors must add up to 180°. Second, to unfold the mechanism into one single plane the sum of all angles must add up to 360°. [36]

By measuring the angles between creases for different insects, it has been found that none of the two rules is followed. This means that the insects are not able to fully unfold and fold their wings. Therefore, they will always have slightly curved wing shapes. An interesting finding of Haas's calculations with the total sum of angles not equal to 360° is that this might be a stiffening mechanism. If the angles do not add up to 360°, the structure will form a kind of pyramid. A "forbidden range" exists, where the opening angle cannot be calculated. The mechanism cannot overcome this range except by external help if there is intrinsic elasticity in the mechanism, as is in a wing membrane. Therefore, the mechanism becomes bistable and the bistability can be exploited as a stiffening mechanism. Fig. 2-25 shows the bistable situation by the sudden change in the angle corresponding to the z-axis before and after the forbidden range. A snapping from one stable state to another is therefore shown. [36]

Comparing the stated folding rules and their consequences with real insect wings, Haas found that the sum of non-adjacent angles "almost always did not match 180°" [36]. This means that the insects are not able to fully fold their wings. This can be explained by looking at the possible space between the abdomen and the elytra. This space is not rectangular but more round. This means that a fully folded and flat wing would not use all the space available (Fig. 2-26, A). In addition, non-complete folding (Fig. 2-26, B) might have a positive effect during unfolding. By unfolding the wing, the elytra is lifted and the wing can slightly expand due to the inner tensions generated by the non-complete folding. This initial stimulus might help to overcome the first few degrees of the unfolding. This might be important because it has been shown that the first few degrees of unfolding are the most difficult in the whole unfolding process. [36]

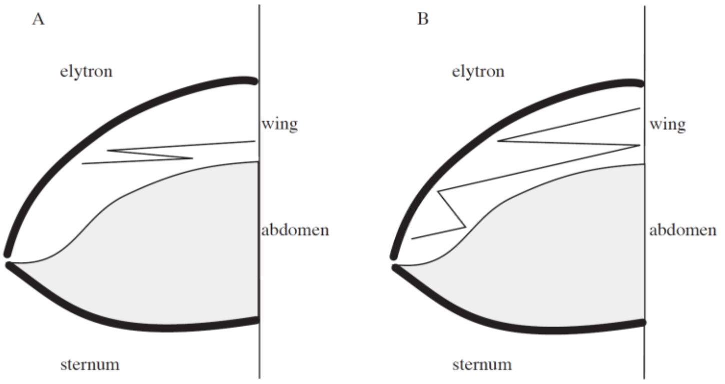

Fig. 2-26: Schematic cross section of the abdomen of a beetle. A completely folded wing does not occupy the whole space available (A), whereas a slightly unfolded wing does (B). [36]

Fig. 2-27 shows a schematic dorsal view of an unfolded left hind wing of the common earwig. One can see the fold lines. Their directions are marked with cv (concave) and cx (convex) as already introduced before. The earwig possesses *radiating veins* running from the *ulnary area* to the outer wing margin and *intercalary veins* emerging near the ring fold and also running to the outer wing margin. The radiating veins are close to the fold lines but move away from them by getting closer to the ring fold. After the ring fold, both sorts of veins lie between the radiating fold lines. Both sorts of veins broaden at the location where they cross the ring fold, forming broadened areas. The veins are all connected by the circumferential *vena spuria*. [36]

The diameter of the veins tends to decrease from the base to the tip, which also decreases the bending torque. This reduces the torque of inertia and therefore the energy required as well as stresses generated in oscillation during flight and it makes the wing-tip more flexible and more easily deflected by excessive forces and unpredicted impacts. The connection of the radiating and intercalary veins with the circumferential veins can also be seen as a kind of truss-lattice mechanism. The circumferential veins hold the radial veins apart and serve as struts, loaded in compression. The radial veins are either in compression or in tension, depending on the direction of the wing forces. [41]

The wing of the earwig folds in a complicated manner and has four stages and is well explained in [36].

1. The large fan-like area of the wing folds fan-wise with folding lines between the radiating and intercalary veins.
2. The apical (upper) part of the wing bends downwards at a line between the outer apical area plus the squama and the inner apical area plus the base of the radiating veins and ulnary area.
3. The radiating and intercalary veins bend upwards along the ring fold.
4. The ulnary area bends downwards relative to the squama and encloses the folded fan-like area.

It should be kept in mind that the steps are not done one after another, but in one process.

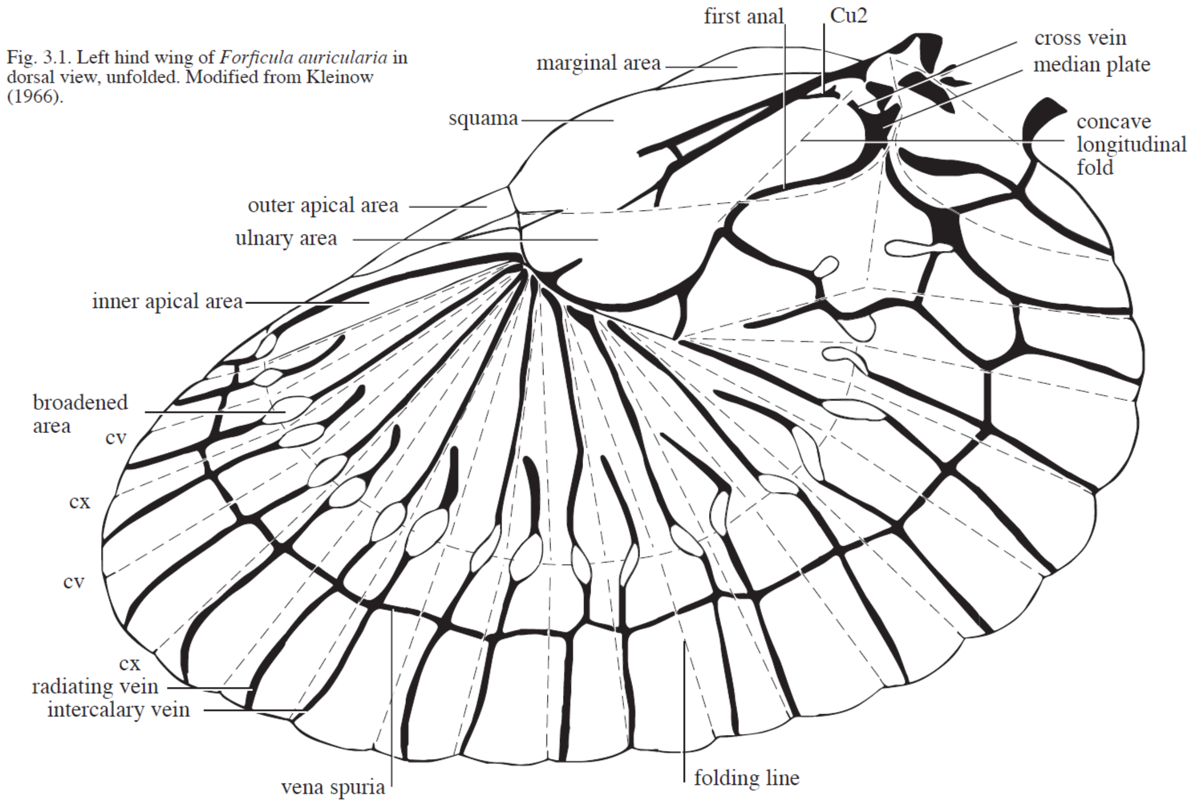
Fig. 3.1. Left hind wing of *Forficula auricularia* in dorsal view, unfolded. Modified from Kleinow (1966).
first anal
Cu2
cross vein
median plate
marginal area
squama
concave longitudinal fold
outer apical area
ulnary area
inner apical area
broadened area
cv
cx
cv
cx
radiating vein
intercalary vein
vena spuria
folding line

Fig. 2-27: Schematic of unfolded left hind wing of Forficula auricularia (common earwig) in dorsal view [36]

The relaxed position of the earwig's wings is the folded one. This is in contrast to the goal of this thesis where the deployed structure should be the relaxed and the folded one the tensioned position in order to use the tension for unfolding. Still, it is interesting to know about the mechanisms that keep the wing unfolded because they might bring some inspiration to stiffening mechanisms in the considered application.

There are two mechanisms doing so. The first is the concave longitudinal fold (CLF) which is depicted in Fig. 2-27. The CLF can snap into its concave form when the wing is stiffened and it counteracts the intrinsic elasticity that wants to fold the wing. It could be shown that the elasticity securing the CLF comes from the surrounding membrane. In addition, the absolute value of the difference between the number of convex and concave folds at the knot where the CLF crosses the convex crease between the squama and the ulnary is equal to zero:

$$|n_{convex} - n_{concave}| = 0 \tag{2.2}$$

This gives a criterion where it is easily possible to differentiate between folding creases with the difference of two and the creases for stiffening with zero crease difference at a knot.

The second stiffening mechanism is the so-called "Flügelmittelgelenk" (FMG, wing central joint). This is the region where the outer apical area, the inner apical area, the ulnary area and the squama adjoin. It could be shown that the angles around the FMG only add up to 350°. Therefore, and because of the elasticity of the membrane, the FMG is bistable and important for stiffening the wing. The central area of the FMG, the Zwischenfeld, is "significantly less sclerotized than its surrounding area" [36]. This means that the Zwischenfeld is less stiff than its surroundings. Haas demonstrates the effect of the more compliant Zwischenfeld with two paper models, both not adding up to 360° at their knot (Fig. 2-28). The second model has a rhombic cutout, representing the Zwischenfeld (Fig. 2-28 B). By comparing the effort needed to snap each model from one stable position to the other, it seems to be much easier to snap the one with the cutout. Therefore, it is assumed that the function of the Zwischenfeld is to reduce the forces needed to overcome the bistability and therefore reduce local stresses at the FMG.

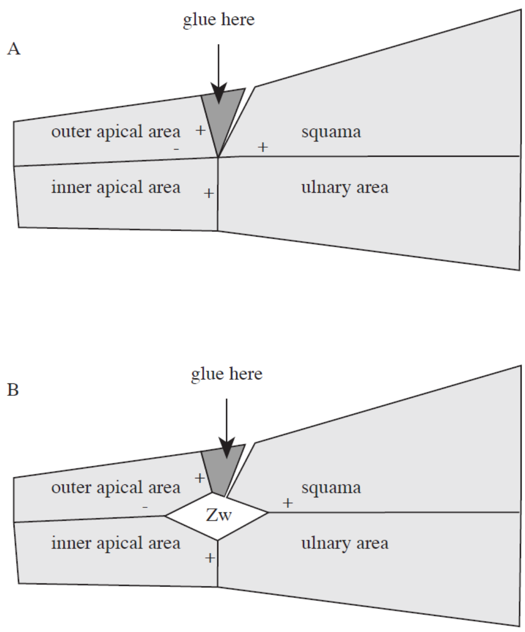

Fig. 2-28: Exemplary structure to show the function of the Zwischenfeld (Zw). In model (A) it is difficult to snap from one stable position to the other. In (B), with the cutout representing the Zwischenfeld, this can be done much easier. [36]

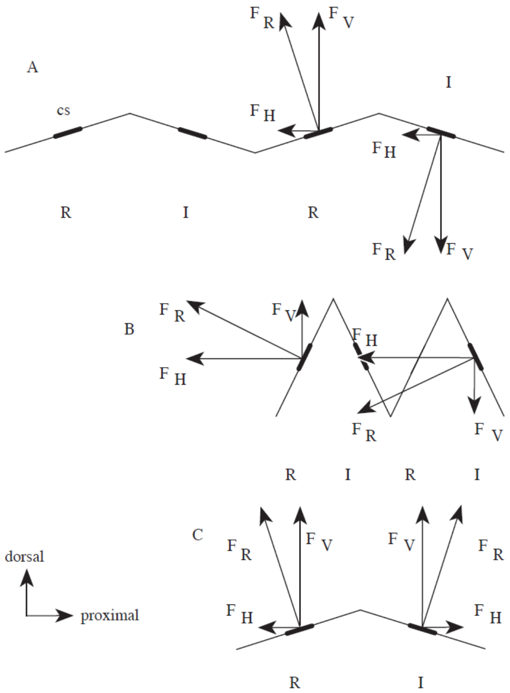

Fig. 2-29: Schematics of the force relations in an unfolded (A) and partly folded (B) wing section. The radial (R) and intercalary (I) veins point in opposite directions. (C) Hypothetical case of broadened areas pointing in the same direction. [36]

Fig. 2-27 also showed broadened areas of the radiating and intercalary veins. Haas could show that the radiating veins actively bend dorsally (to the back), and the intercalary veins actively bend ventrally (to the abdomen) seen from the unfolded wing. This has a positive effect during the fan-like part of the wing folding. A schematic explication of this effect can be seen in Fig. 2-29. The top image shows an almost completely unfolded wing. Each vein generates a force F_R in and perpendicular to the broadened area. This force bends the part depending on its direction. F_R can be split into a horizontal component F_H and a vertical component F_V. Since the fan is folded in the horizontal plane, only F_H is important. The magnitude of F_R changes with the extension of the veins and depends on the situation.

In the unfolded wing (Fig. 2-29, A), F_H is small compared to F_V. The vertical forces counteract each other and the horizontal forces sum up to the fan-wise folding force. If the fan is already partly folded (Fig. 2-29, B), the horizontal forces increased by decreasing the vertical forces. Still F_V counteract each other and F_H add up getting larger the more the fan is folded. Therefore, F_H has the largest value in the completely folded wing. If the broadened areas of the radiating and intercalary veins would all bend in the same direction, the horizontal forces would counteract and the vertical forces would add up (Fig. 2-29, C). With this set-up it would not be possible to achieve a folding. [36]

A very recent study showed the possibility of replicating the explained mechanism with 4D printing. Faber et al. [21] proposed printing stiff faces with PLA or ABS connected by joints made out of an elastomeric component (TPU) by using fused deposition modeling (FDM). By doing so, they could preprogram the folding pattern by printing the samples directly in the folded state. They could also tune the energy barrier between the bistable states of being folded or unfolded by using simple geometrical and material properties. With this approach, they could build a gripper, which can hold a specimen without constant actuation as depicted in Fig. 2-30. In addition, they could rebuild a foldable model of an earwig's hindwing (Fig. 2-31). [21]

Their approach was to rebuild the function of the resilin. Depending on the through-thickness distribution of resilin in the earwig's joints, a different spring type can be characterized. A symmetric distribution can be substituted by an extensional spring and an asymmetric distribution leads to a rotational spring. The authors wanted to explore the role and capabilities of extensional springs to create multistable folding systems. They found that the extensibility of the joints facilitates folding of complex patterns and makes it possible to get closer to "bioinspired features that were previously out of reach." [21] They especially investigated the mid-wing mechanism consisting of four facets and being responsible for the bistability of the wing. They modeled the four-facet cell by connecting the rigid facets with rotational and extensional springs at each joint. Therefore, they could tune the bistability mechanism by simply adapting the spring constants and the missing angle at the facets' knot. This ability to tune the energy barrier between the bistable states by only using geometrical and material properties might allow the manufacturing of spring origami structures, which are able to change their shape quickly, only triggered by an environmental stimulus. [21]

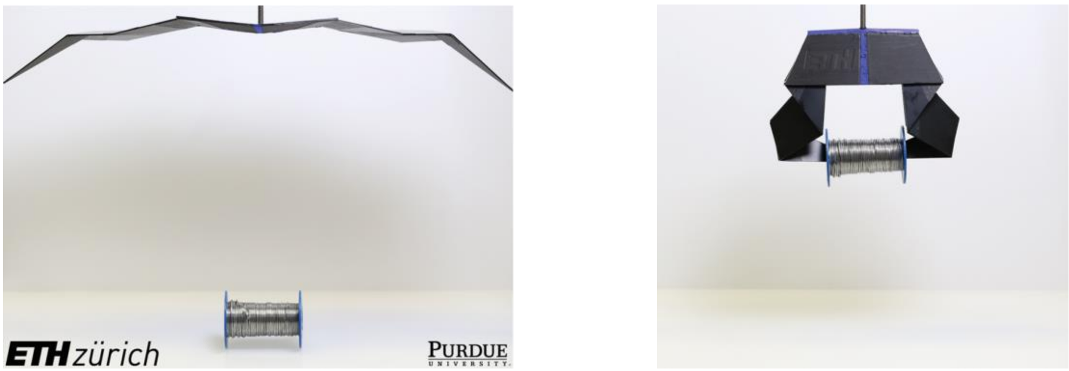

(A) Open state (B) Closed state

Fig. 2-30: Bistable gripper in open, first stable state (A) and closed, second stable state (B) [21]

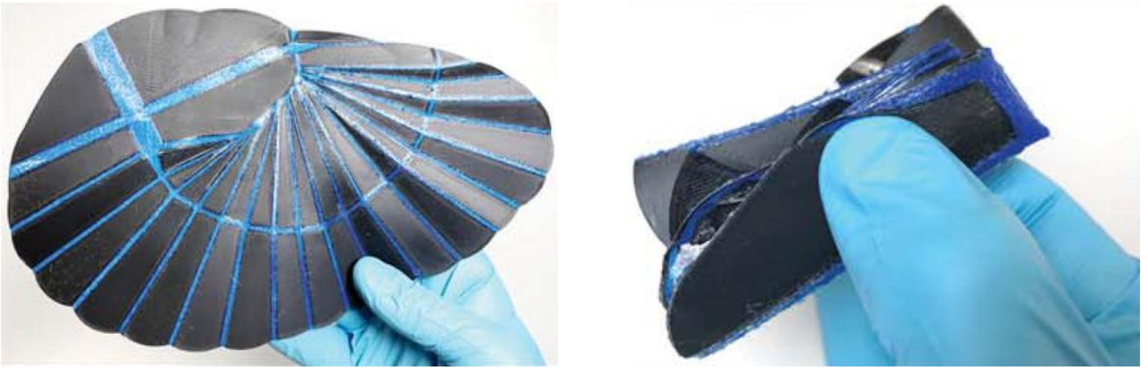

(A) Unfolded (B) Folded

Fig. 2-31: 4D-printed artificial earwigs hindwing unfolded (A) and folded (B) [21]

In this thesis, another bioinspired spring origami approach to elastic deployment will be studied. The idea is printing a vein-structure onto the membrane with FDM. The vein-structure consists of rods connected by elastic joints. A qualitative test showed that deployment with this idea might be successful and that the strain energy can be used for a self-deployment of the structure. [42]

2.2.4 Rip-Stop

The here-studied structures will need to keep their stability and stay functional in a harsh environment. Micrometeorites or space debris can hit the structures and induce holes in the tensioned membrane. These holes need to be stopped quickly before the membrane gets ripped apart and would lose its functionality. An example for such a rip-stop mechanism are thermal spot bondings, where layers of the membrane and reinforcing stripes are thermally bonded together. These stripes form a pattern where a rip is kept within a given grid area. The thermal spot bonding has been used for the JWST. [17]

Another possibility is to use fused deposition manufacturing to print rip-stop patterns directly onto the membrane. This has been investigated in [42]. The idea is that the load carrying structure should also be used as a rip-stop device in order to diminish non-structural mass on the membrane. This has also been inspired by mechanisms from nature. Dragonflies and other insects can tolerate the loss of a wing area of up to 30% and can still have predation success, even though the flight behavior was clearly influenced [43]. This indicates a rip-stop mechanism in these wings because only few cases have been reported where a rip resulted in complete inability to fly. One can see the rip-stop pattern as being the wing vein framework in the insect’s wings where the veins are thicker than the membrane and therefore prevent the rips on the membrane from growing outside the confined area of the surrounding veins [42]. The same idea is proposed in [2] by directly printing the reinforcing structure with FDM onto the membrane. Tests showed that a higher tear resistance than neat film of equivalent mass could be achieved and that such rip-stop structures could stop rip propagation for a certain load and strain. [2]

2.2.5 Synthesis of folding & deployment techniques

Different deployment methods, stiffening structures and packaging methods have been compared by Jannic Völker [6] in his master thesis at DLR. His findings where that 3D printing of rods onto the membrane seems to be the most promising method for the investigated type of application. The rods forming a pattern need hinges at the fold lines to avoid permanent deformation. Therefore, these hinges have been defined as critical components because they will be the key component for folding and deployment. The hinges need to be able to fold elastically without any plastic and therefore permanent deformation. In addition, they need to inhibit enough energy after being folded such that they deploy themselves after being released. Hence, for the self-deployment the hinges need a high stiffness and a high opening force or torque. [6]

2.2.6 Elastic Hinges

Traditionally stiff or rigid parts, which are connected with hinges, are used when a mechanism is developed. An example is a door on its hinge. However, as seen in section 2.2.2, in nature a different idea from rigid parts connected at joints appears as most moving things in nature are merely flexible than stiff and the motion comes from bending these flexible parts. When the mechanism is bent, strain energy is stored which can either be an advantage or a disadvantage. For the idea investigated in this thesis, this strain energy would be an advantage because the compliant element integrates both a spring and a hinge function into one component. This component has an initial position where it will go back to when it is unloaded. This function will be used by deploying the folded structure. [44]

Two important ideas need to be kept in mind when designing compliant mechanisms: fatigue life and stress relaxation. Because the motion of a compliant mechanism comes from bending flexible parts, stresses are experienced at the bending locations. When this motion is repeated many times during its lifetime, fatigue loads will appear allowing the joint to deteriorate. The mechanisms must be designed in such a way that their expected lifetime is set below their fatigue point. This is not expected to be an issue in this thesis because the compliant mechanism will only be folded and deployed a few times during ground qualification and will then be deployed once during service life. Therefore, the endured stress cycles will not induce fatigue. The second point however might have a significant impact on the deployment of the satellite structure. Stress relaxation appears in certain materials when they are held under stress for an extended period of time or if they are exposed to elevated temperatures. If the mechanism is held in such a state it can take on the new shape associated with the stressed position and be released from stresses over time. This would mean that it also loses the elastic energy and might not deploy as expected. [44]

The four primary ways to influence the flexibility of a mechanism are material properties, geometry, loading as well as boundary conditions. As the loading and the boundary conditions are given by the application and material properties are restricted by available printers and suitable printing materials the only property to focus on, is geometry. There, reducing the torque of inertia of the element in bending is a common way to increase its deflection. Another possibility is increasing the length of the element in bending. Without increasing the stress in the element this will increase the deflection. However, it may also decrease the stiffness, which might be disadvantageous. Arranging deflecting members in series can also increase the deflection. [44]

As the elastic hinges have been defined as key components for the deployable structure they have been investigated more deeply by Jannic Völker in his Master's thesis [6]. He compared different 3D printing methods, printers and printing materials. His findings are that FDM with materials such as *Durable* or *Nylon* seem to work best for the considered application.

It could be shown that bending a simple rod would lead to permanent deformation inhibiting full deployment. Thus, various hinge designs have been developed to reduce the bending radii leading to lower bending stresses and strains. These designs are presented in Fig. 2-32. As these designs are based on decreasing the cross-section at the center of bending this would weaken the rods and the smaller section parts might break before the rod itself. To overcome this, changing from bending to torsion has been proposed with the designs in Fig. 2-33. These torsional hinges have the advantage that the length of the twisted rod, also called *Torsion Rod* can be adjusted to material characteristics and folding requirements.

The torsional hinge has first been introduced by Jacobsen [45]. He called the torsion hinge *Lamina Emergent Torsional (LET) Joint*. This joint is made from a single planar layer but is able to withstand large angular deflections by providing rotational motion out of its plane. The symmetry of the joint with two torsion rods as shown in Fig. 2-33 (B) allows that each torsion rod experiences less than the total hinge motion and therefore reduces the stress in the individual members. [45] This Lamina Emergent Torsional Joint and related methods have been patented [46].

Since the function of the stiff rod and the elastic hinge are different, the possibility of combining two materials has also been investigated. In order to accomplish this, stiff material (grey) was used for the rods and flexible material (yellow) was used for the hinges. This can be seen in Fig. 2-34. A drawback of this method is that the flexible material reduces the overall stiffness and that the connection between the two materials is a possible weak spot due to manufacturing imperfections at the bonding during printing.

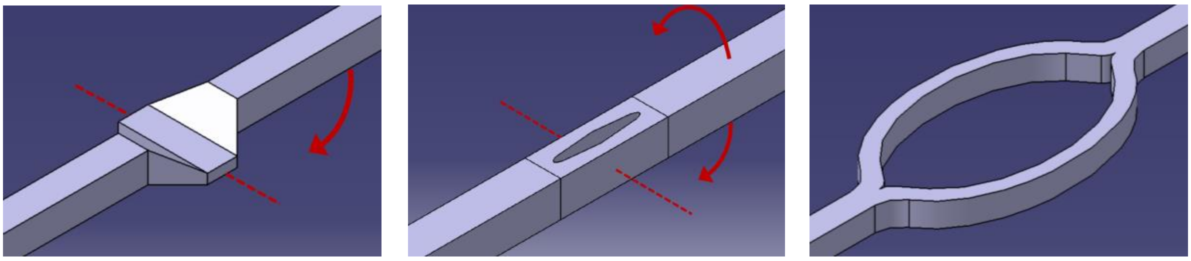

(A): Wide-and-Flat Hinge (B): Bowl Hinge (C): O-Hinge

Fig. 2-32: Bending Radii Difference Designs [6]

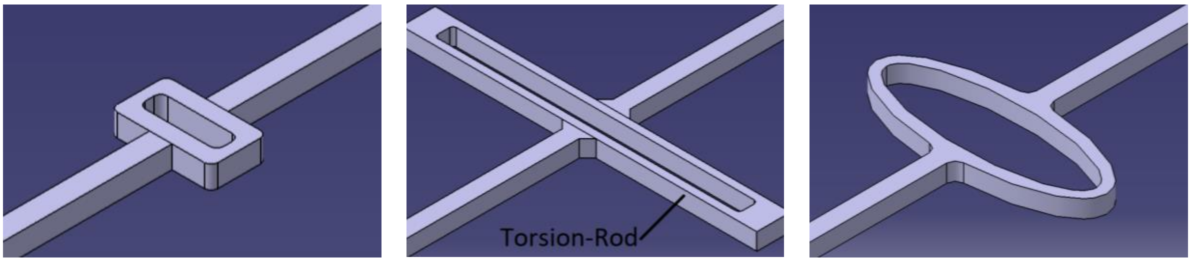

(A): Small Torsion Hinge (B): Long Torsion Hinge (C): Oval Hinge

Fig. 2-33: Torsional Hinge Designs [6]

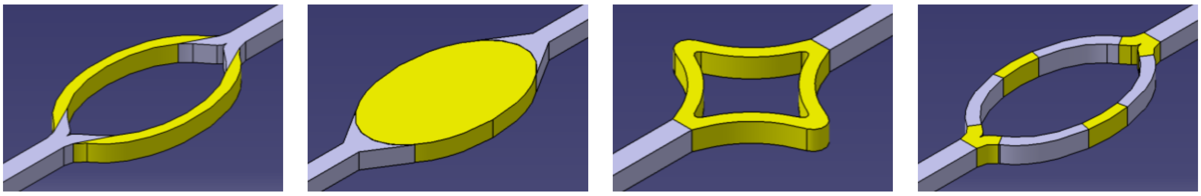

(A): O2-Hinge (B): Filled O-Hinge (C): Parabola-Hinge (D): O4 -Hinge

Fig. 2-34: Multiple Material Designs [6]

Tests with different printers and printing materials have shown that the O2-Hinge, the filled O-Hinge and the torsion hinge had sagging angles under its own weight (SOW-angle) below 5° and showed a good reopening angle of around 170°. The torsion hinge has been chosen for further FEM analysis and optimization by J. Völker [6] as it is much simpler to manufacture and to analyze because it is made out of only one material. Furthermore, a filled O-hinge requires more material increasing its mass.

J. Völker [6] performed an initial finite element analysis of the torsion hinges with the materials *Nylon* and *Durable*. The used model and its boundary conditions are shown in Fig. 2-35. The left rod (purple) is fixed on the backside all along the area except for the 5 mm closest to the torsion rod (orange). On the same area on the right rod (green), a pressure is applied to the surface towards the positive z-direction. This pressure moves with the surface and therefore with the displacement of the rod. A linear elastic material model has been chosen, given that the hinges should stay in the elastic regime. The analysis did not include any contact conditions. Hence, it was possible that opposing parts moved inside each other during folding which is not physical. Nevertheless, it is stated that the results are accurate enough for an improvement of the design. The specimens were named after the width (w) of their torsion rod (B2_w), which appeared to have the most influence on the results. It has been found that a thin torsion rod (B2_l) strongly decreases the von Mises stress. As this goes along with a significant reduction of stability and reopening force, multiple thin torsion rods could be used. This brought up the idea of the so-called *2 Torsion Rods Hinge* (2TR-Hinge) which has two thin torsion rods besides each other (Fig. 2-36). A model of a 2TR-Hinge has been calculated and compared to a normal torsion hinge with the same dimensions. The only difference was that two torsion rods have been introduced with 0.3 mm space in between. It could be shown that maximum von Mises stress increased by 10 % but that the reopening force could be doubled with this approach. [6]

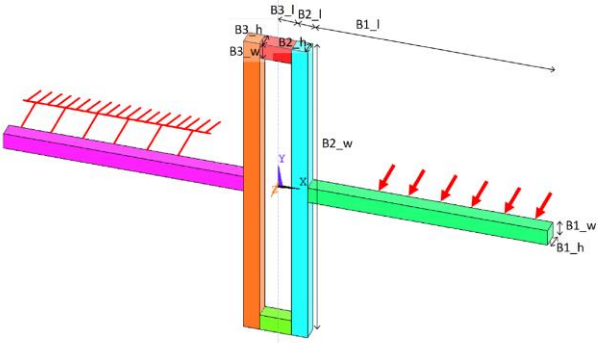

Fig. 2-35: Parameters and boundary conditions of the torsion hinge model [6]

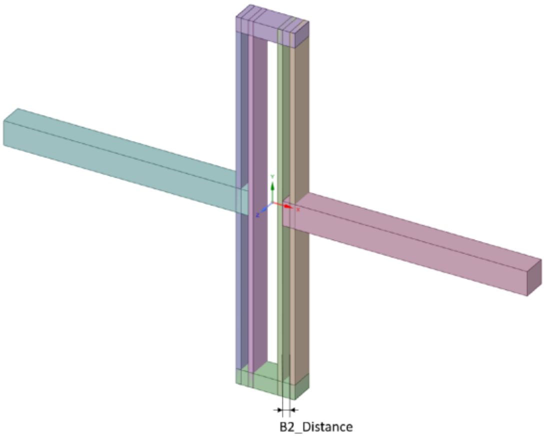

Fig. 2-36: CAD model of a 2TR-Hinge [6]

The most important characteristic, the reopening angle could not yet be provided by the analysis. Nevertheless, tests with printed specimens with the same parameters as the ones analyzed with FE showed good reopening angles for Nylon and confirmed a correlation between reopening angle and maximum von Mises stress. The reopening angles for the *Durable* material where not as good as expected and deployment took place very slowly. This indicates a small reopening force. In addition, the parts could not be printed as precise as expected. This was due to curvatures after separating the specimens from the platform for the *Durable* material printed with a Form 2 printer and printing limitations on the Mark Two printer, which thickened small parts so that they could be printed. [6]

In conclusion to Völker´s work it can be stated that the *Durable* material takes too long to reopen and that the printing quality is not as good as expected. On the other hand, printing Nylon has the drawback of requiring thicker parts for precise hinges. However, Nylon still seems to be a good material for the validation tests.

2.3 Existing Test Mechanisms

The elastic hinges need to be tested in order to define their mechanical properties not only by FEA but through experimental results as well. The experimental results are important in order to collate the FE model and to be able to make better predictions on the hinges and their systematic implementation into a deploying structure in the future. The motion of an elastic hinge and its stiff rods during folding can be described as a bending because the two rods connected by the hinge are folded together with the center of rotation at the mid-position of the hinge (Fig. 2-37).

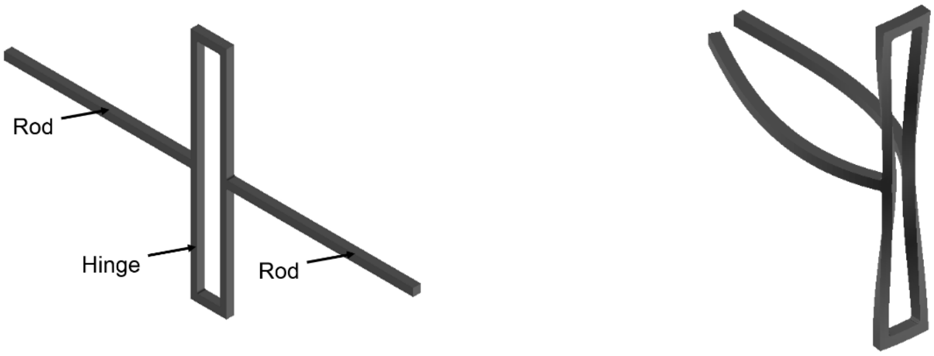

(A) Initial, flat position (B) Final, bent position

Fig. 2-37: Schematics of initial and final position of rods and connecting hinge during folding

There are many different possibilities to test this sort of bending. This section will describe possible testing methods already developed by other researchers.

One of the most common test methods to determine flexural or bending properties of bars with a rectangular cross-section is the three-point bending test (Fig. 2-38, left). This test is standardized and the corresponding standard for three-point bending of unreinforced and reinforced plastics and electrical insulating materials is called ASTM D 790 [47]. The specimen rests on two supports and is loaded in its center. According to the standard, the specimen is deflected until rupture occurs in the outer surface of the specimen or until a maximum strain of 5% is reached. In this thesis, the goal is to fold the specimens completely while remaining in the elastic regime. Therefore, the specimens shall not break and the strain will go higher than 5%. Hence, this simple and common test is not well suited for large deformations as required for the considered tests in this thesis. A similar test is the four-point bending test (Fig. 2-38, right) described in the ASTM D 6272 standard [48]. The only difference is that two load introduction points are used with the four-point bending test instead of only one as for the three-point bending test. According to ASTM D 790: “the basic difference between the two test methods is in the location of the maximum bending torque and maximum axial fiber stresses. The maximum axial fiber stresses occur on a line under the loading nose in 3-point bending and over the area between the loading noses in 4-point bending.” [47]

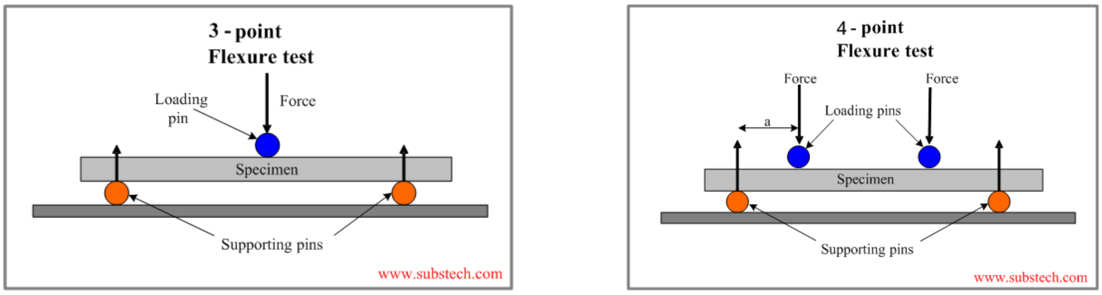

(A) Three-point flexure (B) Four-point flexure

Fig. 2-38: Schematics of flexure tests [49]

Fernandez and Murphey [50] investigated test methods for large deformation bending of thin high strain composite flexures. They describe that the three-point and four-point bending tests are not suitable for large elastic deformations because they could not adapt to large configuration changes. [50] Therefore, they investigated other, more developed flexure tests for large deformations.

The first test is called *Simple Vertical Test* and is shown in Fig. 2-39 (A). The specimen is fixed vertically onto the holding blocks by a tape. This tape acts as a hinge allowing specimen rotation and therefore the specimen is compressed and rotates into a U-shape when compressed. This permits large displacements and applies a uniform bending torque and curvature onto the center region of the specimen. [51] A drawback of this method is that the simple vertical test is prone to gravity-induced horizontal lateral loads that induce shear distortions at large curvatures. This problem is especially pronounced for stiff coupons requiring a stronger fixture at the holding blocks. [50]

In another test, the *Platen Test*, U-shaped specimens are placed between two flat compression plates (See Fig. 2-39 B). The plates are driven together and therefore the specimen’s curvature increases. This testing method, however, is better suited for curved specimens. The curved specimens are flattened by clamps as shown in Fig. 2-40. This is not ideal for specimens with a smaller radius. Flat coupons show a non-circular curvature and therefore a non-perfect torque distribution. Hence, this testing method is well suited for determining an upper limit on maximum coupon curvature or strains at failure but not for pure bending states. Furthermore, the steel strips, which hold the specimens flat, might come into contact for very small specimen radii, which stops the test without getting the maximum curvature before failure. [50]

To overcome the mentioned drawbacks of the beforehand explained test methods, an improved test fixture has been designed which generates a uniform stress state transitioning from flat to fully curved at the coupon grips. This test method is called *Large deformation four-point bending* (LD-FPB) and is shown in Fig. 2-39 (C). Both ends of the specimen are clamped to a cart. As the load is increased and the load cell is driven downward, the carts rotate and bend the sample (Fig. 2-41). Still, the LD-FPB has some drawbacks regarding clamping. Clamping the specimen’s edges results in stress concentrations, which might lead to failure at the grips. In addition, the LD-FPB needs precision-machined and polished components, which make this, test method relatively expensive. [50]

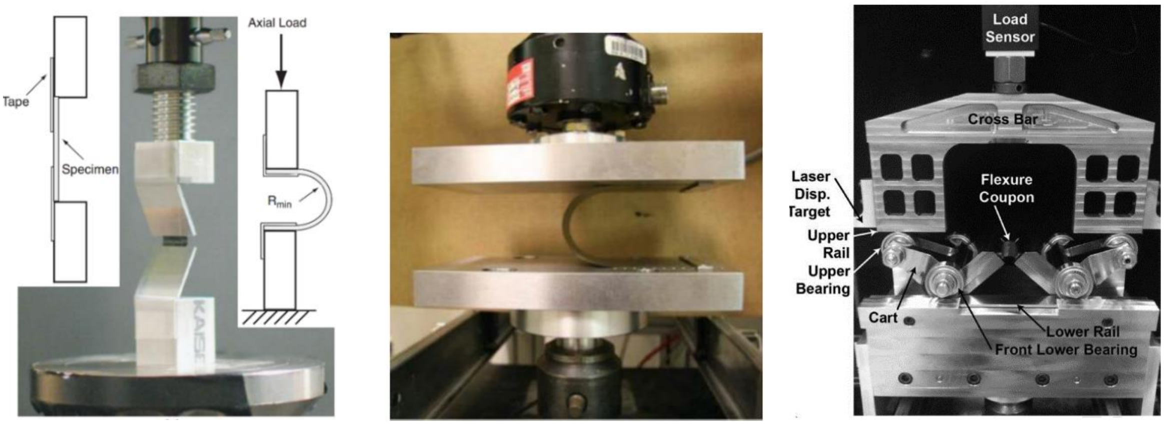

(A): Simple Vertical Test (B): Platen Test (C): Large Deformation 4-point Bending Test (LD-FPB)

Fig. 2-39: More developed flexure tests for large deformations [50]

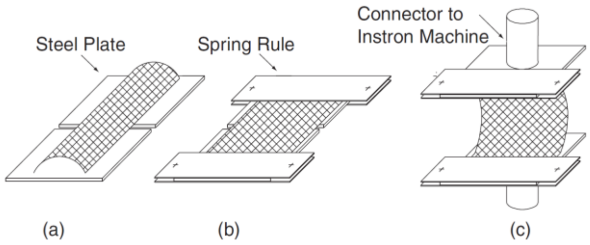

Fig. 2-40: Test set-up for biaxial bending of CFRP specimen: (A) Initial Stage. (B) Spring rule added to attach specimen. (C) Readily installed test. [52]

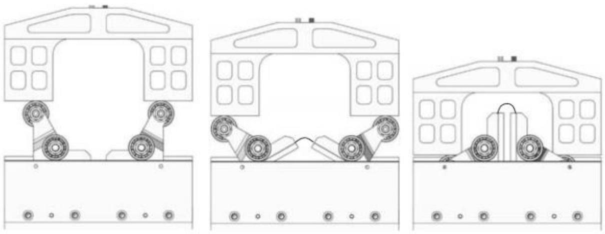

Fig. 2-41: Progressive schematic views of the LD-FPB during a test [53]

Combining the advantages and rejecting the disadvantages of the discussed testing methods, Opterus R&D developed the so-called "Column Bending Test" (CBT) because it resembles a column under axial compression. Fernandez & Murphey [50] further developed the CBT in order to test ultrathin laminates. The specimen is fixed vertically on each side to an upper and a lower arm, respectively. These arms are pinned at their ends with the pin axis offset from the specimen's neutral axis. This creates a bending torque when the arms are driven together (Fig. 2-42 & Fig. 2-43). The specimen's axial stress is negligible compared to the bending stress generated in the specimen. This introduces a mostly uniform stress state and simple kinematic analyses are needed to estimate the torques and the curvature. Compared to the LD-FPB the curvature at the grips is reduced and therefore the specimens should not fail at the grips. In addition, a larger volume of material is subjected to high stress compared to the platen test, which provokes more precise results. [50]

Unfortunately, the CBT still exhibits a major drawback: the influence of gravity. As the test is positioned vertically, the weight of each fixture arm decreases or increases the reaction force at the upper and lower pin, respectively. Due to the symmetry of the system, this error can be corrected by simply adding or subtracting the weight of one arm depending if the load is measured at the upper or lower pin, respectively. During the test, the arms will move closer to a horizontal position. There sagging of the test fixture under gravity influence appears leading to shearing distortion in the specimen (Fig. 2-45). To avoid this one could try to keep the test fixture mass as low as possible and minimize the ratio between the center of mass of the fixture arm and the pin-to-pin separation by keeping the test fixture center of mass close to the loading pin. A free body diagram of the situation is shown in Fig. 2-44. [50]

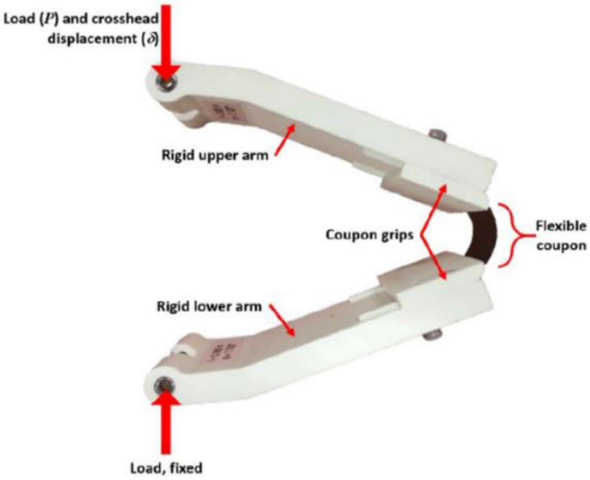

Fig. 2-42: CBT fixture with a thin specimen clamped during bending test [50]

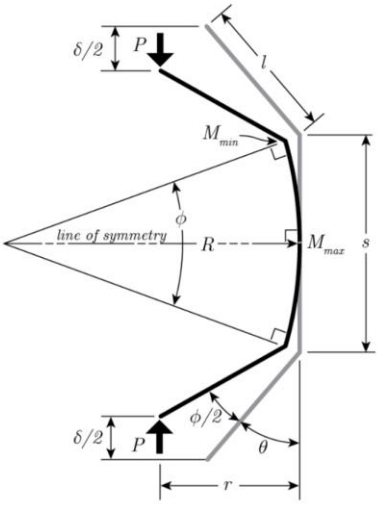

Fig. 2-43: Idealization of the CBT showing all test parameters involved [50]

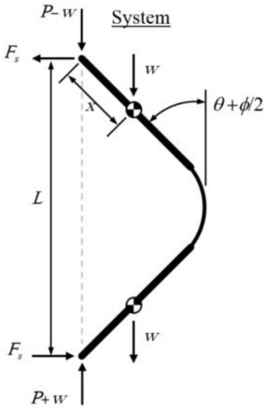

Fig. 2-44: Free body diagram of CBT system [50]

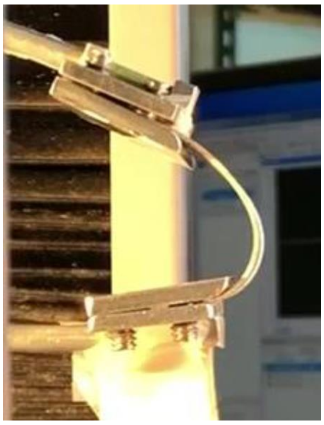

Fig. 2-45: Worst case gravity-induced sagging on CBT fixture [50]

After having investigated and experienced this unfavorable effect of gravity of the CBT, Opterus R&D developed a new design, which is completely weight-balanced. The so-called “Counter-Weight Balanced CBT” (CWB CBT) is double symmetrical about the loading pin axis. This means that the center of mass of the fixture coincides with the load application point at the pin which means x=0 in Fig. 2-44. Hence, the gravity induced shear force and torque are zero and the fixture is freed from gravity loading effects. The test fixture is shown in Fig. 2-46. [50]

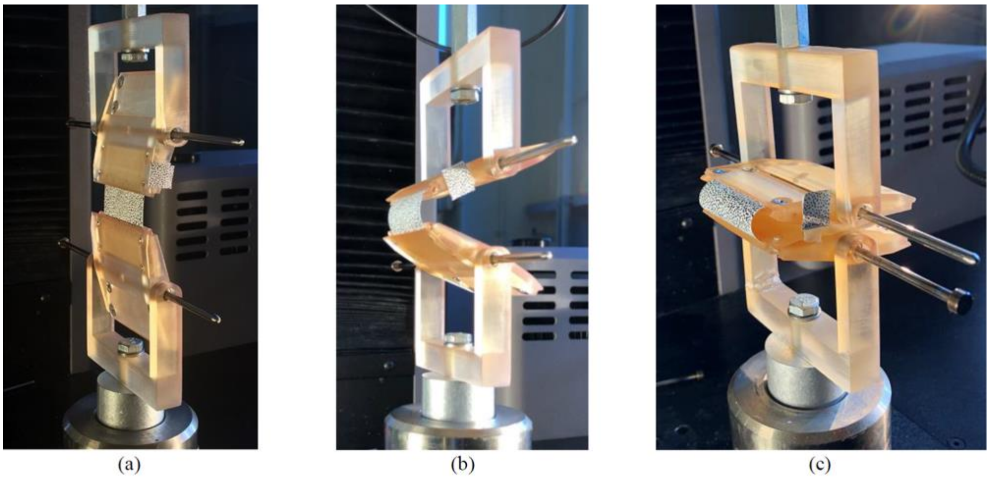

Fig. 2-46:CWB CBT fixture at different stages of rotation during a test. Initial (A), Intermediate (B) & Final stage (C). [50]

Even though, the CWB CBT seems to be a good solution for large deformation flexure further possible test methods will be discussed. A very simple method could be the well-known column buckling. The Euler buckling case 2 with both ends pinned is shown in Fig. 2-47. As the hinge is designed to be much more compliant than the stiffer rods, the specimens would buckle at the position of the elastic hinges. After buckling, the test could go on, decreasing the distance of the load introduction point and the fixation until they come together and the specimens are folded. This method however, cannot control the buckling direction and initial imperfections would have a large influence on the test results because each of the small 3D-printed specimens is expected to have different deficiencies due to printing imperfections.

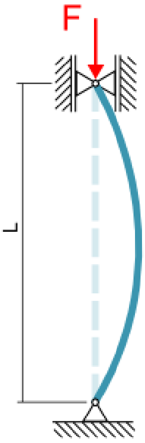

Fig. 2-47: Buckling with both ends pinned, Euler buckling case 2 [54]

By investigating elastic mechanisms to replace rigid body mechanisms, flexure hinges are a field of research in mechanical engineering. As opposed to rigid body mechanisms, there is a relocation of the axis of rotation by bending flexure hinges. To predict the path accuracy of the mechanism it is important to investigate this relocation of the axis of rotation. For this reason a corresponding test stand has been developed. The idea of the test stand could not only be used to investigate the relocation of the axis of rotation but also to measure folding forces and the corresponding angles by folding an elastic hinge mechanism. The test stand fixes the specimen on one side and a force tappet pushes the other side of the specimen, which induces the bending. During the complete test, the position of the elastic hinge is measured with an optical method. The realized test stand with a close-up of the load introduction system is shown in Fig. 2-48. [55]

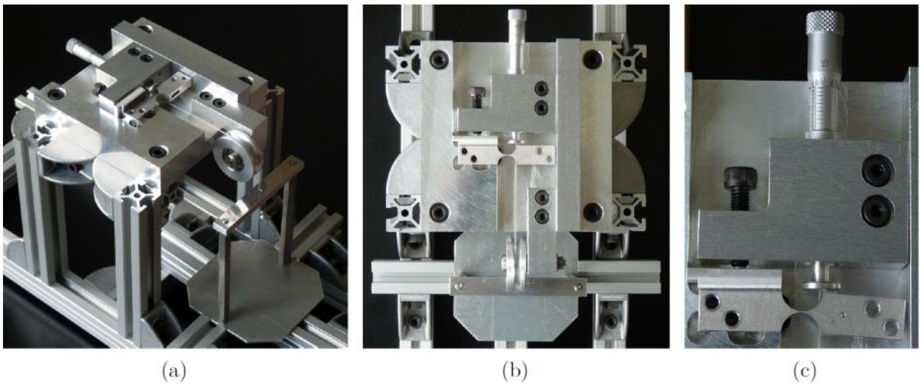

Fig. 2-48: Test stand to investigate the relocation of the axis of rotation by bending flexure hinges. (A) Test stand. (B) Load introduction. (C) Deflected specimen. [55]

Most of the time the flexure hinges are used for cyclic engineering applications where the fatigue behavior of the compliant joints is important to know. To be able to experimentally verify the life cycle of these hinges, Schoenen built a fatigue test bench [56]. As the flexure hinges change the position of the axis of rotation during deflection, the axis of rotation shall not be fixed because this might lead to additional stresses in the joints and falsify the test results. As a consequence, a single staggered shear loop has been chosen as a mechanism to move the joints with a predefined angle. The continuous movement of the relapsing component number 3 in Fig. 2-49 is done by an upstream powered non-displaced crank mechanism. To get a higher performance of the test it is possible to fix six specimens onto the same mechanism as shown in Fig. 2-50. A drawback of this test stand is that the maximum angle of deflection is defined by the dimensions of the slider-crank system and therefore a complete bending of the hinge might not be possible. [56]

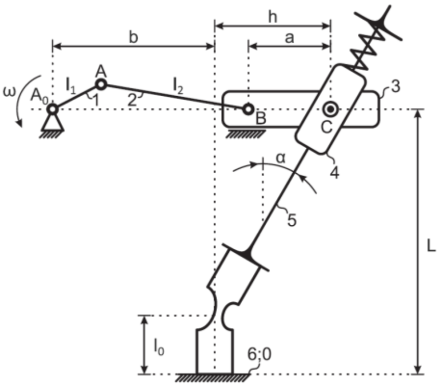
h
b
a
ω
A_0
l_1
A
1
l_2
2
B
C
3
4
α
5
L
l_0
6;0

Fig. 2-49: Schematic mechanisms of fatigue test stand [56]

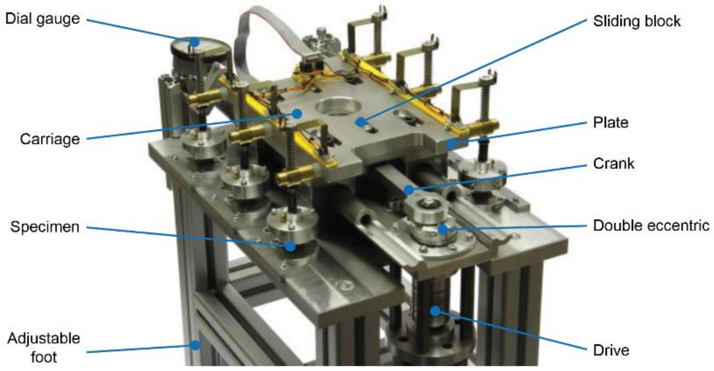
Dial gauge
Sliding block
Carriage
Plate
Crank
Specimen
Double eccentric
Adjustable foot
Drive

Fig. 2-50: Built fatigue test stand with possibility to test 6 specimens at a time (Adapted from [56]

Another possibility would be to only test discrete positions during the folding process. This means that only a fixed number of positions are tested and results are not continuous during folding but only available at a discrete number of points. Such a test has been developed by Seçkin et al. [57]. They tried to build a test stand as simple as possible and with available materials and tools to be easily reproduced by others. They have two fixed positions, the initial undeformed hinge and a position with the hinge folded to 45 degrees. The second, deformed position is simply fixed by a stud mounted onto the mechanism (an Allen key in Fig. 2-51). The two configurations can be seen in Fig. 2-51. [57]

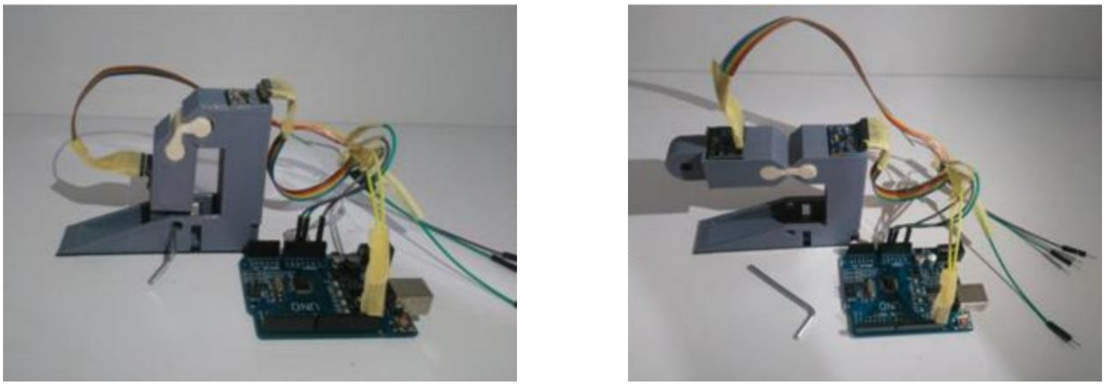

(A) Hinge in tension

(B) Free hinge

Fig. 2-51: Fixed position bending test system with hinge in tension (A) and free hinge (B) [57]

3 Finite Element Simulation & Optimization

One goal of this thesis is to collate experimental data with a finite element model in order to get a model that can further predict the behavior of different elastic hinge designs. To do so, the FE model needs to be adapted to experimental results obtained with the test stand developed in this thesis. This chapter describes the generation of the FE model as well as its outcomes. Furthermore, new elastic hinge designs have been developed and parametrized. They have been optimized by using FE results. The optimization procedure and its results are described in section 3.3.

3.1 Model generation & mesh convergence study

The finite element model developed in this thesis is based on an initial script written by Jannic Völker during his master's thesis at DLR [6]. However, numerous changes needed to be done to adapt the boundary conditions of the test stand and to adjust new modelling ideas. The entire FE model is written in ANSYS APDL, a parametric design language that works like a programming language. Writing input files with APDL has the advantage that no user inputs are needed during the calculations and therefore the calculations are repeatable and can be automated. The used modeling approach is shown in a flowchart in Fig. 3-1.

As parameter studies and optimizations of the model are intended, the model needed to be parametrized. To do so, the geometrical dimensions of the model are used as variables, which are read by the FE script. The geometry is then built up by keypoints defined by these variables.

During post-processing, the bending angle as well as the final reaction force and reaction torque are calculated. In addition, displacements in x- and z-direction and the equivalent von Mises stresses are stored in external data files for all substeps. These data files can be read by other post-processing software.

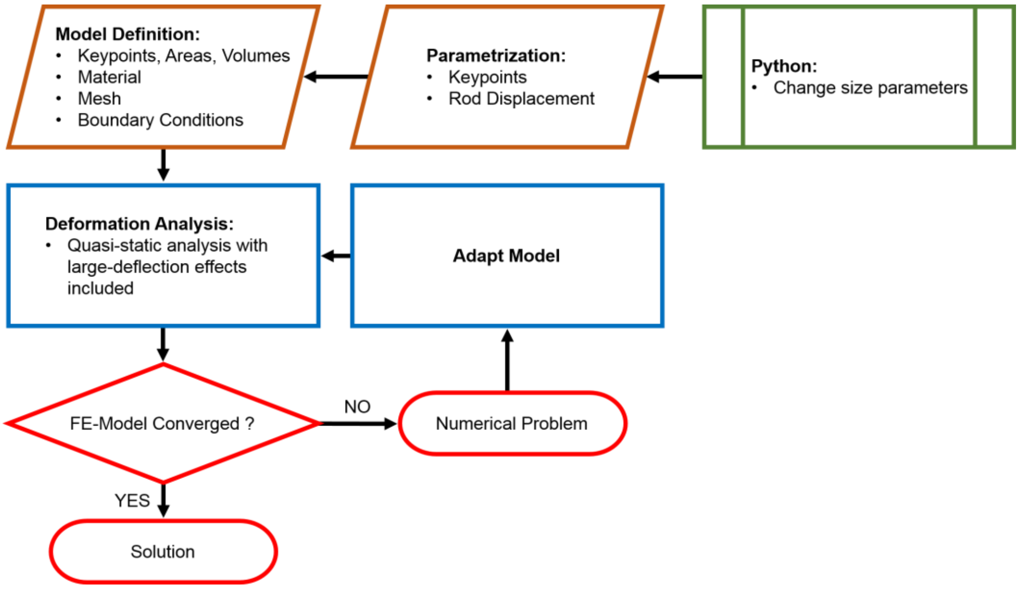
Model Definition:
• Keypoints, Areas, Volumes
• Material
• Mesh
• Boundary Conditions
Parametrization:
• Keypoints
• Rod Displacement
Python:
• Change size parameters
Deformation Analysis:
• Quasi-static analysis with large-deflection effects included
Adapt Model
FE-Model Converged ?
NO
Numerical Problem
YES
Solution

Fig. 3-1: Flowchart of FE modeling approach

The boundary conditions are assigned as closely to the real ones as possible and in the coordinate system as shown in Fig. 3-2. The left-hand side of the specimen is clamped and on the right-hand side, a prescribed displacement is applied. The prescribed displacement is calculated such that the model gets fully folded at the end of the simulation time. This means that the right-hand side moves towards the left-hand side on a circular path until their ends get in touch. Therefore, the outermost line of nodes of the right-hand side gets a prescribed displacement, U, of a half-circle defined in small steps with the respective X- and Z-coordinates as in equation (3.1).

$$\begin{gathered} U_X = \frac{L_{tot}}{2} * \cos(n * \alpha) - \frac{L_{tot}}{2} \\ U_Z = \frac{L_{tot}}{2} * \sin(n * \alpha) \end{gathered} \tag{3.1}$$

Where L_{tot} defines the diameter of the displacement circle and is the total length of the specimen from left to right and n is the increment's number. α is defined as $\alpha = \frac{\beta}{N}$ in radians, with β the prescribed angle of the final displacement and N the number of displacement increments.

The influence of gravity is added to the whole model. This is the same as the real specimens will experience during the experiments. All evaluated models have been manufactured from Nylon with material properties shown in Tab. 3-1.

Tab. 3-1: Material properties of Nylon [58] used in FE model

Material property	**Symbol**	**Value**
Young's modulus	E	940 MPa
Poisson's ratio	v	0.4
Density	ρ	1.1 g/cm^3
Maximum yield stress	$R_{p0.2}$	31 MPa

The described modelling approach has been the same for all subsequent models including the optimization models. The only difference is that during folding of some torsion hinge models the two torsion rods get into contact during folding and are sliding on each other. Therefore, after meshing the geometry, two contact pairs have been created. Each of the contact pairs is composed of the inward-facing area of one torsion rod (Fig. 3-3, red area for the first contact area) and the edge on the inside of the folding pattern of the other torsion rod (Fig. 3-3, blue line for the associated contact line) and vice versa. During folding, first one edge gets into contact with the face of the other torsion rod and detaches again after a certain angular displacement of the specimen. However, then the edge of this other torsion rod gets into contact with the face of the first torsion rod. The contact has been modelled as a frictional contact with a friction coefficient of 0.2 which is the friction coefficient of the modeled material [59].

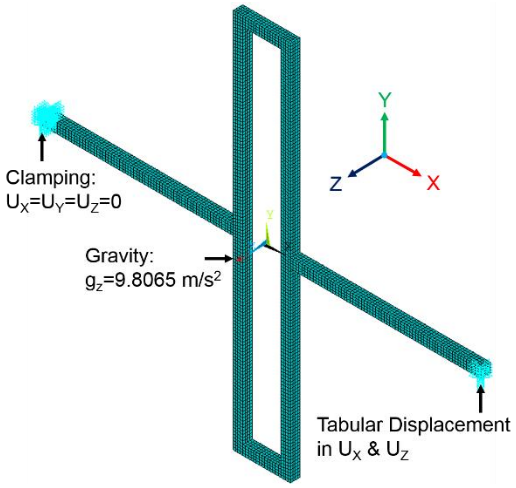

Fig. 3-2: Boundary conditions for torsion hinge model (the same boundary conditions have been applied to all models)

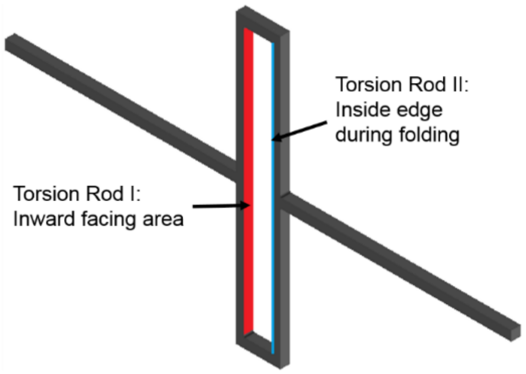

Fig. 3-3: Contact pair definition for torsion hinges

A mesh convergence study has been performed with the torsion hinge model TH-19-5-30-2-2. During this mesh convergence study, stress singularities appeared at the hard edges where the different rods connect. This can be seen in Fig. A-1 - Fig. A-3 in Appendix A.1 for the finest mesh used during the mesh convergence study. One can clearly see that the stress is much larger close to the hard edges compared to the stress at some distance away from the hard edges.

An idea to overcome this was to introduce fillets in order to avoid, if possible, or at least alleviate these stress singularities. The filleted volumes are assigned with a different mesh size than the simple rods. During the mesh convergence study, this has been smaller or equal to the global mesh size, as the most important stresses will appear in the filleted volumes and the total number of nodes can be reduced by only refining the mesh where needed.

However, adding fillets at the hard edges increased the stress singularities even more. Even for the same mesh size, the maximum von Mises stress increased by almost 25%. When refining the fillet areas, these local stresses increased even more. This can be explained by the small fillet radius applied. The fillet radius needed to be small enough such that fillets at the inside of the torsion rods could have been created. However, for the used model TH-19-5-30-2-2 there is only a space of 1 mm between the two torsion rods leading to a maximum fillet radius that ANSYS is still able to create of 0.5 mm. This induces that the elements at the fillets needed to be smaller than this fillet radius, which was not favorable for a smooth mesh. Even for a very fine mesh, which took a very long time to calculate, some edges appear at the fillet areas creating other local stress singularities and increasing the maximum stress again. This is shown in Fig. A-4 - Fig. A-6 in Appendix A.1, where the maximum von Mises stress is 50 % higher than the solution with the finest mesh without fillets. Comparing the results for the maximum total displacement (Fig. 3-4) and the reaction force (Fig. 3-5) one can see that the models with and without fillets only have minor differences, especially pronounced for a coarse mesh. The reaction force is an important result for this study, because it can be measured during the experiments, whereas the stress cannot be measured directly and it can only be approximated by whether or not plastic deformation has occurred. In addition, the comparison of the two models shows that without fillets the convergence in both displacement and reaction force is much smoother and even a coarse mesh has less deviation in the results compared to a fine mesh. This shows that the model without fillets is more stable than with fillets.

As introducing fillets did not improve convergence but only increased the calculation time without adding more precision for other results like the reaction force, the fillets have been discarded and the torsion hinge models have been modelled with hard edges keeping in mind that stress singularities might appear. In addition, the stresses at the surrounding nodes closest to the one experiencing the maximum stress are also stored in the data files. This is a common method when experiencing stress singularities. The stress one element away from the singularity is considered being the maximum stress as singularities are not physical and should not be taken into account while post-processing FE results [60].

Fig. 3-6 shows the normalized results for the minimum displacement in X-direction (UX_Min; minimum because displacement is in negative X-direction), maximum displacement in Z-direction (UZ_Max), the maximum von Mises equivalent stress (SEQV_Max) and the reaction force in Z-direction (F_Z) (see Fig. 3-2 for coordinate definition). The results are all normalized with respect to the corresponding solution of the coarsest mesh. One can see, that for the mesh with 9072 nodes (global mesh size of 0.4) all results converged, except for the von Mises stress, which has a singularity. Therefore, this mesh is assumed as being converged. The subsequent hinge models are not expected to show such stress singularities due to their smoother geometry. They will have a similar size too. Therefore, the mesh size found in the mesh convergence study can be adopted for all considered models.

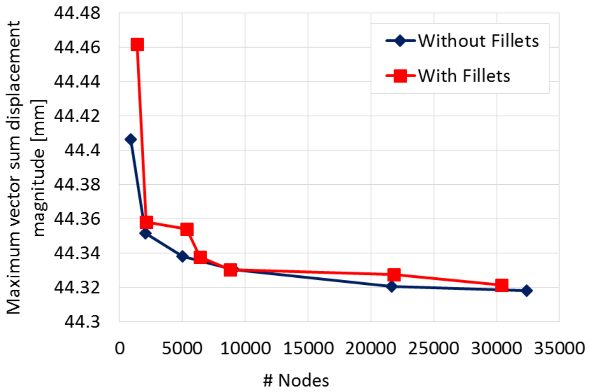

Fig. 3-4: Comparison of maximum total displacement for model with fillets and without fillets

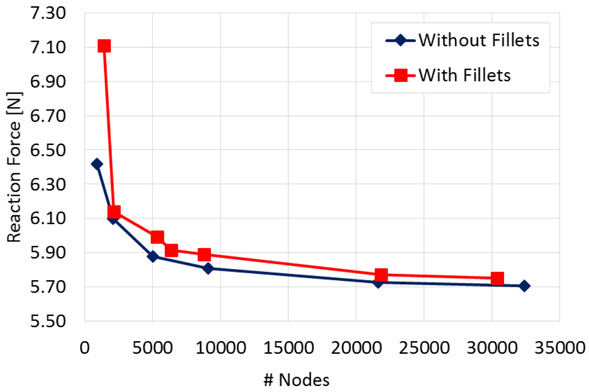

Fig. 3-5: Comparison of reaction force for models with fillets and without fillets

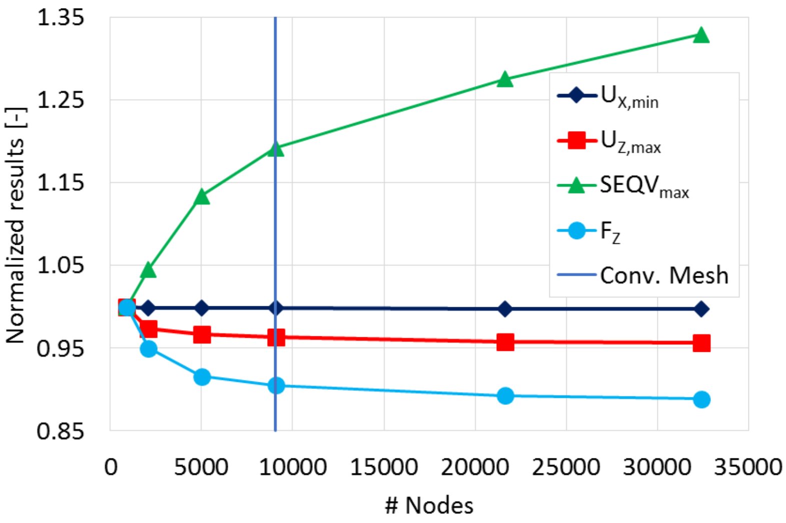

Fig. 3-6: Normalized results for model without fillets

3.2 Simulations of torsion hinges

Finite element simulations have been done on all tested elastic hinges. After comparing the results with the experimental data, the models have been adapted such that they can predict results for further model changes without the need of verifying the results with experiments. This subsection shows the results of the finite element simulations for all investigated torsion hinges. For all models, the most interesting results for comparison with experimental data are made available in this subsection. These include displacement, reaction force and reaction torque as well as equivalent von Mises stress during each simulation. As observed in section 5.2.2, the tested specimens did not have the exact same dimensions as prescribed. In addition, as seen in section 5.3, due to geometrical reasons, the specimens could not be fully folded in the test stand during the experiments. Therefore, the geometries and prescribed displacements of the FE models have been adapted such that their results can be compared with the experiments.

The first model is the torsion hinge TH-19-5-30-2-2 which has been used for the mesh convergence study. It has already been tested during the preliminary tests. The model TH-19-5-30-2-2 has been tested with two different printing configurations, an individual print, where every specimen has been printed onto the build plate individually and an assembly print, where always eight specimens have been printed and held together with area increasing cylinders to increase the adhesion with the build plate. The assembly print configuration showed better printing qualities and its dimensions are closer to the prescribed values.

Fig. 3-7 shows the prescribed displacement during the simulation with the bending angle on the X-axis. This is the region with the prescribed displacement. During the experiments, it is also the bending angle, which will be the measure of displacement. As the specimen is bent circular-wise in negative X-direction, UX tends towards the negative of the total specimen length and UZ increases until the angle of 90° and then decreases again such that the specimen is fully folded in the end, describing a circular displacement. This displacement is the same for all subsequent models with the only difference that it is adapted to the total specimen length such that the models can be fully folded.

The equivalent von Mises stress is steadily increasing during the simulation (Fig. 3-8). The increase is almost linear because the material model is linear and the applied boundary conditions (prescribed displacement) only change linearly.

As described above, stress singularities appear at the stress peaks. Therefore, the stress at the nodes around the node with the maximum stress is averaged in order to get a smoother stress distribution and to remove the high peak stress of the singularity. This new maximum stress is subsequently called averaged maximum von Mises stress around the maximum ($\sigma_{vM,\ avg.\ max}$).

The reaction forces in x- and z-direction at the nodes where the prescribed displacement has been applied change in a nonlinear way (Fig. 3-9). This can be explained by the fact that the forces are bound to the global coordinates and the investigated nodes move in a half circle. Therefore, the local x- and z-axes are not parallel to the global axes. However, in this study it is important to know the opening force of the specimens which is the total reaction force calculated by vector addition of the forces in x- and z-direction. The force in y-direction is a parasitic out-of-plane force which cannot be measured in the test stand. For the torsion hinge models it is zero as they do not show any out of plane movement during bending. However, the total force is still not increasing linearly which might be due to the large deflection and therefore appearing geometrical nonlinearities.

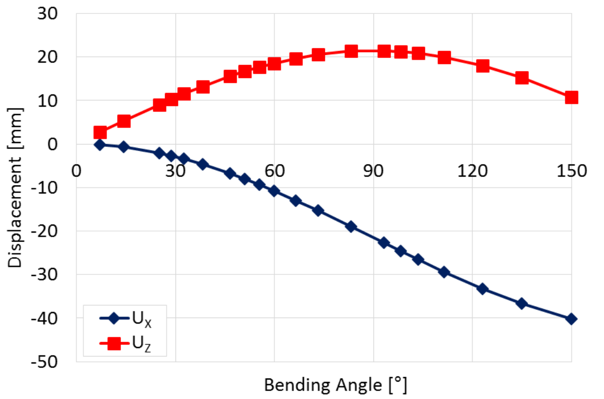

Fig. 3-7: Displacements of TH-19-5-30-2-2 during simulation

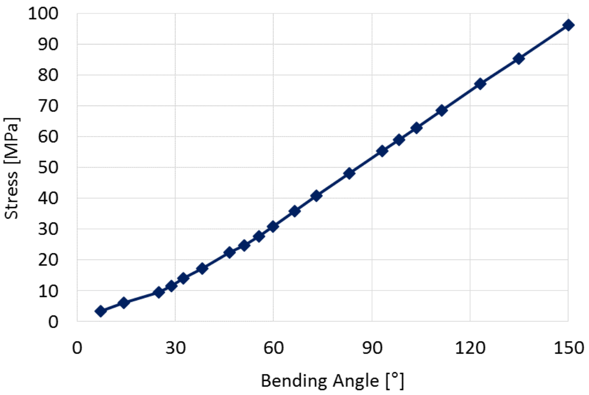

Fig. 3-8: Von Mises stress of TH-19-5-30-2-2 during simulation

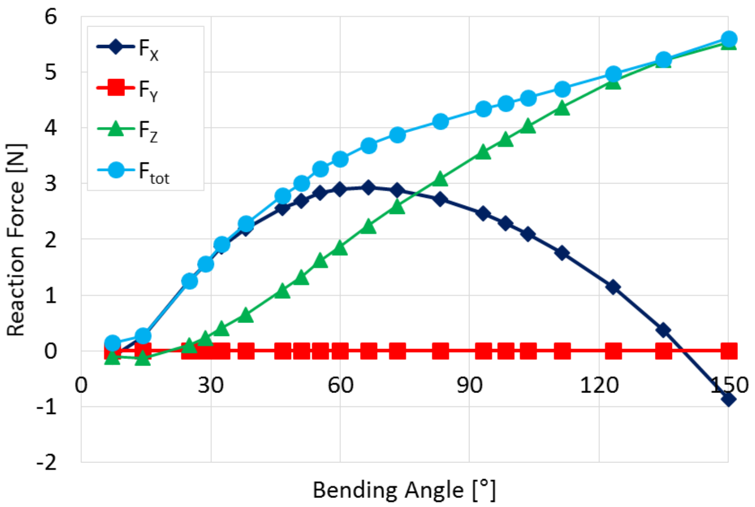

Fig. 3-9: Reaction forces of TH-19-5-30-2-2 during simulation

The reaction torque is calculated from the reaction force with equation (3.2):

$$M_{react,final} = F_{react,final} * \frac{L_{tot}}{2} \tag{3.2}$$

Where L_{tot} is the total specimen length from left to right as explained in the previous section.

To be able to compare the model's efficiency of reaction force and weight with other models, the total model volume has been calculated. The total model volume is calculated with ANSYS by summing up all element volumes. The total mass is the volume multiplied with the material specific density of Nylon ($\rho = 1100\ kg/m^3$ [58]).

The simulated values for all torsion hinge models are presented in Tab. 3-2. The averaged stress around the maximum von Mises stress shows that there exists a stress singularity, as its value is smaller by 6.35 to 20.51 % compared to the maximum. However, this difference can be accepted, as it is not the main goal to get the exact stress value but to get the reaction torque, which can then be compared with the experimental data. The mesh convergence study showed that the reaction torque converged well.

Tab. 3-2: Results for FE simulations of all torsion hinge models

Model	Maximum von Mises stress [MPa]	Avg. stress at maximum [MPa]	Final reaction force [N]	Final reaction torque [mNm]	Total model mass [mg]
TH-19-5-30-2-2: Assembly Print Configuration	96.276	82.830	5.602	120.443	676.31
TH-19-5-30-2-2: Individual Print Configuration	81.581	76.399	4.811	103.437	661.93
TH-28-6-30-2-1.5	51.722	43.644	0.956	29.636	385.44
TH-28-4-30-1-1.5, t_{rod} = 1.5 mm	34.030	27.051	0.453	13.590	453.64
TH-28-4-30-1-1.5, t_{rod} = 2 mm	41.258	36.909	0.671	20.130	586.07

When comparing the values of the individual print and the assembly print configuration of the model TH-19-5-30-2-2 it can be seen that the individual print model achieved slightly smaller values for all results parameters. This is due to the fact that the individually printed specimens showed a larger offset from the prescribed dimensions and are therefore slightly smaller and more compliant resulting in less stress and less reaction force.

The models TH-28-6-30-2-1.5 and TH-28-4-30-1-1.5 are thinner than the TH-19-5-30-2-2 and therefore more compliant. This is resulting in lower stresses and reaction forces.

Model TH-28-4-30-1-1.5 has been tested and simulated in two different configurations, one where the whole specimen has the same height and one where the rods are thickened in order to investigate the influence of the rods. These rods have a thickness of 2 mm resulting in a much larger stiffness of the rods. This increases the overall stiffness of the model and therefore the stress but also the reaction force.

Tab. 3-3 shows the performance of each torsion hinge model. The performance has been defined as the ratio of the reaction torque and the total model mass. This shows how much reaction torque can be expected by the hinge model in relation to the added weight when using it as a deployment method. It can be seen that the model TH-19-5-30-2-2 performs much better than the other models. It compensates its higher weight with a much larger reaction torque.

Tab. 3-3: Reaction torque to weight ratio for all torsion hinge models

Model	Reaction torque / total model mass [Nm/g]
TH-19-5-30-2-2: Assembly Print Configuration	0.178
TH-19-5-30-2-2: Individual Print Configuration	0.156
TH-28-6-30-2-1.5	0.077
TH-28-4-30-1-1.5, t_{rod} = 1.5 mm	0.030
TH-28-4-30-1-1.5, t_{rod} = 2 mm	0.034

3.3 Optimization of elastic hinge design

To improve the mechanical properties of the elastic hinges and to find alternatives for the patented torsion hinge, various designs need to be tested and their properties need to be compared. The goal is to find an optimal hinge design, which has a high stiffness and can still be folded such that it has no plastic deformation. In addition, it needs to be lightweight. The hinge designs mentioned in section 2.2.6 have already been compared in [6]. It has been shown that the torsion hinge has a good performance. However, the foldable wings of insects show different design patterns, as shown in section 2.2.3. These insect wings have evolved over thousands of years and the evolution brought up very efficient designs. However, the insect wings are not purely mechanical parts, but they are incorporated into a living body. This means that differences in blood pressure inside the insect's veins or external forces from legs are able to change the behavior of the foldable structure. As the here-studied deployment mechanism should deploy itself without external inputs, but only with the stored internal energy, the studied insect vein design needs to be adapted to the different boundary conditions. Therefore, the design of the insects' wing veins is studied further in this chapter. Then, a base body for each biological design will be developed which will further be optimized with the help of a parameter study with ANSYS.

Tab. 3-4: Overview of elastic hinges for wing folding in insect wings (picture source section 2.2.3)

Design Name	**Species**	**Comments**	**Picture**	**Schematics**
Round- / Oval-shape	Earwig (Forficula auricularia)	Not the same shape on the whole wing, some connecting rods are shifted or tilted.	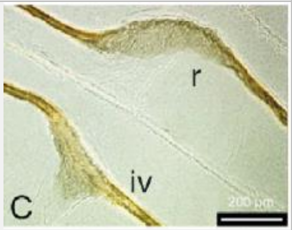	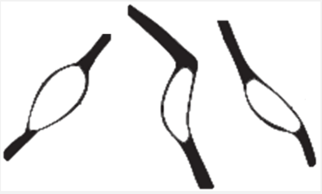
L-shape	Beetle (Monochamus sartor F.)	Reduced cross-section at fold line	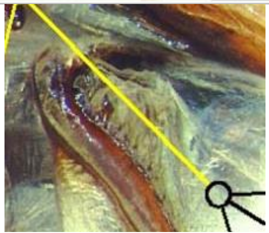	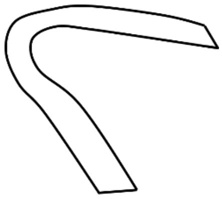
Z-shape	Beetle (Monochamus sartor F.) & wasp beetle (Clytus)	Rotation around central rod	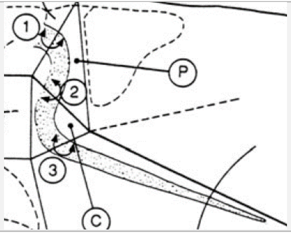	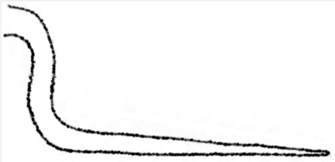
Annular shape	Drone fly (Eristalis tenax) & desert locust (S. gregaria)	Increases flexibility in between two adjacent annuli	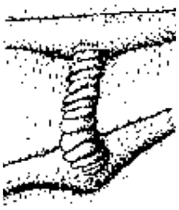	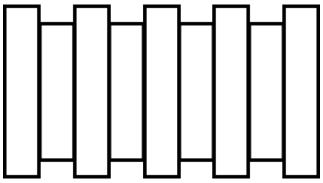

Tab. 3-4 shows an overview of different elastic hinges used for wing folding in insect wings. More details about the different vein designs can be found in section 2.2.3. All discussed insect wing veins contain resilin, which is a rubberlike protein preventing material fatigue [34]. It is not the goal to rebuild the same structure containing resilin but a good approach might be to introduce a second, very flexible material at the center of the hinges in order to get enough overall stiffness, but only low stresses. Also, the resilin is often distributed anisotropically [34], which might be recreated by changing the cross-sectional area of the elastic hinges.

Comparing the vein structures in Tab. 3-4 with respect to further 3D-printing possibilities and design approach, two vein designs can be removed from further investigations. The L-shape needs to have a reduced cross-section at the fold line, thus working similarly to the “wide-and-flat hinge” or a pure rod from section 2.2.6 for which no satisfactory results have been shown. The annular shape design will also be removed from further investigations because a fully round structure with different cylinder cross-sections would be difficult to manufacture with FDM and even more difficult to fix onto a membrane due to the small bonding area. The round- or oval-shape and the Z-shape seem to be promising starting points for a further analysis. They both include an out of plane displacement during folding, distributing the stresses over a larger distance than pure folding. The pure mechanical capabilities of these two vein shapes will further be optimized in this section. To start off, a topology optimization after the theory of Bendsøe and Kikuchi [61] will be made. This optimization will be done with the analysis system “Topology Optimization” incorporated in ANSYS Mechanical.

3.3.1 Topology optimization

3.3.1.1 Introduction to topology optimization

This subsection explains the basic ideas of topology optimization after Bendsøe and Kikuchi [61], the most common topology optimization method. The goal of an optimization of mechanical structures is most often to get the stiffest structure while ending up with a lightweight product. This means that an algorithm has to decide which parts of an initial mechanical structure are important or load-bearing and which parts could possibly be removed. To do so, topology optimization is a good approach as it is well established for minimum compliance design, leading to a maximum stiffness under the applied loads and boundary conditions [62]. It is based on finite element models and checks whether elements need to be retained or if they could possibly be removed. However, checking every possible combination of elements would not be practical or is even impossible as the number of different possibilities n_P increases exponentially with the number of finite elements n: [62]

$$n_P = 2^n \tag{3.3}$$

To overcome this, Bendsøe and Kikuchi [61] introduced a homogenization method by altering the objective function continuous. This is done by introducing a distribution function, called density. This density is able to vary continuously between a minimum value of zero and a maximum value of one. This renders the problem from checking every possible combination of elements in the design space to controlling the density of each individual element, thus enormously simplifying the number of possible solutions. The element density shows how much the individual element is stressed compared to the overall model. If the density tends to go to zero, the element is not stressed much and is therefore obsolete. On the other hand, if the density tends to go to one, the element is highly stressed and is very important for the overall structure to be able to bear the applied loads.

Maximizing the stiffness can be passed onto a global objective function by minimizing the work W done by the external forces r onto the displacements u:

$$\min W = u^T r \tag{3.4}$$

The displacements depend on the stiffness K of the system as:

$$Ku = r \tag{3.5}$$

The structural stiffness depends on the individual stiffness of each finite element. This means it depends on the Young's modulus E of each element. This is where the homogenization takes place [61]:

$$E = E_0 \rho^p \tag{3.6}$$

Where:

- E_0: reference stiffness value corresponding to the used material
- p: $3 \leq p \leq 4$, justified by material modelling considerations and to push Young's modulus against the bounds of zero or one more quickly.
- ρ: density distribution function, $\epsilon \leq \rho \leq 1$ with ε a small number close to zero

Thus, the Young's modulus of each element will tend either to zero or to one, depending on its density distribution function. However, it stays a continuous function where well-known optimization methods as gradient optimization or penalty methods can be used to optimize it.

An example of a simple topology optimization is shown in Fig. 3-10. The beam is clamped on the left-hand side and pushed by a pressure on the right-hand side. The goal of the optimization was to minimize the compliance under the constraint to retain 30% of the initial mass.

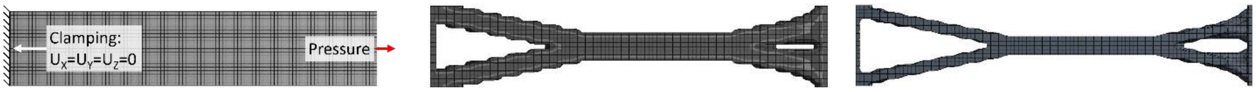

(A) Initial Model (B) Solution after 12 iterations (C) Final solution after 24 iterations

Fig. 3-10: Topology optimization of a beam under axial pressure

In ANSYS Mechanical, topology optimization is a built-in analysis system. First of all, one has to give an initial model to the solver. This defines the workspace of the algorithm, as it cannot add material, but only remove it. Then, the boundary and loading conditions need to be applied to the model and it needs to be meshed. It is important to keep in mind, that the homogenized topology optimization is mesh-dependent as it optimizes the density of each individual element. If the mesh changes, also the final result might change and is therefore influenced by the initial meshing. After preparing the model as for a normal FE calculation, the optimization space has to be defined. Important geometries that should not change, like areas with boundary conditions or certain holes for bolts for example, can be excluded from the optimization and they will keep their initial geometry. Furthermore, the objective function needs to be defined. This is mostly minimizing the compliance but could also be minimizing the mass. The restrictions need to be added for the optimization. There are several different possibilities for restrictions. The most common one is to specify a certain percentage of mass that should be kept compared to the initial model. Other restrictions could be symmetries, extrusion directions or to specify a certain maximum value for global equivalent stress that should not be exceeded in the final model.

After reaching convergence in the optimization model, each element still has an individual density value. It is clear, that it is not the idea to build porous specimens after the optimization. Therefore, a threshold value for the density needs to be specified. Elements with an individual density, which is lower than the threshold, shall be removed from the structure and elements with a density higher than the threshold shall be fully filled with material. In ANSYS Mechanical it is recommended to remove elements with a density lower than 0.4 and to keep elements with a density higher than 0.6. In between 0.4 – 0.6 it is case dependent. However, the default threshold is set to 0.5. It has also been found that restrictions like the retainment percentage of mass are obeyed with a retaining threshold of 0.5.

3.3.1.2 Topology optimization approach

In order to do a topology optimization of a fully filled model between the two opposing rods, a starting model and the restrictions need to be defined. This subsection defines the setup for the topology optimization and shows its results. First, the objective function and restrictions are defined. Second, the starting model is designed and explained.

The objective function for the optimization model is minimizing the compliance in order to get a stiff hinge design, which is able to store enough energy to deploy itself after release. Restrictions are made either on the value of maximum stress or the amount of retained material compared to the initial model. The maximum equivalent von Mises stress in the model shall not exceed the admissible stress of the material to stay in the elastic regime. Another restriction is that the lower area of the structure needs to stay flat in order to be able to print on a build plate or bond it onto a membrane. Therefore, the exclusion regions for the optimization are the areas where the boundary conditions are applied and the area parallel to the xy-plane in negative z-direction (see Fig. 3-11 for initial model and coordinate system). A summary of the setup for the topology optimization is shown in Tab. 3-5.

Tab. 3-5: Setup for topology optimization

	Parameter	**Value**
Objective Function	Compliance	Minimum
Restrictions	Von Mises Stress	$\sigma_{vMises} < \sigma_{adm}$
	Mass	$m_{final} = x * m_{initial}$, where x describes the percentage of retained material
	Exclusion region	Areas of boundary condition & area parallel to the xy-plane in negative z-direction

The initial model has been designed as shown in Fig. 3-11. The two opposing rods are connected by a block with size 40 x 20 mm. The left-hand side of the model is clamped and a displacement is applied onto the right-hand side such that the model gets folded. The displacement is highly nonlinear and therefore this nonlinearity should be accounted for. However, the optimization solver in ANSYS Workbench is not able to do this and is therefore not very well suited for large displacements. In addition, this nonlinearity issue also induced that the restrictions on the maximum von Mises stress did not reach feasible solutions, but only somehow randomly scattered elements in the domain area. Still, some results could be obtained by using the mass restriction. Fig. 3-12 shows the results for a mass restriction of 20% compared to the initial mass. All the outer material has been removed by the algorithm, making the solution model thinner where it is bent. In addition, the flatter central part is broadened towards the center of the model. This result reminds of the mentioned “wide-and-flat hinge” from section 2.2.6. However, it has been shown that this design is not suitable for the considered application.

By trying to oblige the algorithm to change the load path, a hole has been introduced into the initial model and the height has been increased as shown in Fig. 3-13. Restraining the solver to 8% of the final mass reached the solution in Fig. 3-14, which reminds of the oval-shaped hinges in earwigs.

These two results show that one cannot simply let the topology optimization solver guess for a solution from a too large solution space. In addition, the geometry of both solutions is very similar to already known hinge possibilities. This and the fact that the topology optimization solver in ANSYS Workbench is not well suited for large displacements brings up the conclusion, that further optimization of the chosen vein shapes needs to be done in a different way, namely a optimization of parametrized designs as performed in section 3.3.3.

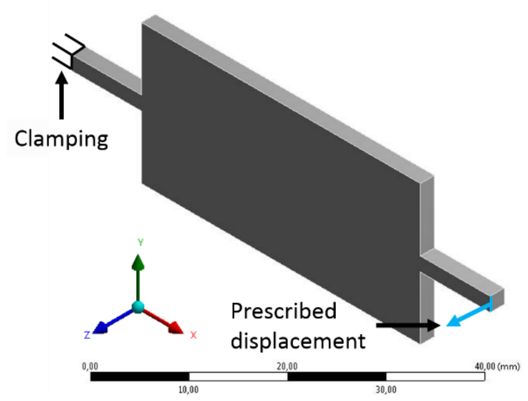
Clamping
Y
Z
X
Prescribed displacement
0,00
20,00
40,00 (mm)
10,00
30,00

Fig. 3-11: Initial model for topology optimization

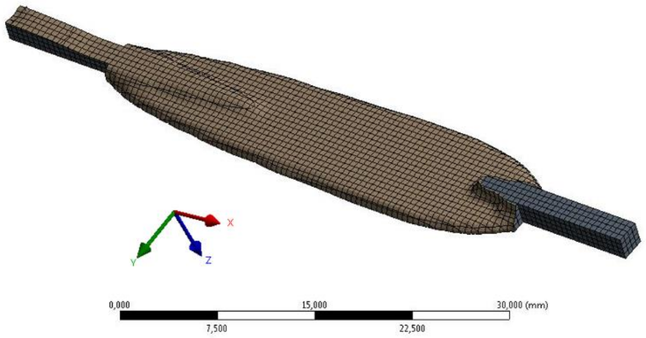
X
Y
Z
0,000
15,000
30,000 (mm)
7,500
22,500

Fig. 3-12: Result for a mass restriction of 20% of the initial mass

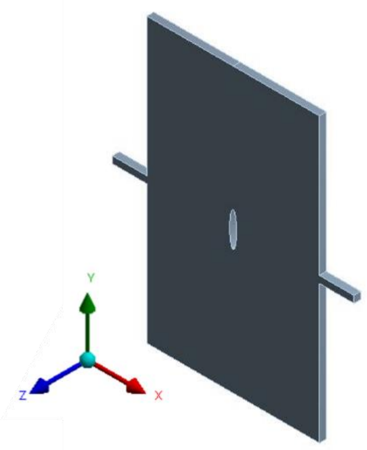

Fig. 3-13: Initial model with central hole for topology optimization

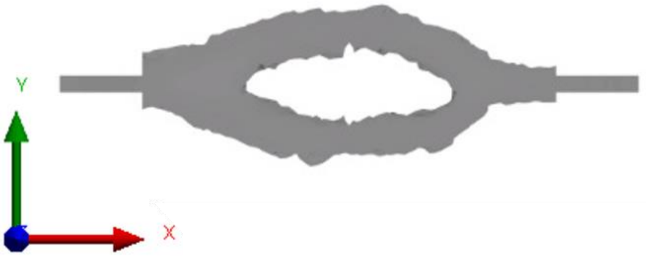

Fig. 3-14: Result with initial hole for a mass restriction of 8% of the initial mass

3.3.2 Parameter study & sensitivity analysis

In order to optimize the oval-shape and the Z-shape hinges observed in foldable insect wings, the hinges have been designed using as few independent parameters as possible. Further, the influence of these parameters onto the mechanical properties of the hinge have been investigated with a full factorial parameter study and a sensitivity analysis. This section describes the hinge parametrizations and the results of the parameter studies starting with the simpler model of the *Z-shape* and then describing three different versions of the oval-shape, the so-called *straight*, *tilted* and *spring* models (Fig. 3-15).

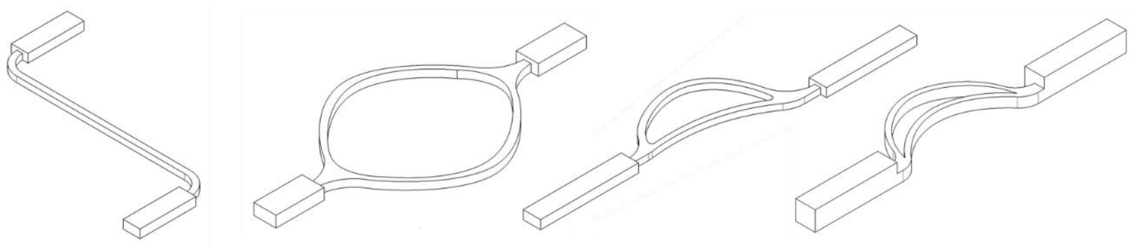

Fig. 3-15: Overview of parametrized hinges: *Z-shape*, *oval-shape straight*, *tilted* & *spring* (from left to right)

The *Z-shape* is a simple geometry to parametrize and only needs five parameters to be fully defined. Fig. 3-16 shows a drawing of the hinge design. The used parameters are:

- *t*: Thickness
- *w*: Width
- *L1*: Length of the two rods
- *L2*: Length of the central part
- *R*: Radius of curvature of the connection between the rods and the central part

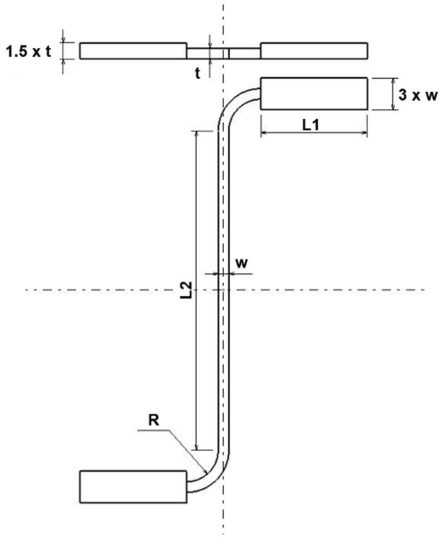

Fig. 3-16: Parametrization of *Z-shape* hinge

First of all, one can see that the model is point-symmetric about the origin, which facilitates the parametrization. As the final application of the investigated hinges is not yet defined, the rod length cannot be defined so far and will not be changed during the parameter study. Furthermore, the two rods have been made three times as wide and 1.5 times as thick as the actual hinge in order to increase their stiffness. With this cross-sectional area increase, the rods reach a stiffness, which is about ten times the stiffness without the enlargement. This approach shall focus the parameter study onto the hinge itself, removing the influence of the rods due to their individual bending.

The *Z-shape* hinge works similarly to the torsion hinge. It gets twisted during folding and therefore, it is already clear that the longer the central part, *L2*, the more compliant the model gets. However, to get the influence of every individual parameter and their combination, a full factorial parameter study has been made. To do so, two distinct values have been chosen for every parameter and every possible parameter combination has been evaluated. This leads to a so-called 2-k factorial experimental design. This design needs 2^k experiments, where k is the number of parameters. With such an experimental design, it is possible to determine the influence of every individual parameter as well as their interaction, also called sensitivity analysis.

As already mentioned, *L1* is kept constant during this parameter study and therefore the *Z-shape* hinge has four changing parameters leading to $2^k = 16$ FE simulations. These simulations have been automatized with the programming language *Python*. A script has been written which finds every possible parameter combination of each of the two parameter values. Then, for each parameter combination, the corresponding prescribed displacement as well as a text file containing the parameter values are written into the respective folder. After preparing the needed information, the script runs the ANSYS APDL input file and saves the final results. The workflow of the *Python* script is shown in Fig. 3-17.

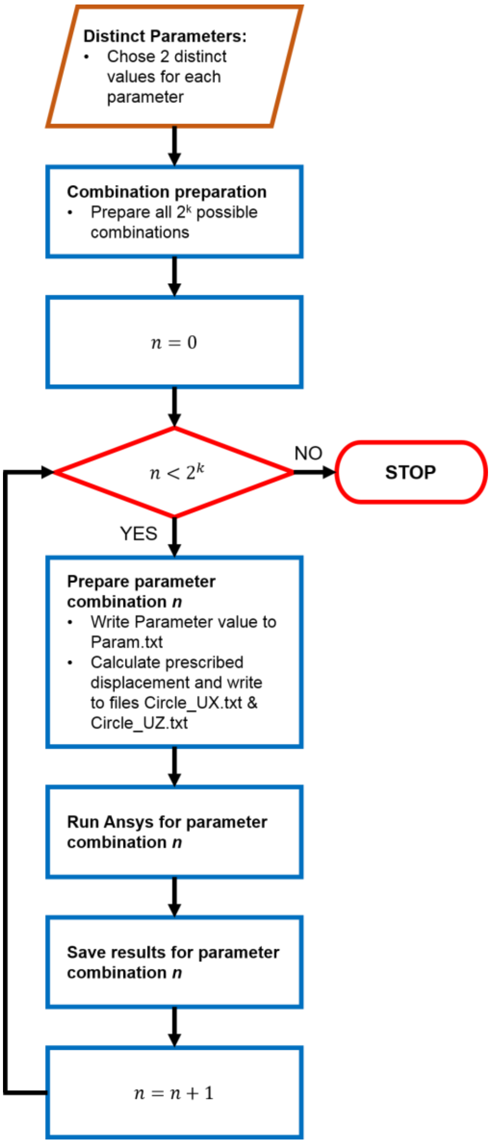
Distinct Parameters:
• Chose 2 distinct values for each parameter
Combination preparation
• Prepare all 2ᵏ possible combinations
n = 0
n < 2ᵏ
NO
STOP
YES
Prepare parameter combination n
• Write Parameter value to Param.txt
• Calculate prescribed displacement and write to files Circle_UX.txt & Circle_UZ.txt
Run Ansys for parameter combination n
Save results for parameter combination n
n = n + 1

Fig. 3-17: Workflow of Python script for parameter studies

The results of the parameter study have been evaluated with the software *Minitab*, a statistical software that is able to evaluate factorial designs of experiments. Fig. 3-18 shows a Pareto diagram of the standardized effect of the individual parameters and the interactions of two parameters with regard to the maximum von Mises equivalent stress in the *Z-shape* hinge. It can be seen, that the interactions between parameters for the *Z-shape* model are very low and therefore do not need to be investigated further. In addition, an order of the individual influence of each parameter is made by the Pareto diagram. One can see, that the order of the four most important parameters is: $L2 > w > R > t$. The same Pareto diagram has been made with regards to the reaction force at the nodes where the prescribed displacement is applied. This is shown in Fig. 3-19. The influence of the parameter interaction is low as well and the order of the four most important individual parameters is: $w > t > L2 > R$. Hence, an optimization algorithm does not necessarily need to account for parameter interactions because their influence on the two target variables maximum von Mises equivalent stress and reaction force at displaced nodes is low. However, optimizing this model is not simple because the parameters influence the von Mises stress and the reaction force in the same direction, which means for example that by increasing L2, both the stress and the reaction force decrease but the goal, is to only decrease the stress while keeping the force high or even increase it.

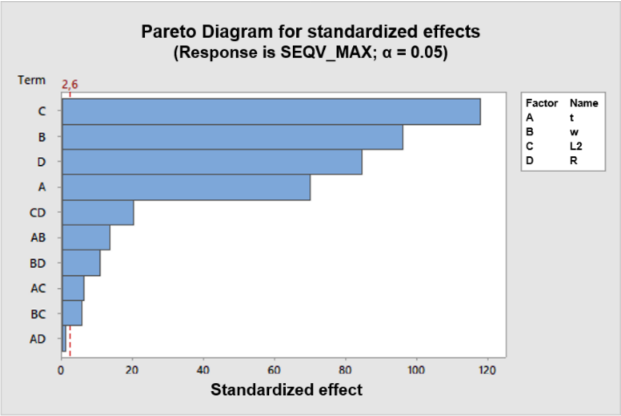

Fig. 3-18: Pareto diagram for standardized effects with regard to maximum von Mises equivalent stress for *Z-shape* hinge

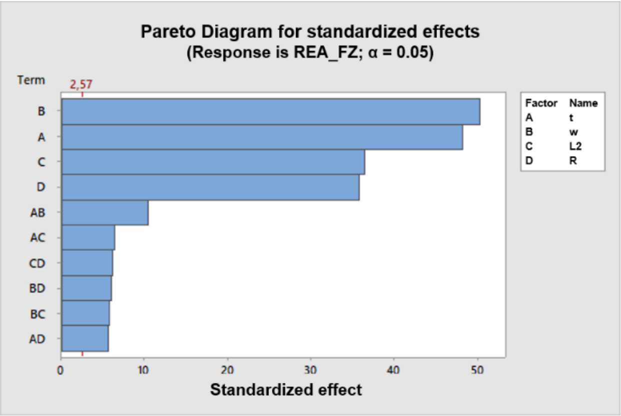

Fig. 3-19: Pareto diagram for standardized effects with regard to reaction force at displaced nodes for *Z-shape* hinge

The oval-shape models need more parameters to be fully determined than the *Z-shape* model. The straight version of the oval-shape model uses 8 parameters:

- *t*: Thickness
- *w*: Width
- *L*: Length of the two rods
- *R1*: Large radius of the center
- *R2*: Smaller radius at the connection between hinge and rod
- *D1*: Axial displacement of center of large circle
- *D2*: Axial displacement of the center of the smaller circle
- R_{fillet}: Radius of fillets at rod-hinge connection

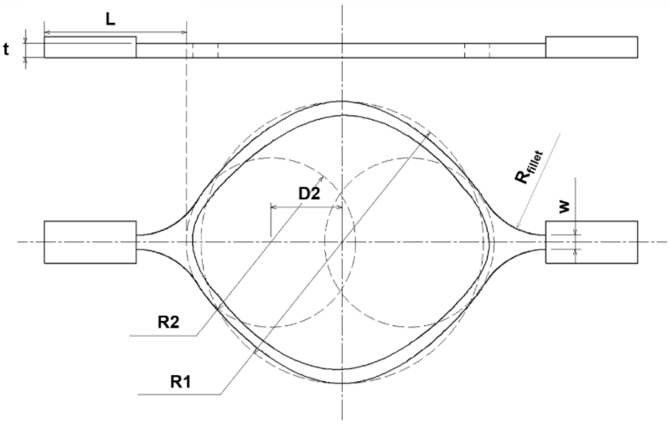

Fig. 3-20: Parametrization of *oval-shape straight* hinge

In Fig. 3-20, D1 is set to zero and not shown in the drawing in order to start with a symmetric model. It defines the axial displacement of the large center circle defined by R1. For D1 larger than zero, the center circle would be shifted along the horizontal axis by the value of D1. However, it appeared that this does not have a significant influence on the maximum stress or reaction force values. Therefore, it will be fixed in subsequent optimizations.

With the same Python script as explained in Fig. 3-17, the $2^k = 64$ FE simulations have been executed, where again, the length of the rod has been fixed and also the fillet radius has not been altered because it does not affect the zone of interest, which is the central part of the hinge. This is true for all following models. Evaluating the Pareto diagrams of the standardized effects again shows the sensitivity of the parameters on the model's reaction (Fig. 3-21 & Fig. 3-22).

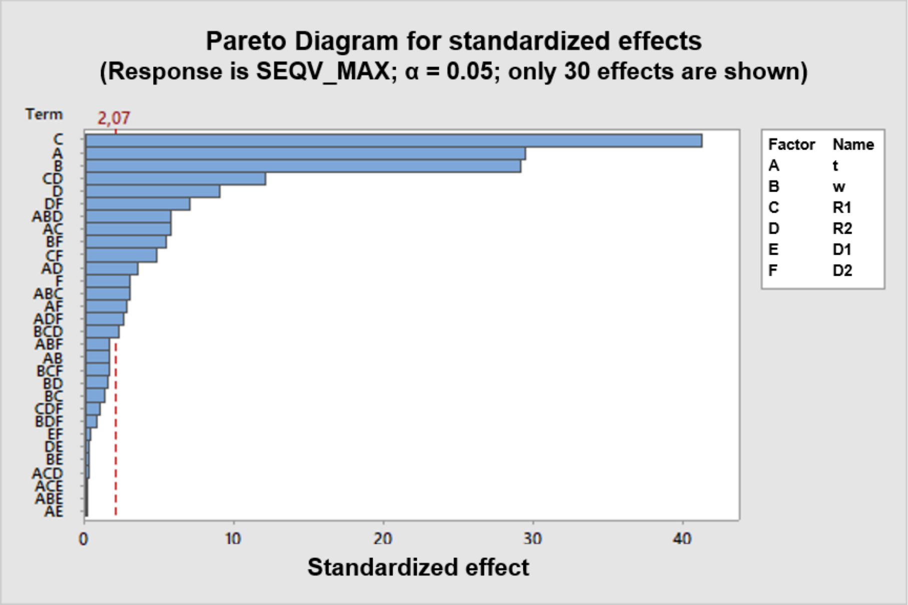

Fig. 3-21: Pareto diagram for standardized effects with regard to maximum von Mises equivalent stress for *oval-shape straight* hinge

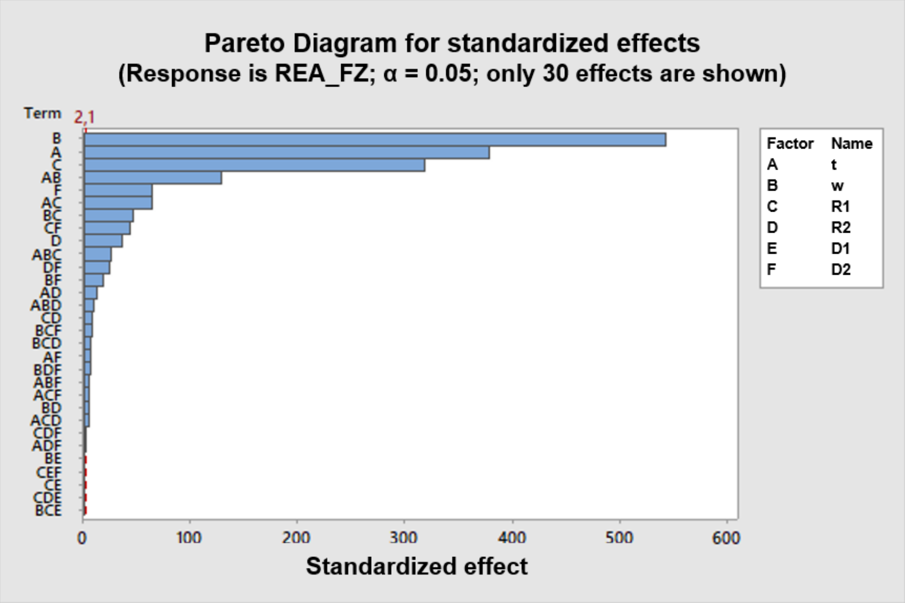

Fig. 3-22: Pareto diagram for standardized effects with regard to reaction force at displaced nodes for *oval-shape straight* hinge

For the *oval-shape straight* hinge, the influence of the interactions is still very low but some interactions are more important than individual parameters. For the maximum von Mises stress, the most important parameters can be ordered as: $R1 > t > w > R1 * R2$, whereas for the reaction force it is: $w > t > R1 > t * w$. In addition, one can see that the parameter *D1* has almost no influence at all and *D2* only has a small influence on the reaction force but almost none on the maximum stress. On the interaction plots (Fig. 3-23 & Fig. 3-24) one can see the direct influence of each combination of interaction. For the reaction force, the corresponding blue and red lines indicating the low and high value of the second interacting parameter, are very close to being parallel except for $t * w$. This means that almost no interaction occurs. However, for the equivalent stress, the lines of $R1 * R2$ are not parallel at all and cross each other which means that there is a negative interaction in between those two parameters. It can be seen, that increasing *R1* has more influence when *R2* is kept smaller.

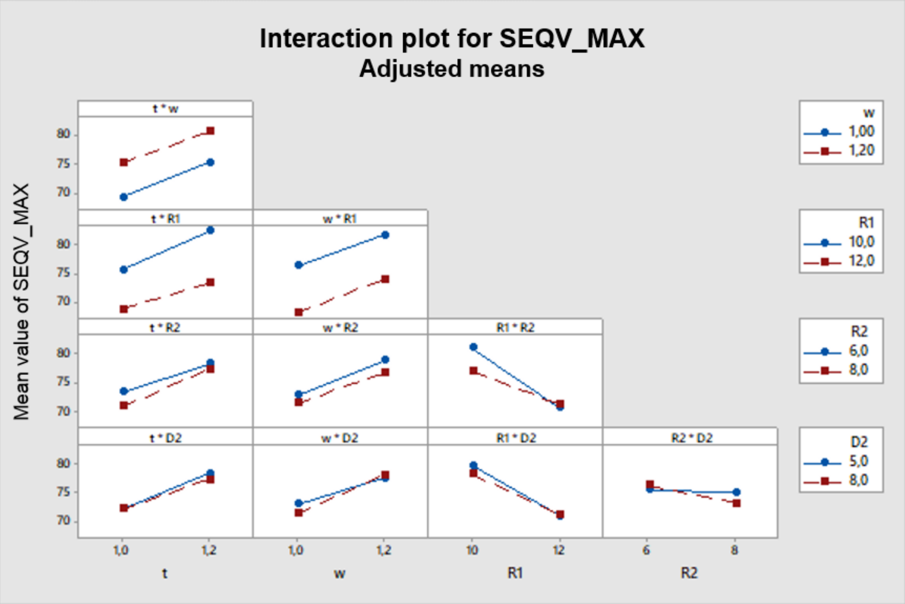

Fig. 3-23: Interaction plot for adjusted means with regard to maximum von Mises equivalent stress for *oval-shape straight* hinge

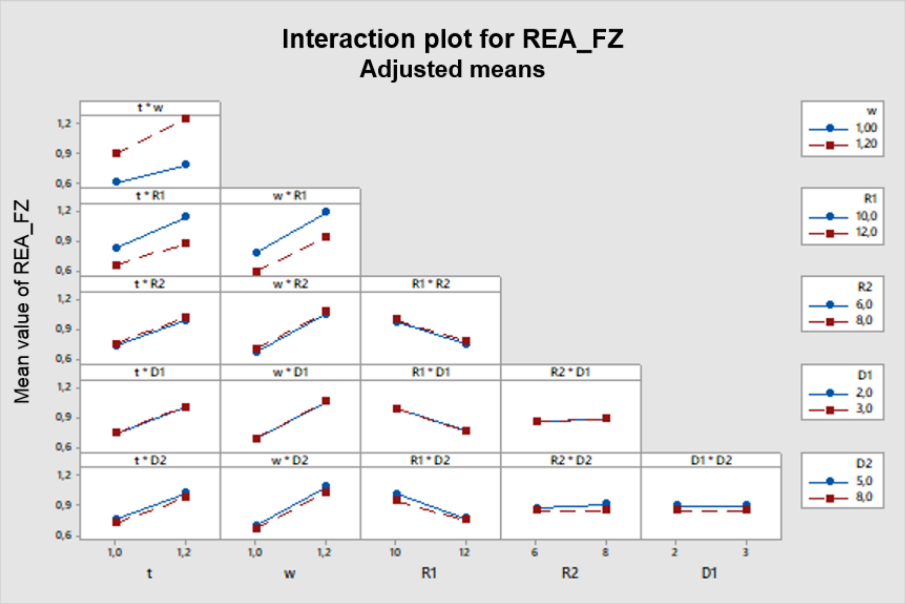

Fig. 3-24: Interaction plot for adjusted means with regard to reaction force at displaced nodes for *oval-shape straight* hinge

Similar to the *oval shape straight* model, the tilted version of the oval-shape model needs 8 parameters as well:

- *t*: Thickness
- *w*: Width
- *L*: Length of the two rods
- *R*: Radius of the central part
- *X*: Axial displacement of center circle
- *Y*: Vertical displacement of center circle
- *D*: Distance between center of circle and inside hinge part
- R_{fillet}: Radius of fillets at rod-hinge connection

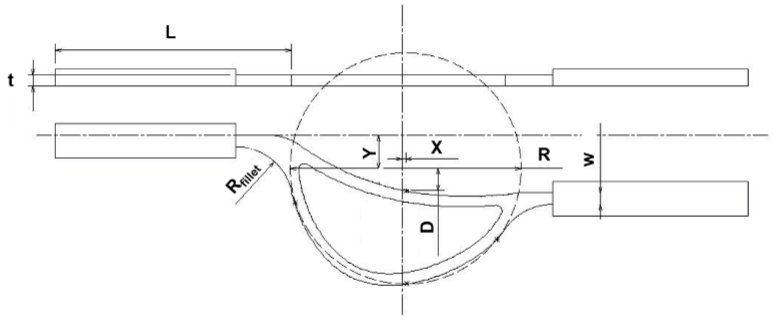

Fig. 3-25: Parametrization of *oval-shape tilted* hinge

One can see in Fig. 3-25 that the wider part of the hinge does not perfectly follow the drawn circle. This is due to the fact that the circle is used to define points along its circumference, but the model is built with splines containing these points but also others in order to have a smooth model and therefore slightly deviating from the circle.

The Pareto diagrams for the *oval-shape tilted* model are shown in Appendix A.2. Ordering the parameters according to their influence for the four most important parameters or interactions between them for the maximum stress gives: $R > t > R * Y > R * X * Y$, and for the reaction force: $t > w > Y > R$. One can see that for the stress, the interaction between R, X and Y seems to be important, as they are ranked third and fourth of the most influential parameters or combinations. However, already RY only has about 40 % of the influence of R whereas RXY only gets about 25 %. Still, for further optimizations, these parameters might be important for reaching good results.

Last but not least, the third model of the oval shape model, the spring version needs 7 parameters (Fig. 3-26):

- *t*: Thickness
- *w*: Width
- *L*: Length of the two rods
- *R*: Radius of the spring elements
- *Y1*: Vertical displacement of the first spring element
- Y2: Vertical displacement shift of the second spring element compared to the first element
- R_{fillet}: Radius of fillets at rod-hinge connection

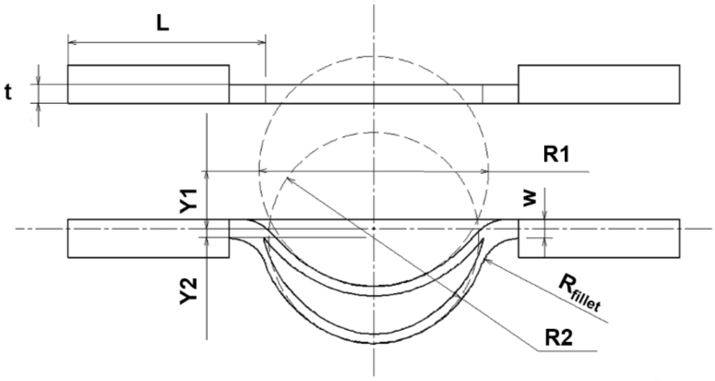

Fig. 3-26: Parametrization of *oval-shape spring* hinge

The results of the parameter study for the *oval-shape spring* model are also shown in Appendix A.2. As for the other models, the four most influential parameters or parameter combinations can be obtained from the graphs in Fig. A-11 and Fig. A-12. One can see, that the order for the maximum stress is: $w > R2 > w * R1 * Y1 > R1 * Y1$, and for the reaction force: $w > w * R2 * Y2 > w * Y2 > t * w$. As for the *oval-shape tilted* model, parameter interactions that are highly ranked appear for both the maximum stress and the reaction force. Again, their influence is only in the range of 35 % to 40 % compared to the influence of the most important parameter. However, one can see in Fig. A-13 and Fig. A-14 that these parameter interactions are important, as there exist strong counter-interactions. This means that the influence of a change in one parameter can strongly depend on the value of the second parameter. In addition, a change of the second parameter might increase the value of the response function depending on the first parameter, even though by changing it itself it would decrease this value.

3.3.3 Optimization of parametrized hinges

The hinges introduced and studied in section 3.3.2 have been optimized regarding their most influential parameters. Therefore, a Python script has been written which runs an FE simulation in ANSYS, reads the results and compares them to the objective function of the optimization and its boundary conditions. Then it changes the values of the geometrical parameters and runs the next FE simulation until the solution has converged or the maximum time or iteration number has been reached. Fig. 3-27 shows the optimization process, including the Python functions and sub-functions.

To be able to start an optimization including FE simulations in ANSYS some preparations need to be done. The Python script needs to know where the ANSYS executable is stored on the hard-drive and in which working directory the simulations should take place. Then, global variables such as the maximum allowable stress or the maximum specimen length are defined and a folder where future results are to be stored is created. Furthermore, the objective function, its boundary conditions and parameter bounds need to be defined. In addition, the maximum number of iterations as well as the maximum run time need to be outlined. Then, the optimization can start at the prescribed starting point. The starting point defines the parameter values of the design variables for the first FE simulation. Afterwards, the prescribed displacement steps are calculated. This displacement, together with the parameter values, is concatenated with the two text files, which define the FE model. All this data is then stored as an input file in the working directory. This input file is run by ANSYS. After finishing the FE simulation, it is checked if ANSYS has converged and the results file has been written. If so, the results file is copied into the results folder. If, for any reason, no results file has been written, the error file as well as the input file are copied into the results folder. With this, one can check what caused the problem at a later stage without interrupting the optimization process. In order to know how to proceed with the optimization, the maximum von Mises stress as well as the final reaction forces are read from the results file. If no results file has been written, the optimization variable is set to a very large value (i.e. 1’000’000) in order to show the algorithm that an inadequate point has been reached where no best solution will be found. Finally, the files written by ANSYS are deleted to save space. With the known information from previous calculation steps, the optimization algorithm defines the next parameter set and a new loop is started.

The simulations stop when convergence is reached or the maximum run time or maximum number of iterations has been attained.

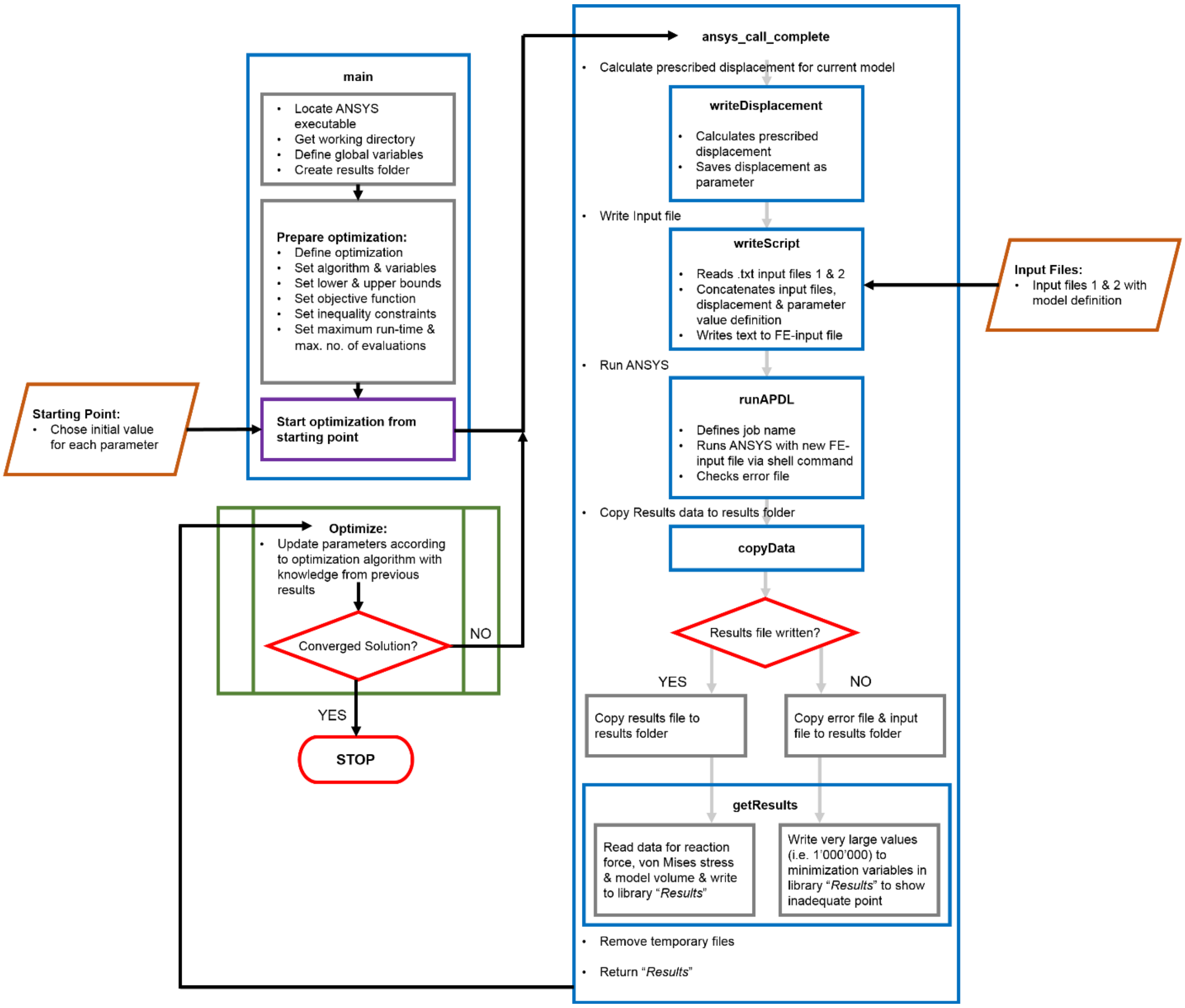
main
Locate ANSYS executable
Get working directory
Define global variables
Create results folder
Prepare optimization:
Define optimization
Set algorithm & variables
Set lower & upper bounds
Set objective function
Set inequality constraints
Set maximum run-time & max. no. of evaluations
Starting Point:
Chose initial value for each parameter
Start optimization from starting point
Optimize:
Update parameters according to optimization algorithm with knowledge from previous results
Converged Solution?
NO
YES
STOP
ansys_call_complete
Calculate prescribed displacement for current model
writeDisplacement
Calculates prescribed displacement
Saves displacement as parameter
Write Input file
writeScript
Reads .txt input files 1 & 2
Concatenates input files, displacement & parameter value definition
Writes text to FE-input file
Input Files:
Input files 1 & 2 with model definition
Run ANSYS
runAPDL
Defines job name
Runs ANSYS with new FE-input file via shell command
Checks error file
Copy Results data to results folder
copyData
Results file written?
YES
NO
Copy results file to results folder
Copy error file & input file to results folder
getResults
Read data for reaction force, von Mises stress & model volume & write to library "Results"
Write very large values (i.e. 1'000'000) to minimization variables in library "Results" to show inadequate point
Remove temporary files
Return "Results"

Fig. 3-27: Flow chart of optimization process

3.3.3.1 Optimization algorithm and approach

In order to find a good optimization algorithm and impose a well defined objective function with its corresponding boundary conditions, different approaches have been made using optimization algorithms from the Python packages NLOPT [63] and MIDACO [64]. The initial optimization approaches have been done on the different parametrized hinges. The used objective functions were to minimize the maximum stress in order to not get plastic deformation, minimize the ratio of volume to the reaction force in order to have a small and therefore lightweight model with a large reaction force and last but not least to maximize the reaction force itself.

As neither analytical objectives or boundary functions nor analytical gradients of these functions existed, optimization algorithms without a gradient approach have been chosen in order to save calculation time that would be needed by approximating the gradients with finite differences. However, not many of the NLOPT algorithms can handle inequality constraints which where needed for the here-posed problem. Therefore, only the algorithms COBYLA (Constrained Optimization BY Linear Approximations) [63] and ISRES (Improved Stochastic Ranking Evolution Strategy) [63] could be tested from the NLOPT library.

The COBYLA algorithm is a variation of the Simplex algorithm. Its documentation states that: "It constructs successive linear approximations of the objective function and constraints via a simplex of n+1 points (in n dimensions), and optimizes these approximations in a trust region at each step" [63]. The ISRES algorithm is a global optimization algorithm, which would be preferable if a local minimum has been reached.

Initial optimization attempts showed that the COBYLA algorithm exhibited a fast convergence. For the various models less than 50 iterations where needed to get close to the optimum and less than 100 iterations where needed to reach convergence. However, it was not clear if it was only a local minimum as the used algorithm cannot escape local optima.

The ISRES algorithm has not been successful, as it used too many iterations and proceeded changing the parameters somehow randomly. Also, in literature describing the algorithm it is stated that the improvement regarding efficiency and effectiveness made with this algorithm for some problems might come at the cost of being trapped in a local minimum for other problems [65].

A promising algorithm is the MIDACO algorithm (Mixed Integer Distributed Ant Colony Optimization). This solver can be used for many different problems and it can handle equality and inequality constraints in addition to the lower and upper bounds of the variables. It works as a "derivative-free, evolutionary hybrid algorithm that treats the problem as a black-box which may contain critical function properties such as non-convexity, discontinuities or stochastic noise." [64] These are promising properties for the unknown function used in this thesis. In addition, the MIDACO algorithm implements a very efficient parallelization strategy, which is simple to use. This might improve the calculation time drastically. [64]

Preliminary optimization passes showed that the MIDACO algorithm needs more iterations to converge than the COBYLA algorithm does. However, its performance seemed to be better regarding constraint violations and trapping into a local minimum. When the algorithm has a converged solution it disperses the parameters again to get a new starting point. A drawback of MIDACO is that it only supports four parameters with the free version, which has been used. However, the parameter studies described in section 3.3.2 showed the parameter's influence and therefore, the four most influential parameters regarding stress and reaction force could be used to vary whereas the remaining parameters could be fixed.

Regarding the objective function, it has been shown that minimizing the maximum stress did not reach a good performance in the converged solution regarding reaction force and therefore the reaction force for opening the specimen after folding might not necessarily be enough. Furthermore, the ratio of the specimen volume to the reaction force ended up with an optimal solution, which had a small volume, but also the reaction force was not high enough. Finally, the best solution was to maximize the reaction force under the constraint that the maximum stress shall be smaller than a certain level while the total specimen length shall be smaller than a maximum specimen size.

The mathematical formulation of the optimization problem used in the following optimization is shown in equation (4.5):

$$
\begin{array}{lll}
 & \min \; -F_{react}(x_i) & i = 1, \dots, n \\
\text{s.t.} & g_1 = \sigma_{max,model} - \sigma_{max} \le 0 & \\
 & g_2 = L_{model} - L_{max} \le 0 & \\
 & g_k = x_i - x_j \le 0 & \forall i, j = 1, \dots, n; \; \forall k = 3, \dots, m \\
 & x_{l,i} - x_i \le 0 & i = 1, \dots, n \\
 & x_i - x_{u,i} \le 0 & i = 1, \dots, n
\end{array}
\tag{3.7}
$$

where,

- F_{react}: Reaction force
- g: Inequality constraint
- L_{model}: Total length of model
- L_{max}: Maximum allowable length
- m: Number of inequality constraints in addition to stress & length constraints
- n: Number of parameters
- $\sigma_{max,model}$: Maximum von Mises stress of current model
- σ_{max}: Maximum allowable stress
- x_i: i-th model parameter out of n parameters
- $x_{l,i}$: Lower bound of parameter i
- $x_{u,i}$: Upper bound of parameter i

The additional inequality constraints, g_k, are not used by all models. They are only confining the parameters if in some models one parameter is not allowed to be larger than other parameters in order for the model to build up a correct specimen geometry. The same stress and length limits have been applied to all models and the other boundary conditions and bounds have been adjusted to each model individually. The stress limit has been defined as 20 MPa regarding the material yield stress of 31 MPa and applying a safety factor of 1.55. Therefore, not plastic deformation shall occur in the optimized models. The length limit has been set to 60 mm. Both values can be changed at a later stage when more information about the used material and maximum model size is known.

After having compared the different optimization algorithms the MIDACO solver will be used for further optimization of the parametrized hinges. The justification is that the MIDACO solver should be able to emerge from local minima and because it can be parallelized without large effort.

3.3.4 Optimization results

This subsection shows the results from the parameter optimization of the four considered models. For every model, two independent optimizations have been made, starting from two individual starting points. The used parameters and their starting points, the model's geometrical bounds and the additional boundary conditions, g_k, if they have been needed, are shown. Convergence is shown for each design and the best solutions are presented and discussed. Every independent optimization has been run until 3000 iterations have been calculated or until a maximum simulation time of five days has passed, whichever came first.

As already defined in the parameter study, the length of the rods, *L1* for the *Z-shape* model and *L* for the oval-shape models, has been fixed to 10 mm and the rods have been stiffened with a larger thickness and width than the rest of the model. This has been done because the goal was to study the hinge itself without a large influence of a deformable rod.

The total specimen length of the *Z-shape* design has been defined as $L_{model} = 2 * w + L2 + 2 * R$ which was constraint with the maximum allowable length $L_{max} = 60\ mm$. The *Z-shape* model did not need any additional geometrical boundary conditions.

Tab. 3-6 shows the parameters' lower and upper bounds, the starting points and the best solutions of these starting points for all subsequent optimized models.

It can be seen that the two best solutions do not correspond to the exact same parameter values. Especially the radius R shows a large difference. Therefore, the number of iterations might not be enough to overcome a local minimum. With the same starting points, two additional optimization runs have been executed in order to see if they converge towards the same results. It appeared that the parameter values of the solutions are almost the same, except for the *L2* value for the second starting point, which shows a difference of 7%. The same is true regarding the resulting maximum von Mises stress and the reaction force as shown in Tab. 3-7 where almost the same values have been obtained for the optimization runs 1 & 2 for both starting points. The stress distributions of the best models of each design are depicted in Fig. A-15 to Fig. A-20.

Comparing the resulting maximum von Mises stress, reaction force and specimen volume in Tab. 3-7 between the two runs for each of the same starting points one can see that the second optimization runs provided slightly better results for all parameters except the maximum von Mises stress. However, the stress is still lower or equal the prescribed bounding value. The relative difference for the thick *Z-shape* model is therefore calculated between the second runs of both starting points. Subsequently, there exist only one run per starting point and the relative difference will be calculated from the values between these two starting points.

As the volume has not been considered during the optimization, it is only shown to get a complete overview of the model. It is clear that for a final use of any of the hinges, a small volume and therefore a small mass is important for a space structure. However, during this initial optimization, the goal was to find elastic hinges with a large reaction force. Therefore, the solution from starting point I, run 2 is considered as being the best solution of the four optimization runs for the *Z-shape* model. It shows the highest reaction force and reaction torque of the four solutions while keeping the maximum von Mises stress below the threshold of 20 MPa.

Tab. 3-6: Definition of optimization variables and best solution values for all models

Model	Var.	Lower Bounds [mm]	Upper Bounds [mm]	Starting Point I [mm]	Best Solution I [mm]		Starting Point II [mm]	Best Solution II [mm]	
					Run 1	Run 2		Run 1	Run 2
Z-shape thick	t	1.00	10.00	1.00	9.54	9.56	2.00	10.00	10.00
	w	1.00	10.00	1.00	1.87	1.87	5.00	1.51	1.51
	L2	1.00	60.00	40.00	6.85	6.85	35.00	6.12	5.70
	R	1.00	30.00	5.00	21.89	21.88	10.00	17.10	17.10
Z-shape thin	t	1.00	2.00	1.00	2.00		2.00	1.20	
	w	1.00	10.00	1.00	1.02		5.00	1.07	
	L2	1.00	60.00	40.00	7.85		35.00	6.10	
	R	1.00	30.00	5.00	9.80		10.00	8.22	
Oval-shape straight thick	t	1.00	10.00	3.14	9.21		1.00	8.97	
	w	1.00	10.00	2.94	1.87		34.27	11.82	
	R1	1.00	50.00	10.48	34.27		20.00	41.64	
	R2	1.00	40.00	4.29	11.82		10.00	14.58	
Oval-shape straight thin	t	1.00	2.00	2.00	1.60		1.00	1.00	
	w	1.00	10.00	4.00	1.00		2.00	1.00	
	R1	1.00	15.00	12.00	15.00		15.00	14.53	
	R2	1.00	15.00	8.00	15.00		10.00	3.06	
Oval-shape tilted	t	1.00	10.00	1.00	1.00		2.00	1.00	
	R	10.00	20.00	10.00	15.87		15.00	16.06	
	X	1.00	2.50	1.00	2.50		2.00	2.50	
	Y	1.00	5.00	2.00	5.00		3.00	4.41	
Oval-shape spring	w	1.00	10.00	1.00	1.00		2.00	1.00	
	R	10.00	20.00	18.00	19.12		20.00	17.83	
	Y1	1.00	20.00	8.00	7.72		12.00	3.46	
	D	1.00	20.00	4.00	3.63		6.00	1.00	

Tab. 3-7: Results for best solutions for all optimized models

Model	Starting Point	Max. von Mises stress [MPa]	Reaction force [N]	Reaction torque [mNm]	Volume [mm^3]
Z-shape thick	I, Run 1	19.90	4.71	154.65	3014.95
	II, Run 1	19.99	4.02	111.90	2299.23
	I, Run 2	19.91	4.73	155.08	3012.66
	II, Run 2	20.00	4.15	115.65	2291.96
	Relative difference	0.45 %	-12.26 %	-25.43 %	-23.92 %
Z-shape thin	I	20.00	0.31	6.26	265.66
	II	20.00	0.24	4.54	158.69
	Relative difference	0.00 %	-22.58 %	-27.48 %	-40.27 %
Oval-shape straight thick	I	19.61	3.14	76.48	4345.81
	II	18.33	3.88	105.18	3256.02
	Relative difference	-6.53 %	23.57 %	37.53 %	-25.08 %
Oval-shape straight thin	I	25.01	0.25	6.94	289.16
	II	20.00	0.08	1.18	126.50
	Relative difference	-20.03	-68.00	-83.00	-56.25
Oval-shape tilted	I	33.32	0.28	7.37	146.30
	II	33.70	0.29	7.47	147.02
	Relative difference	1.14 %	3.57 %	1.36 %	0.49 %
Oval-shape spring	I	20.64	0.37	10.64	167.43
	II	18.60	0.44	12.32	159.17
	Relative difference	-9.88	18.92 %	15.79 %	-4.93 %

Fig. 3-28 shows the results for each iteration regarding maximum von Mises stress and reaction force for the optimization run 1 of the first starting point. One can see that the algorithm is converging for both the stress and the reaction force. In the beginning, the algorithm changed the parameters largely to get to know their influence on the results. Then, these parameters are only changed slightly and therefore a converging look appears in the figure. However, one can see that the best solution is not the last one. This means, that the algorithm still slightly changed the parameters in the end, but did not get a better result. All the *Z-shape* optimizations stopped after 800 to 1300 iterations due to the time limit of five days. This might be an explanation for the differences between the optimization results.

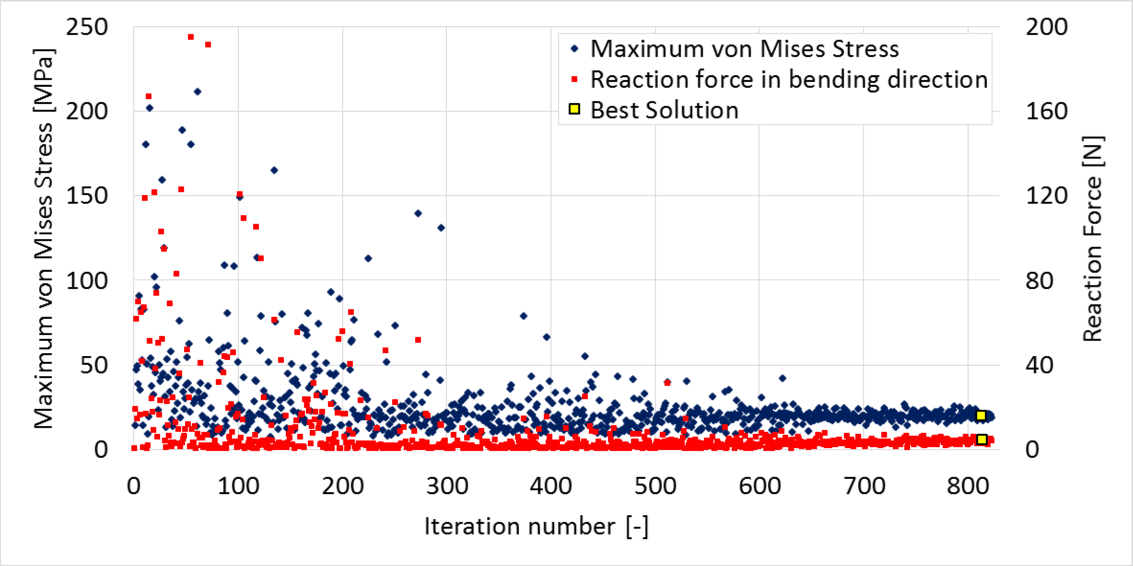

Fig. 3-28: Stress and reaction force for each iteration of the thick *Z-shape* model optimization run 1, starting point I

The resulting optimized model of the *Z-shape* design is very large and heavy compared to the already developed torsion hinges. Even if the large weight of one specimen could be compensated with its large reaction force needing less hinges for the same membrane size, the packaging would not be good enough as the hinges are very thick compared to the torsion hinges. Therefore, the upper bound of the parameter t has been changed to 2.00 mm and the total model length, L_{model}, and width, W_{model}, have been set to $L_{model} = w + 2 * L1 + 2 * R < 60$ and $W_{model} = 2 * w + L2 + 2 * R < 30mm$, respectively. With these adaptations the maximum design space is comparable with the other models and therefore also the reaction forces are expected to be in the same order of magnitude. With the adapted bounds, the thinner models have been optimized again from two starting points with the results shown in Tab. 3-6.

Again, the resulting parameter values show differences even though the optimization runs calculated all of the demanded 3000 iterations for both starting points. Also, the resulting reaction forces and torques differ largely (see Tab. 3-7) which means that the optimization algorithm was not able to overcome local minima in the given amount of time even though it seems that it converged four times and restarted itself after having converged. This can be seen in Fig. 3-29 where the peaks in stress and reaction force indicate a new starting point as the algorithm tries to find out the sensitivity of the parameters at a new point. The best solution has been found after the fourth restart. One can see, that the best solution appeared quite early in this restart and the algorithm did not find a better solution afterwards and therefore starting a next restart which has been interrupted as the prescribed maximum number of iterations has been reached.

Comparing the volumes with the models below, the volume of result II would match better. However, at the moment, the optimization has been set up regarding reaction force and therefore the results of starting point I have been chosen to be better as it shows much larger reaction force and reaction torque.

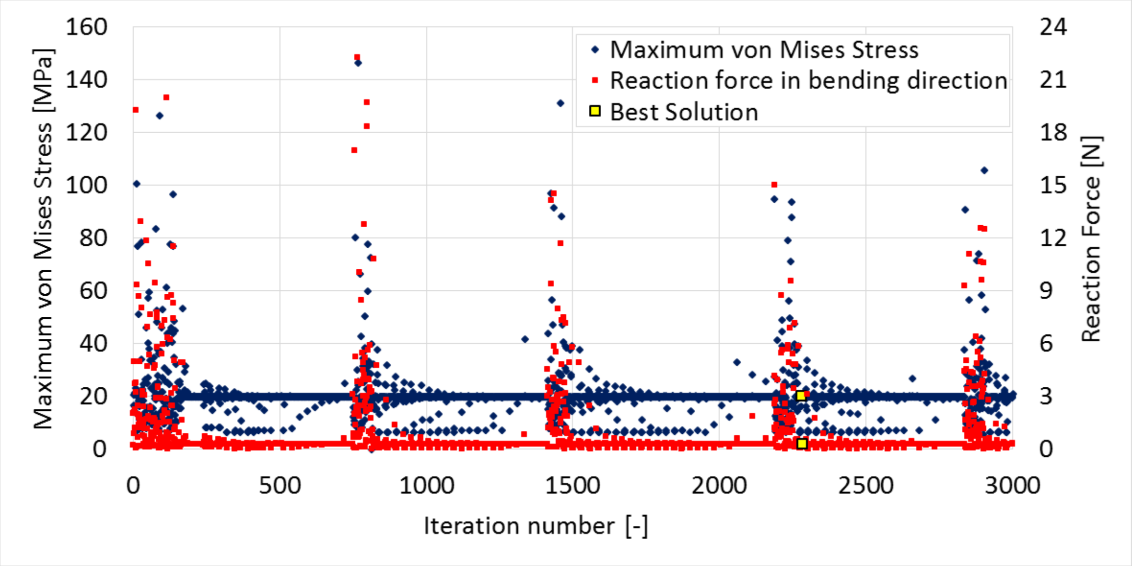

Fig. 3-29: Stress and reaction force for each iteration of the thin *Z-shape* model optimization run I

Similar findings have been made with the oval-shape designs. The diagrams showing the maximum stress and reaction force all behave similarly to Fig. 3-28 and Fig. 3-29 depending on the number of iterations.

The total specimen length for the *oval-shape straight* model has been defined as $L_{model} = 2 * (L + R2 + D2)$ which was constraint with the maximum allowable length $L_{max} = 60\ mm$. According to the parameter study of this model, the parameters *D1* and *D2* have very little influence on the result. Therefore, they have been fixed at $D1 = 2\ mm$ and $D2 = 5\ mm$. For geometrical reasons two additional boundary conditions have been introduced to this model as shown in equation (4.6). These conditions are needed in order to get a reasonable and functional geometry.

$$\begin{aligned} g_3 &= \frac{R_1}{3} - R_2 \leq 0 \\ g_4 &= R_2 - R_1 \leq 0 \end{aligned} \tag{3.8}$$

Here, the differences of the solutions of the two different starting points is much larger than for the previous model. This is due to the fact, that the *oval-shape straight* FE model has a more complicated geometry and has more difficulties in converging or at least takes more time until each model is converged. Therefore, only a small number of 431 and 319 iterations could be calculated. Hence, the algorithm could not converge in such a small number of iterations and large differences in between the two starting points have been expected.

Comparing the resulting maximum von Mises stress, reaction force and specimen volume (Tab. 3-7) it is shown that the second starting point provided much better results for all stress, reaction force and volume.

Fig. 3-30 shows the results for each iteration regarding the maximum von Mises stress and reaction force for the better second starting point. One can see that the algorithm did not fully converge after the small number of iterations and still changed the geometrical parameters, which is shown with the large scatter of the data points. To converge this model, more time would have been required.

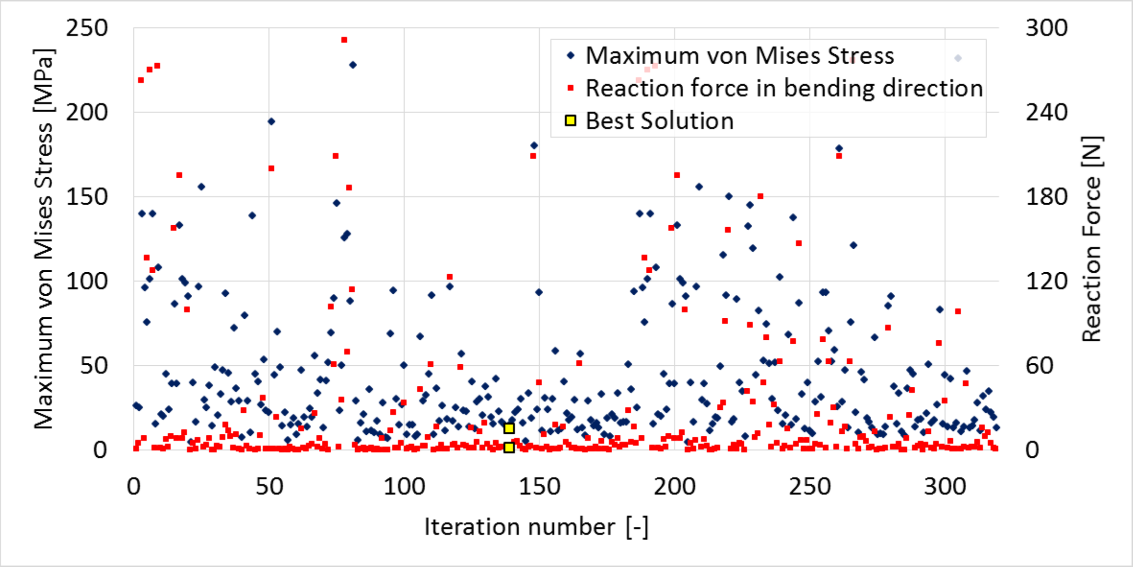

Fig. 3-30: Stress and reaction force for each iteration for the *oval-shape straight* model optimization run I

Again, as for the *Z-shape* model, the resulting *oval-shape straight* models are too large and thick to achieve a good packaging for the envisioned CubeSat demonstrator. Therefore, the upper bounds have been adapted in the same manner as for the *Z-shape* model and optimization runs have been done again with two starting points. The new upper bound for *t* has been set to 2.00 mm and the upper bounds for *R1* and *R2* have been set to 15.00 mm. This gave the resulting parameter values shown in Tab. 3-6.

The differences in runs for the parameter values as well as the reaction force, reaction torque and volume are enormous (see Tab. 3-7). However, this time it is not due to local minima but because the first optimization run only calculated 700 simulations whereas the second optimization run calculated 2600 simulations. In this short time, the first optimization did not find a feasible solution as the maximum von Mises stress is above the allowed 20 MPa. Therefore, it also has a much larger reaction force. The second optimization reached a feasible solution, however, the reaction forces and torques are very small. The solution of the first optimization will be taken as the better solution as the stress is still smaller than the stress which appeared in some of the FE simulations of the tested torsion hinges in section 3.2 and 6.1 where they showed a maximum von Mises stress of more than 30 MPa without getting a permanent deformation during the experiments. The convergence diagrams have a similar shape as shown in Fig. 3-30 for the unconverged first starting point and in Fig. 3-29 for the second starting point, where it is clear that the values are different. However, not all convergence diagrams are shown for simplicity.

Regarding the *oval-shape tilted* model, the parameters *w* and *D* have been fixed to w$= 1\,mm$ and $D = 5\,mm$. The total specimen length has been defined as $L_{model} = 2 * (L + R)$ which was constraint with the maximum allowable length $L_{max} = 60\,mm$. Some geometrical boundary conditions have been needed for this model as well. However, as they corresponded to the fixed parameter D, these conditions have been introduced directly into the lower and upper bounds definition, which simplified the problem.

The two starting points for the *oval-shape tilted* model almost converged towards the same solution except for the parameter Y that shows a larger relative difference (Tab. 3-6). However, regarding the maximum von Mises stress and the reaction force and reaction torque, the two best solutions are almost the same (Tab. 3-7). The second starting point provided slightly better results regarding reaction torque, while the volume is almost the same.

It is important to see that both optimization runs could not satisfy the boundary condition that the maximum von Mises stress should be lower than the threshold of 20 MPa. In addition, except for R, the parameter values went towards their upper and lower bounds. This indicates that the fixed maximum specimen length might be too small for the *oval-shape tilted* model and the bounding box needs to be adapted to lower the stresses in the model. However, the experiments showed that the given stress threshold can be surpassed without getting a permanent deformation during the experiments (see section 5.3). Hence, the result of the second starting point will still be included in the further studies.

The last considered model is the *oval-shape spring* model. For this model the total specimen length has been defined as $L_{model} = 2 * (L + R)$ which was constraint like all models above. Also for this model, additional geometrical boundary conditions have been needed

$$\begin{aligned} g_3 &= D - Y_1 \leq 0 \\ g_4 &= Y_1 + w - R \leq 0 \end{aligned} \tag{3.9}$$

The large differences, especially in *Y1* and *D* (Tab. 3-6) can be explained with the fact that the first optimization only reached 562 iterations while the second optimization run reached 1327 iterations. The second optimization run found the best solution after getting out of the first local minimum, which never happened, with the first optimization run. Therefore, it is clear that the two results cannot be the same. In addition, the first optimization has not yet been able to find a feasible solution regarding the stress constraint, while the second optimization run clearly achieved this. Hence, comparing the resulting maximum von Mises stress, reaction force and specimen volume in Tab. 3-7 one can see that the second starting point provided much better results.

3.3.4.1 Summary of optimization results

Tab. 3-8 shows an overview of the parameter values and the maximum von Mises stress, reaction force, reaction torque and total model mass of the best solution of each model. One can see that the models can be split into two categories, very stiff, large models and compliant, small models. The thick *Z-shape* and *oval-shape straight* models are able to get a much higher reaction torque than the rest of the models. However, they are also much larger and therefore heavier. Both differences are in the order of one magnitude. This gives ratios between the reaction torque and the total model mass between 0.022 and 0.070. Hence, all ratios are in the same order of magnitude. This shows that the reaction torque behaves proportionally to the specimen volume. The large designs are not favorable for a good packing design and therefore the *Z-shape* and the *oval-shape straight* models have been optimized in a second optimization loop with changed geometrical bounds. As the goal of every space application is to be as lightweight as possible, the lighter and smaller models are preferred. However, it is not yet clear if their reaction force will be enough to be able to open a folded membrane. To ensure this, the exact application and a generative first version of an assembled hinge system needs to be defined. This is envisioned for subsequent research to this work. A draft concept is developed and described in section 7.

While only studying the small and more compliant designs, the *oval-shape tilted* and *spring* models show a ratio, which is much higher, compared to the *Z-shape* and the *oval-shape straight* models (more than the double for the *tilted* model and more than the triple for the spring model). Therefore, the *oval-*

shape tilted and the *oval-shape spring* models should be favored while choosing among the here-investigated designs and their solutions are marked green in Tab. 3-8.

Tab. 3-8: Summary of optimization results

Model	**Changed Parameters [mm]**				**Max. von Mises Stress [MPa]**	**Reaction force [N]**	**Reaction torque [mNm]**	**Mass [mg]**	**Reaction torque / total model mass [Nm/g]**
Z-shape thick	**t**	**w**	**L2**	**R**					
	9.56	1.87	6.85	21.88	19.91	4.73	155.08	3313.93	0.047
Z-shape thin	**t**	**w**	**L2**	**R**					
	2.00	1.02	7.85	9.80	20.00	0.31	6.26	292.23	0.021
Oval-shape straight thick	**t**	**w**	**R1**	**R2**					
	8.97	2.32	41.64	14.58	18.33	3.88	105.18	3581.62	0.029
Oval-shape straight thin	**t**	**w**	**R1**	**R2**					
	1.60	1.00	15.00	15.00	25.01	0.25	6.94	318.08	0.022
Oval-shape tilted	**t**	**R**	**X**	**Y**					
	1.00	16.06	2.50	4.41	33.70	0.29	7.47	161.72	0.046
Oval-shape spring	**w**	**R**	**Y1**	**Y2**					
	1.00	17.83	3.46	1.00	18.60	0.44	12.32	175.09	0.070

4 Design and evaluation of a new test stand

4.1 Concept determination

This section describes possible methods and solutions for developing a well-suited testing method for the investigated elastic hinges. Ideas from state-of-the-art testing mechanisms and other inspirations for possible testing methods are collected, explained and subsequently listed in a morphological box. From this box, individual elements can be combined to generate new concepts for a test mechanism. These concepts are explained and evaluated.

First of all a list of requirements needs to be done in order to know what to look for in a test design. The test needs to present a realistic load introduction as would appear during folding and deployment of the structure. Simple measurements of the applied forces or the reaction forces or torques during the test as well as the corresponding folding angle of the specimens need to done. External imprecisions/distortions should be avoided such that a high repeatability can be achieved. Regarding manufacturing and cost, the test should be of low complexity to avoid high expenses and to keep its reliability. A very important factor, especially when testing a large number of specimens, is that efficient testing needs to be possible to test a high number of parts in a short time. Last but not least, a high precision of the test is required to avoid erroneous values into the finite element simulation after comparing the results. The test stand needs to be designed in a way that small structures/specimens can be tested. The specimens will have a length in the range of 30 to 50 mm and a cross section of about 1 to 4 mm^2 where clamping of the specimens should take place. The small size and the material properties of the specimens predict only small forces appearing during the test. Therefore, already small errors in the designed test might have a big impact on the results.

4.1.1 Partial Solutions

The morphological box is divided into five different categories, which are explained in this section. The categories are the load introduction, how the deformation is applied, the measurement of force or torque, the measurement of the bending angle and the test format or device size.

4.1.1.1 Load Introduction

The movement for the elastic hinges is defined from a starting, non-stressed, planar state to a completely folded state. This deformation can be achieved by different load introductions and boundary conditions. The most straightforward load introduction systems are explained in the following.

Point Load Beam Bending

Point load beam bending is a standard beam bending except that the hinge in the middle of the beam is the most compliant part leading to its deformation. If the load follows the end of the deflecting rod, the hinge will fold and the two rods will touch at the end of the deformation.

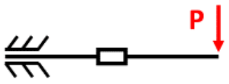

Fig. 4-1: Point Load Beam Bending

Distributed Load Beam Bending

This is the same as the point load beam bending except that a distributed load is applied instead of a point load. This shows a more realistic load introduction as point loads do not exist in reality because every load introduction system has at least a small area and is not a single point.

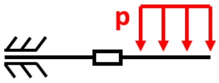

Fig. 4-2: Distributed Load Beam Bending

Central Beam Torsion

During central beam torsion, a torque is applied in the center of the beam, which is the center of the elastic hinge. The torque is increased until the two beam-ends touch and the specimen is completely folded.

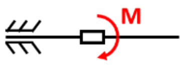

Fig. 4-3: Central Beam Torsion

Oblique Bending

Oblique bending is similar to point load bending. The difference is that the load is not introduced perpendicularly to the straight beam but with a different angle leading to a slightly different deformation. Nevertheless, with oblique bending the specimens can be fully folded if the load follows the deflecting beam.

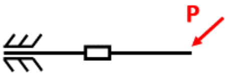

Fig. 4-4: Oblique Bending

Three-Point Bending

In three-point bending, a load perpendicular to the beam is applied in its center, which is also the center of the elastic hinge. The beam is kept in place by fixations at both its ends, which are fixed vertically, but are able to move horizontally.

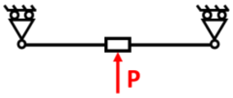

Fig. 4-5: Three-Point Bending

Four-Point Bending

Four-point bending is almost the same as three-point bending except that two load introduction points are used. These load introductions are symmetrically distributed and are positioned near the center of the beam.

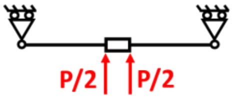

Fig. 4-6: Four-Point Bending

Beam Bending from Two Sides

In this load introduction system, the beam is held in its center and therefore at the elastic hinge. Then the load is introduced perpendicularly to the beam at both its ends and in the same direction. When the loads follow their respective beam end, this also leads to a complete folding.

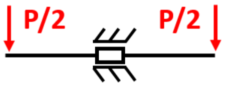

Fig. 4-7: Beam Bending from 2 Sides

Offset Buckling

Introducing the load parallel and in the cross-sectional center of the beam will lead to a buckling. By displacing the parallel load from the cross-sectional center, a torque is introduced leading to a bending. If the loads follow their respective beam-ends this will again lead to a complete folding.

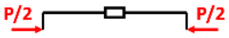

Fig. 4-8: Offset Buckling

4.1.1.2 Application of deformation

This subsection defines the possibilities on how to apply a flexural or bending deformation onto a flexure hinge with one stiff rod on each side of the hinge.

Standard Testing Machine

Most of the time bending tests are done with standard static universal test machines manufactured for example by ZwickRoell or Instron. A 3-point bending test for example can easily be done with such a machine. This test is even defined in an ASTM Standard [47]. Standard test machines are expensive but usually available at laboratories, which work on material testing.

Motor Device

It is clear that a standard testing machine is also brought to motion by a motor. Nevertheless, the motor should be taken as a separate possibility for a deformation application because it can be used in several different configurations. By using a stepper motor for example, one always knows the position of the motor without the need of extensive external measurement devices and installations. This might simplify the design of a new testing device.

Tensioned spring

A spring in tension can actuate a mechanism by using the inherently stored energy. The tensioning of the spring does not always need to be done by a machine but could also be done by hand before the start of the test. The stored energy could then actuate a possible testing device.

String

Instead of a load cell in a standard test machine a string could be used to pull a specimen and inducing flexure. The string could for example be fixed on the specimen and then be furled onto an axle by a turning motor. The furling would shorten the remaining string length and induce a pulling force. It is important to note that a string might expand elastically depending on its cross-section and material properties. The elastic deformation of the string should be taken into account during the test or it should be ensured that it is much less than the specimen's deformation and therefore could be neglected.

4.1.1.3 Force / Torque measurement

During the test one wants to measure the reaction force or torque of the specimen during its flexure. This can be done with different mechanisms and is dependent on the used testing device and configuration.

Load Cell of Testing Machine

Standard universal testing machines already have a load cell installed that can measure the reaction force. These load cells can normally be calibrated and connected to the test program, which comes together with the universal testing machine. There also exist load cells with different resolutions.

Force Sensor

Force sensors or force sensitive resistors vary their resistance depending on how much pressure is applied to the sensing area, which is often circular and can be relatively small. The harder the force, the lower the resistance in the sensor will be. Standard force sensitive resistors can measure applied forces in between 100 g to 10 kg. These sensors are simple to use and relatively cheap compared to more sophisticated load cells.

Fig. 4-9: Example of force sensitive resistor [66]

Fig. 4-10: Example of a torque sensor [67]

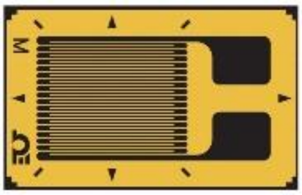

Fig. 4-11: Example of a strain gauge [68]

Torque Sensor

To measure a quasi-static or dynamic torque around an axis, a torque sensor is needed. Torque sensors are quite sophisticated, like load cells of a testing machine, and therefore also expensive. A torque sensor consists of two steel plates where several shear sensitive quartz plates are built in between. The crystal axes of the individual quartz plates are tangential to the circumferential direction and therefore produce an electric charge that is proportional to the torque applied. Such torque sensors also come with a test program to read the produced data.

Strain Gauge for Torque on Shaft

Strain gauges are sensors whose resistance vary with applied force. The tension is converted into a change in electrical resistance, which can be measured. Strain gauges are among the most important sensors of the electric measurement technique to measure mechanical quantities. Normally, strain gauges are used to measure strain in a single direction. However, one can still get the applied torque by using material mechanics theory and placing the strain gauge appropriately. Then, taking advantage of the proportionality between the measured strain and the applied torque, the torque can be specified. Strain gauges are a relatively cheap way to measure deformations and with some background information it is possible to measure torques.

4.1.1.4 Angle Measurement

In addition to the force, the corresponding folding angle is also important to know. The folding angle can be measured by either optical measurement or an inherent measurement depending on the test configuration.

Digital Image Correlation

Digital Image Correlation (DIC) is a non-contact optical technique for displacement and strain. At least two calibrated cameras take pictures of the deforming specimen. The only thing that is needed on the specimen is a unique and randomly generated pixel block. The pixels are then tracked by the system. As the cameras are both calibrated and their position is known to the processing program, the surface position and displacement can be measured and full field 2D and 3D deformation vector fields and strain maps can be built up. This method is much more accurate than manual measurement methods but needs an expensive imaging system and the corresponding software.

Motor Position

An inherent angle measuring system is the angular position of the motor. If the motor is directly used to induce a bending, its angular position can tell about the flexural angle. By using a stepper motor the angular position can simply be tracked by knowing the number of steps and the passing angle per step, which is mostly 1.8° or 0.9° for special stepper motors. The step angle is always given on stepper motors.

Protractor

A protractor is a simple measurement tool and works like a triangle ruler from primary school. The angle can be measured by placing the midpoint of the protractor onto the vertex of the angle. Then one side of the angle needs to be lined up with the zero line of the protractor and the angular degrees can be read where the other side of the angle crosses the number scale.

Laser Distance Sensors

As their name says, laser sensors need a laser as a light source. The ray of these sensors is very focused and can easily be leveled and positioned because of the clearly visible light point. To measure angles, this sensor type recognizes the position of an object. To do so it uses a triangulation method or recognizes the light travel time.

The triangulation method works as follows. By changing the distance between the sensor and the object also the position of the focused light point on the light receiving element (CMOS) is changed. The position of the light point on the CMOS is then used to determine the position of the object. The laser needs to be leveled onto the object. The reflected light of the object is bundled by a receptive lens and is mapped onto the light receiving element. If the distance changes, the bundled light will be reflected at a different angle and the position of the light point on the light receiving element changes. [69]

The method of the recognition of the light travel time works differently. The distance is calculated by measuring the time that passes between sending and receiving a light impulse. It is unaffected by material or surface properties. Therefore, the distance Y is calculated as follows [69]:

$$Y = \frac{c * t}{2} \tag{4.1}$$

Where *c* is the speed of light and *t* is the time between sending and receiving the light signal.

These sensors are very precise and a corresponding software can read the results.

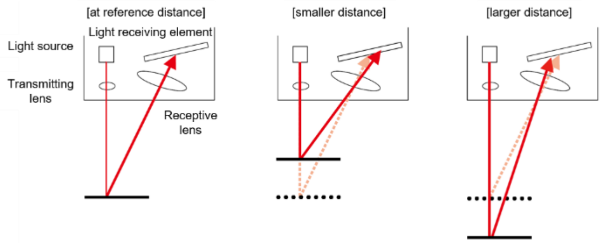

Fig. 4-12: Schematics of triangulation method (Adapted from [69])

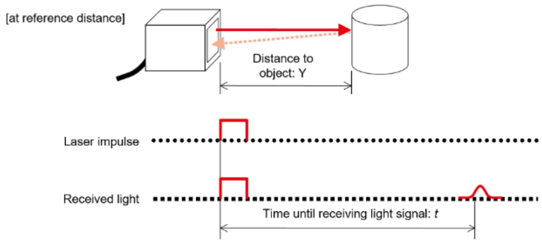

Fig. 4-13: Schematics of light travel time method (Adapted from [69])

4.1.1.5 Test Format / Device Size

Standard Testing Machine

As already described above, universal testing machines are common in material research laboratories and are often used for standardized tests. Regarding test format or the size of a device, a standard testing machine is normally relatively large and heavy. Therefore, it is not easily transportable and the tests always need to be done in the specific laboratory where the testing machine is available. In addition, normally a laboratory does not have several testing machines but only one and a reservation is needed to be able to use the machines, which requires proactive organization.

Tabletop Device

A tabletop device would overcome the drawback of the limited availability of the standard testing machine. By having a compact and simple tabletop device tests can be done without organizing machines far in advance. The drawback of such a device is the uncertainty of its precision because it is normally developed and built in-house without the amount of resources a testing company can provide.

4.1.2 Morphological Box

Dividing the set of partial solutions from section 4.1.1 into columns and splitting their corresponding categories into rows, a morphological box can be obtained (Fig. 4-14). A morphological box can help finding new concepts by combining different principles.

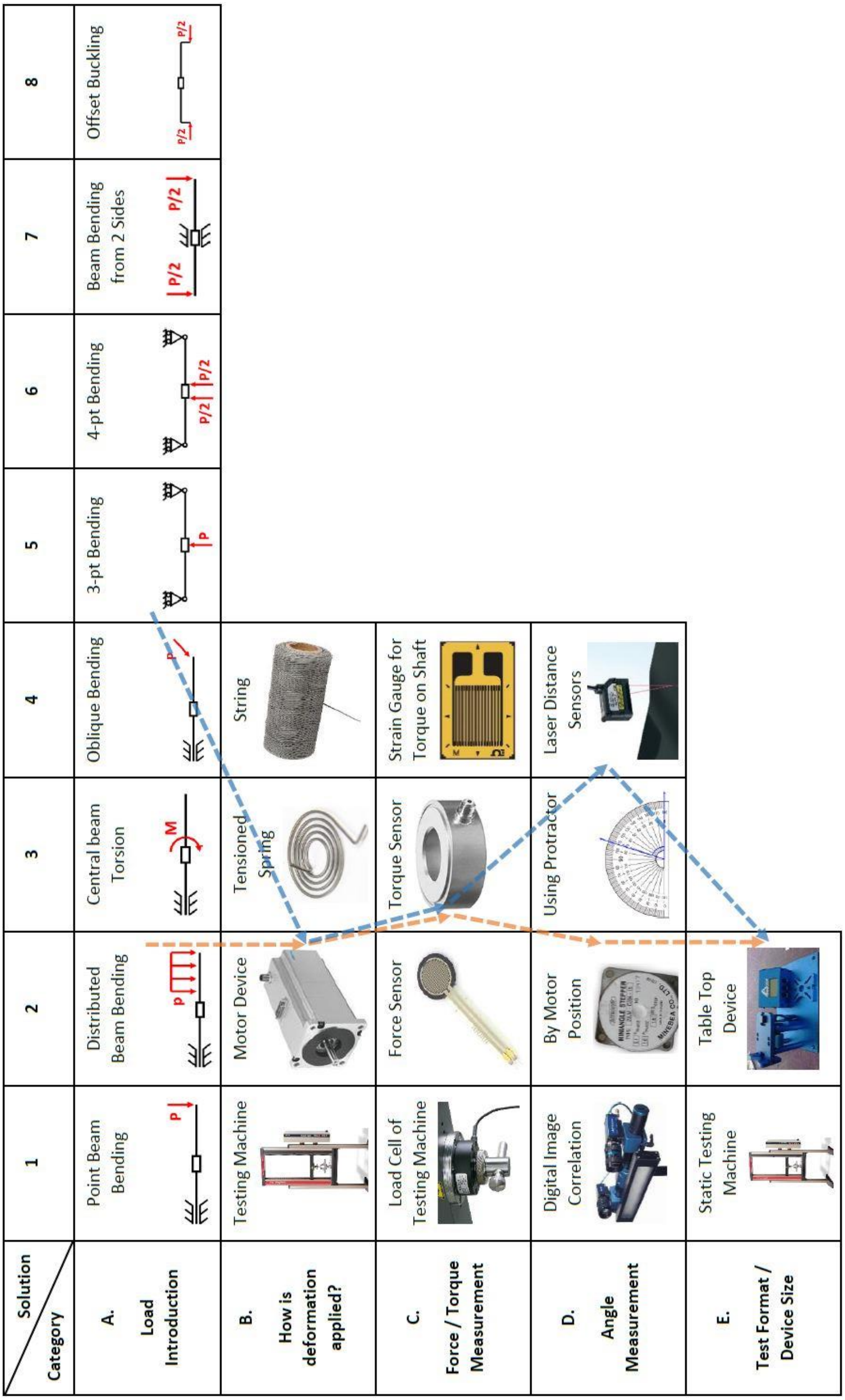

Category / Solution	1	2	3	4	5	6	7	8
A. Load Introduction	Point Beam Bending	Distributed Beam Bending	Central beam Torsion	Oblique Bending	3-pt Bending	4-pt Bending	Beam Bending from 2 Sides	Offset Buckling
B. How is deformation applied?	Testing Machine	Motor Device	Tensioned Spring	String				
C. Force / Torque Measurement	Load Cell of Testing Machine	Force Sensor	Torque Sensor	Strain Gauge for Torque on Shaft				
D. Angle Measurement	Digital Image Correlation	By Motor Position	Using Protractor	Laser Distance Sensors				
E. Test Format / Device Size	Static Testing Machine	Table Top Device						

Fig. 4-14: Morphological box of partial solutions for test stand. Picture source Section 4.1.1 and [70–79]
Found partial solutions marked with orange (section 4.1.3.1) & blue (section 4.1.3.2) arrows

4.1.3 Combination of Concepts

In this section, partial solutions from the morphological box are combined to fit together and to create new testing concepts in addition to the testing mechanisms found in literature and described in section 2.3. It is possible that several solutions of the same category need to be chosen in order to create an appropriate testing device.

4.1.3.1 Motor-driven bending

The concept *motor-driven bending* follows from the chosen partial solution possibilities of Tab. 4-1 and is shown with the orange arrows in Fig. 4-14.

Tab. 4-1: Chosen partial solutions for motor-driven bending

Category	**Solution**
Load Introduction	2. Distributed Beam Bending
Application of Deformation	2. Motor Device
Force / Torque Measurement	3. Torque Sensor
Angle Measurement	2. By Motor Position
Test Format / Device Size	2. Tabletop Device

The specimen is clamped on one side as in normal beam bending. A load introduction block is connected to a motor. As the motor center is positioned in the center of the specimen, while turning the motor also the load block turns and the turning block acts as a rotating load introduction. This bends the specimen. When the motor revolved half of a turn, the specimen is folded completely and the motor shall stop rotating. A torque sensor placed between the motor's rotating axis and the fixation for the load block can measure the reaction torque of the specimen onto the load block. If the motor is a stepper motor, the number of steps the motor has done times the step angle of the motor results in the elapsed angle. For normal stepper motors, the step angle is 1.8°. If a more precise resolution is needed, half steps can be done or the angle can be measured by a different external device as for example a laser distance sensor as an alternative.

Advantages and Disadvantages:

- + Considered load introduction results in a realistic bending
- + Simple measurement of torque with torque sensor
- + Different possibilities for angle measurement
- + Only few parts needed which results in a simple, low cost but still reliable testing device
- + With appropriate fixtures, the test achieves a good repeatability and efficient testing
- – Precision cannot be evaluated as it is an in-house built test
- – Influence of external imprecisions or gravity is unknown

Overall, this test concept would result in a relatively simple tabletop device with some drawbacks regarding precision requirements because it is a self-built test where no comparable test results could be found in literature.

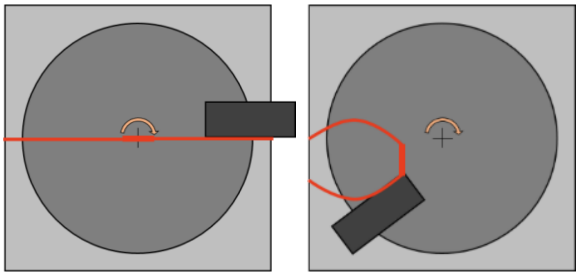

Fig. 4-15: Schematics of motor-driven bending

4.1.3.2 Motor-driven pulling

Motor-driven pulling is a concept associating the chosen partial solution possibilities as shown with the blue arrows in Fig. 4-14. Tab. 4-2 summarizes the chosen partial solutions.

Tab. 4-2: Chosen partial solutions for motor-driven pulling

Category	**Solution**
Load Introduction	5. 3-pt Bending
Application of Deformation	2. Motor Device & 4. String
Force / Torque Measurement	3. Torque Sensor
Angle Measurement	4. Laser Distance Sensor
Test Format / Device Size	2. Tabletop Device

In this test device, the specimen is pinned to a slider on each end. The sliders can only move in the direction parallel to the undeformed specimen. A string is placed around the specimen in its center. The string is then connected to the shaft of a motor by keeping perpendicularity to the undeformed specimen. As the motor is turning its shaft, the string is coiled up and its free length is shortened. The shortening string pulls the specimen and folds it as the sliders come together. Therefore, the test works similar to a three-point bending with the difference that the center of the specimen is pulled by the string instead of pushed by the load introduction block. The reaction torque can be measured with a torque sensor on the motor as for the *motor-driven bending*. The corresponding angle is measured by laser distance sensors as explained in section 4.1.1.4.

Advantages and Disadvantages:

- + Load introduction results in a realistic bending even though in the considered application the bending will be done at the ends of the specimens and not induced in their center
- + Simple measurement of torque with torque sensor
- + With appropriate fixtures, the test achieves a good repeatability and efficient testing
- – Precision cannot be evaluated as this is an in-house built test
- – Only few parts needed but sliders might induce imprecisions due to frictional influence
- – Thin string might expand as well during test, leading to errors
- – Influence of other external imprecisions or gravity is unknown

This test concept would result in a relatively simple tabletop device. However, several factors might influence the test results leading to an unknown precision.

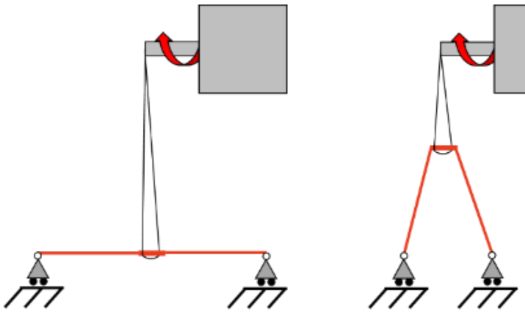

Fig. 4-16: Schematics of motor-driven pulling

4.1.4 Evaluation

In this section, the different test mechanisms already existing and discussed in section 2.3 as well as the newly created concepts are compared and rated in an evaluation matrix. To do so, evaluation criteria have been defined as shown in Tab. 4-3.

As not all criteria are equally important, every possible pair combination of these criteria has been compared and it has been decided which of the pair is more important. This brought up a ranking and with it weighting factors for each criterion. The sum of all the weighting factors equals to one.

The individual criteria and their corresponding weighting factors are shown in Tab. 4-3.

Tab. 4-3: Evaluation criteria and weighting factors

Evaluation Criterion	**Weighting Factor g_i**
Realistic Load Introduction	0.17
Measurement of Force/Torque	0.19
Measurement of Angle	0.17
Influence of external imprecisions	0.11
Repeatability	0.19
Complexity	0.03
Cost	0.00
Efficient Testing	0.06
Precision	0.08
Sum: $\sum g_i$	1.00

One can immediately see that the criteria “Cost” achieved a weighting factor of zero. This is due to the fact, that by knowing what test possibilities exist, it is clear that there will not be very large differences in cost. In addition, it is difficult to know their exact cost to be able to compare them. As the weighting factor is zero, this criterion could be removed because it does not have any influence on the results. Still it is kept to show that cost are important for the test mechanism but as the differences between the individual test mechanisms will be small, it does not influence the final decision.

All test mechanisms and concepts are evaluated by giving points to each evaluation criterion. The points are given from 0 (bad) to 10 (very good). By multiplying the points for each criterion with its corresponding weighting factor and summing up all the weighted points, the final evaluation of each mechanism is realized. Therefore, each mechanism can achieve between 0 and 10 points in total, with 10 being the best possible result. The resulting evaluation matrix is shown in Fig. 4-17.

Evaluation Matrix (Test Design)												
Average Rating of D. Mueller & M. Zander				**3-point & 4-point bending**			**Simple vertical test**			**Platen test**		
No. i	Evaluation Criterion	Weighting Factor g_i	Property Parameter	Property e_{i1}	Value v_{i1}	Weighted Value w_{i1}	Property e_{i2}	Value v_{i2}	Weighted Value w_{i2}	Property e_{i3}	Value v_{i3}	Weighted Value w_{i3}
1	**Realistic Load Introduction**	0.08	Load Introduction	Low	1.5	0.13	Low	1.5	0.13	Low	2	0.17
2	**Simple Measurement of Force/Torque**	0.19	Force/Moment	High	8	1.56	High	8.5	1.65	High	8.5	1.65
3	**Simple Measurement of Angle**	0.17	Angle	Medium	5.5	0.92	Medium	4.5	0.75	Medium	5.5	0.92
4	**Low Influence of external imprecisions**	0.14	External Imprecisions	High	8	1.11	Medium	4	0.56	Low	3	0.42
5	**High Repeatability**	0.22	Repeatability	High	9	2.00	Medium	5.5	1.22	Medium	5	1.11
6	**Low Complexity**	0.03	Complexity	High	8.5	0.24	High	7.5	0.21	High	8.5	0.24
7	**Low Cost**	0.00	Cost	High	8	0.00	High	8.5	0.00	High	9	0.00
8	**Efficient Testing**	0.06	Efficiency	High	8	0.44	Medium	7	0.39	Medium	6	0.33
9	**High Precision**	0.11	Precision	Medium	6	0.67	Medium	6	0.67	Medium	4	0.44
	Sum: $\sum g_i$	1			$\sum w_{i1}$	**7.06**		$\sum w_{i2}$	**5.57**		$\sum w_{i3}$	**5.28**

Evaluation Matrix (Test Design)												
Average Rating of D. Mueller & M. Zander				**Large def 4-pt bending LD-FPB**			**Column Bending Test (CBT)**			**Counterweight-Balanced CBT**		
No. i	Evaluation Criterion	Weighting Factor g_i	Property Parameter	Property e_{i4}	Value v_{i4}	Weighted Value w_{i4}	Property e_{i5}	Value v_{i5}	Weighted Value w_{i5}	Property e_{i6}	Value v_{i6}	Weighted Value w_{i6}
1	**Realistic Load Introduction**	0.08	Load Introduction	High	8	0.67	Medium	5.5	0.46	Medium	7	0.58
2	**Simple Measurement of Force/Torque**	0.19	Force/Moment	High	8.5	1.65	High	8.5	1.65	High	8.5	1.65
3	**Simple Measurement of Angle**	0.17	Angle	Medium	6	1.00	High	8	1.33	High	8	1.33
4	**Low Influence of external imprecisions**	0.14	External Imprecisions	Medium	5	0.69	Medium	5.5	0.76	High	7.5	1.04
5	**High Repeatability**	0.22	Repeatability	High	8.5	1.89	High	8.5	1.89	High	8.5	1.89
6	**Low Complexity**	0.03	Complexity	Low	2	0.06	High	7	0.19	Medium	6.5	0.18
7	**Low Cost**	0.00	Cost	Low	1.5	0.00	High	7.5	0.00	Medium	7	0.00
8	**Efficient Testing**	0.06	Efficiency	Medium	5	0.28	High	7.5	0.42	High	7.5	0.42
9	**High Precision**	0.11	Precision	High	8.5	0.94	High	8	0.89	High	8	0.89
	Sum: $\sum g_i$	1			$\sum w_{i4}$	**7.18**		$\sum w_{i5}$	**7.60**		$\sum w_{i6}$	**7.99**

Fig. 4-17: Evaluation Matrix for Test Design

Evaluation Matrix (Test Design)

Average Rating of D. Mueller & M. Zander

No. i	Evaluation Criterion	Weighting Factor g_i	Property Parameter	Column Buckling			Motor-driven bending			Motor-driven pulling		
				Property e_{i7}	Value v_{i7}	Weighted Value w_{i7}	Property e_{i8}	Value v_{i8}	Weighted Value w_{i8}	Property e_{i8}	Value v_{i8}	Weighted Value w_{i8}
1	**Realistic Load Introduction**	0.08	Load Introduction	Low	1	0.08	High	8.5	0.71	Medium	5.5	0.46
2	**Simple Measurement of Force/Torque**	0.19	Force/Moment	High	7.5	1.46	High	8.5	1.65	High	7	1.36
3	**Simple Measurement of Angle**	0.17	Angle	Medium	5	0.83	High	9.5	1.58	High	6.5	1.08
4	**Low Influence of external imprecisions**	0.14	External Imprecisions	Medium	3.5	0.49	Medium	6.5	0.90	Medium	4.5	0.63
5	**High Repeatability**	0.22	Repeatability	Low	3	0.67	High	8	1.78	High	7	1.56
6	**Low Complexity**	0.03	Complexity	High	8	0.22	Medium	6	0.17	Medium	5.5	0.15
7	**Low Cost**	0.00	Cost	High	8.5	0.00	Medium	6.5	0.00	Medium	6.5	0.00
8	**Efficient Testing**	0.06	Efficiency	Medium	5.5	0.31	High	8	0.44	Medium	6	0.33
9	**High Precision**	0.11	Precision	Low	2.5	0.28	Medium	6	0.67	Medium	5	0.56
	Sum: $\sum g_i$	1			$\sum w_{i7}$	**4.33**		$\sum w_{i8}$	**7.90**		$\sum w_{i8}$	**6.13**

Evaluation Matrix (Test Design)

Average Rating of D. Mueller & M. Zander

No. i	Evaluation Criterion	Weighting Factor g_i	Property Parameter	Axis of rotation test			Life Cycle Test Elastic Hinge			Tension Test of Elastic Hinge		
				Property e_{i8}	Value v_{i8}	Weighted Value w_{i8}	Property e_{i8}	Value v_{i8}	Weighted Value w_{i8}	Property e_{i8}	Value v_{i8}	Weighted Value w_{i8}
1	**Realistic Load Introduction**	0.08	Load Introduction	Low	3	0.25	Medium	5.5	0.46	Medium	6	0.50
2	**Simple Measurement of Force/Torque**	0.19	Force/Moment	High	7.5	1.46	Medium	6	1.17	Low	2	0.39
3	**Simple Measurement of Angle**	0.17	Angle	High	8	1.33	High	8	1.33	Low	2	0.33
4	**Low Influence of external imprecisions**	0.14	External Imprecisions	High	7	0.97	Medium	6	0.83	Medium	4.5	0.63
5	**High Repeatability**	0.22	Repeatability	High	7.5	1.67	High	8	1.78	High	7.5	1.67
6	**Low Complexity**	0.03	Complexity	Low	4	0.11	Medium	5	0.14	High	7.5	0.21
7	**Low Cost**	0.00	Cost	Medium	5.5	0.00	Medium	5.5	0.00	High	8	0.00
8	**Efficient Testing**	0.06	Efficiency	Medium	6	0.33	Medium	5.5	0.31	Medium	6	0.33
9	**High Precision**	0.11	Precision	Medium	5.5	0.61	Medium	4.5	0.50	Medium	5	0.56
	Sum: $\sum g_i$	1			$\sum w_{i8}$	**6.74**		$\sum w_{i8}$	**6.51**		$\sum w_{i8}$	**4.61**

Evaluation Matrix (Part 2)

The resulting weighted values and the ranking of each test method is shown in Tab. 4-4.

Tab. 4-4: Resulting weighted values and ranking of each test method

Test Name	**Weighted Value**	**Ranking**
3-point & 4-point Bending	6.28	7
Simple Vertical Test	5.64	9
Platen Test	5.53	10
Large def. 4-pt Bending LD-FPB	7.03	4
Column Bending Test (CBT)	7.47	2
Counterweight-Balanced CBT	7.78	1
Column Buckling	4.42	11
Motor-driven bending	7.47	2
Motor-driven pulling	6.75	5
Axis of Rotation Test	6.11	8
Life Cycle Test Elastic Hinge	6.36	6
Tension Test of Elastic Hinge	4.42	12

“Column Buckling” and “Tension Test of Elastic Hinges” have the lowest overall rating. For “Column Buckling” this is because the load introduction is not very realistic compared to the real application. In addition, the deformation is not well controlled as the buckling can take place in any direction. Therefore, the repeatability and the precision suffer. The main drawback of “Tension Test of Elastic Hinges” is that the reaction force and angle are not continuously measured but only at discrete points.

Further, the “Platen Test”, “Simple Vertical Test”, “Axis of Rotation Test”, “3-point & 4-point Bending Test” and “Life Cycle Test Elastic Hinges” are not very well suited for the considered application. This is mainly because of external imprecisions and shear distortion influences, as well as issues regarding large deformation known from literature. Also, the “Axis of Rotation Test” and “Life Cycle Test Elastic Hinges” do not yet have a realistic load introduction and significant configuration changes would be needed.

“Motor-driven pulling” and “Large deformation 4-pt bending” achieve good results. Their drawbacks are the relatively high complexity and especially for the “Motor-driven pulling” the uncertainties regarding external imprecisions because it would be a newly developed test method with no comparison possibilities.

The best-rated test mechanisms are the “Counterweight-Balanced Column Bending Test”, the “Column Bending Test” and the “Motor-driven bending”. The CWB-CBT has the best overall rating because it is an efficient, high precision and repeatable test. In addition, it is well described in literature and relatively simple to realize. Compared to the “Counterweight-Balanced” CBT, the normal CBT has an even simpler design and implementation by only lacking some gravitational issues. This keeps the normal CBT interesting as a good test mechanism. The “Motor-driven bending” however, scores with its realistic load introduction and simplicity, as well as the simple measurement of the bending angle through the position of the stepper motor.

The evaluation results are very close and the two second ranked mechanisms only got a lower rating by 4% compared to the maximum rating value achieved by the CWB CBT. Such a small difference is not significant as the evaluation results might slightly change if somebody else would have assessed the test mechanisms. Therefore, one cannot simply decide for the best-rated test mechanism for the hinge testing. Other factors, which have not been assessed in the evaluation matrix as for example the test format or device size might be considered as well. It is much simpler to have a tabletop device where tests can be done anytime and almost anywhere than to use a universal testing machine, which is only available at certain times and needs a reservation. However, designing a tabletop device results in a bigger effort as if one could use a universal testing machine and only design the fixture mechanisms.

Concluding the evaluation, developing a tabletop device following the idea of the motor-driven bending has been chosen as it achieved the second place in the overall ranking with a weighted value not far from the best-ranked test mechanism. The advantage of the all-time availability could hardly be surpassed.

4.2 Test stand design

After deciding for the motor-driven bending test, the test stand had to be fully developed and programmed starting from a basic sketch of first ideas. The basic idea of the test is shown in Fig. 4-18. A motor induces rotation into an arm. This arm pushes a punch onto the specimen. The specimen itself is clamped on the other side. The rotation of the arm and therefore the punch induces a bending of the specimen. The test will be stopped when the motor has fulfilled half a turn (180°) and the specimen is completely folded.

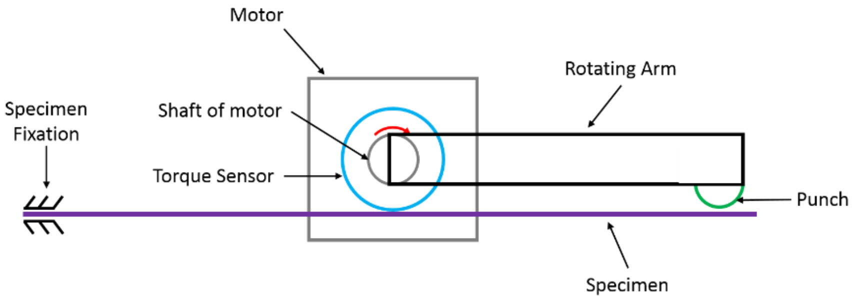

Fig. 4-18: Simplified idea of motor-driven bending test device

Finally, the designed test stand looks as shown in Fig. 4-19. It can be split into two separate assemblies, the rotating part and the clamping part. These two parts are then connected together by the large vertical support and supported by an additional smaller vertical support as shown in Fig. 4-19.

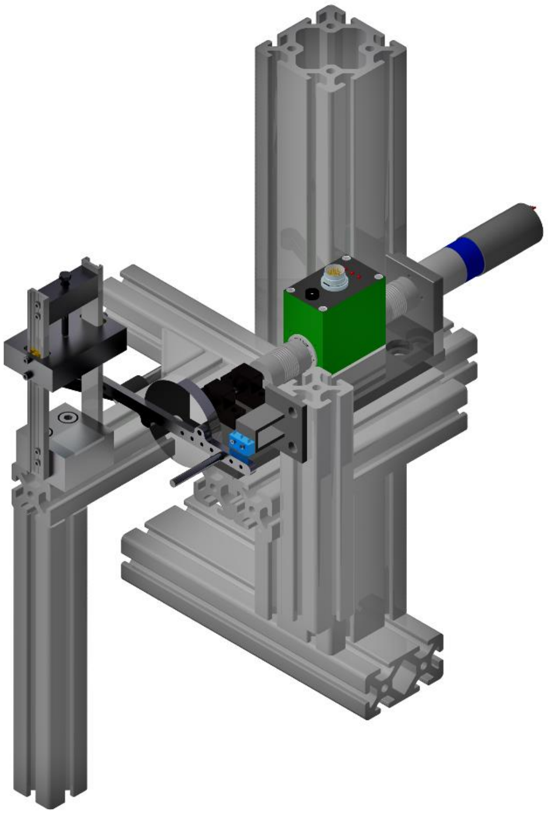

Fig. 4-19: Complete assembly of developed test stand

The rotating part of the test stand includes the motor and its baseplate, the torque sensor, the rotating arm and its punch (Fig. 4-20). To remove possible rotational causes of disturbances and non-parallelity for the torque sensor, the sensor has been placed in between the motor fixation and a block-bearing unit as shown in Fig. 4-21. The self-aligning coupling in between the motor and the torque sensor is responsible for removing minor manufacturing tolerances in order to have a straight shaft between the motor and the torque sensor. On the other side of the sensor, the torque-bearing shaft is placed in between two block-bearing units to fix the shaft such that it is perfectly horizontal in between the punch deforming the specimens and the torque sensor measuring the torque during deformation. All parts are built symmetrically and the weight of the punch is counterbalanced by bolts on the other side of the rotating arm in order to have a balanced system with as few external torques as possible.

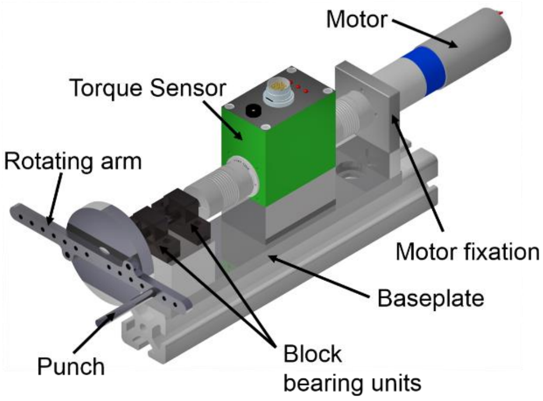

Fig. 4-20: Rotating part of test stand

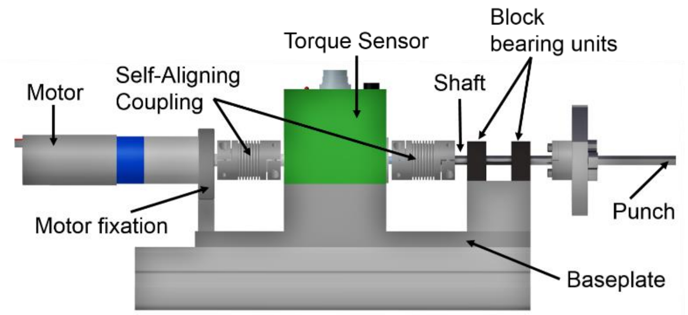

Fig. 4-21: Rotating part of test stand, side-view

To achieve good quality results a high precision torque sensor from Burster (type 8661) has been used in this test stand. This sensor is especially built for rotating applications and measures the torque without transmission contact. [80] The sensor consists of three elements, the measuring shaft, an electronics box and the sensor unit (Fig. 4-22). As a torque deforms the torsion shaft, the mounted strain gauges elastically and reversibly elongate. Proportionally to the elongation, their electrical resistance changes. Four strain gauges are arranged as a Wheatstone bridge circuit and are supplied with a DC voltage. Thus, the output voltage of the strain gauges changes proportionally to the applied and measured torque. The output voltage has been calibrated by the supplier. With the help of the calibration certificate, the output voltage can be converted to the applied torque. The used sensor has a range of ±1 Nm and has an output signal of ±10 V at its nominal value. The sensor range has been chosen based on the results from the preliminary tests where a maximum torque of 0.288 Nm has been obtained whereas the aim is to increase the specimen’s reaction force and therefore also their reaction torque. The sensor has a relative tolerance in sensitivity of 0.1% of its full scale [80]. As the sensor has been calibrated in 20% steps in the calibration certificate, the precision of the sensor is 0.2 mNm.

In addition, the torque sensor has an integrated angular displacement measurement system with an encoder disc with 1024 increments per revolution. Two measurement channels are placed with a phase shift of 90°. By using the four-edge decoding to read all the rising and falling edges one can increase the resolution and reach a precision of:

$$\alpha = \frac{360°}{1024\, Incr.} * \frac{1}{4} = 0.08789°\, Incr.^{-1} \tag{4.2}$$

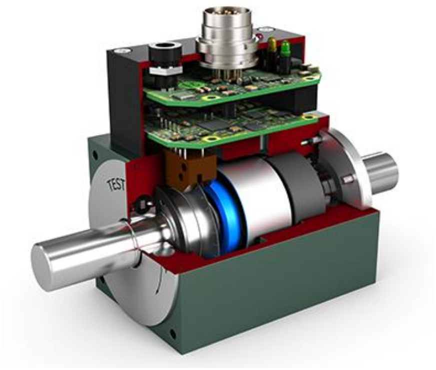

Fig. 4-22: Section through torque sensor [81]

The clamping part (Fig. 4-23) is built up by a lower fixture block positioned on an *item* aluminum profile. Two linear guide rails (igus drylin NK-02-17-01 [82]) are fixed to the lower fixture block on one side and to the top block on the other side. In between, the upper fixture block is bolted onto the sliders of the linear guide system. To clamp a specimen, it is placed onto the alignment block which itself is placed into the pocket of the lower fixture block. Then the fixation bolt is tightened until the upper fixture block is pressed onto the specimen fixing it in between the upper and the lower fixture blocks (Fig. 4-24).

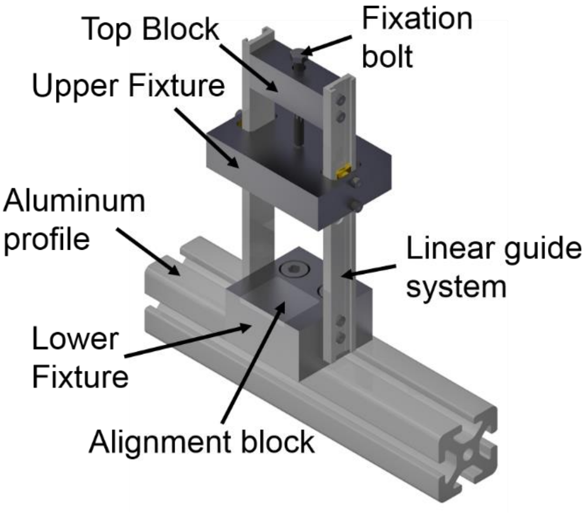

Fig. 4-23: Clamping part of test stand

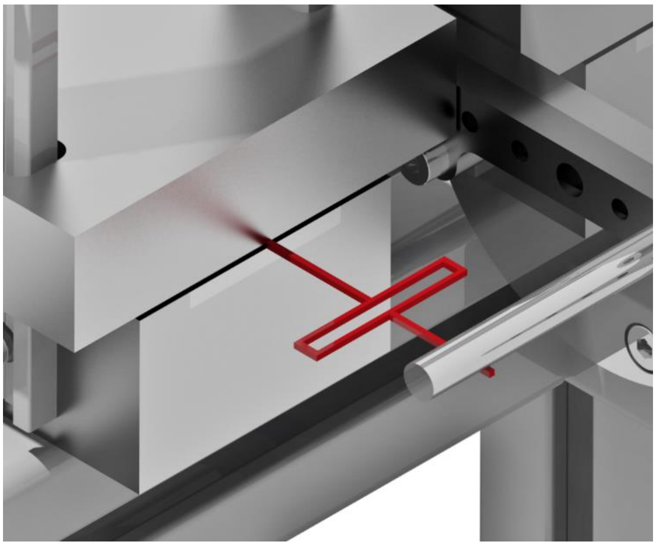

Fig. 4-24: Fixed specimen

To ensure that all the tested specimens are placed and fixed in the same manner, the alignment block is placed into the pocket of the alignment jig as on Fig. 4-25. Then, the specimen is aligned along the upper block of the alignment jig and fixed to the alignment block with a tape. Afterwards, the alignment block and the specimen are removed from the alignment jig and placed into the pocket of the lower fixture. To simplify this process, the upper fixture has to be held at a distance far enough to be able to handle the alignment block at the lower fixture. To do so, a fixation has been developed and produced with a 3D printer. This fixation can be placed into the central bore of one of the linear guide rails. Like this, the upper fixture block cannot move against the lower fixture block anymore (Fig. 4-26).

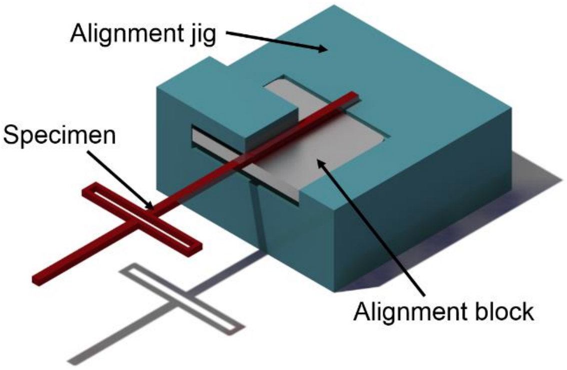

Fig. 4-25: Alignment of specimen onto alignment block

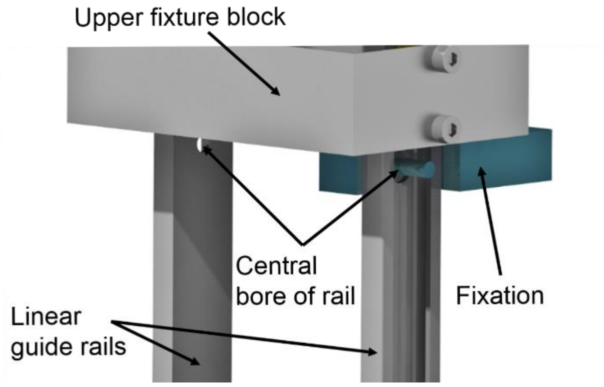

Fig. 4-26: Fixing the upper fixture block with a fixation to change specimen

Connecting the rotating and the clamping part together onto two different sides of a vertical support, the test stand has only to be adjusted to the specimen size. It is important that the center of the specimen and therefore the center of the elastic hinge is aligned with the rotational axis of the motor. To do so, the aluminum profile of the clamping part can be moved until this is accomplished. Furthermore, the pin acting as punch needs to be bolted to the rotating arm at the corresponding bore, depending on specimen size. A completed alignment of the test stand is shown in Fig. 4-27.

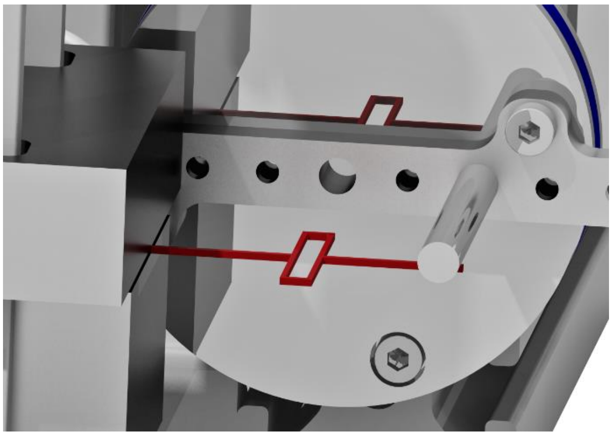

Fig. 4-27: Clamped and aligned specimen, initial set-up

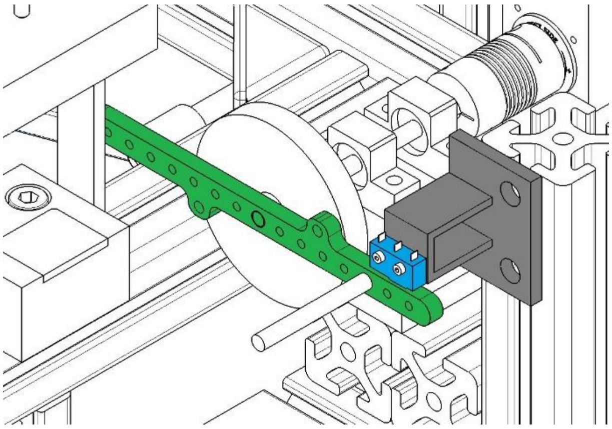

Fig. 4-28:Position switch (blue) for initial adjustment of horizontal position of rotating arm (green)

In order to have a repeatable starting point of the rotating arm, a mechanical switch mechanism has been introduced. This is shown in Fig. 4-28. To home the starting position, the rotating arm (green) is driven slowly towards the mechanical switch (blue). Once the switch is pressed, the motor is immediately stopped and the motor’s angular position counter is homed to its starting zero position. The switch has been placed such that the rotating arm is exactly horizontal at the end of the homing sequence. This placement can be done with a self-leveling laser while moving the switch fixture (grey) on the *item* profile.

4.3 Test stand software

The program to control the motor and to collect and store data is based on the LabVIEW program used in the preliminary tests and has been introduced in [83]. The basic initial program has been adapted to the requirements of the new test stand and new functions have been introduced. The LabVIEW program can be split into three subprograms. These are the motion control, data collection and switch control. The user interface, called front panel in LabVIEW, is depicted in Fig. 4-29. The front panel has an input field where the user can enter the code needed for the motor motion and then needs to push the “ENTER” button. The commands are explained just besides the motor motion control panel. On the right-hand side, the output of the motor is shown. There, all motion commands and replies of the motor are written. Data can be collected by activating the “Acquire Data” button and the data acquisition system (DAQ) can be stopped by switching the “Stop DAQ” button. The LED called “Switch” will turn on if the position switch is pressed by the rotating arm. Additionally, the graphs show real time data of the angular position, force and torque sensor data. The force sensor will not be used during the tests in this thesis; nevertheless, the program is configured, such that it could also include force sensor data. The force and torque sensors can be zeroed with their respective zero adjustment field.

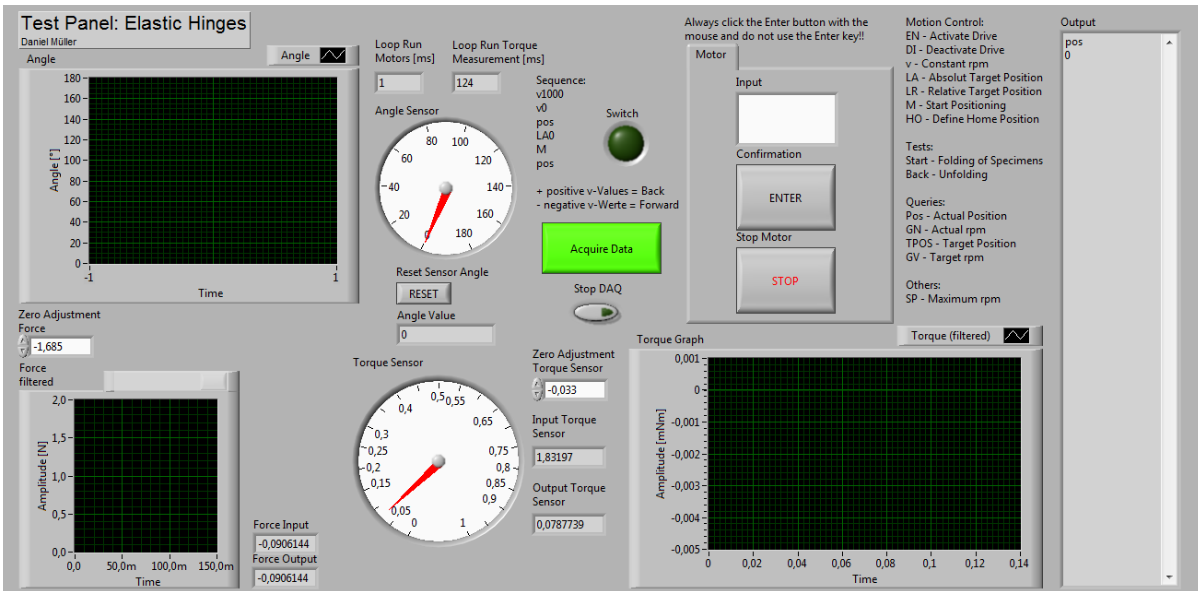

Test Panel: Elastic Hinges
Daniel Müller

Loop Run Motors [ms]: 1
Loop Run Torque Measurement [ms]: 124

Sequence:
v1000
v0
pos
LA0
M
pos

+ positive v-Values = Back
- negative v-Werte = Forward

Always click the Enter button with the mouse and do not use the Enter key!!

Motion Control:
EN - Activate Drive
DI - Deactivate Drive
v - Constant rpm
LA - Absolut Target Position
LR - Relative Target Position
M - Start Positioning
HO - Define Home Position

Tests:
Start - Folding of Specimens
Back - Unfolding

Queries:
Pos - Actual Position
GN - Actual rpm
TPOS - Target Position
GV - Target rpm

Others:
SP - Maximum rpm

Output: pos 0

Zero Adjustment Force: -1,685
Angle Value: 0
Zero Adjustment Torque Sensor: -0,033
Input Torque Sensor: 1,83197
Output Torque Sensor: 0,0787739
Force Input: -0,0906144
Force Output: -0,0906144

Fig. 4-29: Front panel of test stand program

The motion control program is shown in Fig. A-21 in Appendix A.4. It checks if there has been an input by the user. Then, it inspects if the input has been “start” or “back”. If so, the subprograms for the folding or unfolding motion are executed, respectively. If the input has been a normal motor command, the motor performs it until there is a new input. The subprograms “start” and “back” initiate the motor motion from deployed to folded or vice versa by turning the punch which folds or unfolds the specimen.

Data is saved by the data collection subprogram (see block diagram in Fig. A-22). It takes the inputs from the data acquisition system (NI-DAQ) and filters the information. If the button “Acquire Data” is pushed, the collected data is written into a new text file. The subprograms “start” and “back” automatically activate this button and always save the data to a text file.

Another separate subprogram is the switch control (block diagram in Fig. A-23). It checks if the mechanical position switch is pushed or not. When the rotating arm touches the switch and activates it, the motor stops immediately and its position is homed, setting the position counter to zero. This homed position is the starting and the final position for every folding and unfolding process.

5 Experiments and Mechanical Characterization

Different experimental testing has been done during this thesis. In order to define an appropriate measurement range for a new test stand, preliminary tests have been done with an already existing test stand, which had been built for a different purpose and was adapted to the current needs. Then a new test stand has been developed, validated and experiments have been carried out. This section explains the preliminary as well as the mechanical tests with the new test stand and shows their results.

5.1 Preliminary Testing

An initial test has been performed on already existing 3D printed hinges to verify the order of magnitude of the simulations made by Jannic Völker [6] and to choose appropriate sensors regarding measurement range and precision. The goal of this test was not to get exact values for bending angles and forces but to choose the order of magnitude of the latter. An already existing test stand could be used (Fig. 5-2). The test stand has been developed by Nils Gerrit Kottke in his semester thesis at DLR/iAF. [83]

The test stand is based on the *item* building kit system and a linear unit from *IGUS*. The linear unit is driven by a servomotor and data are collected through laser triangulation for the deflection and a force sensor. The used laser has a linearity of 0.25% in the measurement range of 250 mm and a precision of 50 µm [84]. The force sensor is an S-Form sensor based on strain gauges. It features a nominal force of 20 N and an accuracy class of 0.1% [85]. The control and data acquisition has been done by using an already existing LabVIEW application. The application is able to acquire synchronized data from the force sensor and the laser triangulation. The actuation of the motor is also done through LabVIEW. Signal inaccuracies are eliminated by a Butterworth low-pass filter of third order with a cutoff frequency of 5 Hz. Fig. 5-2 shows the total test stand and important parts are depicted in Fig. 5-3.

The specimens are fixed by a 3D-printed clamping fixture on one side. They have all been placed such that one of their arms is fixed completely, only leaving 1 mm of free length. This means that only the free arm and the elastic hinge where free to bend. A triangular punch is fixed onto the force sensor. The sensor is driven downwards by the linear unit which results in specimen bending.

Three different configurations have been tested. For the first, the punch has been placed at the center of the free arm. Then, the specimen has been bent to an angle of approximately 55° where the punch lost direct contact with the specimen due to geometrical reasons. The only difference from the first to the second test is that for the second test, the punch has been placed as close to the hinge as possible leading to a higher bending angle before losing contact with the specimen. The configuration for the third test is different. The specimens are fixed as explained before but they are manually bent over 180°. The punch is placed at a distance of 6 mm from the hinge on the free arm measuring the reaction force from bending the specimens. Then, the punch is moved upwards releasing the bending state and decreasing the reaction force. The test is stopped when the free arm is not touched by the punch anymore. This third test sequence is expected to be the most accurate regarding maximum force and bending torque because it can measure the fully bent state. For all tests, the maximum force and the translation of the punch during the test has been recorded.

Torsion hinges, O-hinges and Oval-hinges printed from Nylon and Durable printing filament have been tested. In total, 15 different hinge designs have been tested. A name code describing the hinge design was assigned to each specimen. The name code is built up as follows: *D-L1-L2-W-T-H*. *D* is the design name, which means in those tests either *TH* (Torsion Hinge) or *RD* (Round, as the O-hinge and the oval-hinge are both basically round hinges with different lengths and widths). The rest of the name code are geometrical dimensions explained in Fig. 5-1.

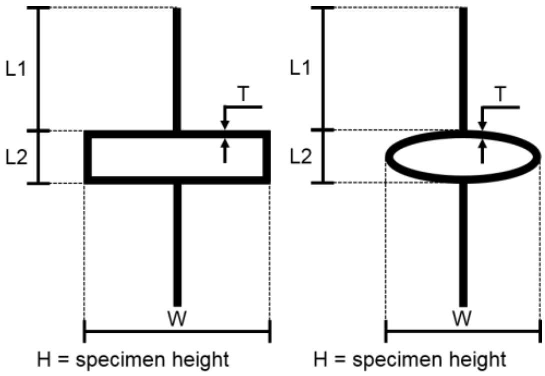

Fig. 5-1: Specimen design with geometry naming

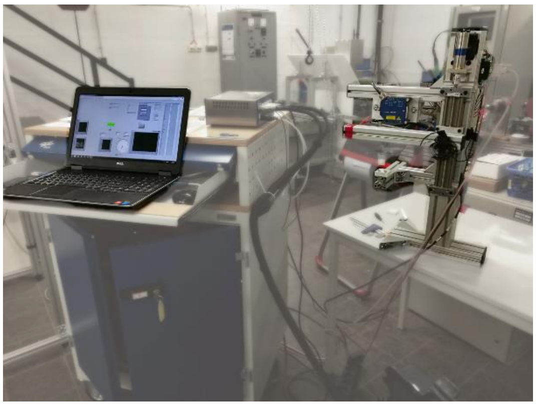

Fig. 5-2: Test stand during testing

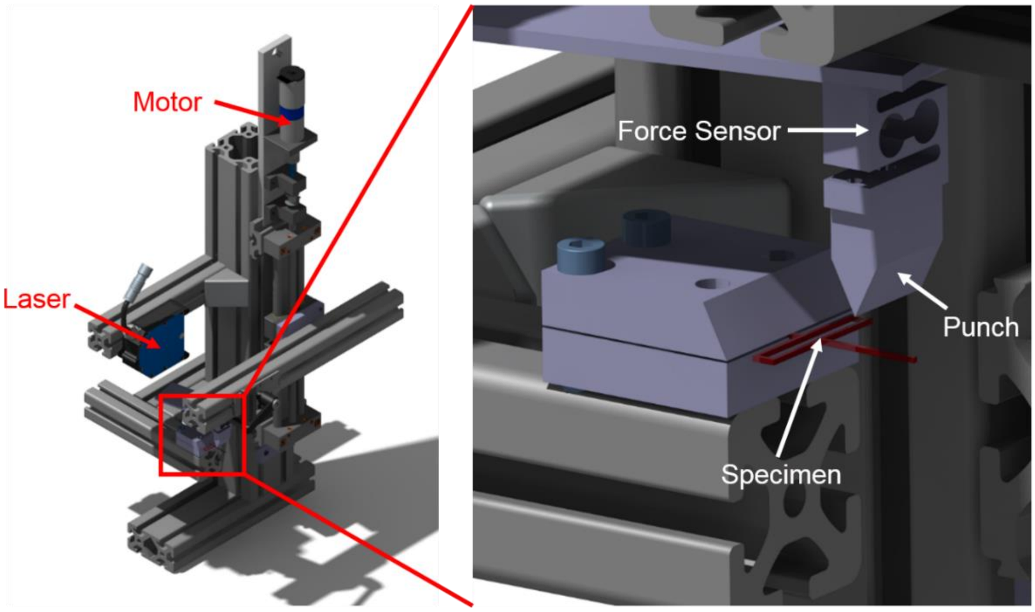

Fig. 5-3: 3D-Model of used test stand for preliminary tests

5.1.1 Results from preliminary tests

Test 1 has been performed on 15 different hinge designs. Therefore, the measured forces strongly vary from 0.06 N up to 0.88 N (Fig. 5-4). This large range is mostly influenced by the material parameters, hinge cross-section and hinge design. Regarding hinge dimension parameters, the width *W* has a large influence on the reaction force. The larger the width, the smaller the reaction force. This can be seen in Fig. 5-5, where torsion hinge designs with the same parameters for *L1*, *L2* and *T* are shown. TH-20-4-48-1-2 and TH-20-4-48-1-1.5 even have a larger specimen height, which should stiffen the specimen because it will influence the torque of inertia with its third power. Nevertheless, the width *W* has a larger influence because by increasing *W* from 40 mm to 48 mm the force is only increased by 4.6% while doubling the specimen height. The force even decreases by 9.9% while still increasing the specimen height by 50%. The width influence can even be seen better by keeping all other dimensions the same. By increasing the width from 40 mm to 45 mm (an increase of 12.5%) decreases the force by 74.7%.

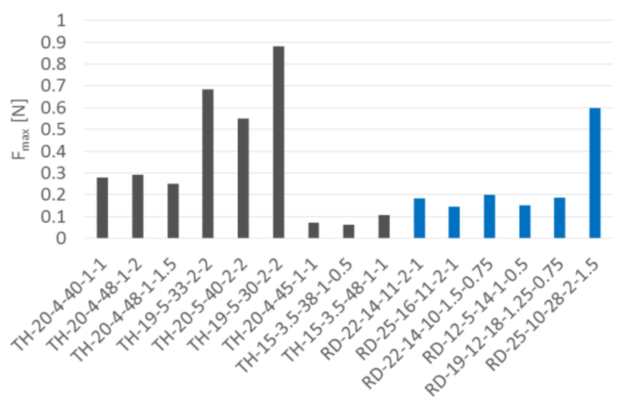

Fig. 5-4: Maximum force reached during bending up to ≈ 55° for all specimen types (torsion hinges black, round hinges blue)

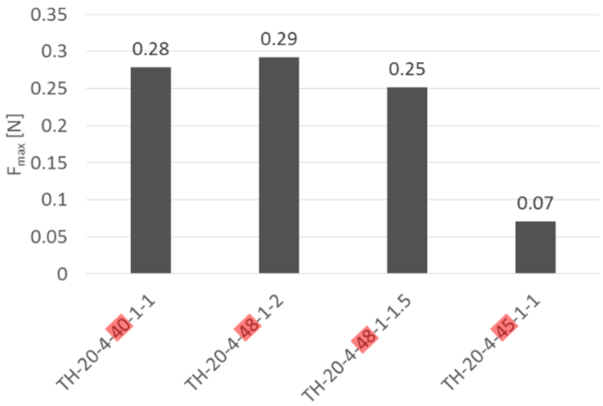

Fig. 5-5: Influence of width parameter W on maximum force during bending up to ≈ 55° for comparable specimen types

Fig. 5-6 shows that the maximum force is not reached at the end of the bending *Test 1*. This is clearly due to the preliminary character of the test itself. As the punch is driven downwards, it only gets into orthogonal contact with the specimen at the beginning of the test. During the test, the punch is not loaded orthogonally but also perceives shear loads which transmits as bending torque to the force sensor. Therefore, at larger bending angles the force sensor does not measure the correct load anymore but only a part of it which is shown in the decrease of force at the end of the experiment in Fig. 5-6. In addition, the punch is sliding on the specimen while being pushed downwards. This can be seen by the oscillations on the force curve. The initial and final states of the test are shown in Fig. 5-7 where one can see the non-orthogonality between specimen and punch at the end of the test.

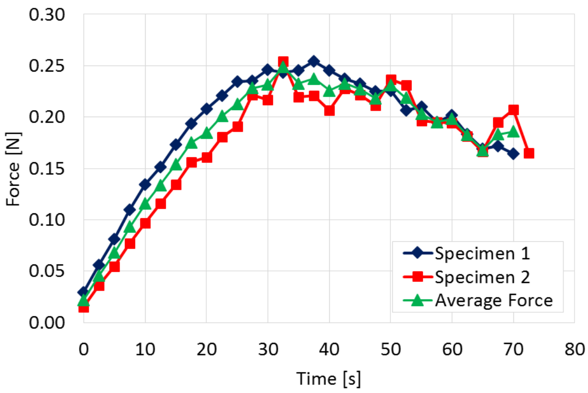

Fig. 5-6: Exemplary force diagram for specimen type TH-20-4-48-1-1.5 with individual specimen reaction force and averaged force for bending during Test 1

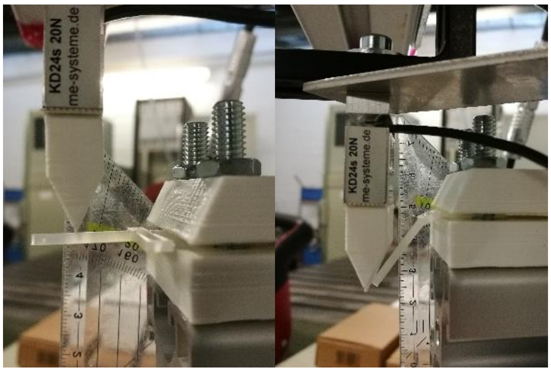

Fig. 5-7: Initial state and end of ≈ 55° bending during Test 1

Test 2 shows that the force increases strongly when bending is increased. Therefore, 3 specimens that have already been tested during *Test 1* have consecutively been placed in the test stand such that it was possible to get a larger deflection. To do so, the punch has been placed as close to the hinge as possible to be able to keep the contact for a higher bending radius. By increasing the bending from 55° to 70°-80° deflection (depending on specimen design) the measured forces increased strongly by a factor between 2.1 to 3.2 (Fig. 5-8). This shows, that the force will increase the more the specimen is bent.

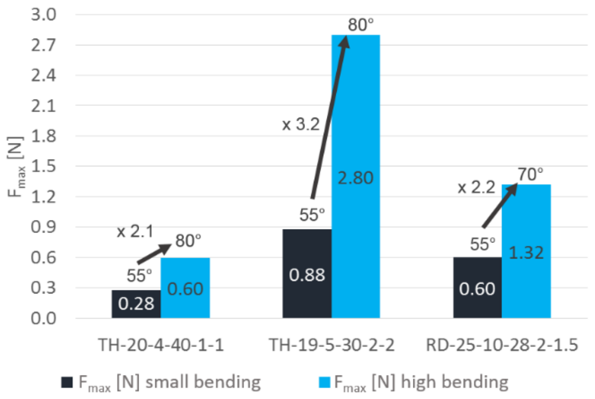

Fig. 5-8: Increase of maximum force when bending angle is increased for chosen specimens

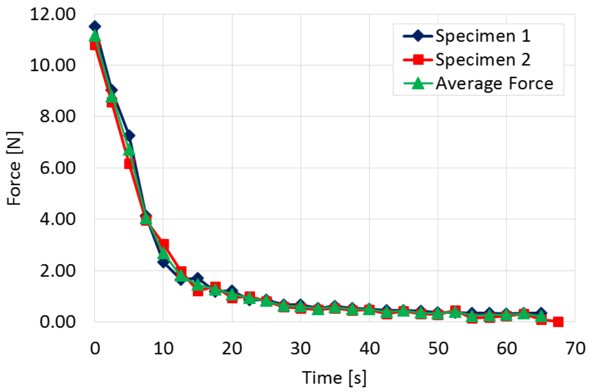

Fig. 5-9: Exemplary force diagram for specimen type TH-19-5-33-2-2 with individual specimen reaction force and averaged force for release during Test 3

To observe the maximum bending force another series of tests has been done. *Test 3* shows the reaction force while unloading the fully bent specimen. Reaction forces range from 0.85 N up to 12.01 N (Fig. 5-11). It can be seen that for the torsion hinges, the fully bent reaction force is larger by a factor of 13.5 to 28.2 compared to the 55° bending (Fig. 5-10 black bars). For the round hinges, this factor is smaller (6.6 – 9.1) (Fig. 5-10 blue bars). The bending torque has been calculated by multiplying the measured force with the half-length of each individual hinge (dimension *L2*) plus 6 mm. This has been done like this because the force sensor has been placed 6 mm away from their hinge in order to be as far away as possible but still be able to measure for a long time span without losing contact to the specimen. The obtained torques are in the range between 6.6 up to 102 mNm (Fig. 5-13). This large variety imposes the need of a torque sensor with a measurement range which is large enough but still very precise for torques in its low measurement range.

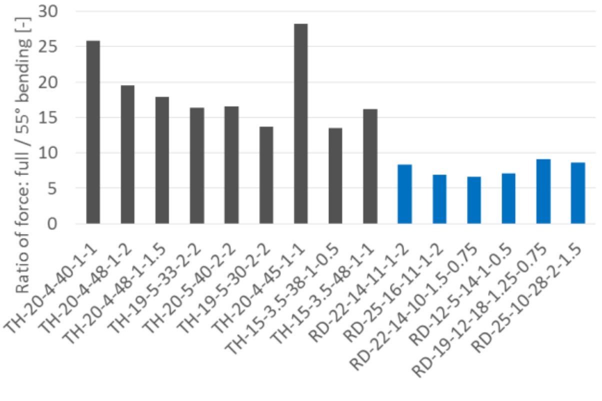

Fig. 5-10: Ratio of reaction force between full bending and 55° bending for every specimen (torsion hinges black, round hinges blue)

The same influence of the width parameter *W* can be drawn from *Test 3*. By increasing *W* the force decreases strongly (Fig. 5-12). During *Test 3* the force decreased by 72.3% while increasing *W* by 5 mm (12.5%). The decreasing factors comparing TH-20-4-40-1-1 and TH-20-4-45-1-1 are very similar for *Test 1* (74.7%) and *Test 3* (72.3%). This proves the strong influence of W during the complete folding process.

It can also be seen that for both *Test 1* and *Test 3* the influence of the size and material parameters on abolute values are not as large for the round hinges as for the torsion hinges. For both tests the absolute reaction forces are comparable in between the specimens. This is due to the very low absolute forces measured. The only differing specimen is RD-25-10-28-2-1.5 which has a strong oval form and a larger reaction force.

Fig. 5-9 shows that the maximum force is measured when the specimen is completely folded. During opening, the force decreases drastically until it reaches zero when the punch loses contact with the specimen. The same conceptual flaws as already explained before are included in this test sequence. A permanent deformation could be observed for some of the specimens after the force has been released. One of the goals of this thesis is to avoid this permanent plastic deformation as much as possible such that the hinges can fully open and therefore are able to deploy a main structure.

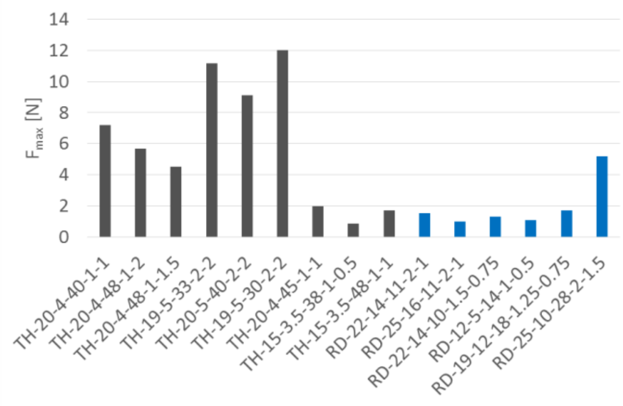

Fig. 5-11: Maximum opening force during release of fully folded specimens for all specimen types (torsion hinges black, round hinges blue)

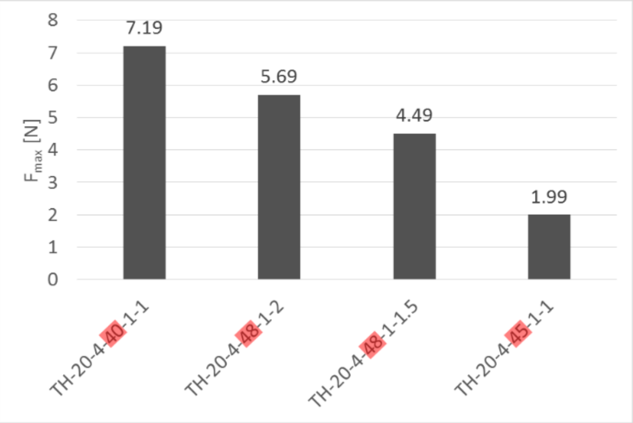

Fig. 5-12: Influence of width parameter W (value red shaded in specimen name [mm]) during release of fully folded specimens for comparable specimen types

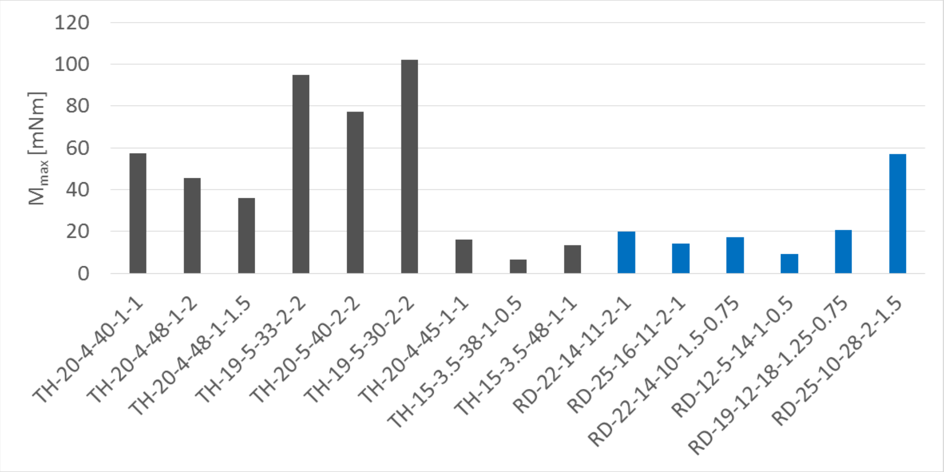

Fig. 5-13: Maximum reaction torque during release of fully folded specimens for all specimen types (torsion hinges black, round hinges blue)

5.1.2 Conclusions from preliminary tests

The tests showed that the test stand which will be developed in this thesis needs to be able to differ very small loads during the beginning of the folding process (0.06 N – 0.88 N at ≈55°) and much larger loads at the end of the complete folding (0.85 N – 12.01 N). In addition, a large variety of models leads to a large range of expected forces to be measured. The measured force of the stiffest model was more than 14 times higher than the force of the most compliant specimen, independent of the bending angle.

The simulation results from J. Völker [6] showed that for a torsion hinge model TH-20-2.6-45-0.8-2 made out of Nylon filament material a pressure of 33 kN/m^2 is expected. This implies a force of 1 N. Comparable specimens from the tests show a much larger reaction force during *Test 3* with 1.99 N for TH-20-4-45-1-1 and 5.69 N for TH-20-4-48-1-2. However, as observed during these preliminary tests, an increase of W (here from 45 to 48 mm) should decrease the force. The same is true for increasing L2. Hence, the reaction force of the tested specimen TH-20-4-48-1-2 should be smaller than the simulated model TH-20-2.6-45-0.8-2.

Regarding the simulation result of a *Durable* filament torsion hinge (TH-15-2.4-47-0.7-1.5) a pressure of 35 kN/m^2 is expected which leads to a force of 0.53 N. Here, no similar specimens have been available.

To conclude the preliminary tests, one can state that the FE results are lower by an important factor but that the order of magnitude is correct. This will help defining the test stand and especially its sensors.

5.2 Mechanical testing

Having developed a test stand for the experimental bending of elastic hinges, tests have been performed. This section explains the test procedure, specimen design & manufacturing and shows the results from the mechanical testing.

5.2.1 Test procedure

For all specimen designs explained in section 5.2.2, 15 individual specimens have been tested with the newly developed test stand. The new test stand has been calibrated and used for several sets of tests on different specimens. Fig. 5-14 shows the test procedure which has been followed for the new test stand. This section explains this procedure starting with commissioning and shows the obtained results.

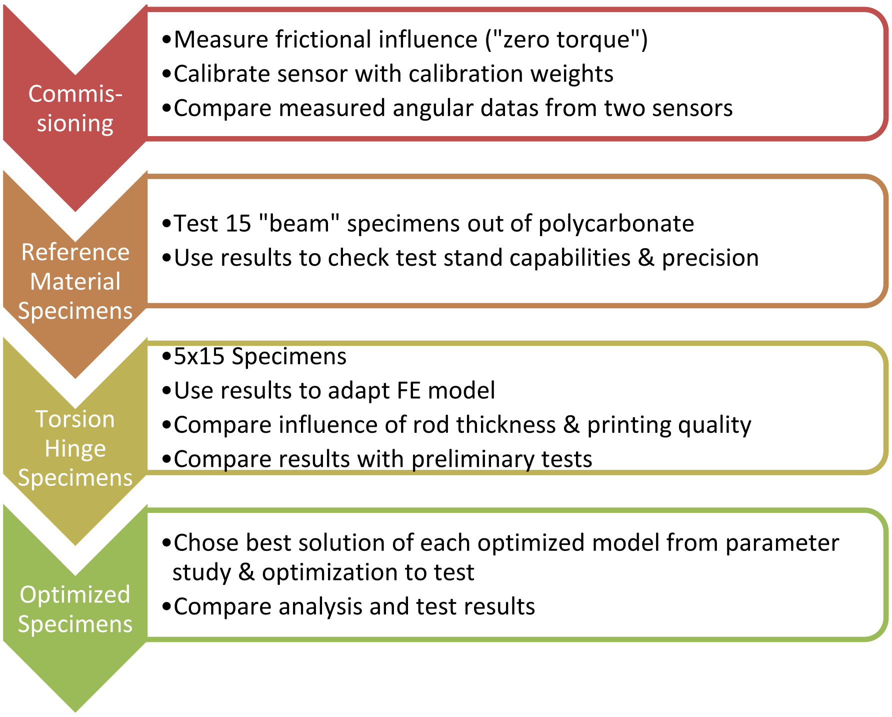

- Measure frictional influence ("zero torque")
- Calibrate sensor with calibration weights
- Compare measured angular datas from two sensors

- Test 15 "beam" specimens out of polycarbonate
- Use results to check test stand capabilities & precision

- 5x15 Specimens
- Use results to adapt FE model
- Compare influence of rod thickness & printing quality
- Compare results with preliminary tests

- Chose best solution of each optimized model from parameter study & optimization to test
- Compare analysis and test results

Fig. 5-14: Test procedure

5.2.2 Specimen Design & Manufacturing

To get various data from different specimen dimensions, different specimen designs have been chosen to test. The first set of specimens are all torsion hinges with different rod and torsion hinge lengths and different thicknesses at the hinge or the rods. To compare the influence of the rod stiffness on the total hinge displacement two specimen designs have been considered (TH-28-4-30-1-1.5) such that all dimensions are the same except for the rod height, which is 33% larger for one design. Another design has almost the same dimensions except that its thickness is doubled on all rods and hinges (TH-28-6-30-2-1.5). Then, to be able to compare the results from the newly designed test with the preliminary tests, two already tested designs have been chosen to be tested again. The first one has been arbitrarily chosen from all the already tested designs (TH-20-4-40-1-1) and the second one is the design that reached the highest forces during the preliminary tests (TH-19-5-30-2-2). The results of all these tests shall be used to adapt the finite element model to the test stand and its boundary conditions and loads.

All specimens have been manufactured with a 3-D printer using the FDM-method. The used printer was an *Original Prusa i3 MK3S 3D printer*. The used material was a Nylon filament (PA6) from Markforged

[58]. This material has initially been chosen due to the results of J. Völker in his Master thesis [6] and due to its high flexibility. However, printing Nylon has some major drawbacks, which made manufacturing of the specimens difficult. The material is transparent, which makes the printers light sensors for controlling the printing process useless. In addition, the material is highly flexible even in its filament state and therefore it appeared that too much material has been pushed into the nozzle and blocked it such that the printing process had to be stopped and the nozzle needed to be cleaned. Last but not least, Nylon does not adhere very well to the printers build plate. By applying glue from a glue stick, the adherence could be increased but delamination still appeared for some prints at their outermost members.

Before printing the specimens, the optimal printing temperature for the specimens had to be found. To check the printing temperature, cubes have been printed at different temperatures. Then, they have been checked for printing quality. It appeared that a temperature between 260° C and 265° C worked well with the used filament. All subsequent prints have been done with a nozzle temperature of 262° C.

Another issue during printing is that even if the specimens stick to the build plate, curvatures appear at their ends. This can be explained due to material retraction during cooling of the individually printed layers. To overcome this problem, cylinders have been added to all specimen ends as shown in Fig. 5-15. The cylinders have two functions. As they have a larger area than the specimens themselves, they increase the adherence on the build plate. In addition, they work similar to risers in casting, such that the shrinking retraction is moved away from the ends of the specimen towards the cylinders. It could be shown that printing with these added cylinders, results in flatter specimens with a higher printing quality than printing individual specimens. The cylinders are cut from the specimens after printing. In addition, it has been found that heating the build plate to 75° C worked best regarding adherence to the build plate.

After printing, the specimens have been measured with an electronic caliper in order to check the printing quality. The large dimensions like the rod lengths have been printed very precise. However, manufacturing defects have been observed regarding the thickness and the width of some models, which are dimensions with a large influence regarding bending stiffness. Therefore, the subsequent FE models needed to be adapted to the measured geometries. Tab. 5-1 shows the desired values and the mean of the actually measured values for the rod thickness, t_{rod}, and the hinge thickness, t_{hinge}. The standard deviation in between a model has been lower than 0.03 mm for all models. Therefore, one can say that the manufacturing error was repeatable and the mean values can be considered. It can be seen that for rod thicknesses of 1.50 mm, the printer had difficulties in producing the exact dimensions as the actual value had a larger offset for this dimension. However, this is only true when the whole specimen had a thickness of 1.50 mm whereas the offset is very small for the model where the rods are 2 mm thick and the hinge is 1.50 mm thick which is also the model showing the most precise printing.

Tab. 5-1: Desired and actual values for thickness for all torsion hinge design specimens

Model	**Desired Value [mm]**		**Actual Value [mm]**	
	t_{rod}	t_{hinge}	t_{rod}	t_{hinge}
TH-19-5-30-2-2: Assembly Print Configuration	2.00	2.00	1.93	1.91
TH-19-5-30-2-2: Individual Print Configuration	2.00	2.00	1.92	1.84
TH-28-6-30-2-1.5	1.50	1.50	1.31	1.26
TH-28-4-30-1-1.5, t_{rod} = 1.5 mm	1.50	1.50	1.38	1.29
TH-28-4-30-1-1.5, t_{rod} = 2 mm	2.00	1.50	1.96	1.47

For the optimized models, printing with the explained assembly print design showed precise values for most of the dimensions. However, there could still be measured some inaccurate values which are shown in Tab. 5-2. It is important to note that the optimization results have been done with the desired values. However, to be able to compare the experimental results with the FE simulations, the FE model parameters have been adapted to the actual values. Therefore, it might appear that some values of the optimization and the final FE simulation may slightly differ.

Tab. 5-2: Desired and actual values for inaccurate dimensions for optimized hinge designs

Model	Dimension	Desired Value [mm]	Actual Value [mm]
Z-shape thin	t_{hinge}	2.00	1.95
Oval-shape straight	w_{hinge}	2.32	2.46
Oval-shape straight thin	w_{hinge}	1.00	1.05
Oval-shape spring	t_{hinge}	1.00	0.96
Oval-shape tilted on foil	t_{hinge}	1.00	0.91

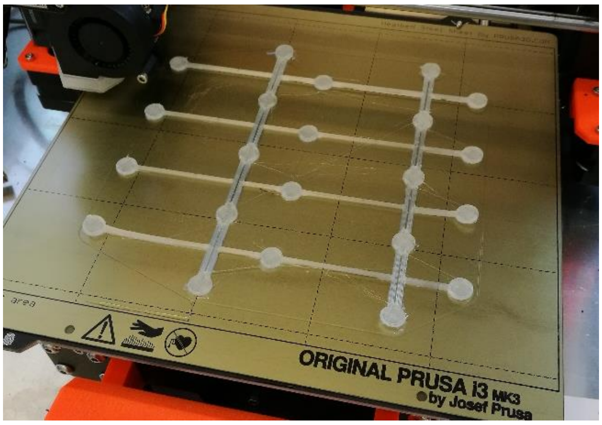

Fig. 5-15: Printing specimens with the assembly design, adding connecting cylinders to increase flatness of specimens

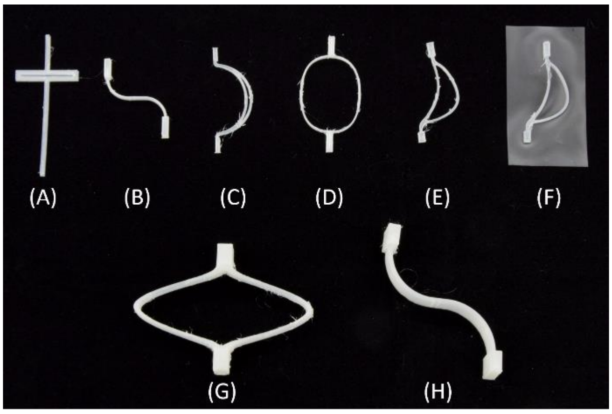

Fig. 5-16: Overview of all specimen models (only one torsion hinge model is shown for simplicity): torsion hinge (A), Z-shape thin (B), oval-shape spring (C), straight thin (D), tilted (E), tilted on foil (F), straight thick (G) & Z-shape thick (H)

The printing process not only induced some inaccurate dimensions but also other defects. Most of the specimens showed little material add-ons and thin threads after printing as is shown in Fig. 5-17, where the *Z-shape* model is shown as an example. This might be explained with the small specimen dimensions and especially with the used filament. The printing quality might be improved with a more precise 3D printer and a higher quality filament.

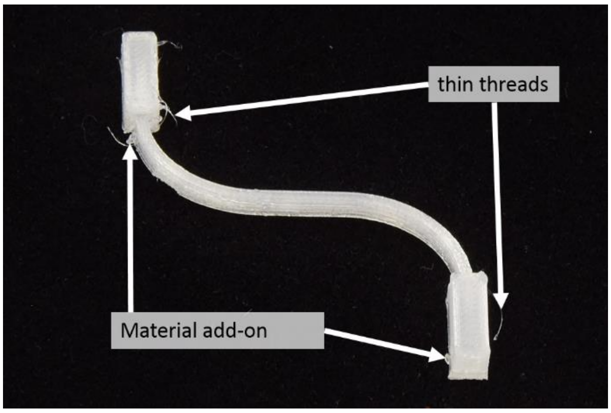

Fig. 5-17: Printing defects for the *Z-shape* model

5.2.3 Calibration & preparations

In order to ensure high quality test results, a high precision torque sensor from Burster (type 8661) has been used. This sensor has a precision of 0.1% of its calibrated scale. As it has been calibrated in 20% steps of its full scale, the measurement precision is 0.2 mNm.

The overall test stand has been calibrated in two steps. First, to remove any external influence, tests at different rotational speeds have been made without any applied load and the torque has been measured with various calibration weights. Therefore, the frictional influence onto the measured torque as well as other influence due to the test stand design could be measured. These influences need to be subtracted from the torque measured during the experiments. The angle measurement can be investigated internally as both the motor and the torque sensor are able to measure the angular position. This is done to ensure a correct angle measurement for all tests.

The motor has an encoder disc with 3000 increments [86] and therefore an angular precision of 0.12° per increment. In addition a gear reduction of exactly 133.530864:1 [87] is mounted on top, increasing the precision largely to a minimum angle of 0.0009° per increment. This is considerably more precise than the 0.08789° per increment for the torque sensor (section 4.2). However, the angle is measured simultaneously by both position sensors and their data can be compared if any measurement issues should appear.

The second calibration step of the test stand has been done by testing standardized samples and comparing the results with hand calculations and FE simulations. This ensures that further test results on more sophisticated models are reliable and repeatable.

5.2.3.1 Sensor calibration

Even though, the sensor used is a high precision instrument, it needed to be checked if the sensor is able to measure correct when it is built into the overall test stand. To do so, frictional influence has been measured by rotating the test several half turns as it would be done during the tests. No additional load has been applied. If the test would have been perfect, the torque should be zero during all movements. Therefore, the measured torque values can be assumed being introduced due to frictional influence and non-perfect geometries, which induce asymmetries. This “zero torque” needs to be subtracted from the torque measured during the experiments. Fig. 5-18 shows the “zero torque” obtained by rotating the motor from the starting position at zero degrees to 180° and back for 16-times. The small deviation in between the different rotations show that this “zero torque” is a repeatable measure, which needs to be subtracted from further test results. It can be seen, that there exist amplitude peaks at both starting phases at 0° and 180°. This might be explained with the change from static to dynamic friction or an acceleration of the motor that is unfavorable. For further simplicity in removing this “zero torque”, the folding and unfolding phases are split into two data sets. Then, the acceleration peaks are split again from their respective phase. These four data sets are approximated by second order functions for the peaks and third order functions for the steady phases. All functions have the corresponding angle as function parameter. The found coefficients of each function are stored for the data analysis of further test results where the “zero torque” can be approximated by calculating the respective function with the corresponding angle and subtracting the found torque from the measured data.

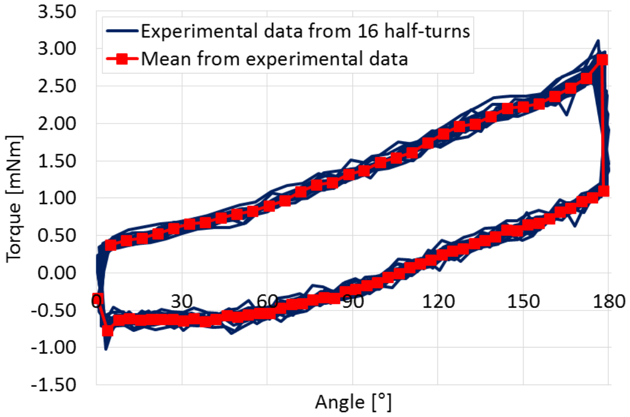

Fig. 5-18: “Zero torque” measured during sensor calibration

In addition to measuring the “zero torque”, the sensor has been calibrated to the overall test stand by using calibration weights covering the entire measurement span of the sensor. The measured data has been compared to the nominal value of the corresponding weight and differences have been analyzed. Fig. 5-19 & Fig. 5-20 show the measured sensor values during the calibration process and the corresponding nominal values of the different calibration weights.

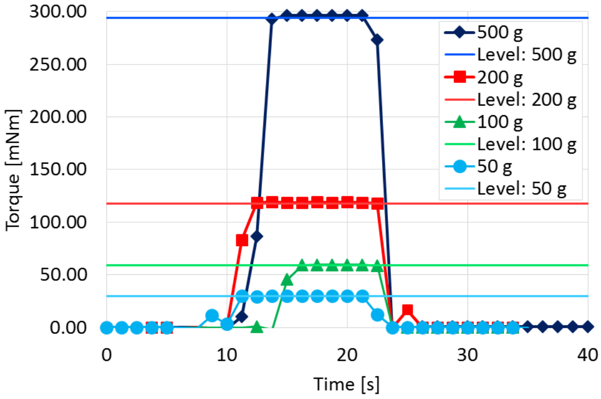

Fig. 5-19: Torque measured during sensor calibration for calibration weights of 500 g, 200 g, 100 g & 50 g

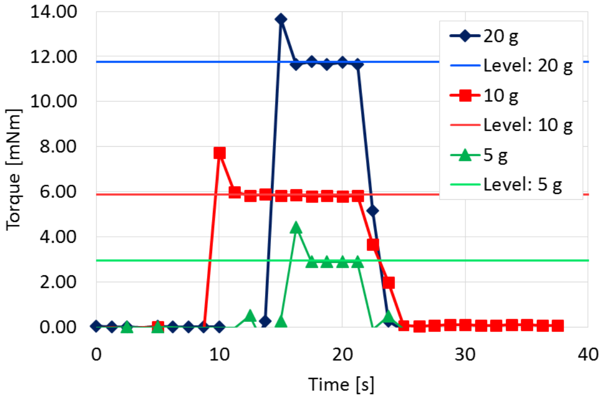

Fig. 5-20: Torque measured during sensor calibration for calibration weights of 20 g, 10 g & 5 g

It could be shown that the achieved precision is very high and the relative error compared to the nominal value is shown in Tab. 5-3. The error is lower than 2% for all measurements which is assumed to be precise enough. The veering part is due to the placement of the calibration weights by hand during the torque measurement, therefore only the steady state results should be used for comparison.

Tab. 5-3: Relative Errors of nominal and measured torque

Weight	Relative Error
500 g	0.71 %
200 g	1.23 %
100 g	1.25 %
50 g	1.70 %
20 g	-0.14 %
10 g	-1.27 %
5 g	-1.80 %

Regarding the angle measurement, Fig. 5-21 shows that the measured angles during the frictional torque test by both position encoders of the motor and the torque sensor are only differing in the range of the precision of the torque sensor. Therefore, one can state that the angular measurement of both sensors is correct. As the motor has a higher angular resolution its data will be used for subsequent tests in order to have the most precise results.

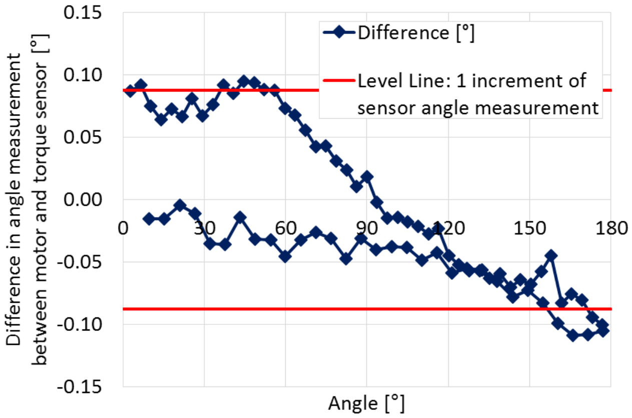

Fig. 5-21: Angles measured during sensor calibration

By subtracting the "zero torque", the measured torques have been adapted to the test stand design and therefore the results will be as precise as possible. A further calibration step has been done by testing sample material specimens, which could be compared with results from both hand-calculations and FE simulations.

5.2.3.2 Sample material specimens

To ensure the reliability and repeatability of the test stand, sample material specimens have been tested and the results have been compared with hand calculations and an FE analysis. The sample material specimens could be obtained from the German reference office for proficiency testing and reference materials (Deutsches Referenzbüro für Ringversuche und Referenzmaterialien, DRRR). The specimens were made out of polycarbonate (PC) and the geometry of the specimens has been a simple rectangular solid (Fig. 5-22) [88]. This could be used to do hand calculations according to the cantilever beam bending theory. The specimens have been clamped on one side over a length of 58 mm such that only 70 mm of their full length has been left free. In the following subsection, *L* is the free length of the beam. Tab. 5-4 shows the material properties and dimensions of the reference specimens.

Tab. 5-4: Material properties and dimensions of reference specimens

Material property	**Symbol**	**Value**
Young's modulus	E	2200 MPa [89]
Poisson's ratio	v	0.37 [90]
Density	ρ	1.2 g/cm^3 [89]
Maximum yield stress	$R_{p0.2}$	60 MPa [89]

Dimension	**Symbol**	**Value**
Beam Length	L	70 mm
Width	b	12.7 mm
Height	h	3.2 mm

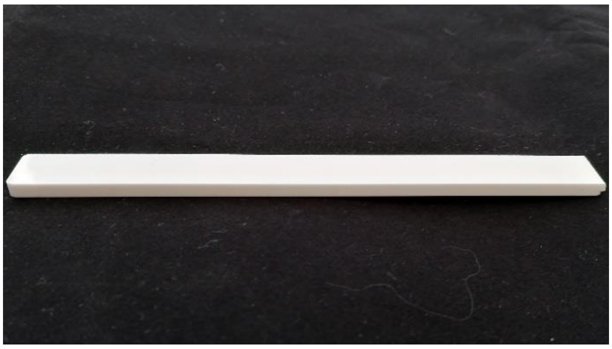

Fig. 5-22: Sample material specimen

It is clear that the sample specimens cannot be fully bent due to their design, which brings up a much higher bending stiffness than the further investigated and tested specimens will have. In order not to surcharge the torque sensor, only a part of the final half turn has been tested and calculated. This circular part has been defined as 1/50 of a full circle, leading to a z-displacement of $w = 8.7733\ mm$ with:

$$w = \frac{L}{2}\sin(\alpha) \tag{5.1}$$

With L, the beam length and α, the bending angle ($\alpha = \frac{360°}{50} = 7.2°$)

Hand-calculations have been made according to the Euler-Bernoulli and the Timoshenko beam theory with the prescribed z-displacement and a torque of inertia of:

$$I = \frac{bh^3}{12} = 34.68\ mm^4 \tag{5.2}$$

Euler-Bernoulli Beam Theory

The simplest approximation of beam bending is the Euler-Bernoulli beam theory. It states that involving equilibrium equations and a 1-D stress-strain relationship, the curvature of the beam can be calculated as:

$$w''^{(x)} = -\frac{M_y(x)}{EI} \tag{5.3}$$

Integrating equation [3] two times and applying the respective boundary conditions the deflection of a clamped beam (B.C.: $w(x = 0) = 0 \,\&\, w'(x = 0) = 0$) with a point load at the free end in positive z-direction as depicted in Fig. 5-23, can be calculated as: [91]

$$w(x) = -\frac{1}{EI}(\frac{1}{6}Fx^3 - \frac{1}{2}FLx^2) \tag{5.4}$$

It is clear that the maximum bending *w(x)* takes place at the free end where *x = L*, which gives the equation for w_{max}, the maximum deflection:

$$w(x = L) = w_{max} = \frac{FL^3}{3EI} \tag{5.5}$$

Where the force *F* is found with:

$$F = \frac{3EIw_{max}}{L^3} = 5.8544\,N \tag{5.6}$$

According to the free body diagram in Fig. 5-24, the force *F* induces a torque M_y at the clamping:

$$M_y = -FL = -409.81\,mNm \tag{5.7}$$

Which brings up the maximum bending stress σ_b with equation (6.8):

$$\sigma_b = -\frac{M_y}{I}c = 18.91\,MPa \tag{5.8}$$

Where *c* is the distance from the neutral axis to the investigated point. The maximum bending stress is found where *c* is largest and therefore *c* is half the beam height (*h/2*).

Timoshenko Beam Theory

As the Euler-Bernoulli beam theory does not account for shear deformation during bending, Timoshenko introduced a more precise beam theory. This theory states that for a clamped beam at x=L, the deflection can be calculated with equation (6.9): [92]

$$w(x) = \frac{Px}{2EI}\left(L^2 - \frac{x^2}{3}\right) - \frac{P(L-x)}{\kappa AG} - \frac{PL^3}{3EI} \tag{5.9}$$

Where:

- *A*: cross-sectional area of the beam
- *G*: shear modulus ($G = \frac{E}{2(1+\nu)}$)
- *K*: Timoshenko shear coefficient ($\kappa = \frac{10(1+\nu)}{12+11\nu}$) [92]

Solving equation (6.9) for the force P in the same coordinate system as on Fig. 5-23 and setting it at the free end of the beam at position x=0 one can calculate the force responsible for the prescribed deflection with equation (6.10):

$$P = -\frac{w_{max}}{\frac{L}{\kappa AG} - \frac{L^3}{3EI}} = 5.8643\ N \tag{5.10}$$

There is only a very small difference between the results of the two beam theories in this example. This can be explained with the small beam dimensions and the small applied forces.

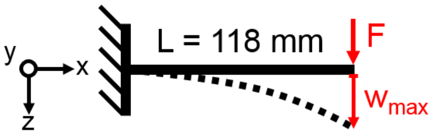

Fig. 5-23: Schematics of the beam bending situation

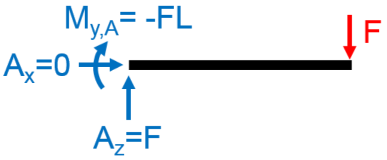

Fig. 5-24: Free body diagram of the beam

Finite Element Simulation

Another approach for calculating the beam deflection and the corresponding force is a finite element simulation of the test. To do so, an FE model of the sample specimens has been developed. The same geometry as already explained above has been built and the identical boundary conditions have been applied such that the specimen is clamped on 58 mm on its left-hand side and a displacement of 8.7733 mm in positive z-direction on its right-hand side is prescribed. In addition, to approximate reality even better, gravitational forces have been applied on the whole body in the same manner as the tested specimens will be exposed to.

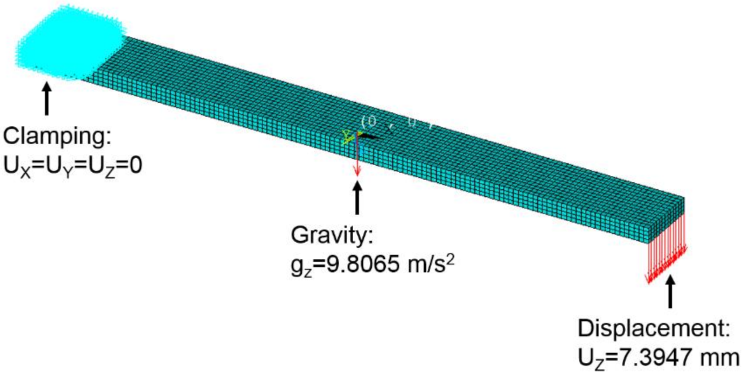

Fig. 5-25: Boundary conditions of FE model

A mesh convergence study has been made which checks if the mesh is fine enough. Fig. 5-26 shows the normalized results of the displacement U_z, stress in x-direction S_x and the equivalent von Mises stress S_{EQV}. The values are all normalized to the corresponding result obtained with the coarsest mesh. One can see that with a mesh of almost 10'000 nodes the slopes of the two stress resultants are strongly decreasing and that the mesh is converged at this stage, even though the stress increases while further refining the mesh. This can be explained by the fact that the stress gets more and more localized while refining the mesh as its elements get smaller.

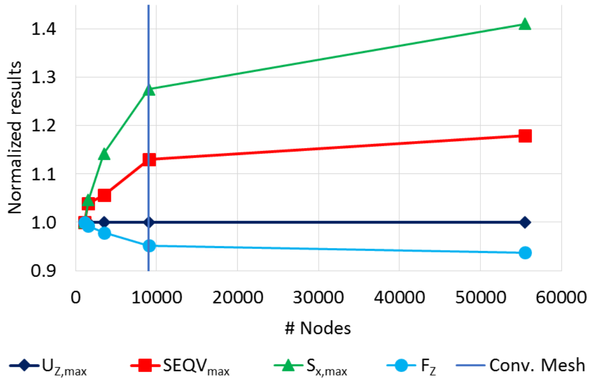

Fig. 5-26: Normalized results of mesh convergence study

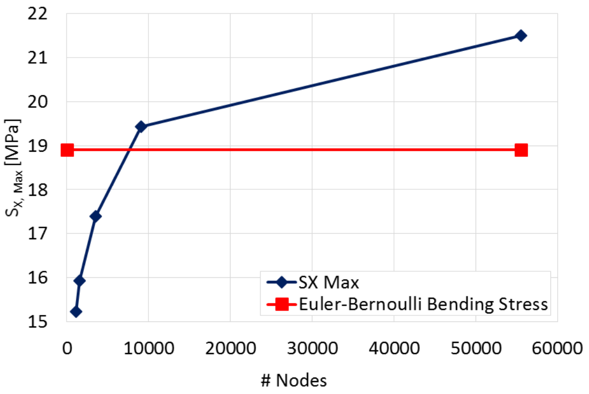

Fig. 5-27: Comparison of maximum stress in x-direction and bending torque

One can see this in Fig. 5-28 & Fig. 5-29, where the results of a global mesh size of 0.5mm (finest mesh in convergence study) for the stress S_x are shown. The maximum stress appears to be a line concentrated at the location where the beam is clamped. The finer the mesh, the more the stress gets concentrated towards the clamping and is therefore distributed over fewer elements, which increases the stress. This is not physical, as the stress would increase to infinity when refining the mesh even more. However, one can see in Fig. 5-26 that the normalized values can be assumed to be converged at the mesh refinement with about 10’000 elements as the slope of the simulated values decreases strongly at this point. In addition, Fig. 5-27 shows that at this stage of refinement the maximum stress of S_x is very close to the calculated bending stress with the Euler-Bernoulli beam theory.

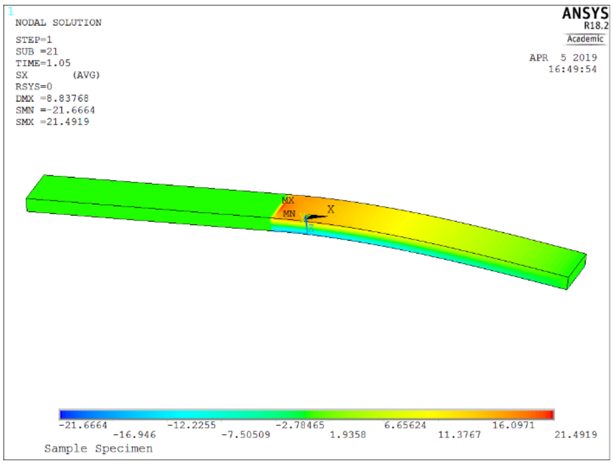
NODAL SOLUTION
STEP=1
SUB =21
TIME=1.05
SX (AVG)
RSYS=0
DMX =8.83768
SMN =-21.6664
SMX =21.4919
ANSYS
R18.2
Academic
APR 5 2019
16:49:54
MX
MN
X
-21.6664
-16.946
-12.2255
-7.50509
-2.78465
1.9358
6.65624
11.3767
16.0971
21.4919
Sample Specimen

Fig. 5-28: Results for S_x with the finest mesh used in the mesh convergence study

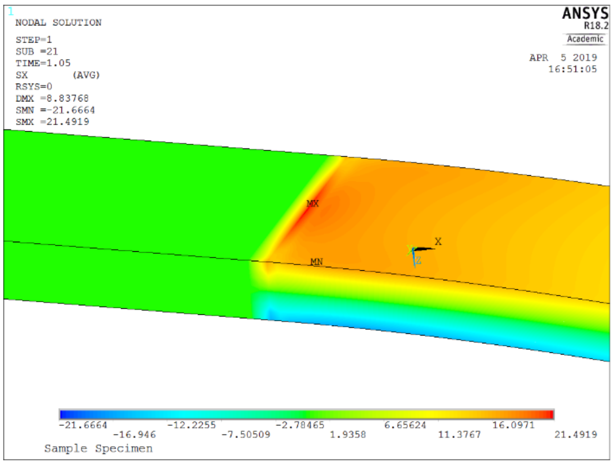
NODAL SOLUTION
STEP=1
SUB =21
TIME=1.05
SX (AVG)
RSYS=0
DMX =8.83768
SMN =-21.6664
SMX =21.4919
ANSYS
R18.2
Academic
APR 5 2019
16:51:05
MX
MN
X
-21.6664
-16.946
-12.2255
-7.50509
-2.78465
1.9358
6.65624
11.3767
16.0971
21.4919
Sample Specimen

Fig. 5-29: Enlargement of results for S_x from Fig. 5-28

The converged model corresponds to a global mesh size of 1 mm and obtains the results as in Fig. 5-30 and Fig. 5-31. The maximum bending stress S_x is 19.42 MPa whereas the reaction force at the right-hand side of the specimen where the displacement has been prescribed sums up to 6.25 N in z-direction, bringing up a reaction torque of 437.50 mNm. Comparing the stress and reaction force with the values obtained with the beam theories one can see that the FE results are higher for both variables. The stress obtained with the FE model is 2.70 % higher and the force is 6.76 % higher than the Bernoulli beam theory and 6.58 % higher than the Timoshenko beam theory. However, it needs to be considered that the beam theories are built up on simplifying hypotheses and the FE model should be able to predict the test results more precise.

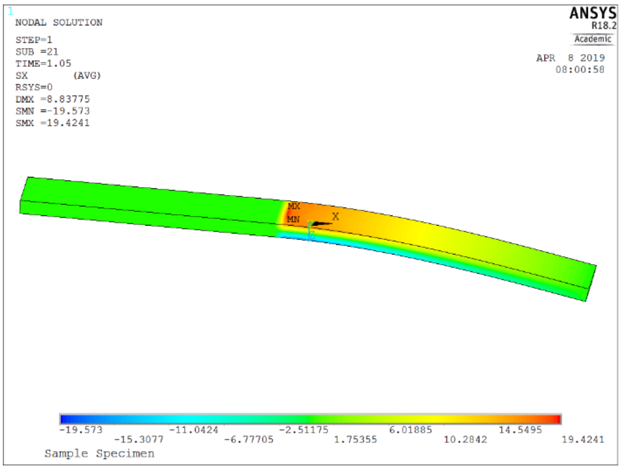
NODAL SOLUTION
STEP=1
SUB =21
TIME=1.05
SX (AVG)
RSYS=0
DMX =8.83775
SMN =-19.573
SMX =19.4241
ANSYS
R18.2
Academic
APR 8 2019
08:00:58
MX
MN
X
-19.573
-15.3077
-11.0424
-6.77705
-2.51175
1.75355
6.01885
10.2842
14.5495
19.4241
Sample Specimen

Fig. 5-30: Results for S_x with the converged mesh size of 1 mm

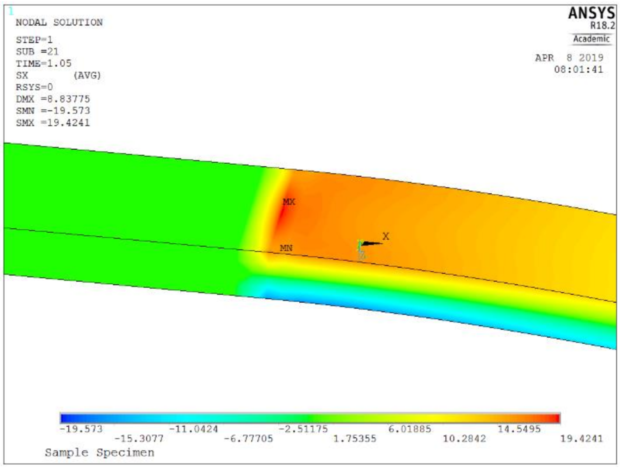
NODAL SOLUTION
STEP=1
SUB =21
TIME=1.05
SX (AVG)
RSYS=0
DMX =8.83775
SMN =-19.573
SMX =19.4241
ANSYS
R18.2
Academic
APR 8 2019
08:01:41
MX
MN
X
-19.573
-15.3077
-11.0424
-6.77705
-2.51175
1.75355
6.01885
10.2842
14.5495
19.4241
Sample Specimen

Fig. 5-31: Enlargement of results for S_x from Fig. 5-30

Tests

To be able to verify the test stand 15 individual sample specimens have been clamped with the clamping device and tested to the prescribed deflection. The deflection has been obtained by rotating the motor by 8012 increments following equation (6.11):

$$N_{incr} = \frac{N_{incr,motor}X}{50} = 8012 \tag{5.11}$$

Where:

- $N_{incr,motor}$: Number of increments of motor inherent angle sensor per turn ($N_{incr,motor}$ = 3000 [86])
- X: reduction ratio of gear unit (X = 133.530864:1 [87])

The specimens have been placed such that the start of the free length has exactly been in the center of the rotational part of the test stand (Fig. 5-32). Therefore, one could ensure that the measured torque could directly be compared with the calculated and simulated results.

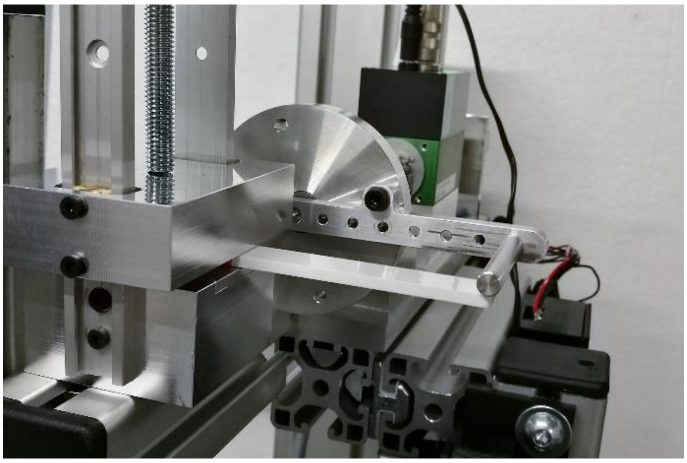

Fig. 5-32: Sample material specimen installed in test stand

The results of the experiments are shown in Fig. 5-33. One can directly see that the maximum on the mean curve of the experimental results is between the calculated values from beam theory and FE simulations. The mean maximum torque has been 419.35 mNm.

In addition, the torque increases almost linearly, which can be explained with the fact that the bending of the beam is not too large. This has been assumed for using the Euler-Bernoulli beam theory. One can see a slight hysteresis during the release of the beams. This might be because during release, even though the tests have been done at low speeds, the test mechanism precedes the specimen as the mechanism controls the movement and therefore reduces the measured torque.

Fig. 5-33 shows the standard deviation between the 16 specimens marked onto the mean curve. The standard deviation at the maximum torque is 7.25 mNm, which is 1.73 % of the maximum torque. This shows that the newly designed test stand is able to reproduce repeatable test results.

Only the reaction torque has been measured directly. However, the torque arm has been defined as being 70 mm and therefore the reaction force can be calculated as 5.99 N. By applying equation (6.8), one can also approximate the bending stress as 19.35 MPa.

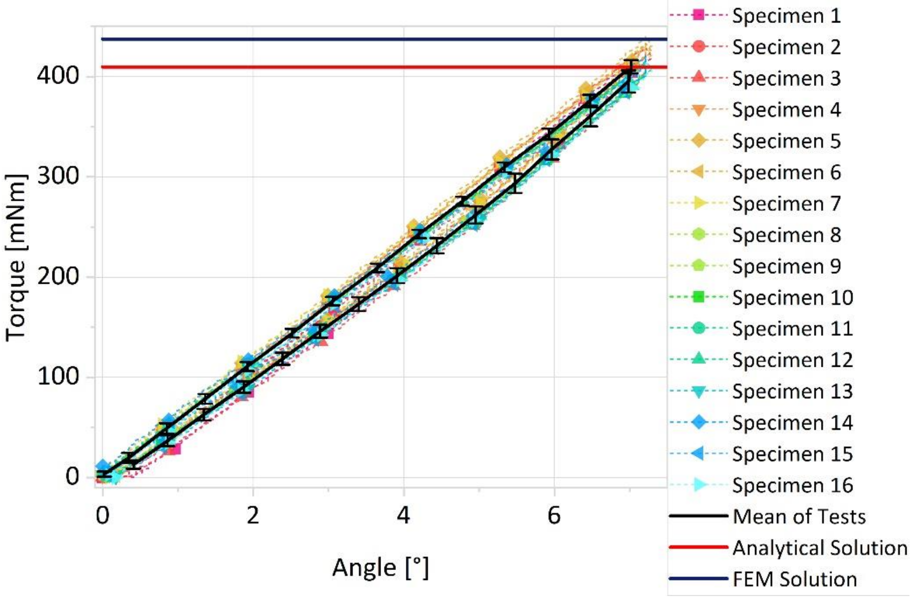

Fig. 5-33: Experimental results for bending torque of sample material specimens with theoretical level lines

Comparison

Tab. 5-5 summarizes the results for the sample material specimens. Comparing the results of the different approaches one can see, that the experimental results lay in between the theoretical beam theory and the FE simulation. All results are close to each other with a maximum difference in reaction torque of 6.33 % between the Euler-Bernoulli beam theory and the FE model. The experimental test results show a torque smaller by 4.15 % compared to the FE model. These results show that the new test stand is able to produce good quality results and could be validated by this test.

Tab. 5-5: Comparison of results for sample specimens

Result variable	**Euler-Bernoulli beam theory**	**FE model**	**Experimental test results**
Bending stress σ_b (or S_x) [MPa]	18.91	19.42	19.35
Reaction force [N]	5.8544	6.25	5.99
Reaction torque [mNm]	409.81	437.50	419.35

5.3 Results of torsion hinges

In order to compare and verify the finite element model for the investigated hinges, five different torsion hinge models have been tested (see Fig. 5-34 for the tested models & Fig. 5-35 for an overview of the complete test stand during testing). The nomenclature of the specimens is the same as for the preliminary tests and is explained again in Fig. 5-36 for simplicity.

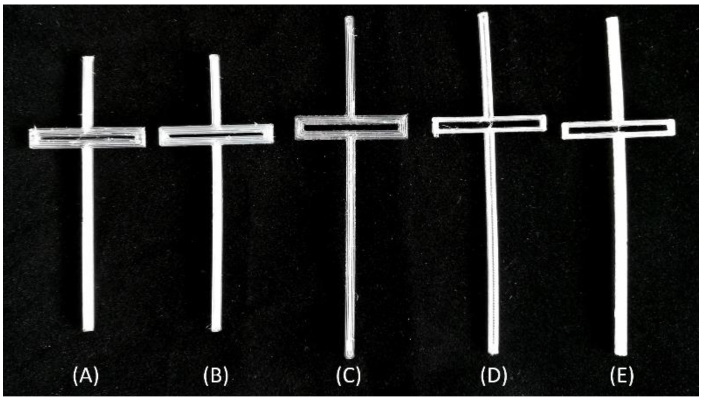

Fig. 5-34: Overview of all torsion hinge models: TH-19-5-30-2-2 Assembly Print (A), TH-19-5-30-2-2 Individual Print (B), TH-28-6-30-2-1.5 (C), TH-28-4-30-1-1.5, trod = 1.5 mm (D), TH-28-4-30-1-1.5, trod = 2 mm (E)

The model TH-19-5-30-2-2 has already been tested in the preliminary tests and has therefore been chosen to be able to compare the results. It seemed to be a good choice as its test results from the preliminary tests showed a good performance resulting in the maximum torque of all tested specimens during the preliminary tests. Model TH-19-5-30-2-2 has been tested with two different sets. For the first set, the specimens have been printed individually. The second set has been printed with the method explained in section 5.2.2, where cylinders connect specimens in order to achieve flatter and more precise parts. These two sets have been tested in order to investigate the influence of the printing quality.

To get more experimental data, the models TH-28-6-30-2-1.5 and TH-28-4-30-1-1.5 have been introduced. The difference between these two models lies in the width of the torsion rod (parameter *W* in Fig. 5-35). TH-28-6-30-2-1.5 has a width of 2 mm, which is the double of TH-28-4-30-1-1.5 in order to investigate this parameter. The last set of specimens is also a TH-28-4-30-1-1.5 with the only difference that the rods with length *L1* have a thickness of 2 mm, which is 1/3 thicker than for the standard TH-28-4-30-1-1.5 and increases the bending stiffness of the rod by a factor of 2.37. This is to investigate the influence of the rod thickness onto the overall folding behavior.

Fig. 5-35: Overview of complete test stand during testing

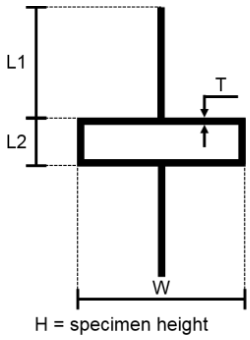

Fig. 5-36: Geometry and naming parameters for torsion hinge models. Nomenclature: TH-L1-L2-W-T-H

For each model, 15 specimens have been tested up to a bending angle of 150°. The bending angle has been constrained by the thickness of the rods. It has been defined such that the rods never touch in order to avoid falsified results due to any contact reaction.

The experimental results of all torsion hinges are summarized in Tab. 5-6.

The model TH-19-5-30-2-2 showed to be a stiff model, which is not easy to fold in the test stand. Some of the specimens did not follow the folding pattern but slipped away from the punch. Therefore, a notch has been introduced at the punch such that the specimens are not able to slip out but need to follow the folding sequence. Fig. 5-37 shows that during the loading phase the torque increases quickly until a certain point where the bending of the hinge dominates the bending of the total specimen. At this point of inflection, the torque increases less quickly which shows a lower stiffness of the specimen when a certain angle has been reached and the hinge folding dominates the overall behavior. This behavior appears during the unloading phase as well. However, this is only true for some specimens. This can be explained as some specimens still slipped out of the notch during unloading and therefore did not follow this stiffness change inflection point. This is also an explanation why the standard deviation increases largely at the end of the experiments (Fig. 5-37). However, the mentioned inflection point is less strong during the release phase than during the folding phase. This brought up the question if the printed polymer specimens need an initial bending in order to put the 3D printed material fibers in place. It might be that due to the manufacturing principle where fibers are placed in layers with the 3D printer, the polymeric chain molecules need a stretch forming and alignment of the fibers. After the specimen is bent once, the fibers are aligned and therefore, the inflection point is reduced. Therefore, and also because the final hinges need to be folded more than once as they need to withstand a certain number of tests before being used in a space structure, the same specimens have been tested again after resting for several hours.

Fig. 5-38 shows the individual test results and the mean curve with its standard deviation of all tests during the second test phase. It is obvious that no sliding occurred at all and therefore the standard deviation at the end is much smaller than for the first test sequence. In addition, the inflection point during folding is much smoother and does not exist at all during the release phase. This shows that the specimens adapted to the folding and some deformations occurred even-though they are not observable as the specimens return to their initial flat state after a certain time. By comparing the maximum values of the mean torque for both test runs one can see that the maximum torque diminished from 56.28 mNm to 55.30 mNm from the first to the second test run. This is a reduction of 1.77%. On the other hand, the standard deviation at the most important point where the maximum torque has been measured diminished from 5.01 mNm to 3.87 mNm and the average standard deviation during the whole experiment was reduced from 2.03 mNm to 1.12 mNm. As the reduction in torque is not too large but the repeatability increases drastically all further specimens will also be tested in two test sequences and the results will be compared again.

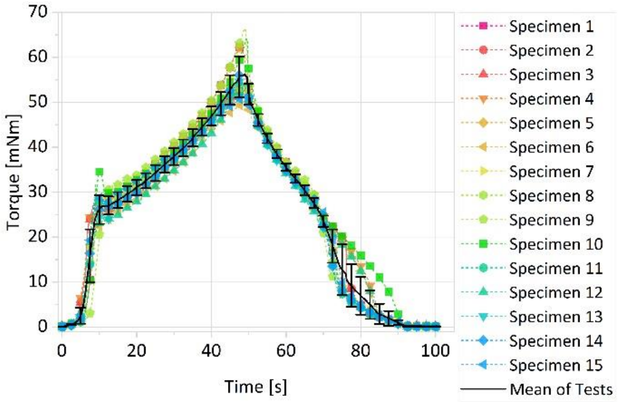

Fig. 5-37: Experimental results for bending torque of TH-19-5-30-2-2 (Assembly Print Configuration) (Experiment 1)

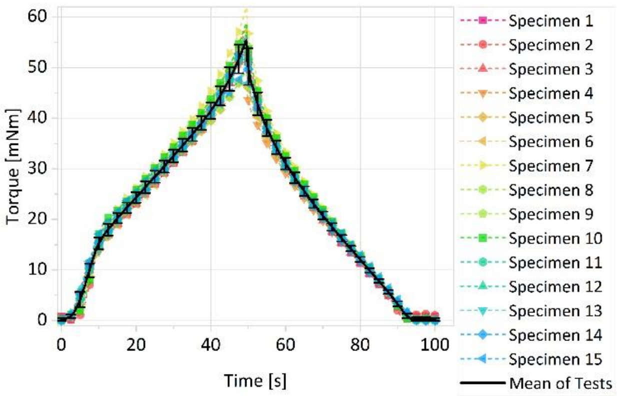

Fig. 5-38: Experimental results for bending torque of TH-19-5-30-2-2 (Assembly Print Configuration) (Experiment 2)

A visco-elastic behavior has been observed during the tests. It can be seen in both Fig. 5-37 and Fig. 5-38 that the torque is constantly zero at the end of the tests. This shows a deformation. The specimens are not directly fully deploying to their flat state and therefore no load is acting on the torque sensor indicating the zero torque. Fig. 5-39 shows the specimen's deformation after deployment where the punch is back at the initial location without being in contact with the rod of the hinge. However, after only a few minutes, the specimens went back to their initial flat state without any external loads (Fig. 5-40). This shows that the deformation is not purely plastic but merely a visco-elastic behavior which appears in most polymers. Therefore, the waiting time should be large enough in order to alleviate these possible visco-elastic strains before testing the specimens again. However, it must be noted that the resulting short-time angle of the deformed specimen is higher after the first test than after the second test (see Tab. 5-6). This is astonishing, as it could be assumed that deforming the specimens induces small remaining strains, which should be responsible for an even larger deformation at the end of the second test run. However, apparently the specimens could fully recover and an initial bending even helped for a better deployment in the subsequent test run.

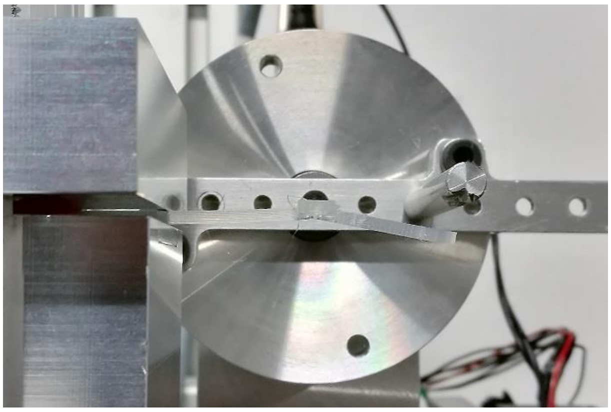

Fig. 5-39: Visco-elastic deformation of specimen

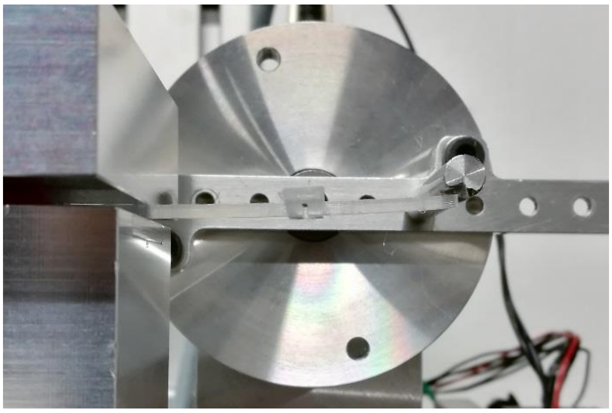

Fig. 5-40: No deformation observable after leaving the specimen for 2 minutes

Like the assembly print configuration of the TH-19-5-30-2-2 model, the individual print configuration showed problems with sliding even by using the notch at the punch. Here, also the second experiments run did not improve as much as for the assembly print configuration (see Tab. 5-6). In addition, the inflection point did not change as drastically as for the assembly print configuration. In addition, some specimens still slided away from the notch during the release phase which can be seen in the large standard deviation at the end of the experiment in Fig. 5-42. This might show that the waiting time in between the two tests should not be too long (here it was more than 10 hours) or otherwise the material behaves as if it would almost have no pre-bending at all. This assumption is based on the findings of the first test. During the first tests, all specimens have been folded and deployed three times. Here, one can see from Fig. 5-41 that the standard deviation and the curvature at inflection point (red circle in Fig. 5-41) decrease as expected from the previous subsection. In addition, one can see that the maximum torque decreases slightly while folding several times. The maximum torques decrease from 47.58 mNm to 44.94 mNm to 43.22 mNm and the standard deviation at the maximum torque increments decrease steadily from 4.72 mNm to 2.97 mNm to 2.35 mNm. This shows a fast stress relaxation in the material that appears during the experiments. This finding is important for future studies of the hinges where also long-term folding behavior needs to be studied.

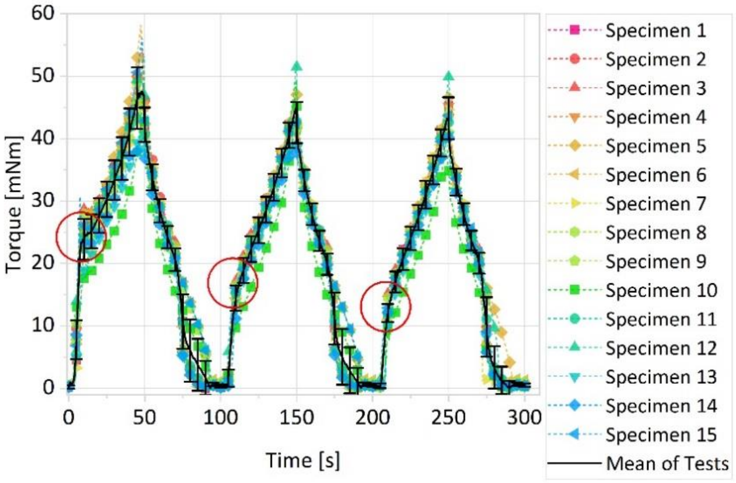

Fig. 5-41: Experimental results for bending torque of TH-19-5-30-2-2 (Individual Print Configuration) (Experiment 1)

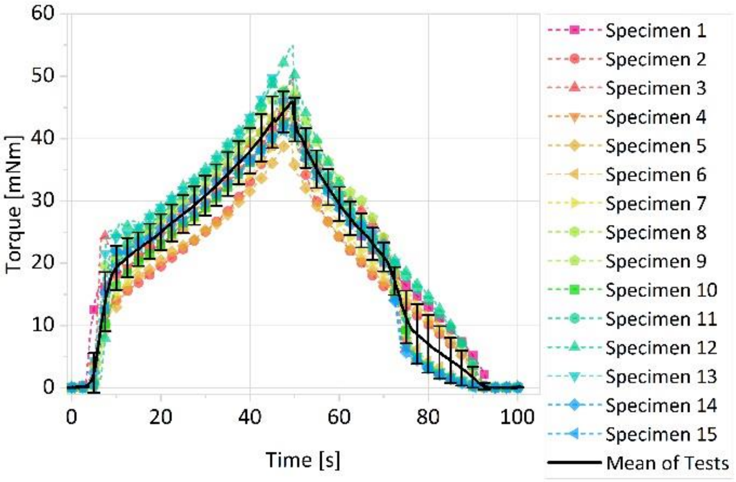

Fig. 5-42: Experimental results for bending torque of TH-19-5-30-2-2 (Individual Print Configuration) (Experiment 2)

The model TH-28-6-30-2-1.5 is less stiff than the TH-19-5-30-2-2 model because it is thinner. Therefore, a smaller torque could be expected as shown in Tab. 5-6. In addition, the standard deviation could be decreased with the second experimental run, however, already the first experiments showed a satisfying standard deviation. It can also be seen in Fig. 5-43 that no sliding occurred. This might be due to the lower stiffness of this model which is favorable for the folding in the test stand. The same factor might also explain why the inflection point is almost non-existent for both the folding and the deploying phase.

For all tests, the measured torque falls quickly during the initial phase of the deployment. This has not been observed for any of the TH-19-5-30-2-2 models. Therefore, it might be that more compliant models need a short time to adapt to the release phase, and the punch moved too fast, even though the tests have been done with a low rotational speed. The small increase after the fall also appears for all specimens and might show that the specimens caught up with the punch and push fully against it. Another explication for the quick fall might be that during the short time in between the end of the folding and the start of the deployment, the stress relaxation already influenced the measured torque.

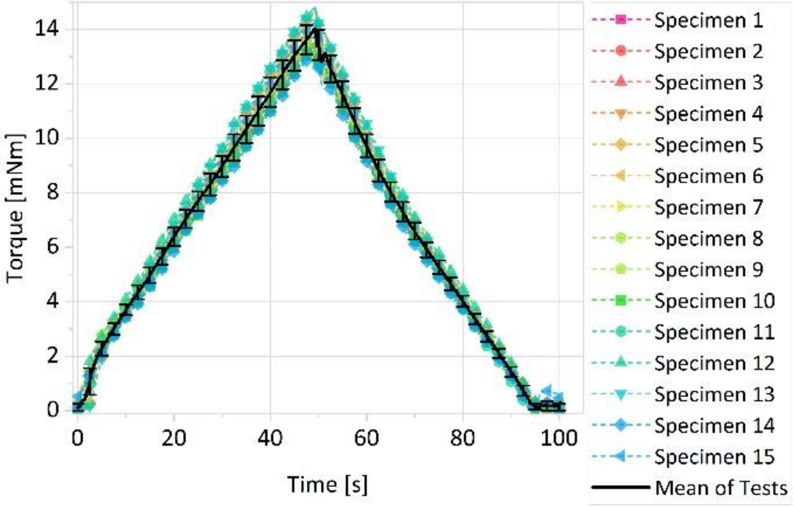

Fig. 5-43: Experimental results for bending torque of TH-28-6-2-1.5 (Experiment 1)

The model TH-28-4-30-1-1.5 with rod thickness t_{rod} = 1.5 mm has the same thickness on all rods. Due to the smaller width of the torsion rods, it is even more compliant than the models above and reaches less opening torque. The experimental results show a similar behavior as for the model TH-28-6-30-2-1.5, including the quick fall at the beginning of the unloading phase and the almost non-existence of the inflection point. An interesting point for this model is that the mean maximum torque is higher for the second test run than for the first. However, the difference is small and within the range of the standard deviation. Still, this shows that the specimens could fully recover from the visco-elastic strains acquired during the first test sequence.

In contradiction to this, one can see that the remaining short-time angle after the deformation is larger for the second test run. Therefore, one might assume that a permanent deformation has occurred. This model is the only model where an increase of the remaining short-time angle could be observed. However, the increase is very small and within the range of the standard deviation. This means that not too many conclusions should be drawn from this measure as all specimens went back to the initial state after only a few minutes.

Compared to the model TH-28-4-30-1-1.5 with rod thickness t_{rod} = 1.5 mm, the same model with rod thickness t_{rod} = 2 mm has an increased rod stiffness and therefore a higher torque could be expected. The average maximum torque of the two test runs is 1.62 times higher than the same value for the previous model with an overall thickness of 1.5 mm. However, increasing the rod thickness from 1.5 mm to 2.0 mm increased the rod's stiffness 2.37 times as the thickness influences the bending stiffness with its third power. This shows that stiffening the rods could increase the reaction torque. However, the stiffness increase of the individual rods has been much higher than the overall increase in stiffness.

Tab. 5-6: Experimental results of torsion hinge models

Model	Test run	Maximum Torque [mNm]	Mean Standard deviation [mNm]	Std. dev. at max. torque [mNm]	Ratio std. dev. at max. torque / max torque [%]	Short-time angle of deformation [°]
TH-19-5-30-2-2: Assembly Print Configuration	Test 1	56.28	2.03	5.01	8.90	21.46
	Test 2	55.30	1.12	3.87	7.00	18.67
	Relative difference	-1.74 %	-44.83 %	-22.75 %	-21.35 %	-13.00 %
TH-19-5-30-2-2: Individual Print Configuration	Test 1	47.58	2.87	4.72	9.92	24.32
	Test 2	45.87	2.86	3.91	8.52	18.06
	Relative difference	-3.59 %	-0.35 %	-17.51 %	-14.11 %	-25.74 %
TH-28-6-30-2-1.5	Test 1	14.01	0.34	0.55	3.93	13.96
	Test 2	13.91	0.24	0.42	3.02	12.80
	Relative difference	-0.71 %	-29.41 %	-23.64 %	-23.15 %	-8.31 %
TH-28-4-30-1-1.5, t_{rod} = 1.5 mm	Test 1	5.96	0.20	0.34	5.70 %	16.12
	Test 2	6.17	0.19	0.26	4.21 %	16.51
	Relative difference	3.52 %	-5.00%	-23.53 %	-26.14 %	1.85 %
TH-28-4-30-1-1.5, t_{rod} = 2 mm	Test 1	9.45	0.26	0.30	3.17	16.23
	Test 2	10.27	0.18	0.26	2.53	15.46
	Relative difference	8.68 %	-30.77 %	-13.33 %	-20.19 %	-4.74 %

5.4 Results of optimized hinge models

The resulting designs from the parameter optimization in section 3.3.4 have been tested on the test stand. As the models have been optimized with the found material factor from the experiments and FE-simulations of the torsion hinges, it is expected that the test results should not be too far apart from the FE-simulations, except if the factor would be highly dependent on the geometry. The experimental results for all optimized hinges are presented in this section.

As explained in section 3.3.4, two different models of the *Z-shape* design have been found with the optimization, a large but stiff model and a small, compliant model. Both models have been tested and compared with their corresponding FE model. The results are shown in Tab. 5-7.

Tab. 5-7: Experimental results of all optimized models

Model	**Maximum Torque [mNm]**	**Mean Standard deviation [mNm]**	**Std. dev. at max. torque [mNm]**	**Ratio std. dev. at max. torque / max torque [%]**	**Short-time angle of deformation [°]**
Z-shape thick	106.38	4.41	6.54	6.15	17.19
Z-shape thin	3.35	0.39	0.46	13.71	27.70
Oval-shape straight thick	153.07	3.97	11.05	7.22	17.58
Oval-shape straight thin	15.28	0.43	1.04	6.81	24.29
Oval-shape tilted	8.68	0.36	0.83	9.56	28.10
Oval-shape spring	5.41	0.37	0.83	15.34	5.81

The thick model could only be bent up to an angle of 110°. For a higher angle, the two rods would have touched due to their thickness. In addition, due to its size, the fixation as well as the punch rod needed to be adapted in order to get appropriate constraints. Fig. 5-44 shows a specimen in the test stand with the fixation adaptations (green parts).

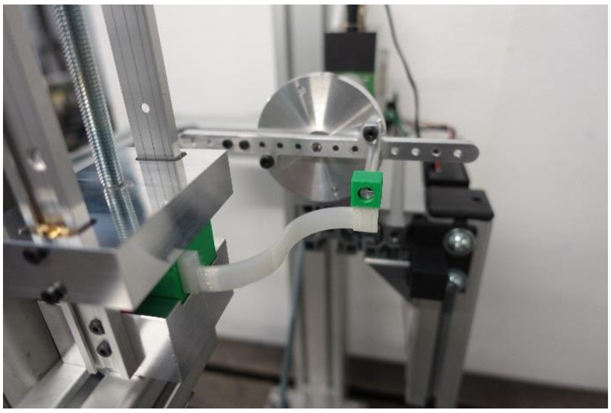

Fig. 5-44: Thick *Z-shape* specimen in test stand with adapted fixation (green parts)

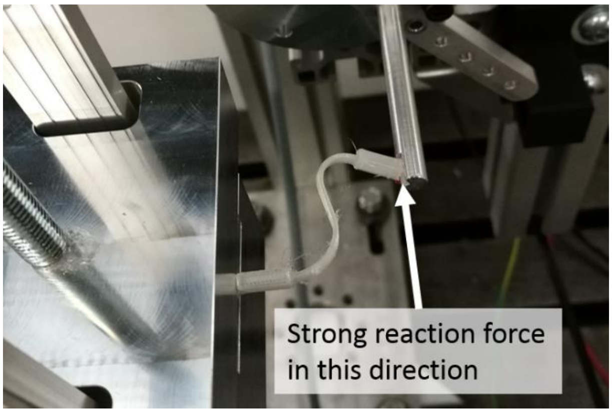

Fig. 5-45: Thin *Z-shape* specimen during testing

The thin *Z-shape* models have been tested up to an angle of 125°. Here, it is important to notice a strong reaction force in the direction of the punch rod (see Fig. 5-45). It is due to the bending of the curves of the specimen. These parts would naturally prefer to straighten up instead of being bent, which causes a strong force in the axis of the white arrow in Fig. 5-45. This reaction force could not be measured because it was not in the direction of the torque sensor but it could be seen during the tests that the specimens wanted to slide out of the small pocket in the punch rod.

It is interesting to compare the two models regarding their short time angle of deformation. This is the angle at which the punch rod does not touch the specimens anymore during the release phase. This happens because the specimens show a deformation directly after the end of the test. Few minutes later, the specimens turned back to their initial flat state. However, comparing the angle for the thick and the thin model, the thin model shows a much larger deformation directly after the test, even though they should have a very similar stress according to the FE results.

As for the *Z-shape* model, the *oval-shape straight* model consists of two solutions. They have been tested with the same maximum angles as the two *Z-shape* models (Fig. 5-46 & Fig. 5-47). The thin specimens where prone to slide out of the pocket in the punch rod at the end of the folding process due to large circumferential reaction forces. Therefore, the fixation at the punch rod has been adapted as in Fig. 5-47. A block is put onto the punch rod, which clamps the specimen and prevents it from sliding out.

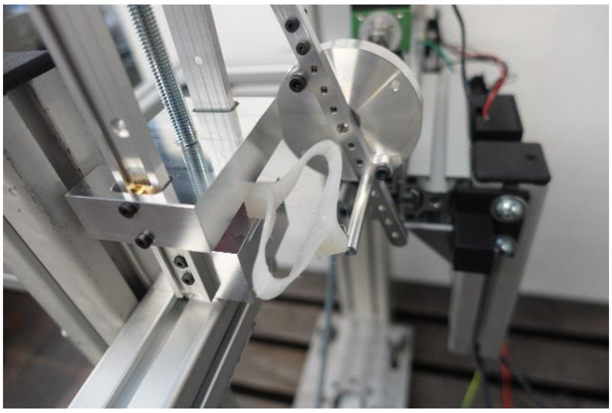

Fig. 5-46: Thick *oval-shape straight* specimen during test

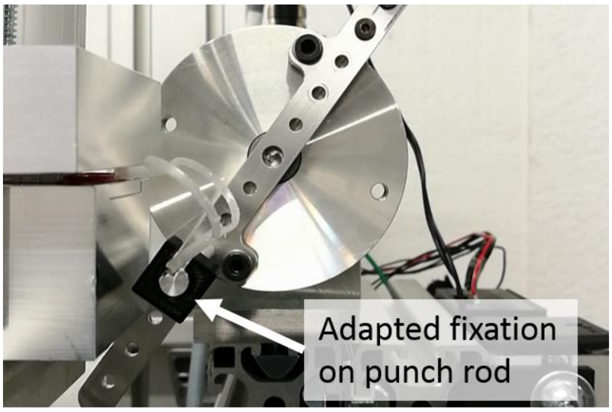

Fig. 5-47: Thin *oval-shape straight* specimen during test with adapted punch rod fixation (black)

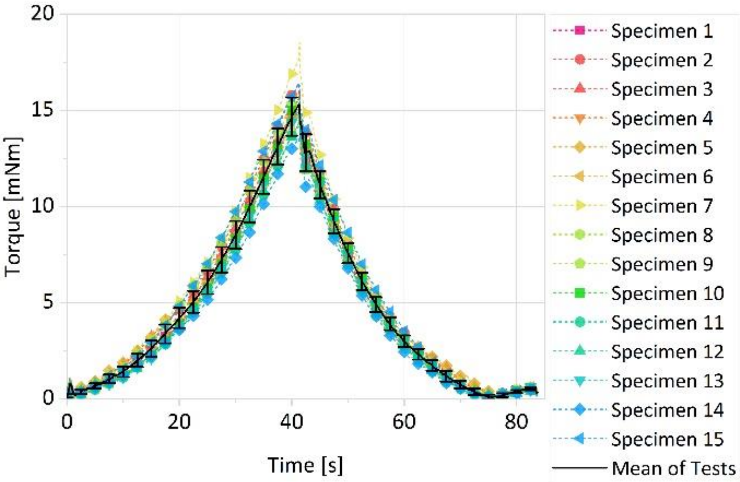

Fig. 5-48: Experimental results for thin o*val-shape straight* specimen

Again, as for the *Z-shape* model, the thinner model shows a larger deformation. Therefore, one could conclude, that the reaction force influences the final deformation directly after the end of the test while comparing the same design models. Fig. 5-48 shows the experimental data for the thin *oval-shape straight* model. It is important to see, that the inflection point seen for the stiff torsion hinge models does not appear at all and the curve is smooth during bending as well as in the release phase. This might be because for the optimized models, the hinge itself is larger and not as concentrated on a small area as for the torsion hinges. Hence, there is not such a sharp change in stiffness but a smooth transition from overall specimen bending to hinge bending. All optimized models show similar curves. For simplicity, only the curve of the thin *oval-shape straight* model is shown.

The *oval-shape tilted* model has been tested up to an angle of 150°. During testing one can see that the two round parts deform out of plane, leading to a torsion in these parts which again reliefs the stresses in the specimens. In addition, the whole specimen slightly bends perpendicularly to the prescribed bending with the same results as the out of plane deformation.

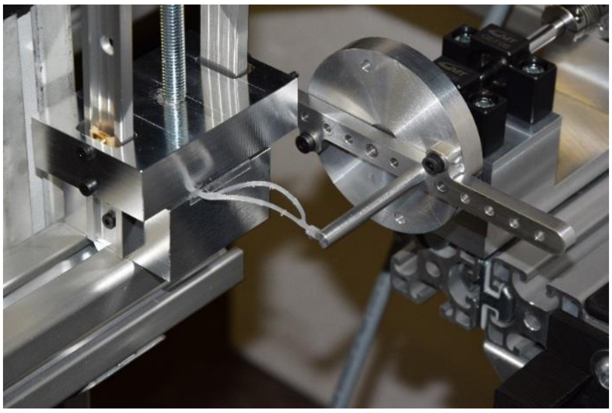

Fig. 5-49: *Oval-shape tilted* specimen in test stand prepared to start bending

The bending axis of the spring model is perpendicular to the bending axis of all other models. However, when turning the specimens, they could be tested in the same test stand.

Comparing the experimental data with the FE simulations one can observe, that the FE model predicts a larger reaction torque by 29.2 %. This can be explained with the observations made during the experiments. In the FE model, the bending occurs purely in the bending plane. During the experiments, however, the two round parts shift and the specimens bend out of plane, which induces a decrease in reaction torque in the bending plane. One can see in Fig. 5-51 that the specimen bends strongly and so does the rod that is in contact with the punch twisted. Therefore, the reaction torque is decreased. Two approaches might improve this test. First, a clamping at the punch would reduce the twist. Second, a more precise manufacturing process might produce more exact specimens where the two round parts would not shift anymore.

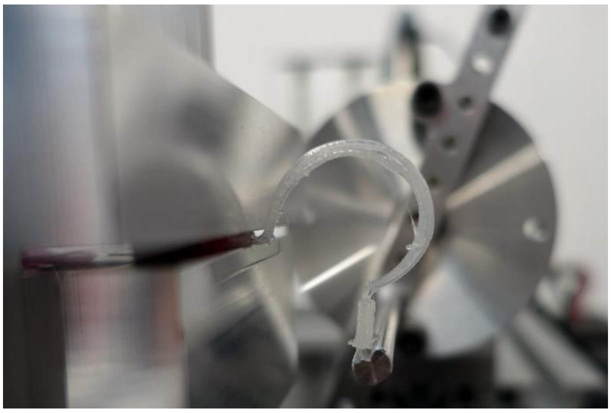

Fig. 5-50: *Oval-shape spring* specimen during test (side view)

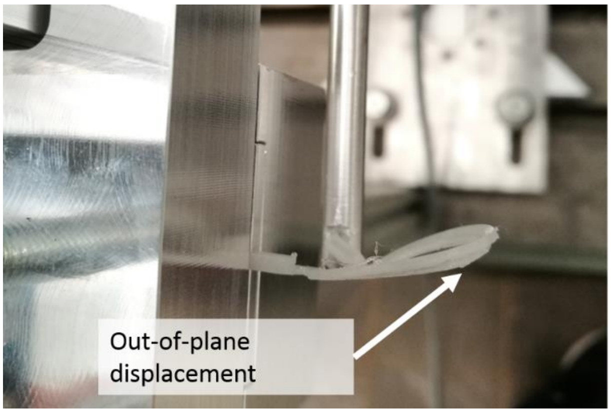

Fig. 5-51: Out-of-plane displacement reducing reaction torque in bending plane (top view)

5.5 Results of hinge models directly printed on a foil

The final goal of this subproject of the DLR-NASA joint project is to be able to directly print the hinges onto a membrane. Therefore, first experiments have been made moving towards this direction. The *oval-shape tilted* model has been chosen because it showed a good performance during the tests and has the best reaction force to weight ratio, except for the spring model, which works out of plane. The tilted model has been printed directly onto a foil. The chosen foil was a standard MAKROFOL® DE 1-4 000000 produced by Covestro. It is a translucent extrusion foil based on Makrolon, a polycarbonate plastic. This foil has been chosen because it was quickly available and because for these initial tests, the material performance of the foil itself has been secondary. The material properties of the foil are listed in Tab. 5-8.

Tab. 5-8: Material properties of Makrofol® DE 1-4 000000 [93]

Material property	**Symbol**	**Value**
Foil thickness	t	175 µm
Young’s modulus	E	2200 MPa
Poisson’s ratio	v	0.37
Density	ρ	1.2 g/cm^3
Maximum yield stress	$R_{p0.2}$	70 MPa
Coefficient of thermal expansion	α	70 10^{-6}/K
Shrink (1h @ 130°C)	S	<0.4 %

A good adhesion between the structure and the membrane is reached when pulling out of plane. However, during bending where the foil is inside, a peel off occurred and the specimens detached from the foil. Experience shows, that the peel off is always the biggest issue while bonding two materials. Here, no glue or adhesive has been used but the high temperature during the print welds the two materials together. This welding might be improved by using a higher temperature such that the material of the foil locally mingles with the printing material. Earlier research has shown that a robust printing on a polycarbonate film is possible. However, a foil with a different melting point and a much higher printing temperature has been used [3]. Unfortunately, this could not be tested due to material and especially printer limitations. Another method was to apply heat to the specimens from their backside (using a regular iron). To do so, the specimens have been laid flat on the printed side and then they have been ironed for a while. It could be observed that the foil got hot, as some small wrinkles have been introduced. The bonding seemed to be better after ironing, however, it was not perfect yet and peel off could still occur. In addition, a thinner foil might improve the bonding quality due to its own decreased stiffness. In addition, ultrasonic welding might be a possibility to increase the bonding strength. However, this would not be cost effective. Despite this bonding issue, the specimens could still be tested in the test stand when bending with the foil outside and the printed hinges inside.

The comparably large thickness of the foil added an important stiffness to the whole specimen. In addition, the bonding has been done on the whole hinge, stiffening the hinge even more and preventing the specimens from the out of plane movement of the central part. The stiffness has been decreased by introducing cuts at the locations where the rods and the hinge are connected. This has been done in order to release the stress in the bonding, such that the bonding has been strong enough to endure the experiments without detaching the foil and the hinge.

A maximum torque, which was higher than 3.5 times the maximum torque of the hinge solely, has been measured during the experiments. In addition, a deformation of the specimens occurred which did not retreat even after letting the specimens sit for several hours. This is also shown in the maximum stress found in the FE simulation. The maximum von Mises stress increased largely and showed to be more than 30% higher than for the independent specimens. A too high stress would not be favorable in any application. However, the permanent deformation might be reduced by using a thinner foil or by using even bigger cuts or cutouts of the foil. This needs to be investigated in future work.

Tab. 5-9: Experimental results of optimized model: Tilted printed on foil

Variable	Experimental Result
Maximum Torque [mNm]	30.92
Mean Standard deviation [mNm]	0.65
Std. dev. at max. torque	0.71
Ratio std. dev. at max. torque / max torque [%]	2.30
Short-time angle of deformation [°]	35.95

Tab. 5-10: Results for FE simulations (150° bending) of optimized model: Tilted printed on foil

Variable	Symbol	Value	Unit
Maximum von Mises stress on foil	$\sigma_{vM,max,foil}$	52.31	[MPa]
Averaged maximum von Mises stress around the maximum on foil	$\sigma_{vM,avg.max,foil}$	47.15	[MPa]
Maximum von Mises stress on hinge	$\sigma_{vM,max,hinge}$	43.37	[MPa]
Averaged maximum von Mises stress around the maximum on hinge	$\sigma_{vM,avg.max,hinge}$	36.75	[MPa]
Reaction force when fully bent	$F_{react,final}$	1.28	[N]
Reaction torque when fully bent	$M_{react,final}$	33.56	[mNm]
Total hinge model volume	V_{tot}	133.79	[mm^3]
Total hinge model mass	m_{tot}	147.17	[mg]

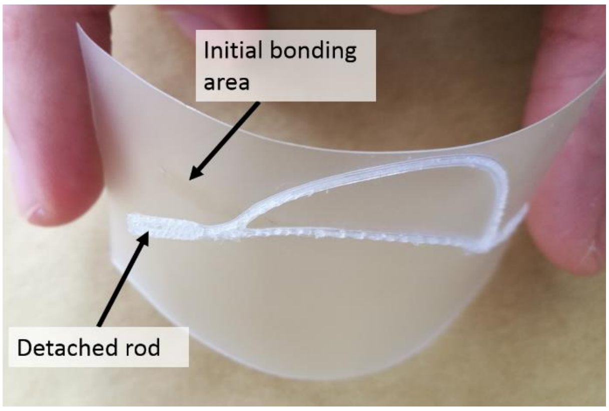

Fig. 5-52: Peel off during bending with foil inside

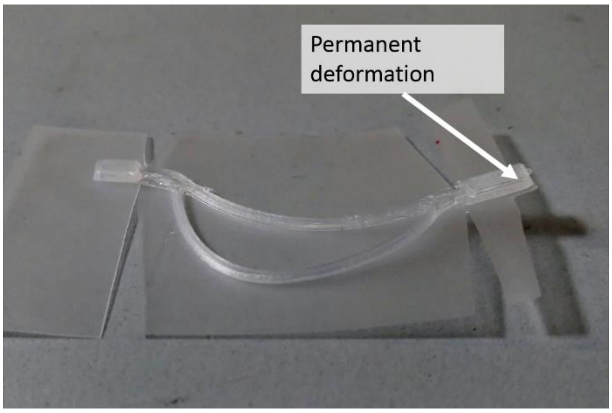

Fig. 5-53: Permanent deformation of *oval-shape tilted* model printed onto foil after being folded in test stand

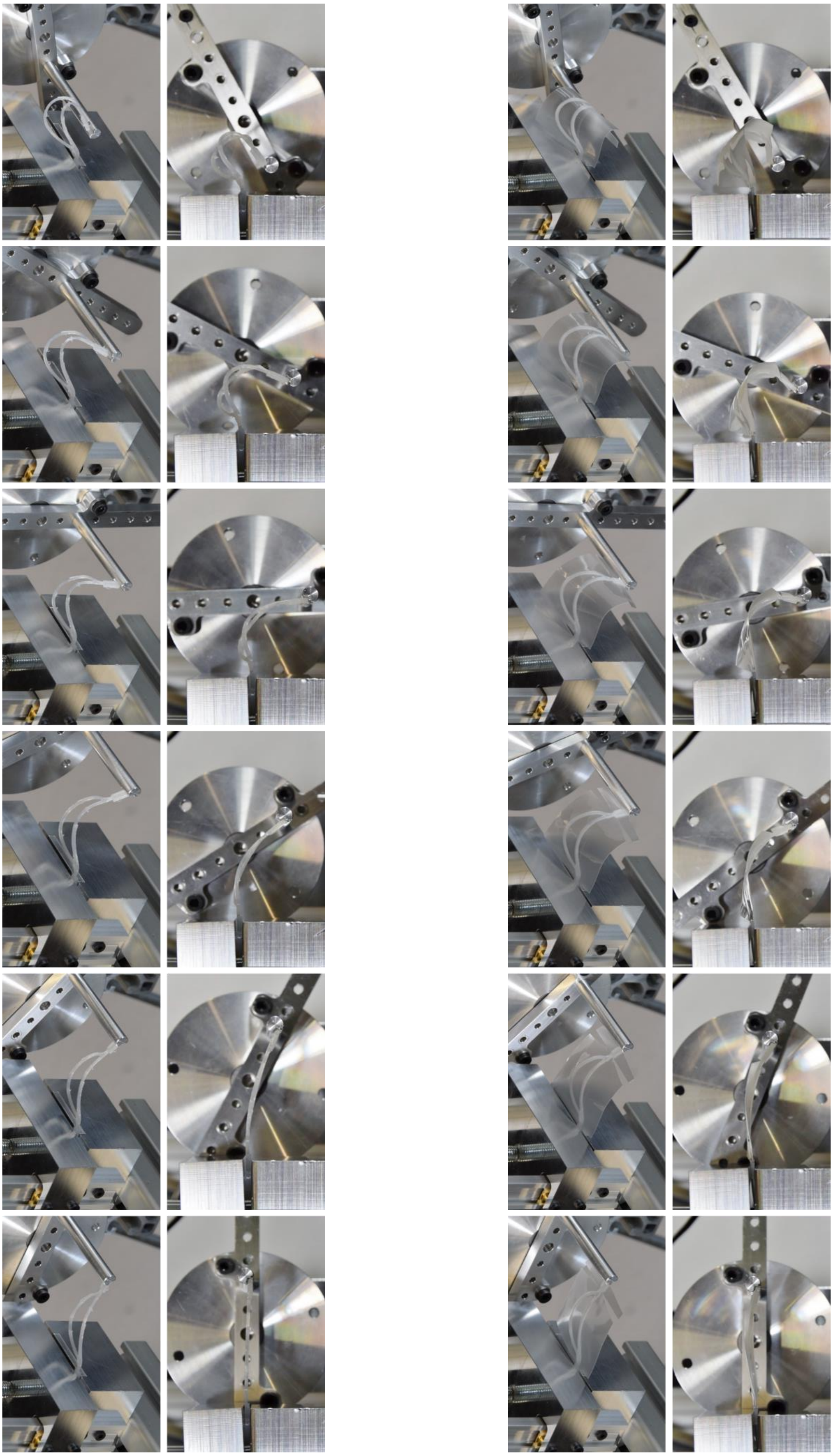

(A) (B)

Fig. 5-54: Testing of the model *oval-shape tilted* solely (A) and printed on a foil (B); one image every ten seconds during folding

5.5.1 Some thoughts on the long-time behavior of polymer hinges

Depending on the final application of the hinges, they will be stowed for a time period between several days and many years. Therefore, a long-time behavior of the hinges would be needed. This was not part of this thesis, however, a first observation has been made. A thin *oval-shape straight* specimen has been folded to an angle of 125° and then kept in this situation for two minutes. One could observe a drastic decrease in reaction torque during this time. However, the reaction torque behaved similar to a decreasing exponential curve:

$$M_{react} = x_1 + x_2 * \exp(x_3 * t) \tag{5.12}$$

The data of the folded specimen could be fitted onto function (6.12) with a root mean squared error of 0.080, which is less than 2.80 % of the difference between the largest, and the lowest data. Extrapolating this fitted function to a longer time, a limit value could be found. Comparing this limit value with the starting maximum torque when the specimen gets folded, the limit value is 25% lower than the starting torque and therefore the specimens have a considerable decrease in opening strength. However, two minutes of folding would not be enough to predict a very long time behavior. In addition, it is assumed that this behavior is highly dependent on the material and as the material will be changed for the final application it needs to be investigated more closely when more information about the application and the used materials are available.

6 Comparison and analysis

This section compares the results of the FE-simulations and the experimental data. As the FE model is based on a linear elastic isotropic material, it is clear that the results of the FE model will not directly match the results from the experiments as the specimens are manufactured with FDM. Therefore, it cannot be assumed that the specimens are isotropic as the FDM process adds the filament layer by layer and the material properties of the specimens depend strongly on the printing quality and the inner layer adhesion. In addition, the used material was Nylon (polyamide, PA), whose material properties are highly dependent on its moisture content, where the humidity decreases the mechanical properties [94]. Even though, the filament has been stored in a dry-box, the material was exposed to the environment during printing, testing and storage. However, for this thesis, it was important to see if a certain factor could be found matching the FE model with the experimental results. This will be discussed in the next subsections while comparing simulation results with experimental data for all tested specimen designs.

6.1 Torsion Hinge Models

The only value that can directly be compared from both the FE model and the test results is the reaction torque. Therefore, a direct comparison of the maximum reaction torque is shown in Tab. 6-1. Two test runs have been done with every specimen. It has been shown that the specimens fully recovered in between the two tests. Therefore, the average of the maximum reaction torque will be used subsequently. By taking the ratio of the test results and the results from the FE simulations one can see that the ratios are closely related. The mean of the ratios gives 0.465 with a standard deviation of 0.017 which is only 3.66 % of the mean ratio. Therefore, the FE model behaves stiffer by a factor of $\frac{1}{0.465} = 2.15$. Various mechanical material tests with 3D printed PLA have been done in literature [95, 96]. Specimens have been tested in tensile tests by investigating the behavior of the specimens' Young's modulus depending on the printing direction. A large difference in Young's modulus has been measured. Calculating the ratio between the lowest and the highest Young's modulus brings up a factor of 0.80 [95] and 0.91 [96]. In addition, comparing the printed parts' flexural modulus with the highest Young's modulus gives a factor of 0.76 [96]. Therefore, it has been shown that large variations in stiffness appear with 3D printed parts depending on their manufacturing process. Hence, regarding the FDM process on such small specimens, as well as the influence of the environment on the used material, the factor found in the experiments seems to be reasonable, especially because the standard deviation in between the different tests is very small.

Therefore, the stiffness of the FE model needs to be decreased. As a linear material model has been chosen, this has been done by multiplying the material's Young's modulus with the factor 0.465. Tab. 6-2 shows the maximum von Mises stress for the tested torsion hinge models and the averaged von Mises stress around the maximum after having adapted the material's Young's modulus. Fig. 6-1 shows the stress distribution for the model TH-28-6-30-2-1.5 with the initial Young's modulus from the material datasheet and Fig. 6-2 shows the same model with the adapted modulus including the experimental material factor. The maximum stress decreased and the stress distribution got smoother, showing less stress singularities. Comparing the obtained stresses with the filament materials yield stress of 31 Mpa, one can see that only the TH-19-5-30-2-2 models surpass this yield stress. However, this is also the model with the highest stress singularities and the averaged von Mises stress around the maximum stress is only surpassed by 14 %. In addition, the experiments showed that the specimens all had a similar remaining short-time bending angle directly after the test and they returned to their initial state after only a few minutes. Therefore, as the material is not a pure elastic material but more a visco-elastic material, the material yield stress of 31 MPa can be retained and with a safety factor of 1.55, 20 MPa has been chosen as being the maximum allowable stress for the optimization of the new hinge models. 20 MPa has been chosen to ensure that no plastic deformation will occur at all. In addition, less stress singularities have been expected for the optimized rounder models. This means that the material yield stress should not be exceeded at all.

Tab. 6-1: Test & FE results of the reaction torque for all tested torsion hinge models

Model	Test Results [mNm]	FE Results [mNm]	Ratio: Test / FEM
TH-19-5-30-2-2: Assembly Print Configuration	55.79	120.44	0.463
TH-19-5-30-2-2: Individual Print Configuration	46.73	103.44	0.452
TH-28-6-30-2-1.5	13.96	29.64	0.471
TH-28-4-30-1-1.5, t_{rod} = 1.5 mm	6.07	13.59	0.447
TH-28-4-30-1-1.5, t_{rod} = 2 mm	9.86	20.13	0.490
Mean ratio			0.465

Tab. 6-2: Maximum von Mises stress for all tested torsion hinge models with adapted stiffness

Model	Maximum von Mises stress [MPa]	Averaged von Mises stress around the maximum [MPa]
TH-19-5-30-2-2: Assembly Print Configuration	44.71	35.42
TH-19-5-30-2-2: Individual Print Configuration	39.06	32.72
TH-28-6-30-2-1.5	27.74	24.12
TH-28-4-30-1-1.5, t_{rod} = 1.5 mm	15.82	12.57
TH-28-4-30-1-1.5, t_{rod} = 2 mm	19.09	17.07

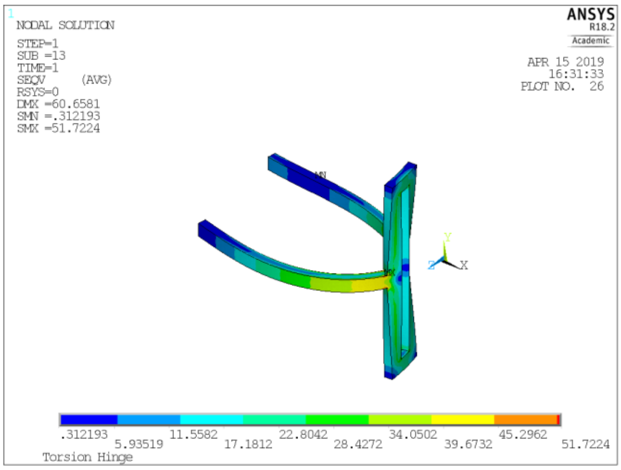
NODAL SOLUTION
STEP=1
SUB =13
TIME=1
SEQV (AVG)
RSYS=0
DMX =60.6581
SMN =.312193
SMX =51.7224
ANSYS
R18.2
Academic
APR 15 2019
16:31:33
PLOT NO. 26
MN
MX
Y
Z
X
.312193
5.93519
11.5582
17.1812
22.8042
28.4272
34.0502
39.6732
45.2962
51.7224
Torsion Hinge

Fig. 6-1: Von Mises stress for TH-28-6-30-2-1.5 with Young's modulus from datasheet

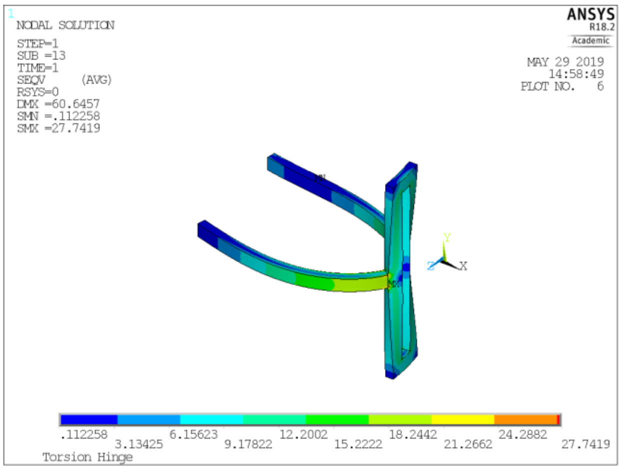
NODAL SOLUTION
STEP=1
SUB =13
TIME=1
SEQV (AVG)
RSYS=0
DMX =60.6457
SMN =.112258
SMX =27.7419
ANSYS
R18.2
Academic
MAY 29 2019
14:58:49
PLOT NO. 6
MN
MX
Y
Z
X
.112258
3.13425
6.15623
9.17822
12.2002
15.2222
18.2442
21.2662
24.2882
27.7419
Torsion Hinge

Fig. 6-2: Von Mises stress for TH-28-6-30-2-1.5 with adapted Young's modulus

Regarding the behavior of the torque during the folding procedure, Fig. 6-3 and Fig. 6-4 show that the torque does not behave exactly the same for the FE model with the adapted Young's modulus and the test results. For the model TH-28-4-30-1-1.5, the results of the two experimental test runs are very close. It can be seen that the test results and the results from the FE simulation are very close at the end of the folding procedure and all the lines are following each other closely. The only difference is the beginning of the folding procedure. The FE simulation behave similar to an exponential function while the tests resemble an opposing logarithmic function. The behavior of the test results has been explained with the fact that the whole specimen wants to bend initially until a certain load level is reached where the lower stiffness of the hinge induces that the specimen bends in its center and therefore loses stiffness and with it less torque is needed for the same folding increment. On the other hand, during the FE simulation the specimens behave ideally and bend directly from the beginning on. This means that without the hindering overall specimen bending only a small torque needs to be applied to the specimen in order to be able to fold the specimens for small angles.

The results of the model TH-19-5-30-2-2 behave different. First of all, the first test run strongly shows the already discussed inflection point whereas it is almost non-existent for the second test run results. Here, the FE simulation follows the test results in the beginning of the folding process and temporarily reaches a higher torque level during intermediate folding angles. At the end of the folding process all values are close to each other again. To conclude this subject, one can state that the final torques of the tests and the FE model with an adapted Young’s modulus are close to each other. During the folding process, differences in the load path appear. However, the differences are not the same for different models. This means that stiffness changes during folding cannot be predicted directly with the FE model.

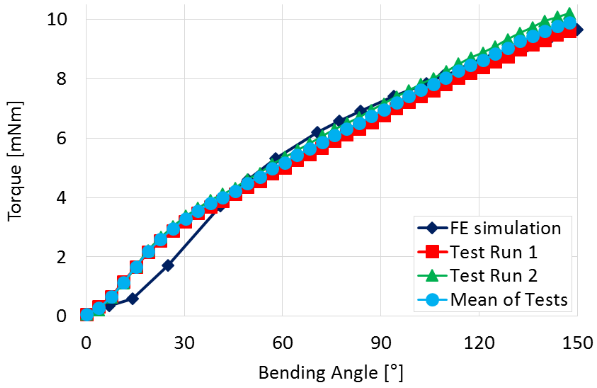

Fig. 6-3: Comparison of Torque during folding for TH-28-4-30-1-1.5 (t_{rod} = 2.0 mm)

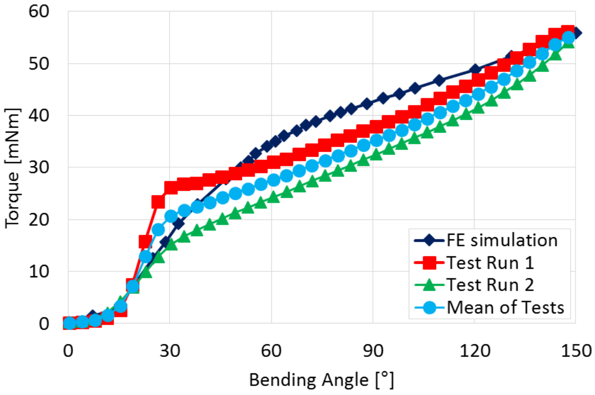

Fig. 6-4: Comparison of Torque during folding for TH-19-5-30-2-2 (Assembly Print)

6.2 Optimized Models

As explained above, the optimized models have been modelled with the material factor found with the experimental data and FE simulations discussed in section 6.1. Therefore, it was expected, that the experiments match the FE simulations closely. Tab. 6-3 shows the experimental and simulated reaction torque for all tested optimized models with regard to their experimental bending angle. It can be seen, that the experimental data and the FE simulations match well. With the exception of the thin *oval-shape straight* model, all other models behaved slightly more compliant in the experiments than simulated. This might be due to non-perfect boundary conditions such that the models are not perfectly constrained as they are in the simulations. An explanation for the smaller FE results value of the thin oval-shape model might be that a different fixation at the punch rod has been introduced for this model in order to be able to test these specimens. However, only the *oval-shape spring* model shows a very large difference. The thin *Z-shape* model and the *oval-shape tilted* model directly printed on a foil show differences around 9 % whereas the rest of the models appeared to have a difference around and below 5 %. However, these deviations can be explained with observations made during the experiments. The thin *Z-shape* models showed a strong reaction out of the bending plane which could not be measured by the torque sensor (see Fig. 5-45). A similar behavior appeared for the *oval-shape spring* model, which also showed an out-of-plane movement reducing the measureable bending torque (see Fig. 5-51). In addition, the spring model is very susceptible for manufacturing deficiencies. The two areas, which get in contact during the folding process should be perfectly parallel and without surface irregularities. However, the used printing process was not able to produce such perfect parts and the irregularities made the specimens more compliant as the contact could not be achieved as perfectly as in the simulations. The difference for the *oval-shape tilted* model directly printed on a foil can be explained with the fact that the bonding between the foil and the hinge model has not been perfect. Therefore, the specimen is more compliant than the FE model and shows a smaller reaction torque than simulated. Apart from these differences, the other models showed a good relation between experimental data and FE simulations. Therefore, one can assume that the geometry of the model does not have a large influence on the material parameter and that this material parameter has been well defined. However, it is still assumed that the influence of humidity onto the specimens' material as well as the printing quality of the 3D printer have a large influence on this parameter. Therefore, similar experiments need to be done if the material or the manufacturing process is changed.

Regarding the models' efficiency, it needs to be stated that the bionically inspired hinges could not reach efficiencies as high as the best torsion hinge models. However, their opening reaction still showed satisfying results and they can be used for further applications without the need of using the patented torsion hinges.

Tab. 6-3: Test & FE results of the reaction torque for all tested optimized models

Model	**Test Results [mNm]**	**FE Results [mNm]**	**Relative difference [%]**
Z-shape thick	106.38	111.54	4.85
Z-shape thin	3.35	3.66	9.25
Oval-shape straight thick	153.07	160.92	5.13
Oval-shape straight thin	15.28	14.70	-3.80
Oval-shape tilted	8.68	8.86	2.07
Oval-shape tilted with foil	30.92	33.56	8.54
Oval-shape spring	5.41	6.99	29.21

7 Implementation of hinges into foldable membrane structure

Two possible designs for the implementation of the discussed hinges into a foldable membrane structure have been developed and are presented in this section.

The first design is inspired by the Earwig as seen in section 2.2.3 (Fig. 7-1, A). *Oval-shape tilted* hinges are used for the radially spreading fold lines and *oval-shape straight* hinges connect the radial fold lines in circumferential direction. At the edge of the membrane, *oval-shape tilted* hinges are used too and the connecting rods are not straight anymore, as they where for the radial and circumferential fold lines. First, the membrane will be folded along its circumference (Fig. 7-1, B & C). The folding procedure is shown schematically in (Fig. 7-1, B – D), where the hinges have been replaced by general circles to improve the understanding of the drawings. Then, it can be folded radially for several times until a small package is left (see Fig. 7-1, D for fold lines). Finally, this package can be folded by 90° such that it is parallel to one of the satellite’s surfaces. To do this, *oval-shape spring* hinges are used. Several of these hinges are placed parallel to each other and are connected by perpendicular rods (Fig. 7-3). The *oval-shape spring* hinges are placed at the outside of the fold line such that they will be able to pull down the whole membrane package during the first stage of the unfolding process.

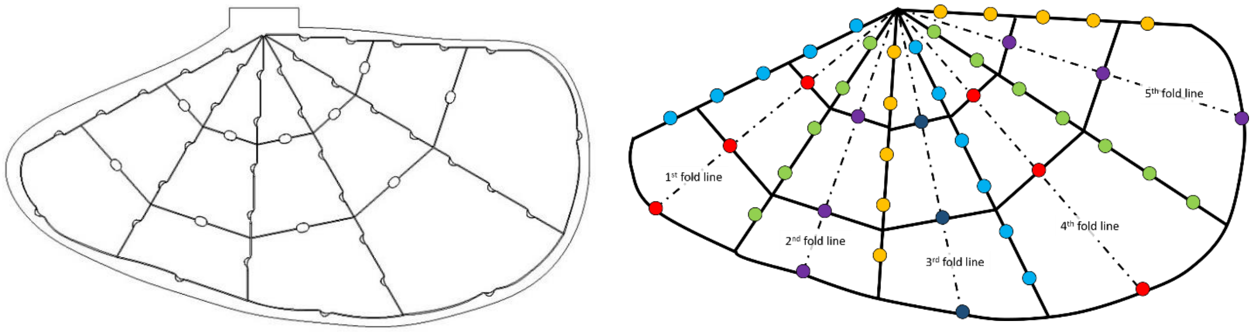

(A) Initial design (B) Circumferential fold lines

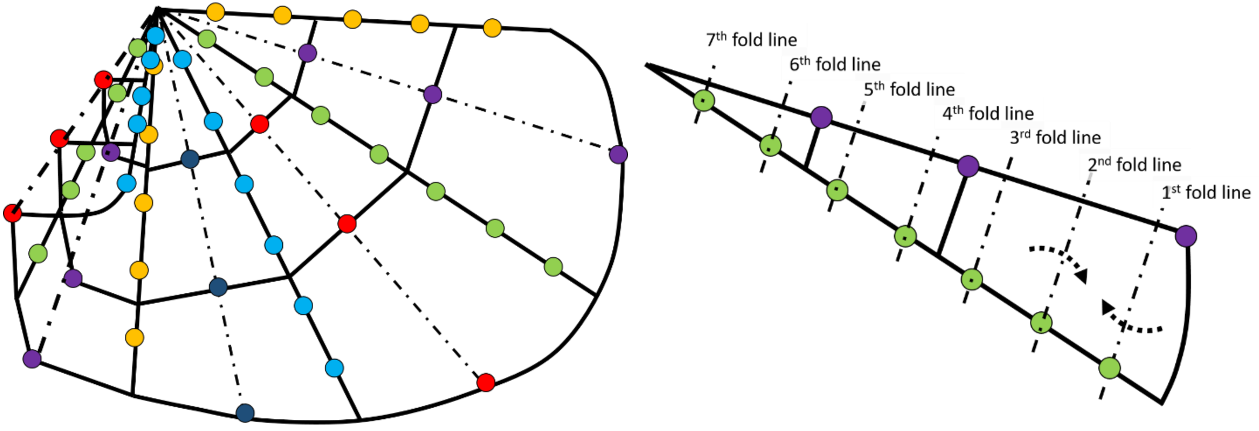

(C) Wing partly folded in circumferential direction (D) Radial fold lines

Fig. 7-1: Wing design 1 (A) with schematic description of folding procedure (B – D)

The second structure is inspired by tree leafs (see Fig. 7-2). Hence, there exists a central fold line as well as fold lines that spread from this center at a certain angle. Here, *oval-shape tilted* hinges have been chosen for the central fold lines. The circumferential fold lines are composed of *oval-shape straight* hinges. The heart of the structure is a large *oval-shape straight* hinge. This design first folds radially (Fig. 7-2, B & C). Then, everything is folded out-of-plane at the large central *oval-shape straight* hinge until a small package is obtained (Fig. 7-2, D). Finally, the package is folded towards the satellite and is aligned with one of the satellite's surfaces with the same *oval-shape spring* arrangement as for the first design approach.

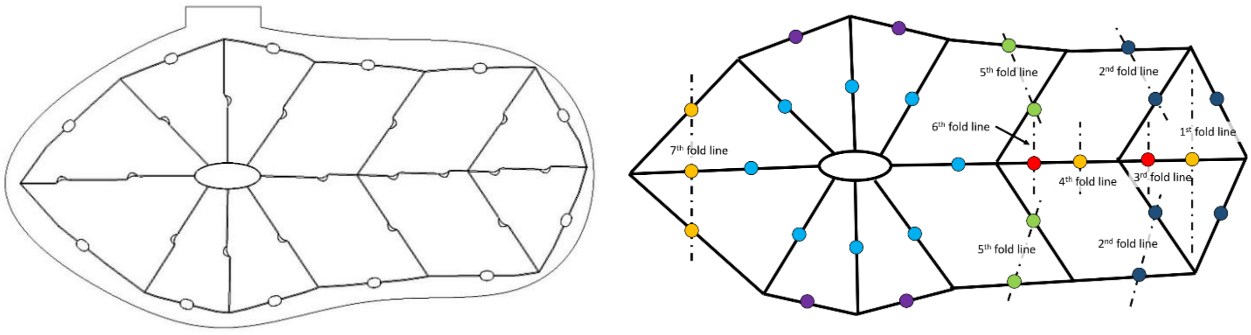
5th fold line
2nd fold line
6th fold line
1st fold line
7th fold line
4th fold line
3rd fold line
5th fold line
2nd fold line

(A) Initial design (B) First steps of folding procedure

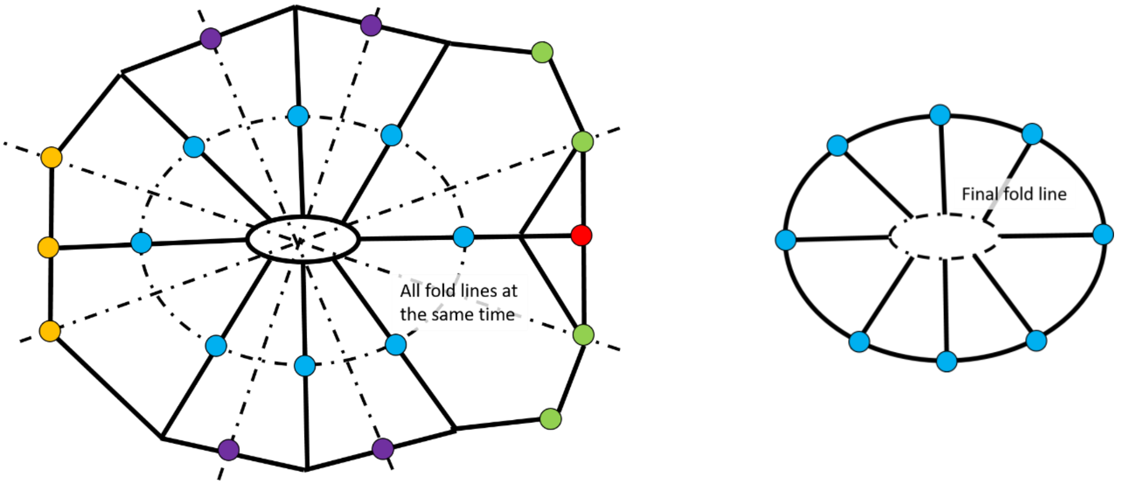
All fold lines at the same time
Final fold line

(C) Radial and out-of-plane folding at the same time (D) Final radial fold at large *oval-shape straight* hinge

Fig. 7-2: Wing design 2 (A) with schematic description of folding procedure (B –D)

In addition to the hinges' principle function, providing the energy needed for the deployment, they might also work as rip-stoppers. The various hinges and rods form closed areas on the membrane. Hence, if one area gets damaged by an impact with space debris, the rip cannot grow larger than the area it is confined in, because the hinges and rods are much stiffer than the membrane and a rip in the membrane will not be able to overcome this barrier. To improve the rip-stop mechanism, one could decrease the confining areas by adding more rods. These additional rods should be thin and less stiff than the hinges in order not to prevent the folding procedure. Such rip-stop mechanisms have been studied in literature [3].

Fig. 7-4 shows a CubeSat with two fully deployed wings. For simplicity, both wing designs have been added to the CubeSat at the same time. However, in reality, using a symmetric arrangement might be preferable.

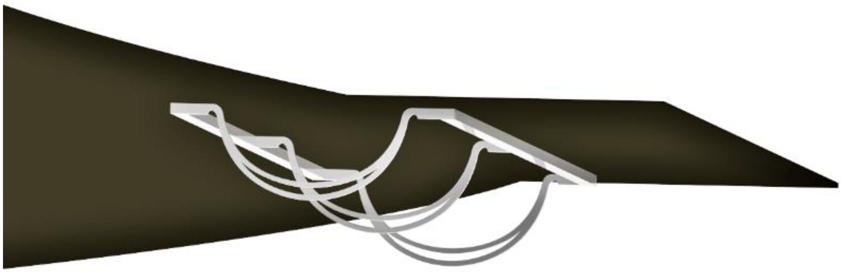

Fig. 7-3: *Oval-shape spring* hinges at connection to the satellite

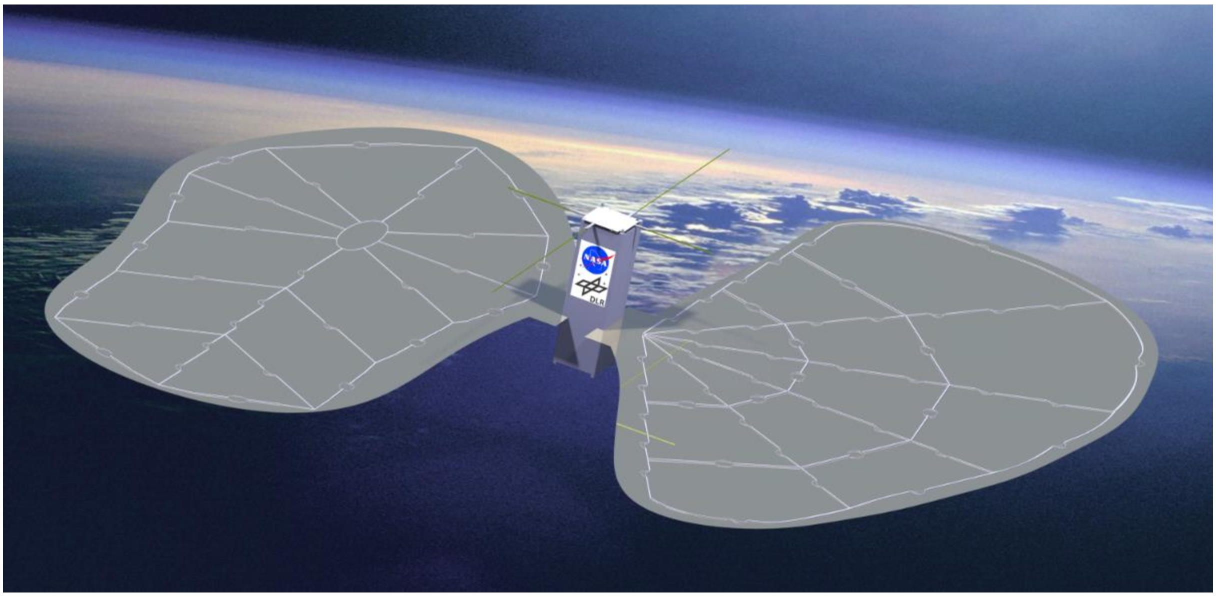

Fig. 7-4: Design study of CubeSat with deployable wings (right wing: Design 1; left wing: Design 2)

8 Conclusion and Outlook

As numerous structures in most technological fields, satellite structures are getting smaller and lighter. This also calls for smaller membrane deployment and stiffening structures for space applications in order to reduce mass and volume of such architectures. Elastic hinges, directly printed onto the chosen application’s membrane, might be a solution to this problem. The present work was done in order to gain more information about the behavior and design of such hinges. The goals of this thesis where to design and develop a test stand capable to represent experimentally how these hinges behave during folding and deployment, compare the experimental results with the corresponding finite element model and find optimal hinge designs adapted from bionical observations.

To do so, a literature review about space structure architectures, folding mechanisms, elastic hinges, test methods and foldable insect wings and joints has been done. The gathered information was processed and a test stand has been developed to test various hinge designs. This test stand has been calibrated with sample material specimens before using the investigated hinges. The experimental results of this test have been used to adapt the FE model in order to be able to predict the behavior of other hinge designs. Furthermore, hinge designs in foldable insect wings have been parametrized and these parameters have been optimized in a specified optimization domain. The found optimal solutions of the different hinge designs have been tested and their results have been compared to the simulations. Finally, an exemplary design of how to implement these hinges into a membrane design has been shown in order to show the possibilities of such elastic hinges.

8.1 Conclusions

The work accomplished and the presented data and discussion in chapters 5 and 6 lead to the following conclusions. The designed test stand is reliable and gives repeatable results. It could be shown that the standard deviation in between specimens of the same design and the same specifications is between 3 to 10 % with the exception of two models, which showed an unexpected out-of-plane movement during the tests. However, this could be improved even more with an improved fixation at the punch side. In addition, the exploitation of the test stand is simple and it can be adapted to many different configurations, which is preferable to get quick results.

Furthermore, collating the FE model with the experimental data showed that it is possible to find a material and manufacturing factor that is repeatable. This facilitates further studies as the material model and its properties in the FE model can be kept simple without the need of going into deep microstructural studies for the printed materials.

Directly printing the elastic hinges onto a foil is possible, however the available foil and printing properties could not prevent a peel off of the specimens while bending them with the foil inside. Nevertheless, it was possible to test this hinge-foil assembly with the foil outside, which showed a strong stiffening influence of the foil as it prevented the torsional movement of the hinge rods.

Regarding design performance, it could be shown that there do not exist very large differences in performance between the different bionically inspired hinges. However, omitting the thick models which are not applicable for thin structures, the *oval-shape spring* and *tilted* models showed the best reaction torque to weight ratio, which means that they can achieve a good opening performance by adding the least weight. However, the differences are small and therefore the choice for a hinge design is dependent on the final application and structure design. For example, the *oval-shape spring* hinges could be used as a link to the satellite structure itself whereas the *oval-shape tilted* hinges are well suitable for in-plane folding of the membrane.

When implementing the elastic hinges into an overall membrane structure, the hinges need to be connected. This should be done by extending the hinges' rods. If these rods are also directly bonded onto the membrane they can work as rip-stoppers, confining possible rips in the membrane due to space debris or other impacts. This would ensure that the overall structure could still carry out its task and that possible impacts with debris are not able to destroy the complete structure but only small parts of it.

8.2 Future work

The presented study showed that it is possible to use 3D-printed elastic hinges in order to fold and deploy a membrane structure. In addition, the opening strength can be measured with the designed test stand. However, there are many different issues to be investigated by further research before a demonstrator could be launched in a parabolic flight. If the experimental data needs to be even more precise, the fixation of the specimen on the punch rod side needs to be improved to have a better-constrained boundary condition and be able to constrain a possible out-of-plane movement. The next step regarding design and size is a more precise functional specification. This should include the overall membrane size and its application. Then, the final material for the hinges needs to be selected. It is only when the material and the membrane's application are defined that the hinges can be optimized further. A more confined bounding box can be defined and even more optimization iterations can be done, as the designs are highly dependent on the bounding box. In addition, the long-time behavior of the material itself and the hinges needs to be evaluated according to their future mission. First tests in this work showed that it is possible to print the hinges directly onto a membrane. However, the adhesion was not yet sufficient. More research needs to be done in this field where it is important to include the final membrane such that an adequate bonding can be achieved depending on the membrane's task.

Finally, the last step before deploying a demonstrator is to improve the folding pattern. The folding pattern can be defined together with the selection of compatible hinges and connection rods. Hinge designs can be mixed and different hinges can be used for different folds as shown by the initial design in section 7.

9 Bibliography

[1] US Federal Aviation Administration. *The Annual Compendium of Commercial Space Transportation: 2018,* 2018.

[2] Belvin, W. K., et al. *Materials, Structures and Manufacturing: An Integrated Approach to Develop Expandable Structures,* 2012. DOI: https://doi.org/10.2514/6.2012-1951.

[3] Zander, M. E., *Development of a Structure supported Membrane for deployable Space Applications*. Diplomarbeit. Faculty of Mechanical Engineering - Institute for Mechanics. Otto von Guericke Universität, Magdeburg. 2010.

[4] NASA, *CubeSats Overview*. 2018 [Online]. Available: https://www.nasa.gov/mission_pages/cubesats/overview. (Accessed October 22, 2018).

[5] Belvin, W. K., et al. *Advanced Deployable Structural Systems for Small Satellites,* 2016.

[6] Voelker, J., *Development of Stiffened Self-Deploying Membranes for CubeSat Applications*. Master Thesis. Chair of Astronautics. Technical University of Munich, Munich. 2018.

[7] Chandler, D. L., *While you're up, print me a solar cell: New MIT-developed materials make it possible to produce photovoltaic cells on paper or fabric, nearly as simply as printing a document.* 2011 [Online]. Available: http://news.mit.edu/2011/printable-solar-cells-0711. (Accessed October 22, 2018).

[8] Straubel, M., Hillebrandt, M., and Huhne, C. *Evaluation of Different Architectural Concepts for Huge Deployable Solar Arrays for Electric Propelled Space Crafts,* 2016.

[9] Kauderer, A., *Photo index 2*. 2012 [Online]. Available: https://spaceflight.nasa.gov/gallery/images/shuttle/sts-116/hires/iss014e10053.jpg. (Accessed October 22, 2018).

[10] NASA, *Hubble solar array deployment on STS-31*. 1990 [Online]. Available: https://commons.wikimedia.org/wiki/File:Hubble_Solar_Array_Deployment_STS-31.jpg. (Accessed October 22, 2018).

[11] Foster, C. L., et al. *Solar-array-induced disturbance of the Hubble Space Telescope pointing system.* Journal of Spacecraft and Rockets, 1995, p. 634–644. DOI: https://doi.org/10.2514/3.26664.

[12] Killian, M., *PHOTOS: ATK Validates New MegaFlex Solar Array Technology for NASA's Future Solar Electric Propulsion Missions*. 2014 [Online]. Available: http://www.americaspace.com/2014/05/04/photos-atk-validates-new-megaflex-solar-array-technology-for-nasas-future-solar-electric-propulsion-missions/. (Accessed October 22, 2018).

[13] Murphy, D. M. *MegaFlex - The Scaling Potential of UltraFlex Technology.* The 53rd AIAA/ASME/ASCE/AHS/ASC Structures, Structural Dynamics and Materials Conference, 2012, p. 1–18. DOI: https://doi.org/10.2514/6.2012-1581.

[14] European Space Agency ESA, *Space for education: Solar sails*. 2018 [Online]. Available: https://www.esa.int/Education/Solar_sails. (Accessed October 22, 2018).

[15] Japan Aerospace Exploration Agency, *Small Solar Power Sail Demonstrator "IKAROS"*. 2010.

[16] Nemiroff, R. and Bonnell, J., *Astronomy picture of the day: NanoSail-D*. 2011 [Online]. Available: https://apod.nasa.gov/apod/ap110128.html. (Accessed October 22, 2018).

[17] NASA, *James Webb Space Telescope*. 2018 [Online]. Available: https://jwst.nasa.gov/index.html. (Accessed October 22, 2018).

[18] Wikipedia, *James Webb Space Telescope*. 2018 [Online]. Available: https://en.wikipedia.org/wiki/James_Webb_Space_Telescope. (Accessed October 22, 2018).

[19] Paez, D., *Rips in 'Sunshield' Keeping James Webb Space Telescope on The Ground*. 2018 [Online]. Available: https://www.inverse.com/article/42894-sunshield-rips-keep-james-webb-telescope-grounded. (Accessed October 22, 2018).

[20] NASA, *NASA Completes Webb Telescope Review, Commits to Launch in Early 2021*. 2018 [Online]. Available: https://www.nasa.gov/press-release/nasa-completes-webb-telescope-review-commits-to-launch-in-early-2021. (Accessed October 22, 2018).

[21] Faber, J. A., Arrieta, A. F., and Studart, A. R. *Bioinspired spring origami.* Science, 2018, p. 1386–1391. DOI: https://doi.org/10.1126/science.aap7753.

[22] Vincent, J. F. V. *Deployable Structures in Nature*. In *Deployable Structures*, Pellegrino, S., Ed. 2001. Springer Verlag, Vienna, p. 37–50.

[23] Arya, M., Lee, N., and Pellegrino, S. *Ultralight Structures for Space Solar Power Satellites.* 3rd AIAA Spacecraft Structures Conference, 2016, p. 1–18. DOI: https://doi.org/10.2514/6.2016-1950.

[24] Arya, M., Lee, N., and Pellegrino, S. *Crease-free biaxial packaging of thick membranes with slipping folds.* International Journal of Solids and Structures, 2017, p. 24–39. DOI: https://doi.org/10.1016/j.ijsolstr.2016.08.013.

[25] Arya, M., Lee, N., and Pellegrino, S. *Wrapping Thick Membranes with Slipping Folds.* 2nd AIAA Spacecraft Structures Conference, 2015, p. 1–17. DOI: https://doi.org/10.2514/6.2015-0682.

[26] Cadogan, D. P. and Grahne, M. S. *Deployment Control Mechanisms for Inflatable Space Structures,* 1999.

[27] Miyazaki, Y. *Deployable Techniques for Small Satellites.* Proceedings of the IEEE, 2018, p. 471–483. DOI: https://doi.org/10.1109/JPROC.2018.2799608.

[28] Soykasap, Ö. *Analysis of tape spring hinges.* International Journal of Mechanical Sciences, 2007, p. 853–860. DOI: https://doi.org/10.1016/j.ijmecsci.2006.11.013.

[29] Brinkmeyer, A., Pellegrino, S., and Weaver, P. M. *Effects of Long-Term Stowage on the Deployment of Bistable Tape Springs.* Journal of Applied Mechanics, 2015. DOI: https://doi.org/10.1115/1.4031618.

[30] Puig, L., Barton, A., and Rando, N. *A review on large deployable structures for astrophysics missions.* Acta Astronautica, 2010, p. 12–26. DOI: https://doi.org/10.1016/j.actaastro.2010.02.021.

[31] Mohd Jani, J., et al. *A review of shape memory alloy research, applications and opportunities.* Materials & Design, 2014, p. 1078–1113. DOI: https://doi.org/10.1016/j.matdes.2013.11.084.

[32] R. Hill, L., et al. *Shape memory alloy film for deployment and control of membrane apertures.* Proceedings of SPIE - The International Society for Optical Engineering, 2004. DOI: https://doi.org/10.1117/12.506311.

[33] Bar-Cohen, Y. *Electroactive polymers as actuators.* Advanced Piezoelectric Materials: Science and Technology, 2010. DOI: https://doi.org/10.1533/9781845699758.1.287.

[34] Haas, F. *Wing Folding in Insects: A Natural, Deployable Structure*. In *IUTAM-IASS Symposium on Deployable Structures: Theory and Applications. Solid Mechanics and Its Applications*, Pellegrino, S. and Guest, S., Eds. 2000. Springer Verlag, Dordrecht, p. 137–142. DOI: https://doi.org/10.1007/978-94-015-9514-8_15.

[35] Deiters, J., Kowalczyk, W., and Seidl, T. *Simultaneous optimisation of earwig hindwings for flight and folding.* Biology Open, 2016, p. 638–644. DOI: https://doi.org/10.1242/bio.016527.

[36] Haas, F., *Geometry and mechanics of hind-wing folding in Dermaptera and Coleoptera*. Master Thesis. Faculty of Science. University of Exeter, Exeter. 1994.

[37] Haas, F., Gorb, S., and Wootton, R. J. *Elastic joints in dermapteran hind wings: Materials and wing folding.* Arthropod Structure and Development, 2000, p. 137–146. DOI: https://doi.org/10.1016/S1467-8039(00)00025-6.

[38] Michels, J., Appel, E., and Gorb, S. N. *Resilin - The Pliant Protein*. In *Extracellular Composite Matrices in Arthropods*, Cohen, E. and Moussian, B., Eds. 2016. Springer International Publishing AG Switzerland, p. 89–136.

[39] Geisler, T. and Topczewska, S. *Analysis of the Wing Mechanism Movement Parameters of Selected Beetle Species (Coleoptera).* International Journal of Applied Mechanics and Engineering, 2015, p. 53–64. DOI: https://doi.org/10.1515/ijame-2015-0004.

[40] Brackenbury, J. H. *Wing Folding in Beetles*. In *Symposium on Deployable Structures: Theory and Applications*. *Proceedings of the IUTAM Symposium*, Pellegrino, S. and Guest, S., Eds. 1998. Springer Science+Business Media, B.V., Dordrecht, p. 37–44.

[41] Wootton, R. J. *Functional Morphology of Insect Wings.* Annual Review of Entomology, 1992, p. 113–140. DOI: https://doi.org/10.1146/annurev.en.37.010192.000553.

[42] Zander, M. E. and Belvin, W. K., Eds., *Concept-development of a structure supported membrane for deployable space applications - From nature to manufacture and testing*. 2012.

[43] Combes, S. A., Crall, J. D., and Mukherjee, S. *Dynamics of animal movement in an ecological context: dragonfly wing damage reduces flight performance and predation success.* Biology Letters, 2010, p. 426–429. DOI: https://doi.org/10.1098/rsbl.2009.0915.

[44] Howell, L. L., Magleby, S. P., and Olsen, B. M., *Handbook of Compliant Mechanisms*. 2013. John Wiley & Sons Ltd.

[45] Jacobsen, J. O., *Fundamental Components for Lamina Emergent Mechanisms*. Master Thesis. Department of Mechanical Engineering. Brigham Young University, Provo, Utah. 2008.

[46] Magleby, S. P., Jacobsen, J. O., and Howell, L. L. *Lamina Emergent Torsional Joint and related Methods.* Patent No. US 9,157,497 B1 , 2015.

[47] ASTM International. *D790–02 Standard Test Methods for Flexural Properties of Unreinforced and Reinforced Plastics and Electrical Insulating Materials.* Annual Book of ASTM Standards, 2002, p. 1–12. DOI: https://doi.org/10.1520/D0790-15E02.

[48] ASTM International. *D 6272: Test Method for Flexural Properties of Unreinforced and Reinforced Plastics and Electrical Insulating Materials by Four-Point Bending.* Annual Book of ASTM Standards, 2017.

[49] Kopeliovich, D., *Flexural strength tests of ceramics*. 2012 [Online]. Available: http://www.substech.com/dokuwiki/doku.php?id=flexural_strength_tests_of_ceramics. (Accessed October 29, 2018).

[50] Fernandez, J. M. and Murphey, T. W. *A Simple Test Method for Large Deformation Bending of Thin High Strain Composite Flexures.* 2018 AIAA Spacecraft Structures Conference, 2018. DOI: https://doi.org/10.2514/6.2018-0942.

[51] Yee, J. and Pellegrino, S. *Folding of woven composite structures.* Composites Part A: Applied Science and Manufacturing, 2005, p. 273–278. DOI: https://doi.org/10.1016/j.compositesa.2004.06.017.

[52] Yee, J. and Pellegrino, S. *Biaxial Bending Failure Locus for Woven-Thin-Ply Carbon Fibre Reinforced Plastic Structures.* 46th AIAA/ASME/ASCE/AHS/ASC Structures, Structural Dynamics and Materials Conference, 2005, p. 1–8. DOI: https://doi.org/10.2514/6.2005-1811.

[53] Sanford, G. E., et al. *High Strain Test Method for Thin Composite Laminates.* 16th International Conference on Composite Structures, 2011, p. 1–2.

[54] Maschinenbau-Wissen.de, *Knicken - Eulersche Knickfälle*. 2009 [Online]. Available: http://www.maschinenbau-wissen.de/skript3/mechanik/festigkeitslehre/134-knicken-euler. (Accessed October 29, 2018).

[55] Linß, S., *Ein Beitrag zur geometrischen Gestaltung und Optimierung prismatischer Festkörpergelenke in nachgiebigen Koppelmechanismen*. 2015. Universitätsverlag Ilmenau.

[56] Schoenen, D., et al. *Entwicklung , Konstruktion und Anwendung eines Prüfstands zur Ermittlung der ertragbaren Lastzyklen filigraner hochgenauer stoffschlüssiger Gelenke,* 2015. DOI: https://doi.org/10.14459/2015md1276135.

[57] Seckin, M., et al. *Test and Analysis System Design for Flexible Hinges,* 2017.

[58] Markforged, *Material Specifications: Composites*. 2018, Watertown, MA.

[59] Engineering ToolBox, *Friction and Friction Coefficients*. 2004 [Online]. Available: https://www.engineeringtoolbox.com/friction-coefficients-d_778.html. (Accessed April 1, 2019).

[60] Acin, M., *Stress singularities, stress concentrations and mesh convergence*. 2015 [Online]. Available: http://www.acin.net/2015/06/02/stress-singularities-stress-concentrations-and-mesh-convergence/. (Accessed March 29, 2019).

[61] Bendsøe, M. P. and Sigmund, O., *Topology Optimization: Theory, Methods and Applications*. 2003. Springer Verlag, Berlin Heidelberg.

[62] Kress, G., Keller, D., and Schläpfer, B., *Structural Optimization*. 2015, Zürich.

[63] Johnson, S. G., *The NLopt nonlinear-optimization package*. 2018 [Online]. Available: nlopt.readthedocs.io/. (Accessed April 25, 2019).

[64] Schlueter, M., *MIDACO-SOLVER*. 2019 [Online]. Available: www.midaco-solver.com/. (Accessed April 25, 2019).

[65] Runarsson, T. P. and Yao, X. *Search Biases in Constrained Evolutionary Optimization.* IEEE Trans. on Systems, Man, and Cybernetics Part C: Applications and Reviews, 2004, p. 233–243.

[66] SparkFun Electronics, *Force Sensitive Resistor 0.5"*. 2018 [Online]. Available: https://www.sparkfun.com/products/9375. (Accessed October 30, 2018).

[67] Kistler Group, *1-Komponenten-Reaktionsmomentsensor, Mz bis ±25 N·m / ±18 ft·lb*. 2018 [Online]. Available: https://www.kistler.com/de/produkt/type-9049/. (Accessed October 30, 2018).

[68] Tacuna Systems LLC, *Omega Uniaxial Strain Gauge SGT-3F/350-TY43 350 Ohm*. 2018 [Online]. Available: https://tacunasystems.com/zc/strain-gauges/omega-uniaxial-strain-gauge-sgt-3f-350-ty43-350-ohm. (Accessed October 30, 2018).

[69] Keyence Deutschland GmbH, *Was ist ein Sensor? Sensor Basics: Grundprinzipien und -funktionen*. 2015, Neu-Ilsenburg, Germany.

[70] Zwick Roell, *Used Test Equipment*. 2018 [Online]. Available: https://www.zwickusa.com/en-us/used-test-equipment. (Accessed October 30, 2018).

[71] Festo Gruppe, *Schrittmotoren*. 2018 [Online]. Available: https://www.festo.com/cat/de_de/products__95370. (Accessed October 30, 2018).

[72] Hwa Jyh Spring Metal Co., Ltd., *Spiral Torsion Springs, Power Springs*. 2012 [Online]. Available: http://www.hjspring.com.tw/products-10.html. (Accessed October 30, 2018).

[73] Walmart, *Polyester Leather Leatherware Crafting Sewing Thread String Reel Spool Gray*. 2018 [Online]. Available: https://www.walmart.ca/en/ip/Polyester-Leather-Leatherware-Crafting-Sewing-Thread-String-Reel-Spool-Gray/PRD1DRQKOHK6F2R. (Accessed October 30, 2018).

[74] Zwick Roell, *Xforce-Kraftaufnehmer*. 2018 [Online]. Available: https://www.zwick.de/de-de/kraftaufnehmer/xforce. (Accessed October 30, 2018).

[75] LIMESS GmbH, *Q400 | Digital Image Correlation*. 2018 [Online]. Available: https://www.limess.com/en/products/q400-digital-image-correlation. (Accessed October 30, 2018).

[76] RN-Wissen, *Schrittmotoren*. 2017 [Online]. Available: https://rn-wissen.de/wiki/images/b/b4/Stepperdaten.png. (Accessed October 30, 2018).

[77] HomeschoolMath.net, *Measuring angles with a protractor*. 2015 [Online]. Available: https://www.homeschoolmath.net/teaching/g/measure_angles.php. (Accessed October 30, 2018).

[78] Keyence Corporation, *Merkmale abstandsbasierter Lasersensoren*. 2018 [Online]. Available: https://www.keyence.de/ss/products/sensor/sensorbasics/laser_location/feature/. (Accessed October 30, 2018).

[79] Scott ParkJet, *RC Lander thrust test stand initial impressions*. 2018 [Online]. Available: http://scottsparkjetblog.blogspot.com/2018/01/rc-lander-thrust-stand-initial.html. (Accessed October 30, 2018).

[80] Burster Präzisionsmesstechnik GmbH & Co. KG, *Data sheet: Precision Torque Sensor*. *Model 8661*. 2019, Gemsbach, Germany.

[81] Burster Präzisionsmesstechnik GmbH & Co. KG, *8661*. *Präzisions-Drehmomentsensor*. 2019 [Online]. Available: https://www.burster.de/de/produkte/p/detail/8661/. (Accessed March 26, 2019).

[82] Igus GmbH, *drylin N-Flachführungen | Lieferprogramm*. 2018, Köln.

[83] Kottke, N. G., *Entwicklung und experimenteller Vergleich eines Führungssystems für entfaltbare, dünnwandige CFK-Masten in Wurzel-Entfaltungskonfiguration ultraleichter Raumfahrtanwendungen*. Studienarbeit. Institut für Adaptronik und Funktionsintegration. Technische Universität Braunschweig, Braunschweig. 2016.

[84] MICRO-EPSILON MESSTECHNIK GmbH & Co. KG. *Betriebsanleitung: optoNCDT 1750*.

[85] ME-Meßsysteme GmbH, *Data Sheet: Force Sensor KD24s ± 20N*. 2018, Henningsdorf.

[86] Dr. Fritz Faulhaber GmbH & Co. KG, *Bürstenlose DC-Servomotoren*. *4-Pol-Technologie*. 3242 024 BX4. 2018, Schönaich.

[87] Dr. Fritz Faulhaber GmbH & Co. KG, *Untersetzungsverhältnis*. *Präzisionsgetriebe*. Technische Informationen. 2018, Schönaich.

[88] Deutsches Referenzbüro für Ringversuche und Referenzmaterialien GmbH, *Material- und Werkstoffprüfung: Produktkatalog 2019/2020*. 2018.

[89] Neon Reiss Kunststoffe GmbH, *Technisches Datenblatt: Polycarbonat*. 2018, Korntal.

[90] Goodfellow GmbH, *Eigenschaften - Polycarbonat*. 2018 [Online]. Available: http://www.goodfellow.com/catalogue/GFCat2H.php?ewd_token=vJj2QzazjEQGkzypYwzZxFeDo7ERnH&n=2vC5WLr1NzarOc1xbR9qosMxIrVWHP&ewd_urlNo=GFCat2L3&Head=CT30. (Accessed December 15, 2018).

[91] David M. Parks - Department of Mechanical Engineering, *Euler-Bernoulli Beams: Bending, Buckling, and Vibration*. 2004 [Online]. Available: https://ocw.mit.edu/courses/mechanical-engineering/2-002-mechanics-and-materials-ii-spring-2004/lecture-notes/lec2.pdf. (Accessed February 14, 2019).

[92] Wikipedia, *Timoshenko beam theory*. 2018 [Online]. Available: https://en.wikipedia.org/wiki/Timoshenko_beam_theory. (Accessed February 14, 2019).

[93] Covestro AG, *Makrofol® DE 1-4 000000*. *Produkt Datenblatt*. 2015, Leverkusen.

[94] BASF Corporation, *Mechanical performance of polyamides with influence of moisture and temperature - accurate evaluation and better understanding*. 2003, Mount Olive, NJ.

[95] Mitkus, R., *Tensile testing - Mechanical properties of PLA*. 2017, Braunschweig.

[96] Innofil 3D, *Technical Data Sheet*. *PLA by Innofil3D BV*. 2017, Emmen, NL.

A. Appendix

A.1. Mesh convergence study

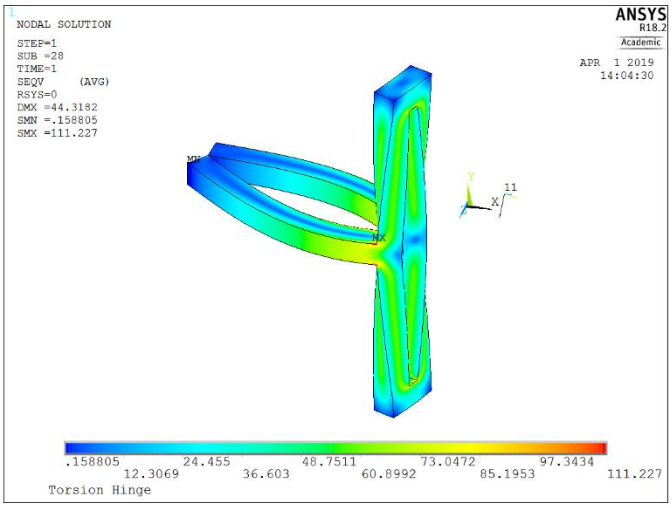
NODAL SOLUTION
STEP=1
SUB =28
TIME=1
SEQV (AVG)
RSYS=0
DMX =44.3182
SMN =.158805
SMX =111.227
ANSYS
R18.2
Academic
APR 1 2019
14:04:30
MX
MN
Y
X
.158805
12.3069
24.455
36.603
48.7511
60.8992
73.0472
85.1953
97.3434
111.227
Torsion Hinge

Fig. A-1: Von Mises Stress for TH-19-5-30-2-2, mesh size: 0.25

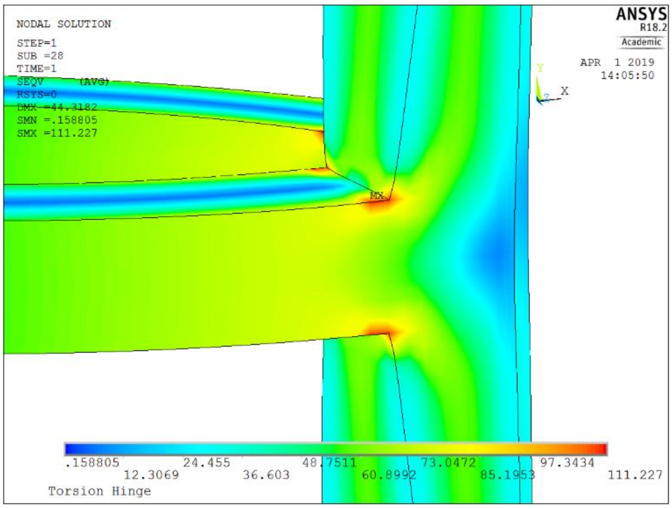
NODAL SOLUTION
STEP=1
SUB =28
TIME=1
SEQV (AVG)
RSYS=0
DMX =44.3182
SMN =.158805
SMX =111.227
ANSYS
R18.2
Academic
APR 1 2019
14:05:50
MX
Y
X
.158805
12.3069
24.455
36.603
48.7511
60.8992
73.0472
85.1953
97.3434
111.227
Torsion Hinge

Fig. A-2: Close-up of von Mises Stress for TH-19-5-30-2-2, mesh size: 0.25

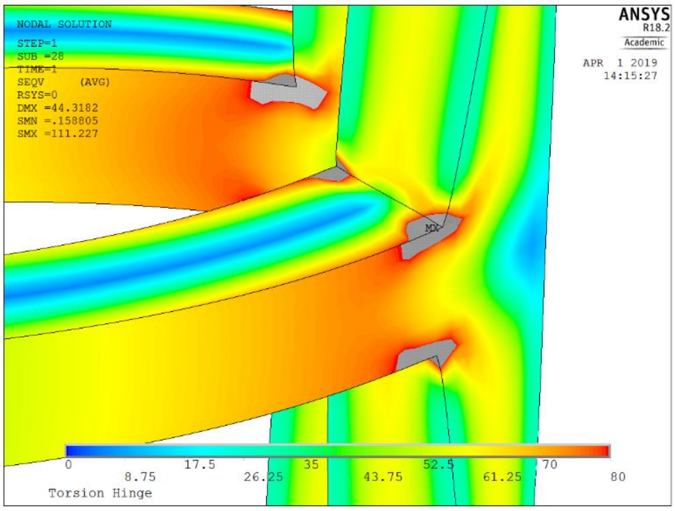
NODAL SOLUTION
STEP=1
SUB =28
TIME=1
SEQV (AVG)
RSYS=0
DMX =44.3182
SMN =.158805
SMX =111.227
ANSYS
R18.2
Academic
APR 1 2019
14:15:27
MX
0
8.75
17.5
26.25
35
43.75
52.5
61.25
70
80
Torsion Hinge

Fig. A-3: Close-up of von Mises Stress for TH-19-5-30-2-2, mesh size: 0.25, maximum stress to plot: 80 MPa

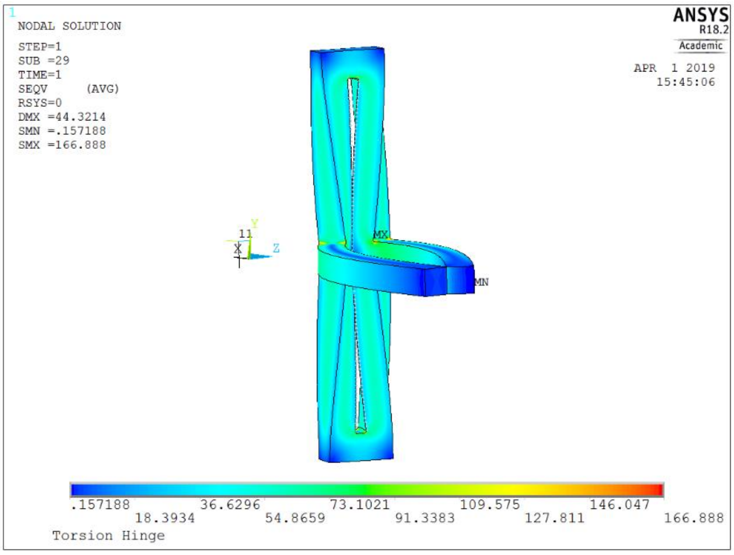
1
NODAL SOLUTION
STEP=1
SUB =29
TIME=1
SEQV (AVG)
RSYS=0
DMX =44.3214
SMN =.157188
SMX =166.888
ANSYS
R18.2
Academic
APR 1 2019
15:45:06
MX
MN
.157188
18.3934
36.6296
54.8659
73.1021
91.3383
109.575
127.811
146.047
166.888
Torsion Hinge

Fig. A-4: Von Mises Stress for TH-19-5-30-2-2, global mesh size: 0.3, fillets: 0.1

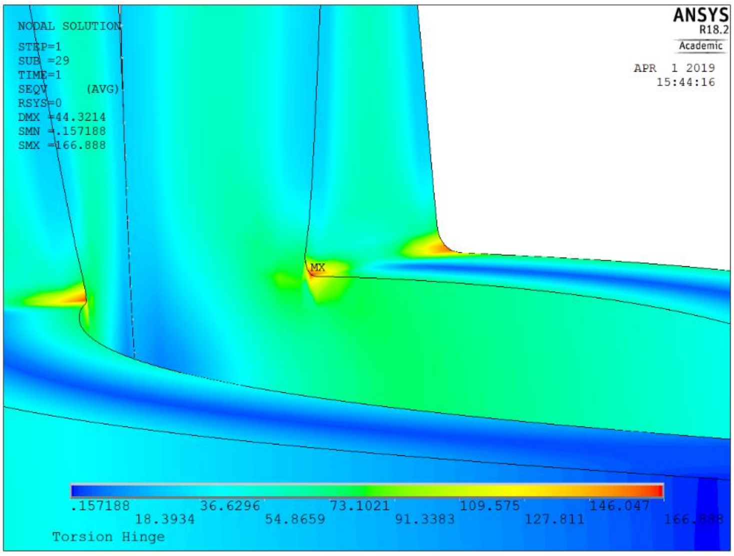
NODAL SOLUTION
STEP=1
SUB =29
TIME=1
SEQV (AVG)
RSYS=0
DMX =44.3214
SMN =.157188
SMX =166.888
ANSYS
R18.2
Academic
APR 1 2019
15:44:16
MX
.157188
18.3934
36.6296
54.8659
73.1021
91.3383
109.575
127.811
146.047
166.888
Torsion Hinge

Fig. A-5: Close-up of von Mises Stress for TH-19-5-30-2-2, , global mesh size: 0.3, fillets: 0.1

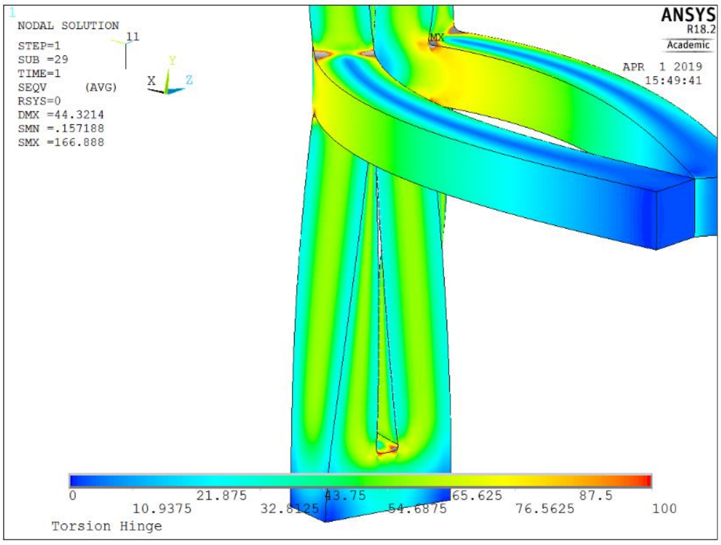
1
NODAL SOLUTION
STEP=1
SUB =29
TIME=1
SEQV (AVG)
RSYS=0
DMX =44.3214
SMN =.157188
SMX =166.888
ANSYS
R18.2
Academic
APR 1 2019
15:49:41
MX
0
10.9375
21.875
32.8125
43.75
54.6875
65.625
76.5625
87.5
100
Torsion Hinge

Fig. A-6: Close-up of von Mises Stress for TH-19-5-30-2-2, , global mesh size: 0.3, fillets: 0.1, maximum stress to plot: 100 MPa

A.2. Parameter study oval-shape tilted & oval-shape spring models

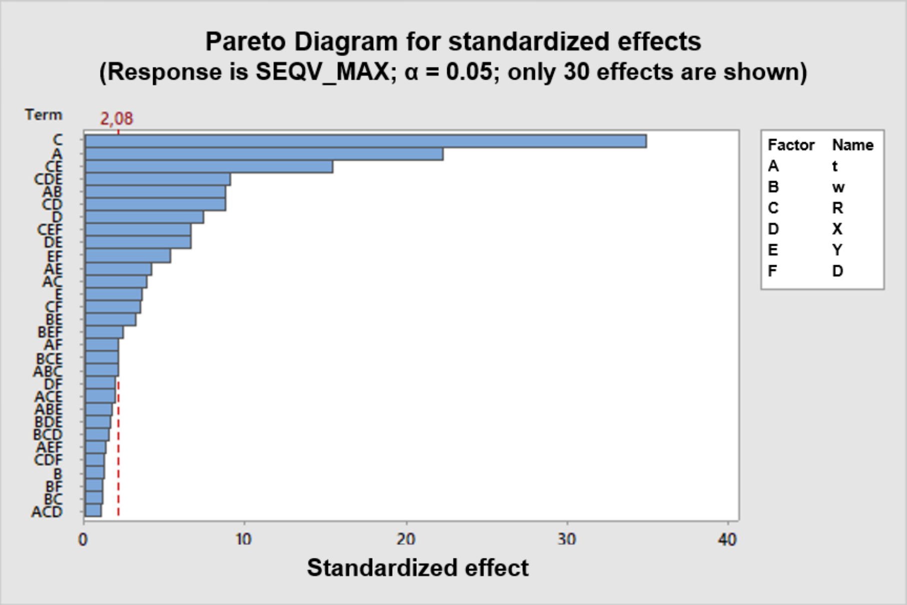

Fig. A-7: Pareto Diagram for standardized effects with regard to maximum von Mises equivalent stress for *oval-shape tilted* hinge

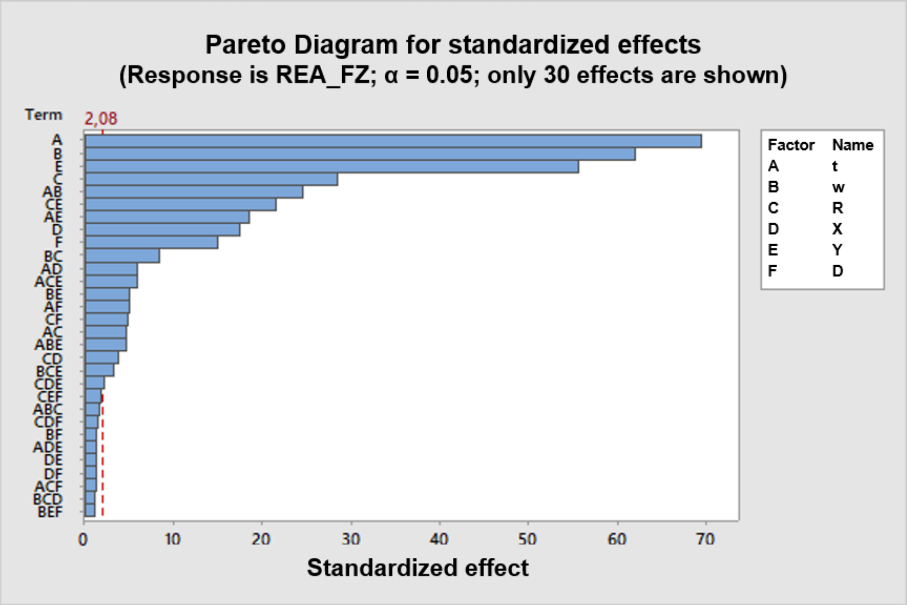

Fig. A-8: Pareto Diagram for standardized effects with regard to reaction force at displaced nodes for *oval-shape tilted* hinge

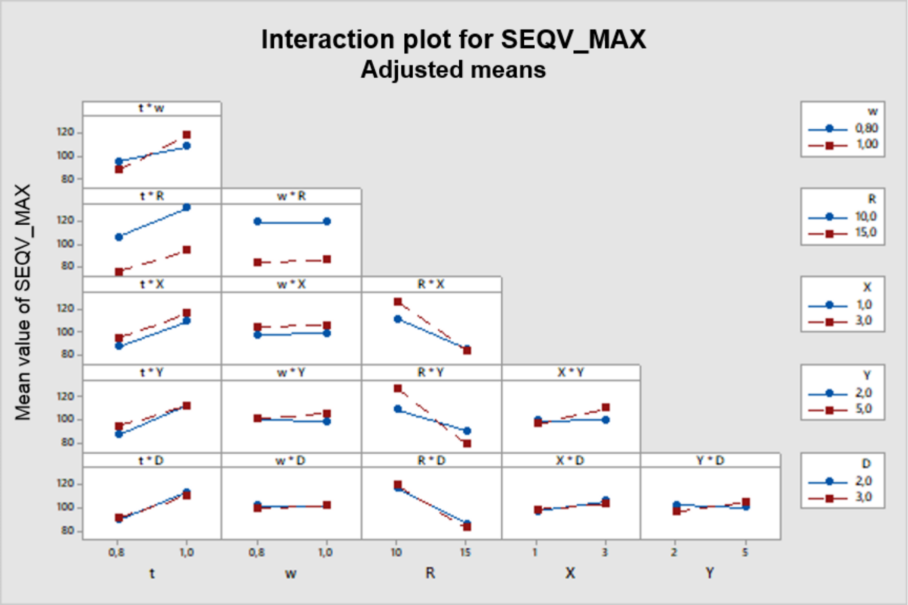

Fig. A-9: Interaction plot for adjusted means with regard to maximum von Mises equivalent stress for *oval-shape tilted* hinge

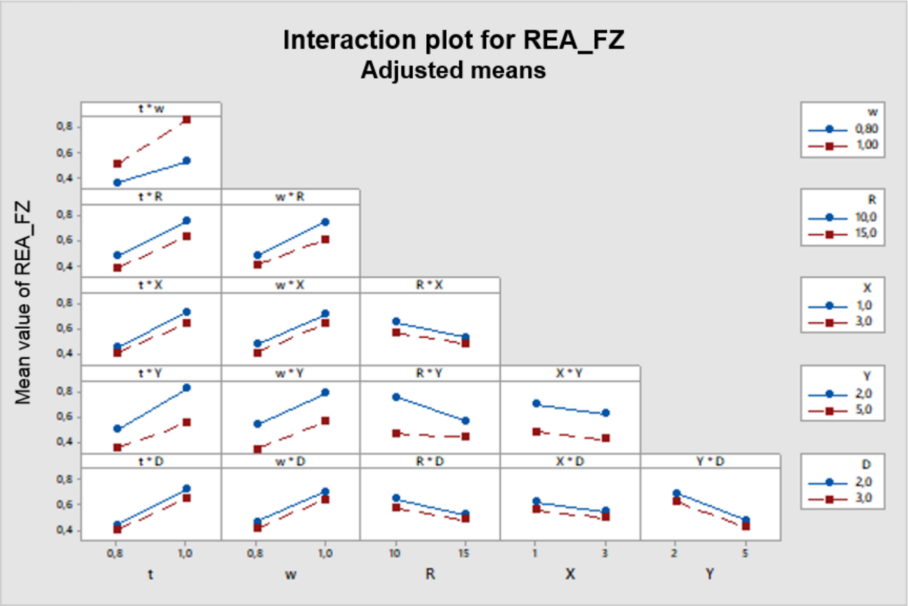

Fig. A-10: Interaction plot for adjusted means with regard to reaction force at displaced nodes for *oval-shape tilted* hinge

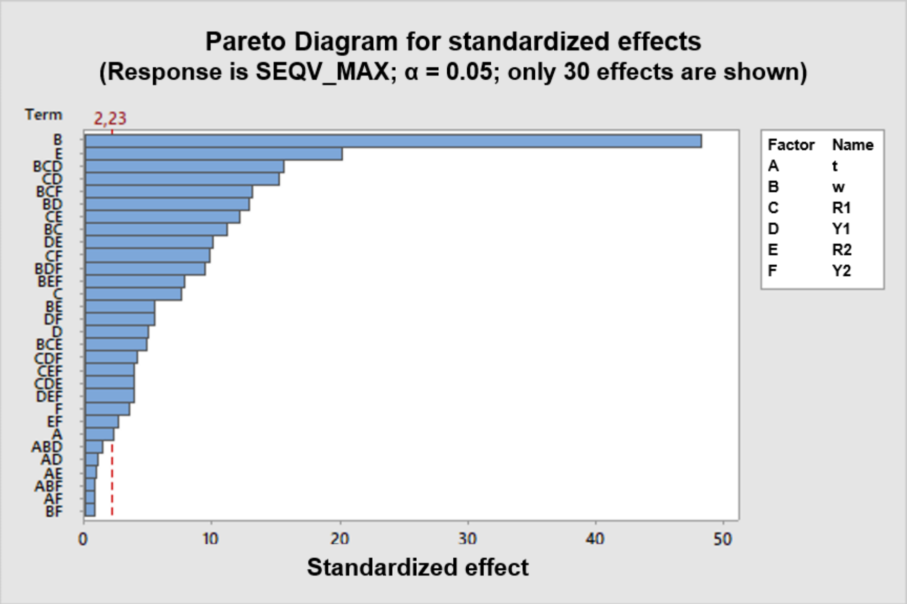

Fig. A-11: Pareto Diagram for standardized effects with regard to maximum von Mises equivalent stress for *oval-shape spring* hinge

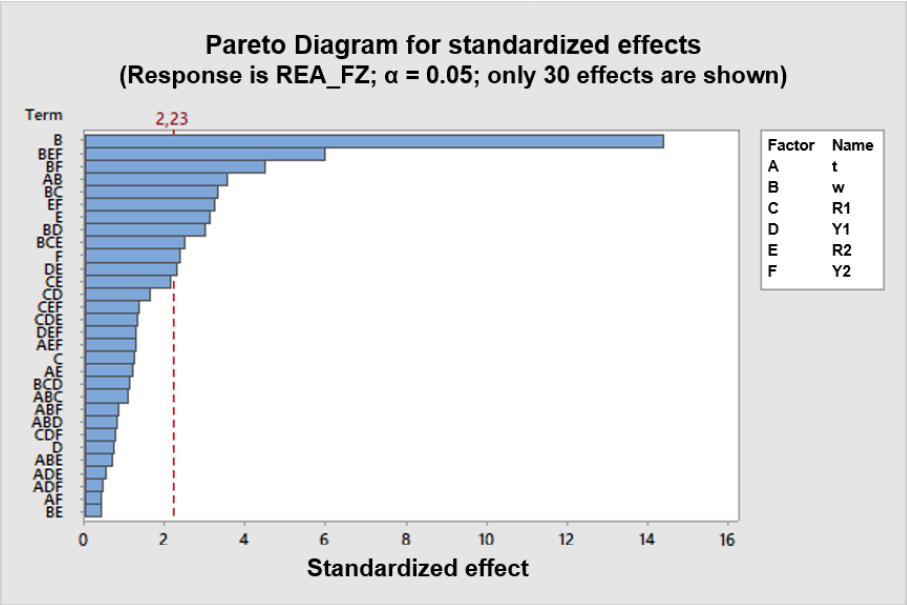

Fig. A-12: Pareto Diagram for standardized effects with regard to reaction force at displaced nodes for *oval-shape spring* hinge

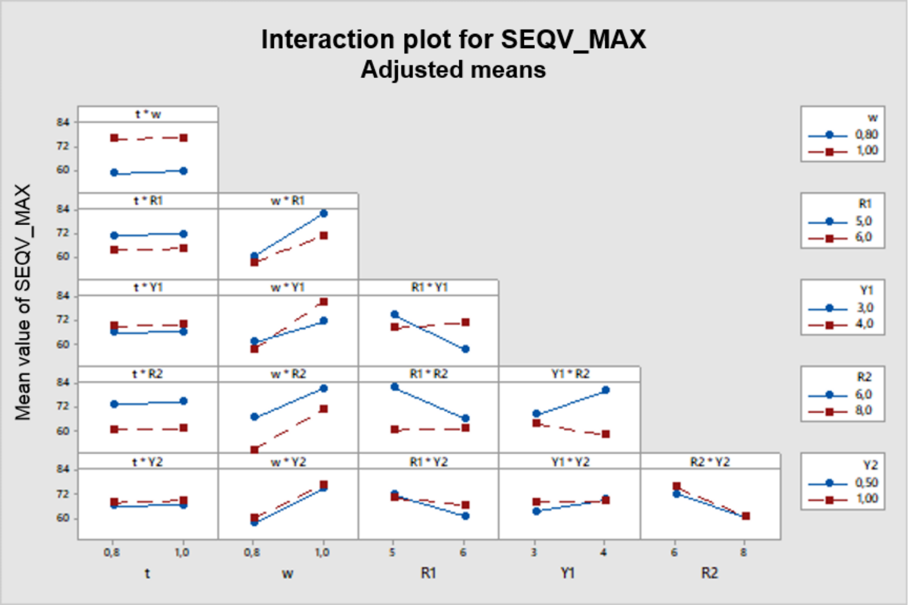

Fig. A-13: Interaction plot for adjusted means with regard to maximum von Mises equivalent stress for *oval-shape spring* hinge

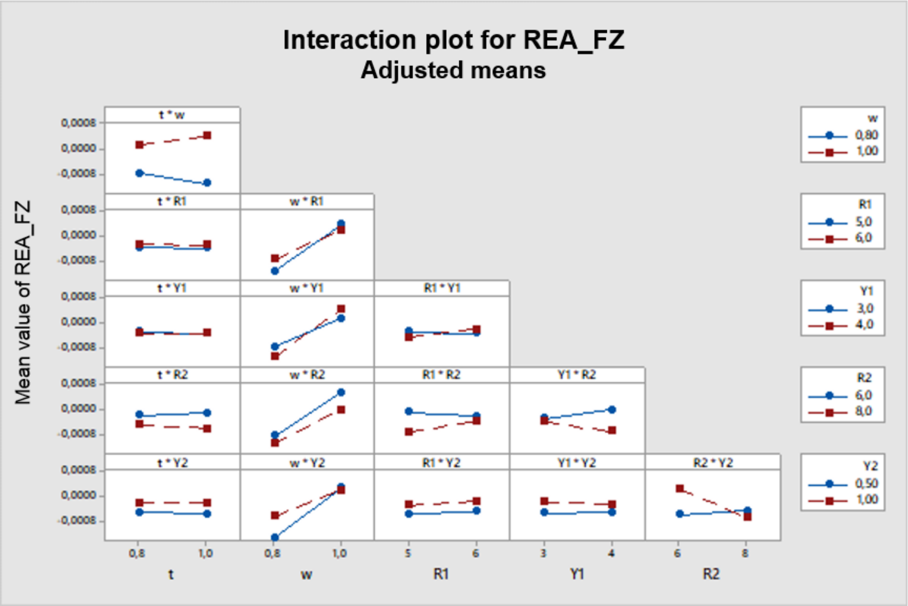

Fig. A-14: Interaction plot for adjusted means with regard to reaction force at displaced nodes for *oval-shape spring* hinge

A.3. Von Mises stress of optimized models

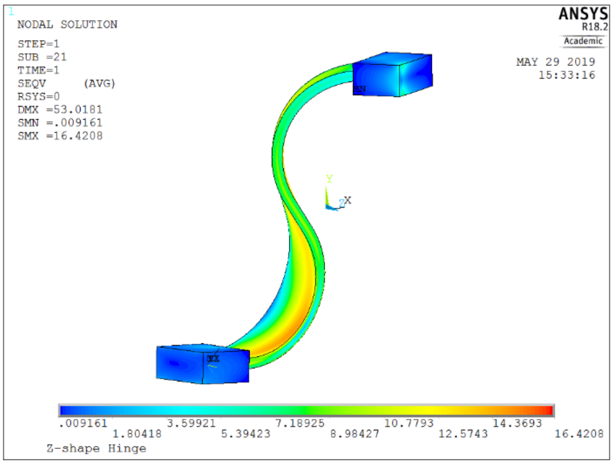
NODAL SOLUTION
STEP=1
SUB =21
TIME=1
SEQV (AVG)
RSYS=0
DMX =53.0181
SMN =.009161
SMX =16.4208
ANSYS
R18.2
Academic
MAY 29 2019
15:33:16
MN
MX
Y
X
.009161
1.80418
3.59921
5.39423
7.18925
8.98427
10.7793
12.5743
14.3693
16.4208
Z-shape Hinge

Fig. A-15: Von Mises stress for best solution of thick model *Z-shape* folded to 110°

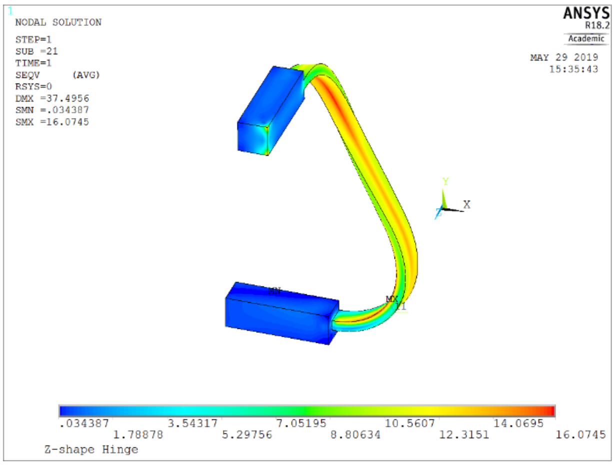
NODAL SOLUTION
STEP=1
SUB =21
TIME=1
SEQV (AVG)
RSYS=0
DMX =37.4956
SMN =.034387
SMX =16.0745
ANSYS
R18.2
Academic
MAY 29 2019
15:35:43
MN
MX
Y
X
.034387
1.78878
3.54317
5.29756
7.05195
8.80634
10.5607
12.3151
14.0695
16.0745
Z-shape Hinge

Fig. A-16: Von Mises stress for best solution of thin model *Z-shape* folded to 125°

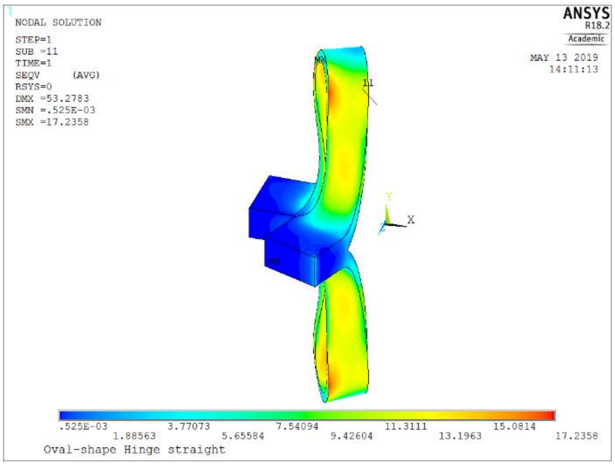
NODAL SOLUTION
STEP=1
SUB =11
TIME=1
SEQV (AVG)
RSYS=0
DMX =53.2783
SMN =.525E-03
SMX =17.2358
ANSYS
R18.2
Academic
MAY 13 2019
14:11:13
MX
MN
11
Y
X
.525E-03
1.88563
3.77073
5.65584
7.54094
9.42604
11.3111
13.1963
15.0814
17.2358
Oval-shape Hinge straight

Fig. A-17: Von Mises stress for best solution of thick model *oval-shape straight* folded to 110°

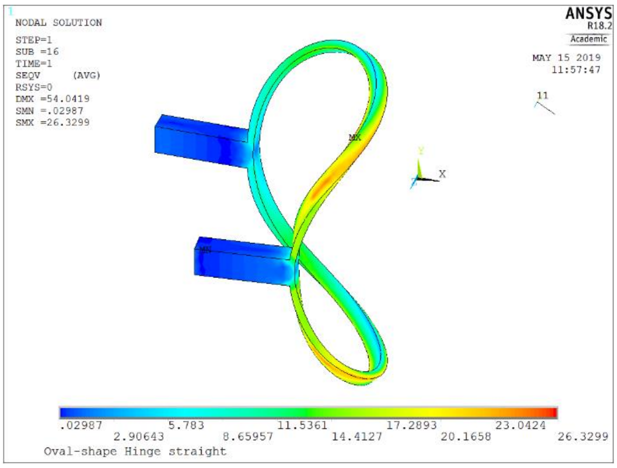
NODAL SOLUTION
STEP=1
SUB =16
TIME=1
SEQV (AVG)
RSYS=0
DMX =54.0419
SMN =.02987
SMX =26.3299
ANSYS
R18.2
Academic
MAY 15 2019
11:57:47
11
MX
MN
Y
X
.02987
2.90643
5.783
8.65957
11.5361
14.4127
17.2893
20.1658
23.0424
26.3299
Oval-shape Hinge straight

Fig. A-18: Von Mises stress for best solution of thin model *oval-shape straight* folded to 125°

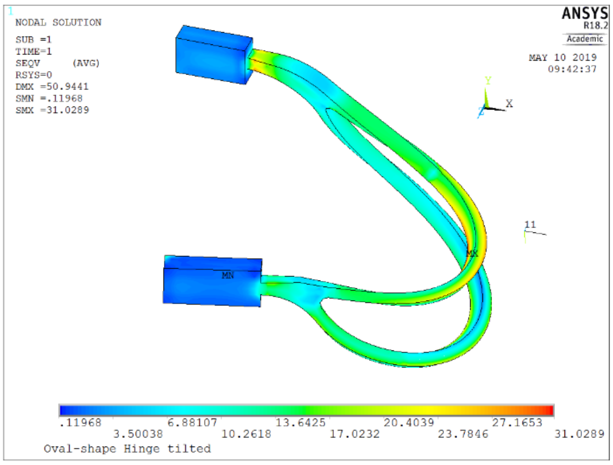
NODAL SOLUTION
SUB =1
TIME=1
SEQV (AVG)
RSYS=0
DMX =50.9441
SMN =.11968
SMX =31.0289
ANSYS
R18.2
Academic
MAY 10 2019
09:42:37
Y
X
11
MX
MN
.11968
3.50038
6.88107
10.2618
13.6425
17.0232
20.4039
23.7846
27.1653
31.0289
Oval-shape Hinge tilted

Fig. A-19: Von Mises stress for best solution of model *oval-shape tilted* folded to 150°

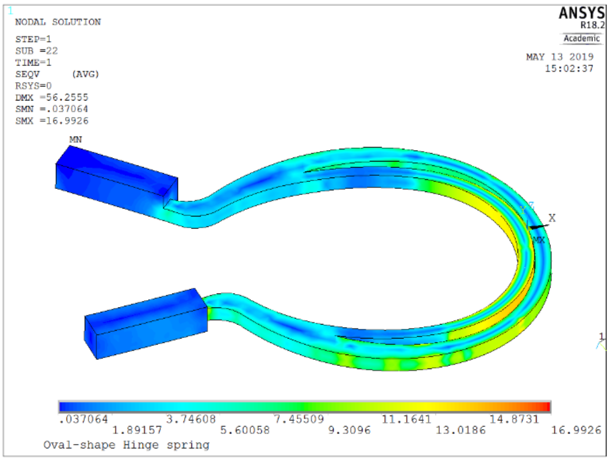
NODAL SOLUTION
STEP=1
SUB =22
TIME=1
SEQV (AVG)
RSYS=0
DMX =56.2555
SMN =.037064
SMX =16.9926
ANSYS
R18.2
Academic
MAY 13 2019
15:02:37
MN
X
MX
1
.037064
1.89157
3.74608
5.60058
7.45509
9.3096
11.1641
13.0186
14.8731
16.9926
Oval-shape Hinge spring

Fig. A-20: Von Mises stress for best solution of model *oval-shape spring* folded to 150°

A.4. Block diagrams of test stand software

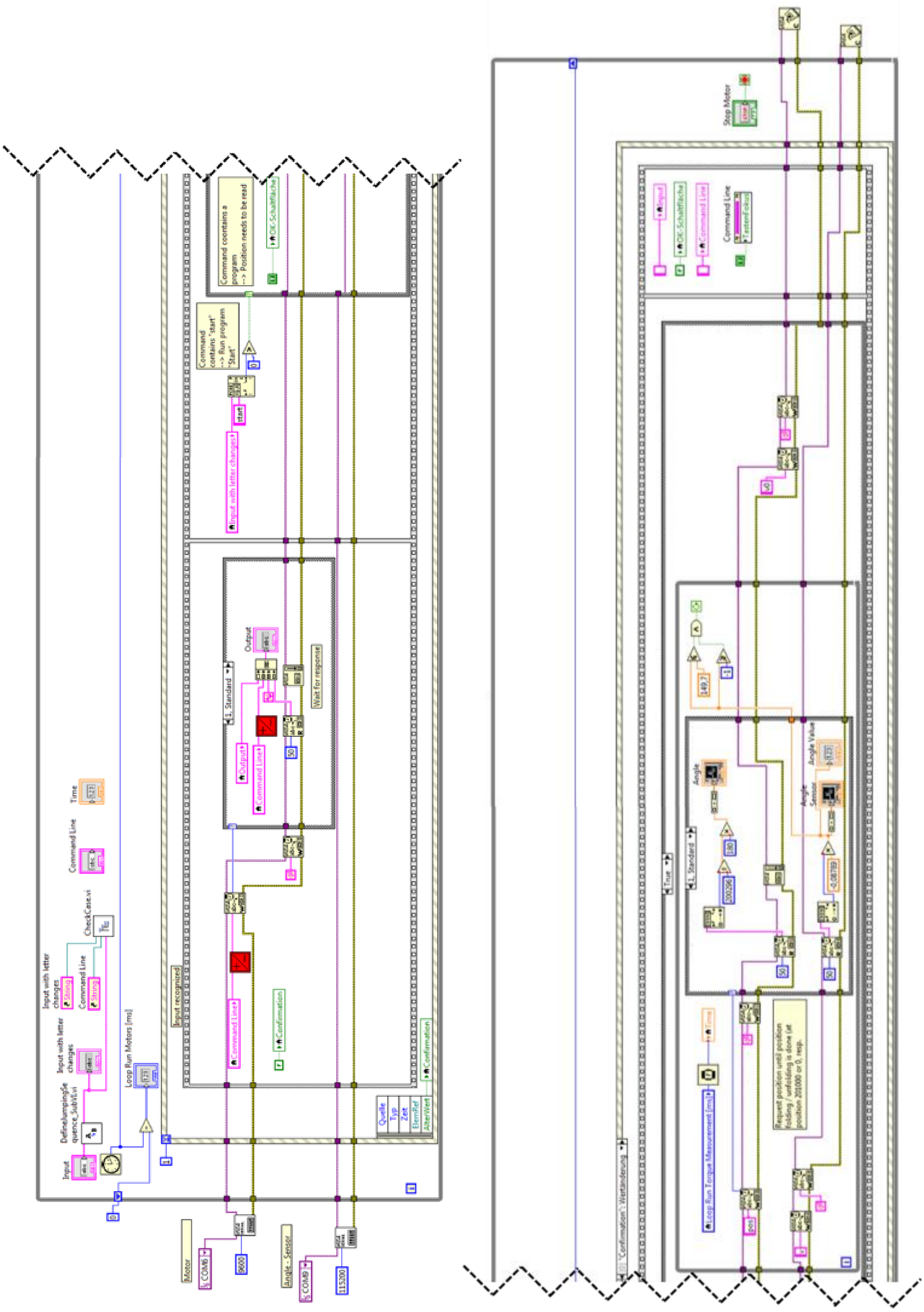
Input
DefineJumpingSequence_SubVI.vi
Input with letter changes
Command Line
CheckCase.vi
Time
Loop Run Motors [ms]
Input recognized
Command contains a program --> Position needs to be read
Command contains "start" --> Run program "Start"
OK-Schaltfläche
Input with letter changes
start
Output
Command Line
Confirmation
Wait for response
Quelle
Typ
Zeit
ElemRef
AlterWert
Motor
COM6
9600
Angle - Sensor
COM9
115200
Stop Motor
Input
Command Line
TastenFokus
"Confirmation": Wertänderung
True
Standard
Angle
Angle Value
Angle Sensor
Loop Run Torque Measurement [ms]
Time
Request position until position folding / unfolding is done (at position 201000 or 0, resp.

Fig. A-21: Block diagram of motion control subprogram

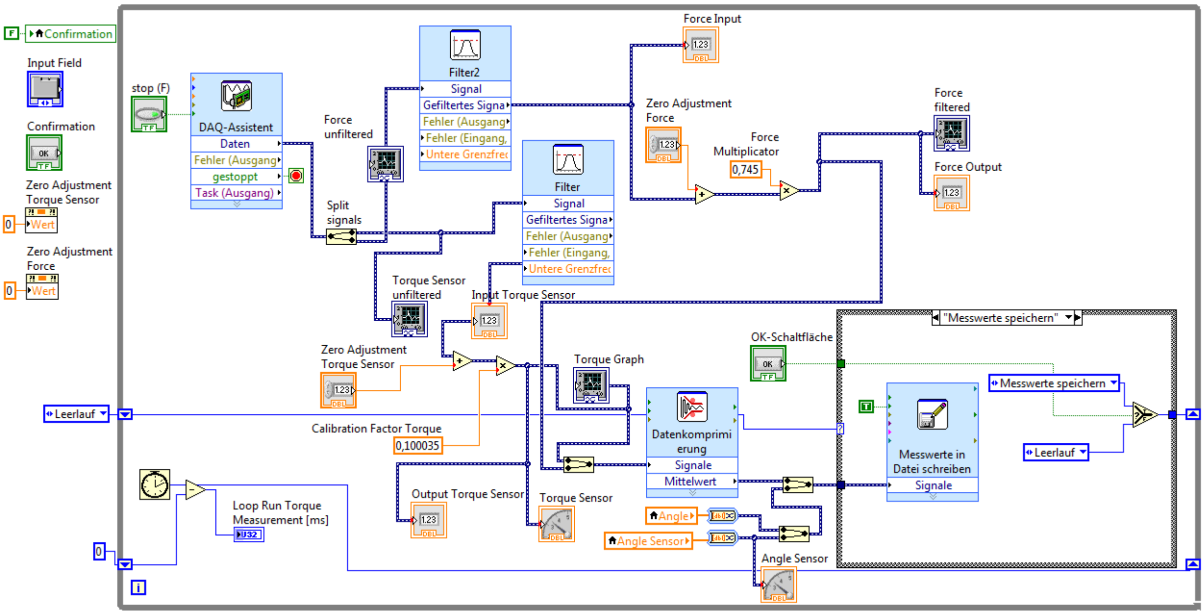
Confirmation
Input Field
Confirmation
Zero Adjustment Torque Sensor
Wert
Zero Adjustment Force
Wert
stop (F)
DAQ-Assistent
Daten
Fehler (Ausgang)
gestoppt
Task (Ausgang)
Force unfiltered
Split signals
Filter2
Signal
Gefiltertes Signal
Fehler (Ausgang)
Fehler (Eingang)
Untere Grenzfrequenz
Filter
Signal
Gefiltertes Signal
Fehler (Ausgang)
Fehler (Eingang)
Untere Grenzfrequenz
Force Input
Zero Adjustment Force
Force Multiplicator
0,745
Force filtered
Force Output
Torque Sensor unfiltered
Input Torque Sensor
Zero Adjustment Torque Sensor
Calibration Factor Torque
0,100035
Leerlauf
Torque Graph
Datenkompriмierung
Signale
Mittelwert
OK-Schaltfläche
"Messwerte speichern"
Messwerte speichern
Messwerte in Datei schreiben
Signale
Leerlauf
Loop Run Torque Measurement [ms]
Output Torque Sensor
Torque Sensor
Angle
Angle Sensor
Angle Sensor

Fig. A-22: Block diagram of data collection subprogram

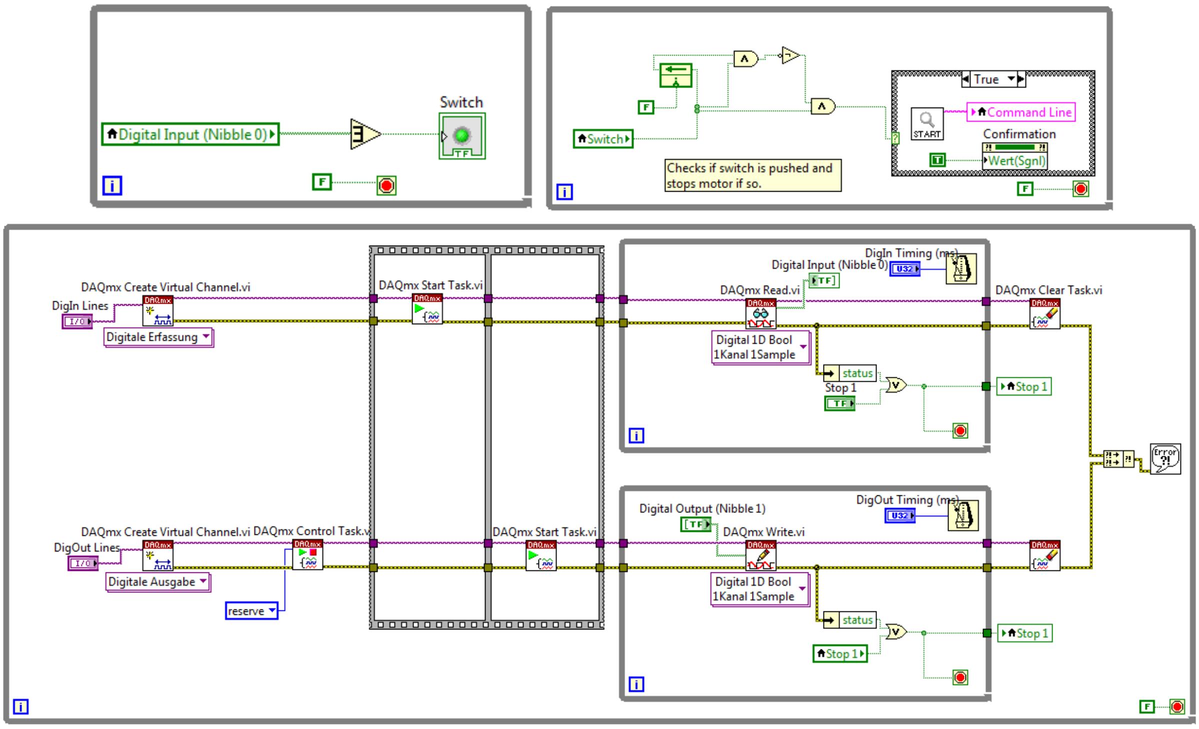
Digital Input (Nibble 0)
Switch
Switch
Checks if switch is pushed and stops motor if so.
True
Command Line
Confirmation
START
Wert(Sgnl)
DAQmx Create Virtual Channel.vi
DigIn Lines
Digitale Erfassung
DAQmx Start Task.vi
Digital Input (Nibble 0)
DigIn Timing (ms)
DAQmx Read.vi
Digital 1D Bool 1Kanal 1Sample
status
Stop 1
DAQmx Clear Task.vi
Stop 1
DAQmx Create Virtual Channel.vi
DAQmx Control Task.vi
DigOut Lines
Digitale Ausgabe
reserve
DAQmx Start Task.vi
Digital Output (Nibble 1)
DigOut Timing (ms)
DAQmx Write.vi
Digital 1D Bool 1Kanal 1Sample
status
Stop 1
Stop 1

Fig. A-23: Block diagram of switch control